Grant Agreement Number 608553

IMAGE
Integrated Methods for Advanced Geothermal Exploration

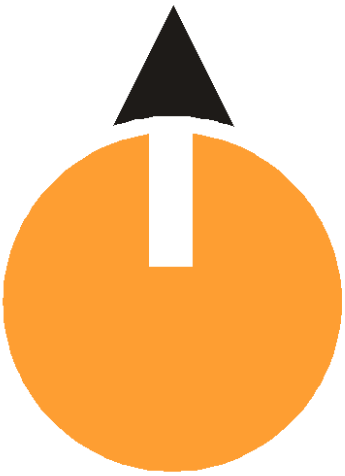

IMAGE-D8.02:
Application of exploration techniques on sedimentary basin fields

Responsible author	Dezayes Chrystel (BRGM)	
Responsible WP-leader	Dezayes Chrystel (BRGM)	
Contributions by:	Afshari Moein Mohammad (ETH Zürich) Bitri Adnand (BRGM) Bretaudeau Ftançois (BRGM) Carpentier Stephan (TNO) Coppo Nicolas (BRGM) Darnet Mathieu (BRGM) Delatre Mickael (BRGM) Dezayes Chrystel (BRGM) Evans Keith (ETH Zürich) Gal Frederik (BRGM) Guglielmetti Luca (University of Geneva) Imtiaz Afifa (BRGM) Lemoine Anne (BRGM)	Manukyan Edgar (ETH Zürich) Meekes Sjef (TNO) Nawratil de Bono Carole (SIG) Reiser Fabienne (ETH Zürich) Sanjuan Bernard (BRGM) Schmelzbach Cédric (ETH Zürich) Tormann Tessa (ETH) Valley Benoît (Univ. Neuchâtel) van Haeringen Dirk (TNO) Vandeweijer Vincent (TNO) Verdel Arie (TNO) Wawryniak Pierre (BRGM) Wiemer Stephan (ETH)

Introduction & summary

This report details the application of exploration techniques (task 8.02) developped in the WP7 and applied on the sites selected following the task 6.02 (IMAGE deliverable D6.02). In this previous task, we defined three targets : the Upper Rhine Graben as a brown site or test site, where a solid experience with standard exploration tools and databases exist, the Molasse Basin and the Lower Rhine graben, as green sites ou new sites, where the geothermal exploration is on-going.

In the Upper Rhine Graben, geophysical tests have been done in the area of Strasbourg, where some geothermal operations are planned managed by FONROCHE Geothermie and ES-G. On this area, a passive seismic network has been deployed in order to test the data acquisition in a noisy environment (close to a large town). This data have been used as two approaches: a joint inversion of group speed of Rayleigh waves obtained through long-range noise correlation and H/V curves associated with the main site effect, and a computation of receiver functions from teleseismic events recorded in a urban area. The aim of these approaches is to precise the depth of sediment-basement interface, which is not reach by the older seismic profile acquired by the oil industry (because it was not the target for the petroleum reservoir). On the exactly the same area, a electromagnetic survey has been done, included a CSEM (Controlled Source ElectroMagnetism) acquisition.

A systematic analysis of the fractal properties of the deep geothermal reservoirs of Basel and Soultz has been performed in order to investigate the scaling relationships of natural fracture, stress and induced seismicity.

In the Molasse Bassin, two sites have been investigated. First, in Switzerland, near Geneva, an old geothermal well has been used to test an acquisition of Vertical Seismic Profile (VSP) and analyse the geochemistry of the fluid. These works were performed with the industrial owner of the weel, SIG (Service Industriel de Genève), who forecast to reuse this well. In the German part of the Molasse Basin, the town of Bal Waldsee is planning a geothermal system and acquired local vintage 2D seismic data from oil and gas companies. In order to better analyse these data, a new NLM (Non Local Means) reprocessing was applied and compared to the classical pre-stack seismic reprocessing.

A another passive seismic survey was done in the Grote Peel area in The Netherlands with the purpose to retrieve surface waves from ambient noise.

Table of Content

Table of Figures

1 Introduction

This report details the application of exploration techniques (task 8.02) developped in the WP7 and applied on the sites selected following the task 6.02 (IMAGE deliverable D6.02). In this previous task, we defined three targets : the Upper Rhine Graben as a brown site or test site, where a solid experience with standard exploration tools and databases exist, the Molasse Basin and the Lower Rhine graben, as green sites ou new sites, where the geothermal exploration is on-going.

In the Upper Rhine Graben, geophysical tests have been done in the area of Strasbourg, where some geothermal operations are planned managed by FONROCHE Geothermie and ES-G. On this area, a passive seismic network has been deployed in order to test the data acquisition in a noisy environment (close to a large town). This data have been used as two approaches: a joint inversion of group speed of Rayleigh waves obtained through long-range noise correlation and H/V curves associated with the main site effect, and a computation of receiver functions from teleseismic events recorded in a urban area. The aim of these approaches is to precise the depth of sediment-basement interface, which is not reach by the older seismic profile acquired by the oil industry (because it was not the target for the petroleum reservoir). On the exactly the same area, a electromagnetic survey has been done, included a CSEM (Controlled Source ElectroMagnetism) acquisition.

A systematic analysis of the fractal properties of the deep geothermal reservoirs of Basel and Soultz has been performed in order to investigate the scaling relationships of natural fracture, stress and induced seismicity.

In the Molasse Bassin, two sites have been investigated. First, in Switzerland, near Geneva, an old geothermal well has been used to test an acquisition of Vertical Seismic Profile (VSP) and analyse the geochemistry of the fluid. These works were performed with the industrial owner of the weel, SIG (Service Industriel de Genève), who forecast to reuse this well. In the German part of the Molasse Basin, the town of Bal Waldsee is planning a geothermal system and acquired local vintage 2D seismic data from oil and gas companies. In order to better analyse these data, a new NLM (Non Local Means) reprocessing was applied and compared to the classical pre-stack seismic reprocessing.

A another passive seismic survey was done in the Grote Peel area in The Netherlands with the purpose to retrieve surface waves from ambient noise.

2 Upper Rhine Graben – Strasbourg area

2.1 Introduction

Some thermal anomalies are presents in the Rhine Graben due to conduction and convection phenomena. The choice of the prospect has been done in relation to the local thermal anomalies and the presence of faults and fractures to expect permeability and fluid circulation (see IMAGE deliverable 6.02). Moreover, the objective of the project being to predict the better drilling position, we also take into account the presence of future geothermal projects. It is the case around the Strasbourg town with future industrial operations of FONROCHE Géothermie and ES-G. The prospect chosen is then located on the thermal anomaly of Strasbourg, at the west of the town (Figure 1). This area is rather good known by oil and gas prospection and constitutes the “green site” for the IMAGE project. The application of exploration methods developed in the WP7 should coufirme what we previously known.

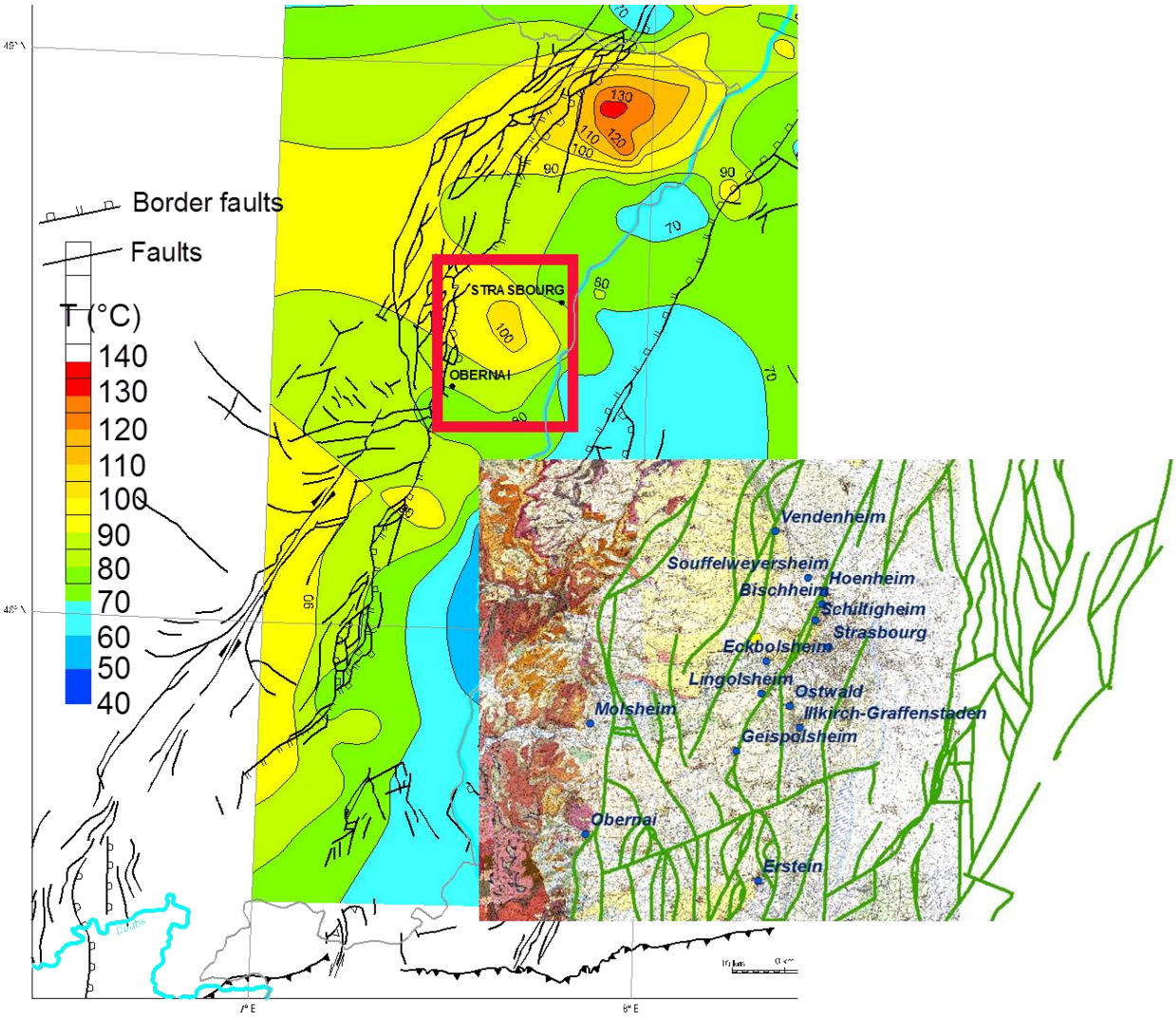

Figure 1 – Location of the application site in the Upper Rhine Graben

2.2 Passive Seismic

This part will detail the setup, the processing and the main results obtained with a small seismological network deployed on the Alsace test field during the winter 2015-2016. Several approaches were simultaneously undertaken :

- A joint inversion of group speed of Rayleigh waves obtained through long-range noise correlation and H/V curves associated with the main site effect was attempted in order to get the depth of the sediment-bedrock interface
- The possibility to compute receiver functions from teleseismic events recorded in a urban area was tested

2.2.1 Data acquisition

In this part, we will detail the design (placement, type of station, etc.) of the network, explain the choices made, do a first analysis and draw the first conclusions for future deployments.

2.2.1.1 Design of the network

For the field study, 8 stations were deployed in a 10x10 km area as shown in the map Figure 2. Datas from the permanent station in Strasbourg were provided by RESIF/EOST for this study. The initial distance between stations was defined by the estimated depth of the sediment-rock interface of 3 kms.

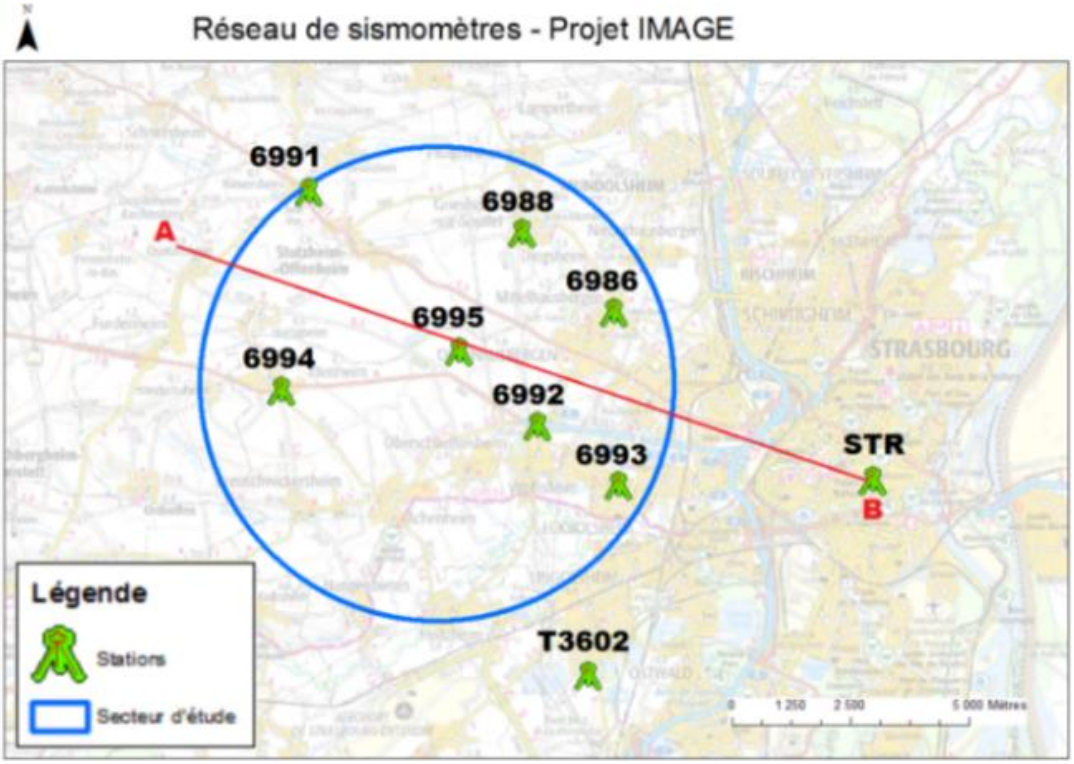

Figure 2 : layout of the network in the Strasbourg area. Stations from 6996 to 6995 and T3602 were deployed by BRGM, STR is the permanent station manned by RESIF/EOST

The following stations were used :

- For stations 6986 to 6995, Guralp CMG-6TD 10s-50 Hz broadband sensors were deployed with internal Flash memory, except for station 6992 where a data logger was installed
- For station T3602, a Guralp CMG-3TD with a broader frequency range (60 s to 50 Hz) was deployed
- Station STR is fitted with a Streckeisen STS2 seismometer, able to go down to 120s for the lower frequency and therefore suited for observatory duty

All stations have a time synchronisation from GPS receivers

As the political context in the area for geothermy is quite sensitive, it was decided to imply as soon as possible local authorities to find suitable locations for the seismometers. Stations were placed in various locations;

- Stations 6986, 6988 and 6991 were placed in the paved basement of the townhall, with heating systems nearby
- Station 6994 was placed in a non-paved basement of a private property
- Station 6992 was placed at the first floor (no basement) of the firefighter regional office, near an hospital
- Station 6993 was placed in a private house garage
- Station 6995 was placed in the basement of a private building company with a heating system, near a quarry6
- Station T3602 was placed in a technical room within a track and field sports center

Because of no satisfactory solution found in the SW corner, it was not possible to place a station to complete the circle.

2.2.1.2 First analysis of the network data

Data was acquired from November 2015 to March 2016, however several stations malfunctioned and did not record for some time. Fortunately, an engineer was scheduled to do regular visits to all stations in order to retrieve the data and could therefore repair the malfunctioning stations.

For several stations, a FFT of the vertical component was performed with sliding windows in order to get an estimate of the evolution of the noise power spectrum with time. All stations exhibit the same behaviour, shown in Figure 3.

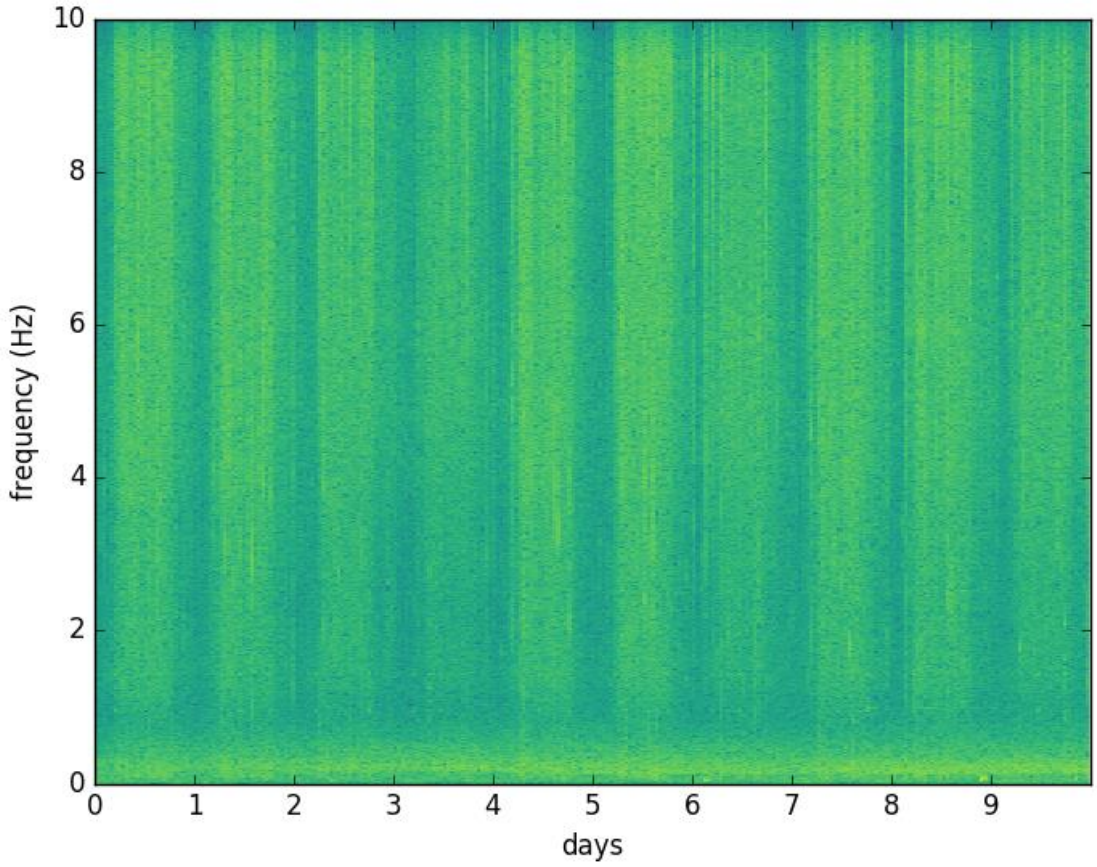

Figure 3 : spectrogram of station 6988 over one week (with 5 mins windows). X axis : time in days, Y axis : frequency in Hz

This figure shows a typical noise environment for semi-urban areas : road traffic during the day generates “high-frequency” (over 1 Hz) noise that quiets down during the night, while natural sources generate a constant background noise below 0.5 Hz. Between these two frequencies noise energy is lacking, which is an advantage to detect events but is an hindrance for noise-based methods. On several sites, heating systems nearby generate high-frequency events when they are activated. These events can be an hindrance for event-based methods, as can be seen on the raw recording :

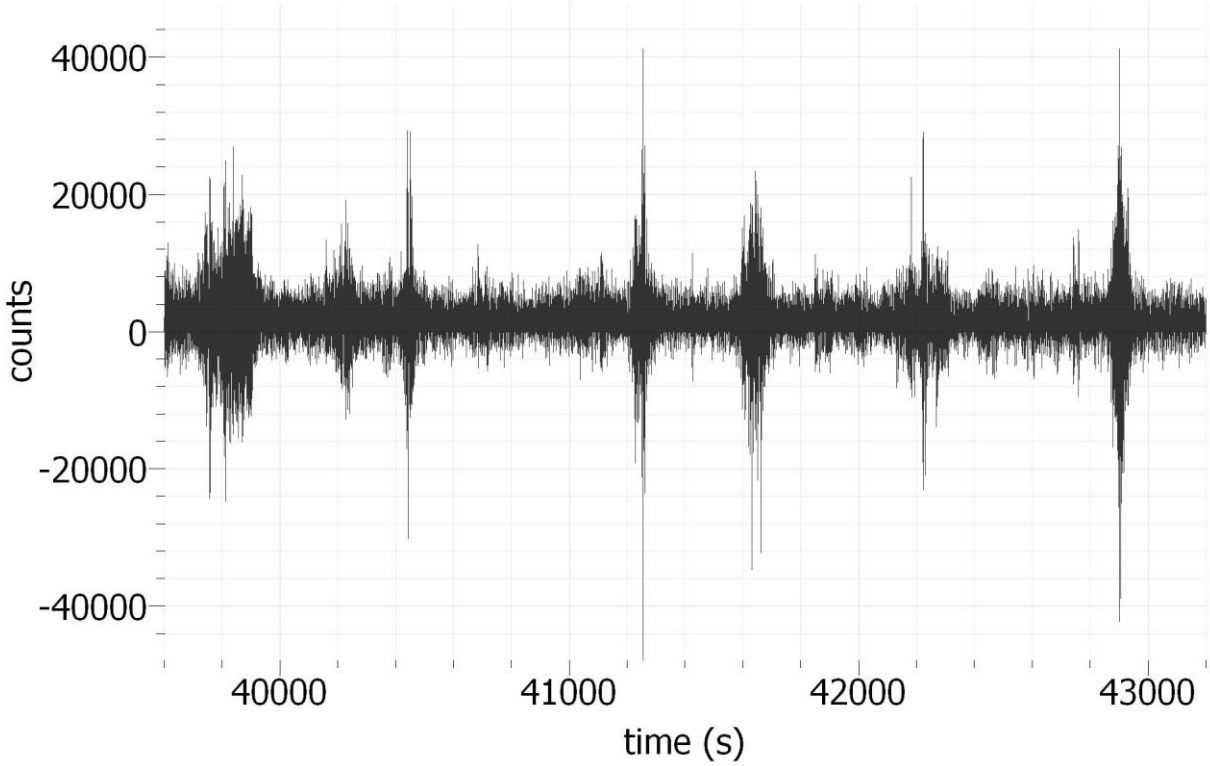

Figure 4 : example of a dayligh recording at station 6988 (12 AM GMT+00). Spikes in recording are linked to the heating system and are not seismic events

2.2.1.3 First conclusions regarding the network design and recommendations for future implantations

The network was deployed quite lately in the project, due to several changes of studied area linked to changes in IMAGE consortium. As such, several points could have been improved and should be kept in mind for future network deployments for geothermal targets in semi-urban areas :

- More time shall be spent for permiting in order to improve the locations and avoid machines in cellars. Given enough preparation, even in semi-urban areas installing stations in open fields should be considered – although the theft problem can be a real issue contrary to deserted areas such as the geothermal fields in Iceland
- Doing a 2D tomography with 8 stations gives sketchy images at best. With few stations, a linear network perpendicular to the main geological axis will get better results for the same investment. More generally, network designing should take advantage of prior geological analysis, and in return should be designed in a way to reduce the main uncertainties of these studies – in this case, a cross-shaped network in order to explore the E-W variability and measure the N-S trend would have been better

- It was discovered thereafter that the sediment-bedrock interface was in fact deeper than thought. It is imperative to set a margin for network design in order to avoid such surprise.

It is however worth noticing that, in semi-urban areas, it is impossible to completely suppress road traffic noise with a temporary network : station T3602, although set in a very calm area, was able to pick up some road traffic noise, likely caused by the major road axis a few kilometers away. This problem is similar to the problem encountered by electromagnetic studies and major electrical power lines. We will show that it causes problems for methods based on event detection and analysis ; however, as shown below, methods based on frequency selection and noise processing are not affected.

2.2.2 Imaging the depth of the interface with seismic noise

This section will describe

- The prior reasons to use seismic noise for deep sedimentary basin imaging
- Processing of data and main results
- discussion about the lessons learned from this experiment and improvements that can be brought depending on the setup chosen

2.2.2.1 Why use seismic noise to get an image of sedimentary basins ?

2.2.2.1.1 Seismic noise as an alternate source for studies

Seismic noise commonly refers to the seismic waves recorded by a station that cannot be attributed to a clear source, such as an earthquake, a rock fall or an explosion. Seismic noise is generated by a wide range of sources, depending on the frequency considered : for periods over 3 seconds, ocean waves are identified as a reliable source (Ardhuin et al. 2011), while frequencies over 1 Hz are populated with anthropic generated sources (road traffic, power lines poles, etc.).

Several studies have shown that these wave sources can be used as alternate seismic sources to the seismic events and man-triggered source (explosives, vibrator trucks) even if noise sources are not evenly distributed, provided that enough data is gathered (see for example Derode et al. 2003). Hardware developments for the last 20 years allowed to increase the memory capacity of the sensors and therefore their ability to record the large amounts of data needed for such studies

2.2.2.1.2 Processing methods used in this study and their relevance for large sedimentary basins

Over the past decades, several methods relying on different assumptions and different network settings were devised in order to exploit to the fullest the data gathered to get velocity profiles. For example, small circular arrays are best used with MSPAC methods (Bettig et al. 2001) ; small but less regular arrays under a dominant source backazimut are best processed using HRFK (Capon 1969)

The scale of the study (a 10 by 10 km area) suggested strongly the use of long range noise correlation (Shapiro and Campillo 2004, Bensen et al 2007). This method relies on the retrieval of Rayleigh wave arrivals between pairs of stations and the measurement and inversion of the group velocity ; this method allows to measure different speed profiles along pair's segments, however the speed profile obtained is an average of the speed profiles.

It is possible to take advantage of the fact that the study is focusing on deep sedimentary basins over a crystalline bedrock : these basins exhibit usually what is called a "site effect", an amplification of the ongoing waves for certain frequencies caused by the wave bouncing between the surface and the strong sediment-bedrock interface. It is possible to measure the frequency response of the basin with H/V method (Nakamura 1989) and, in conjunction with a an estimate of the velocity profile,

perform a joint inversion of the group dispersion and the frequency peak of the H/V curve associated with the sediment/bedrock interface.

2.2.2.2 Data processing and inversion

2.2.2.2.1 Processing the data for long-range correlation method

a) Processing raw data to retrieve Rayleigh waves

The processing method used follows closely the recommendations of Bensen et al (2007), summarized in the following chart :

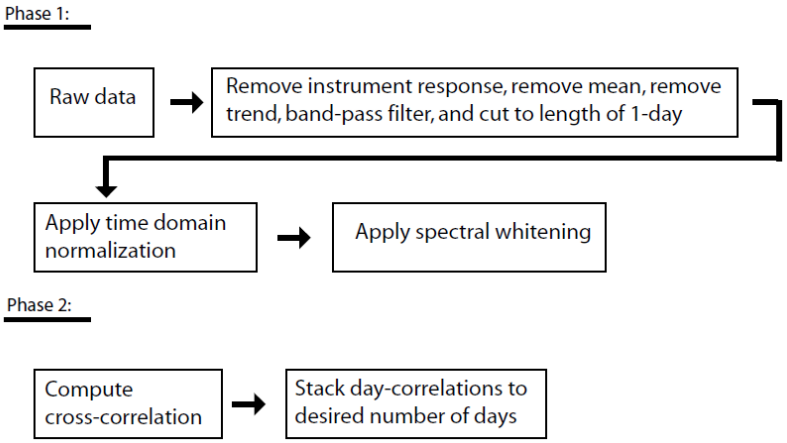

Figure 5 : workflow chart for long-range correlation, from Bensen et al (2007)

Vertical component data was band-pass filtered between 0.2 and 1 Hz without any instrument response removal, as it was estimated that this frequency band is well within the flat response of all sensors. The time-domain normalization used was the one-bit temporal whitening : Bensen et al (2007) show that it is reasonably effective and it is extremely simple and computer cost effective to implement.

For spectral whitening, a simple but effective method was defined : for each signal, the amplitude of its spectrum was set to 1 between 0.2 and 1 Hz. The amplitude spectrum of the correlations obtained this way was compared to correlations without spectral whitening :

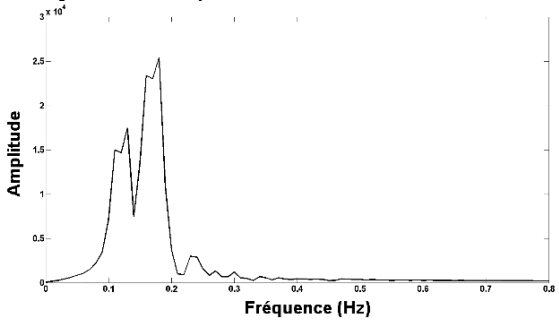

Figure 6 : amplitude spectrum of long-range noise correlation without spectral whitening

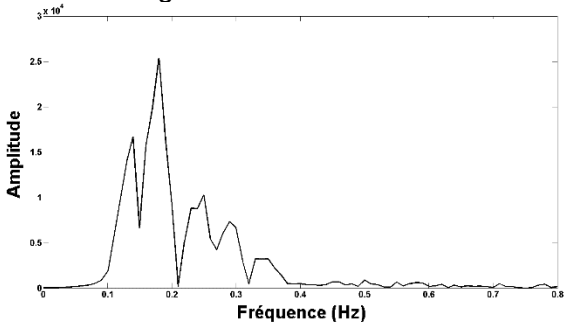

Figure 7 : amplitude spectrum of long-range noise correlation with spectral whitening

We have a distinct improvement in the 0.2-0.5 Hz frequency range ; however, above this band, the signal is still lacking. Spectral whitening, while useful, struggles to fill the seismic gap observed in the frequency band ; it is therefore mandatory to collect enough datas to compensate for this lack of energy.

Data were then crosscorrelated using 1 hour chunks of data, and the crosscorrelations produced were stacked. 15 days stacks were used as a compromise between computing time and Rayleigh wave recovery precision. The figure below shows one example of result :

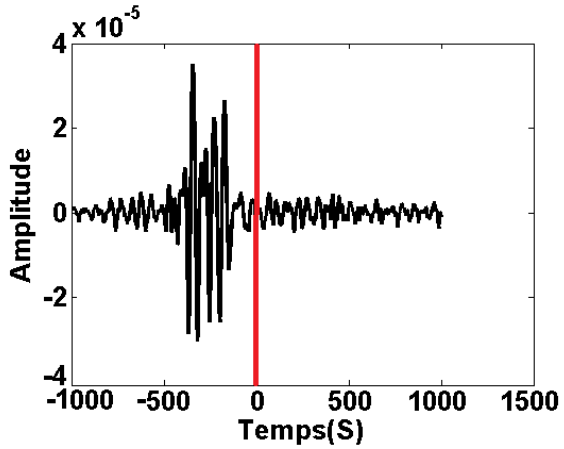

Figure 8 : example of crosscorrelation obtained with the 6991-STR station pair

These crosscorrelations are then processed through a time-frequency analysis in order to measure the dispersion of the extracted waves. The figure below shows all the dispersions obtained between all pairs of stations available :

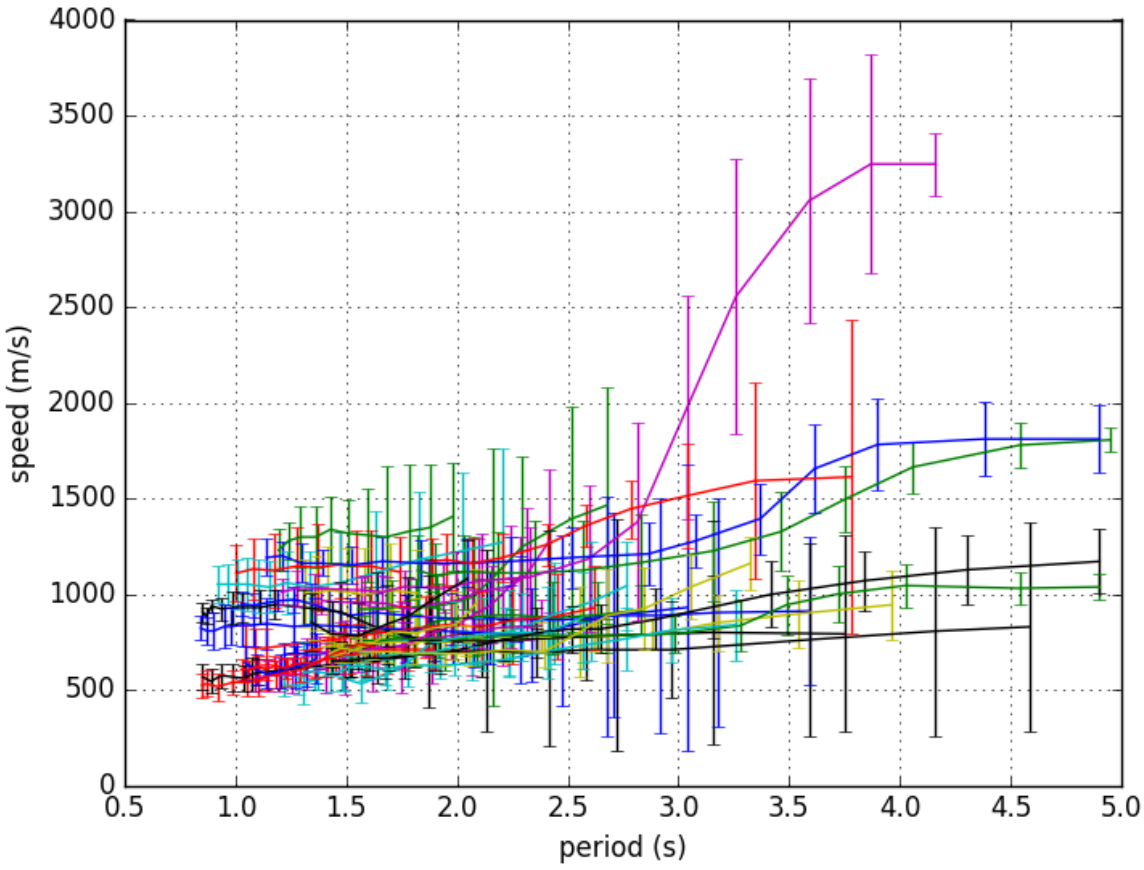

Figure 9 : dispersion between all station pairs measured through long-range correlation time_frequency analysis

Figure 9 shows that several dispersions fall into the same speed brackets at high frequency (two to three brackets) and at low frequency (three brackets), which is a strong indication that we extracted in fact overtone modes of Rayleigh waves. Given the error bars, we can therefore build an “average” dispersion for fundamental mode and mode 1 of Rayleigh waves.

2.2.2.2.2 Processing individual station data with H/V method

H/V method does not require as much data as long-range correlation. For each station, data during one night (in order to avoid human-induced events) was gathered and then processed through the GEOPSY software, implemented within the SESAME project and following its guidelines. Given the large amount of data available and the lack of low-frequency events, we chose 240 s. windows. H/V ratios were smoothed using Konno and Ohmachi spectral smoothing methods (Konno and Ohmachi 1998).

The H/V main curves are plotted in the 0.1-1 Hz range below :

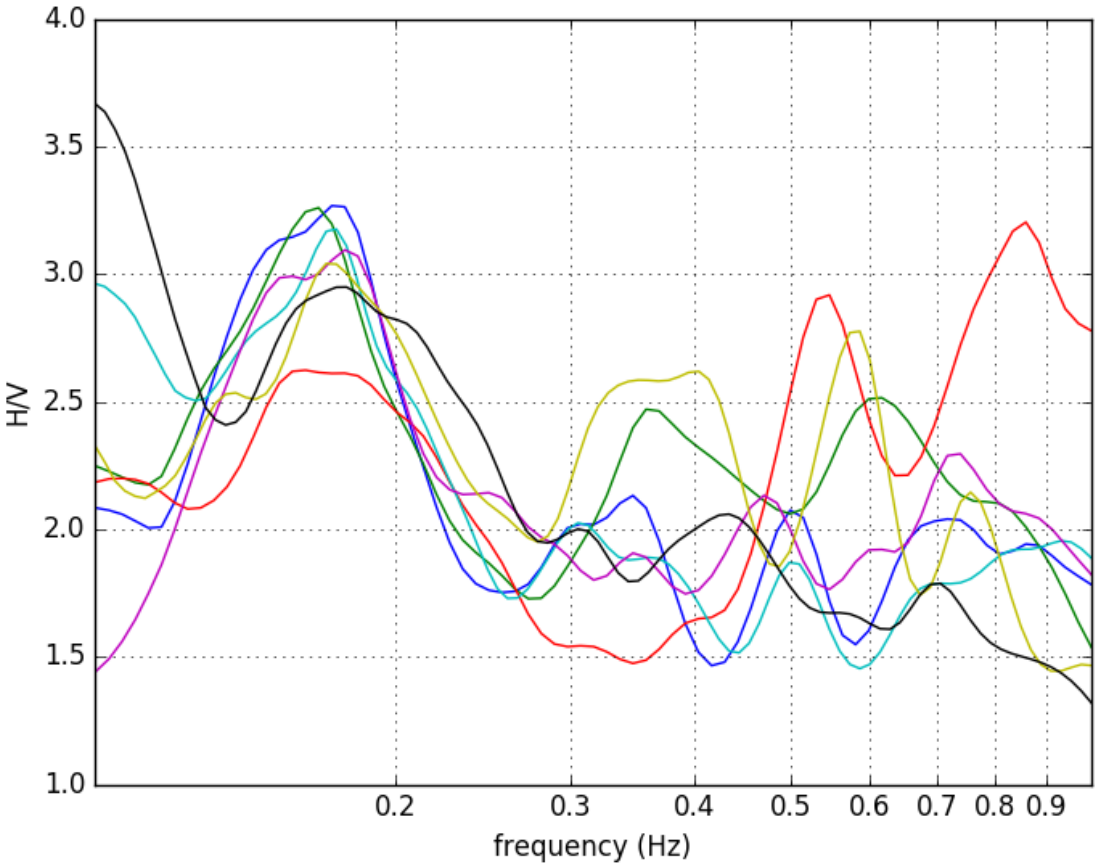

Figure 10 : H/V main curves for all stations

All stations exhibit a H/V peak around 0.17 Hz, and for a majority of stations this peak can be qualified as a site effect using SESAME criteria. Using simulations with simple 1D models consisting of an single sedimentary layer over the bedrock, this peak can be identified as the correct peak associated with the sediment-bedrock interface.

2.2.2.3 Joint inversion of dispersion and H/V curves

2.2.2.3.1 Inversion procedure and choices

The goal of the inversion process is to determine the depth of the sediment layer at different points. H/V peak is a signature of the sediment-bedrock interface ; for a simple model with a single layer above an half-space, the H/V frequency can be calculated with the following formula :

$$f_0 = {}^{Vs}/_{4h}$$

With Vs the S wave speed in the sediment layer and h the thickness of this layer.
This formula shows that H/V peaks alone cannot determine the thickness of the layer, as an estimate of the seismic wave speed is also needed. This is why joint inversion of H/V and dispersion is needed in order to retrieve the desired information.

Dispersion used for joint inversion was extracted from Figure 9, using two dispersion curves clearly identified as mode 0 and mode 1. The curves used are shown below :

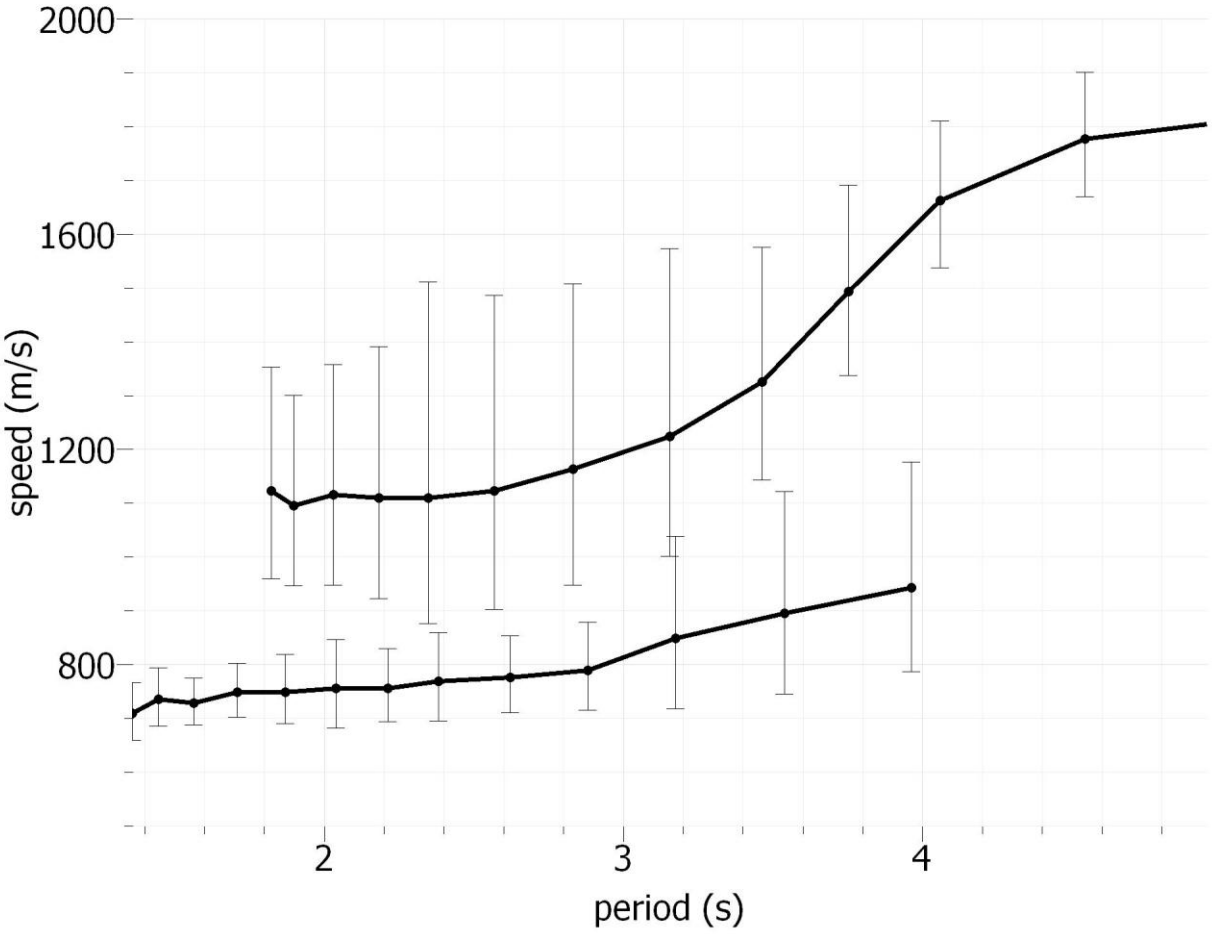

Figure 11 : group velocity dispersion : mode 0 and mode 1 used for inversion

For each station, the corresponding H/V curve was limited to the 0.1-0.35 Hz frequency range in order to isolate the peak associated with the desired interface.

The inversion method used is the neighbourhood algorithm implemented by Marc Wathelet in the GEOPSY software (Wathelet 2008). The initial parameter space was chosen very large on purpose, in order to be sure not to miss a plausible solution ; in order to get close to the geological logs available, 4 layers above an half-space were set with wide thickness and speed range. In order to limit the number of parameters to be inverted, Vp to Vs ratio was shared with all layers, while density

was fixed at 2000 kg/m3. Putting a fixed value for density is a common procedure in seismological inversions, as this value is known to be very poorly constrained by observations in this frequency range.

The last choice is to consider the relative weights of dispersion and H/V for the inversion process : we chose to put more emphasis on H/V in order to enhance the response to the half-space upper boundary. The rationale behind this choice is that dispersion will constrain the velocity profile while H/V will use this information to put more constrain on the thickness parameter. The Dinver module of GEOPSY proposes to add a weight for misfits ; we chose 0.2 to dispersion measurements and 1 to H/V measurements.

2.2.2.3.2 Example of the added value of H/V measurement : the 6986-6991 station pair

In order to show the resolution power added by H/V measurements, we selected the 6986-6991 station pair. We inverted first only the dispersion measurement, and we obtained the following velocity profile :

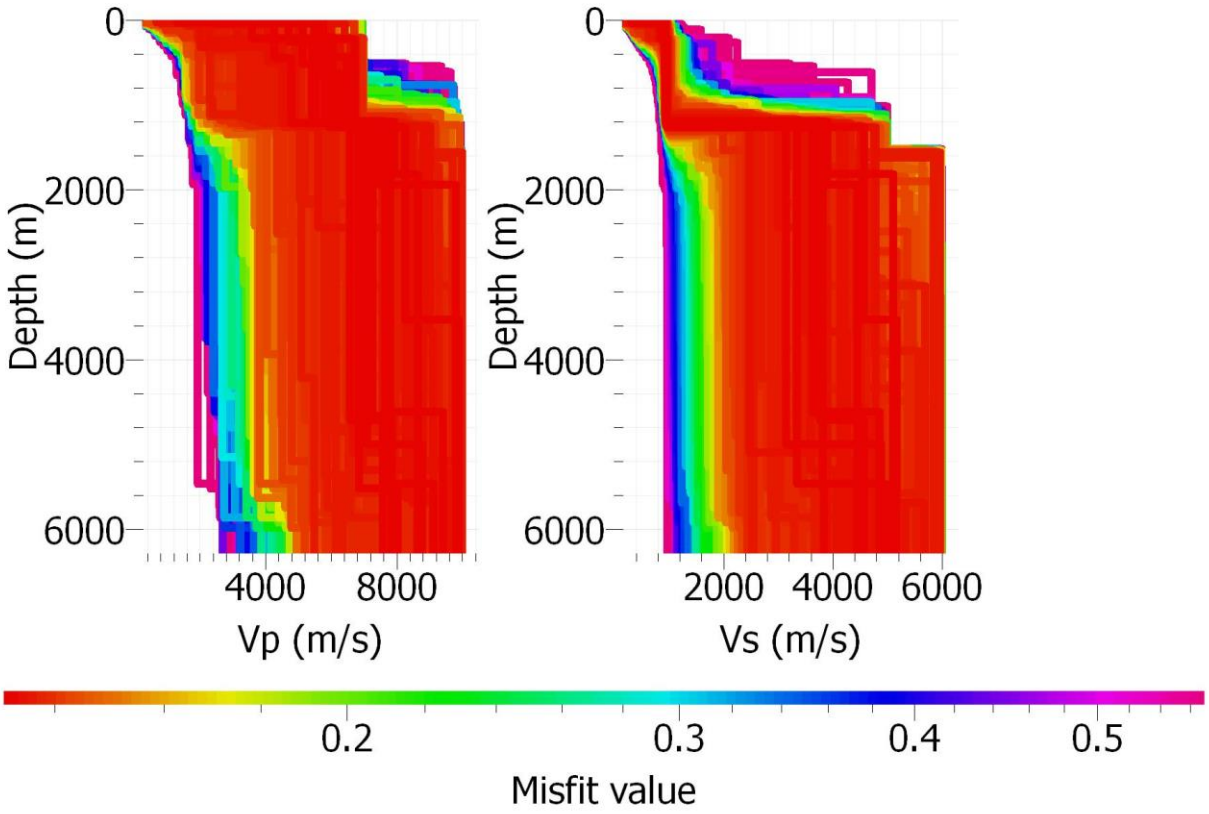

Figure 12 : velocity profiles obtained using the neighborhood algorithm and with only dispersion data for 6986-6991 , classified by misfit (see Wathelet 2008)

H/V measurements from station 6991 were then added following the procedure detailed above. The results obtained are shown in the figure below :

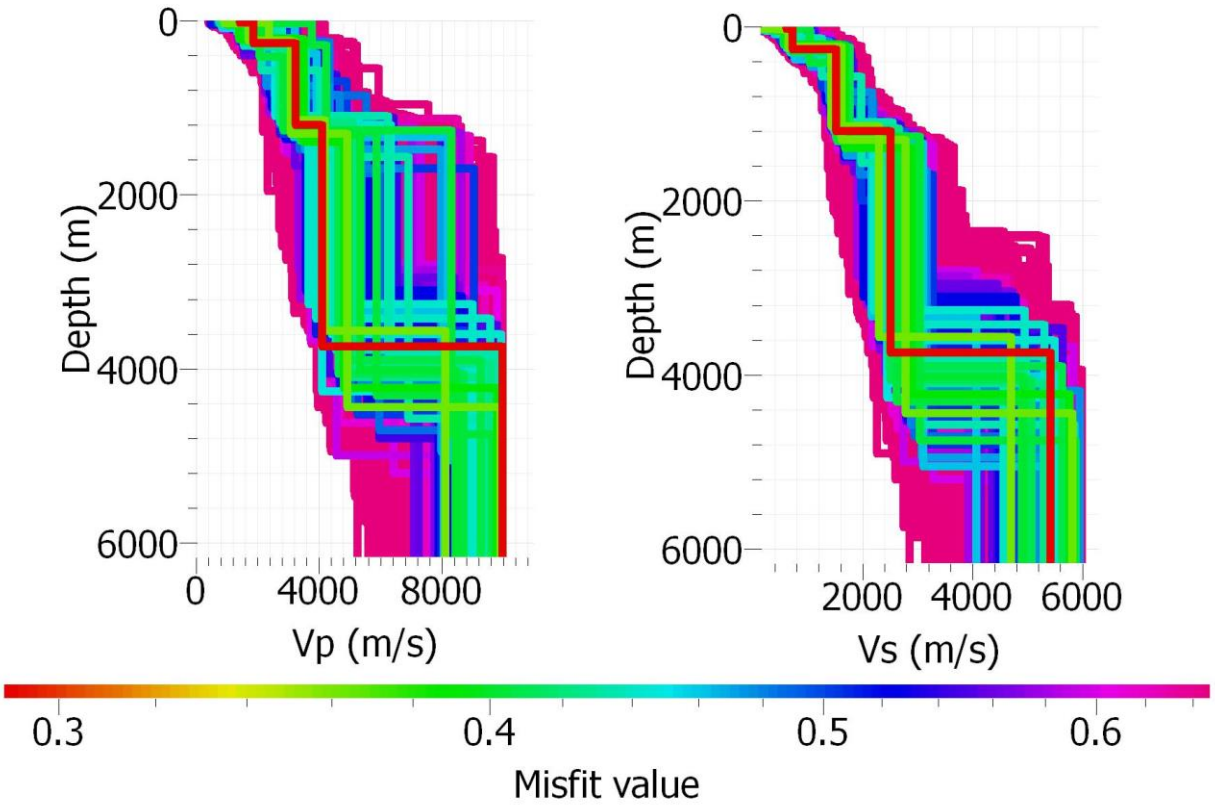

Figure 13 : velocity profiles obtained using the neighborhood algorithm, datas used : dispersion data for 6986-6991 and H/V curve for 6991 station, classified by misfit (see Wathelet 2008)

These figures show that H/V curves, in the case of a sedimentary basin above a strong bedrock, can improve greatly the precision of dispersion inversions for long-range noise correlations in the case of station distances falling short of the needed distance.

2.2.2.3.3 Results of joint inversion for all stations

We show below the results for all stations. For several stations, we managed to “force” the inversion to respect strictly the error bars, and therefore all results are equally plausible (red only curves) ; for some stations, this constrain did not manage to guide correctly the inversion, and therefore the results with misfit values are shown – these results respect on average the misfit threshold of 1, but some points may be outside the error bars. In both cases, all models shown have a misfit below 1, meaning that these models explain (totally or on average) the datas with error bars.

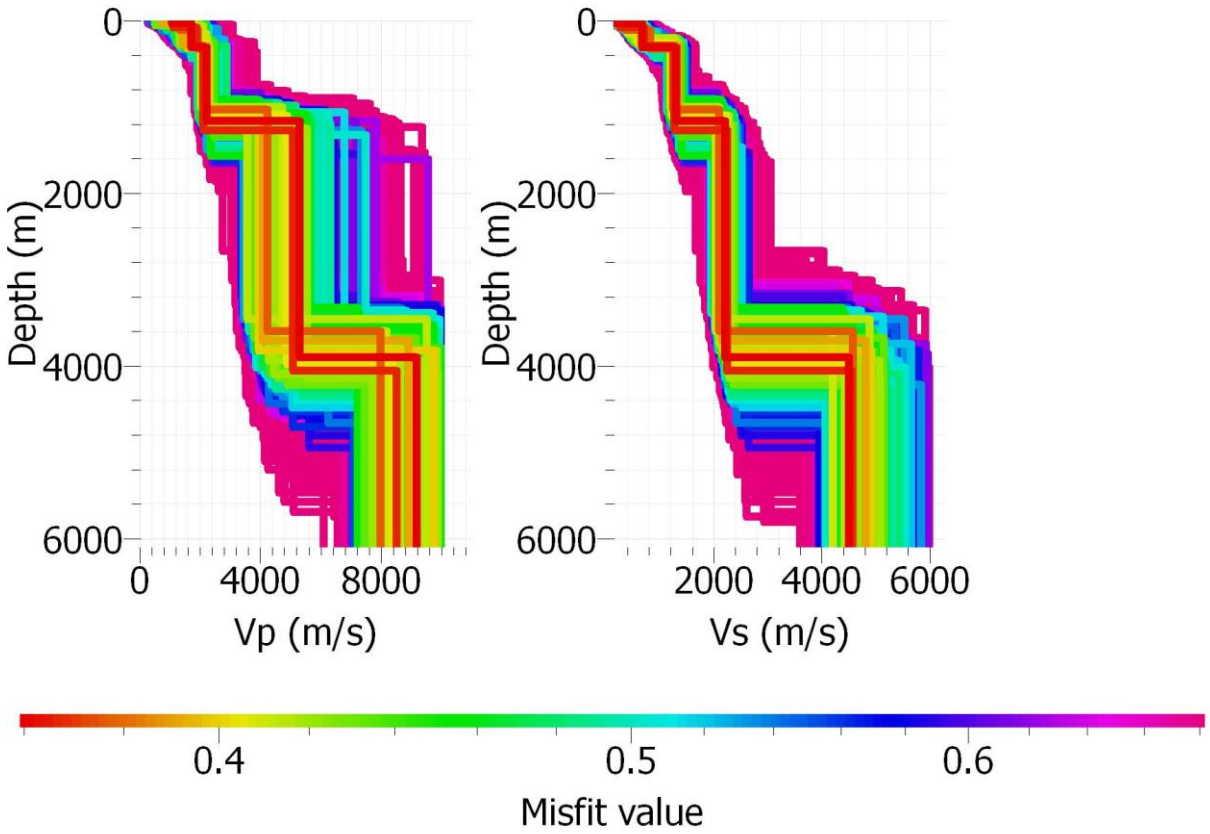

Figure 14 : Vp and Vs profiles produced by joint inversion for station 6986

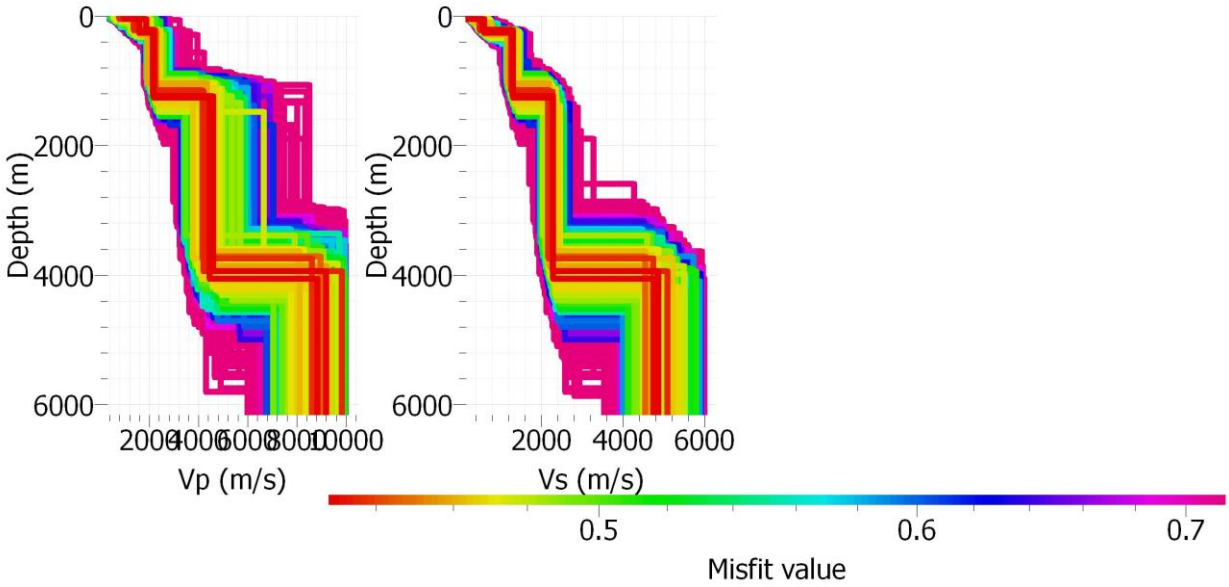

Figure 15 : Vp and Vs profiles produced by joint inversion for station 6988

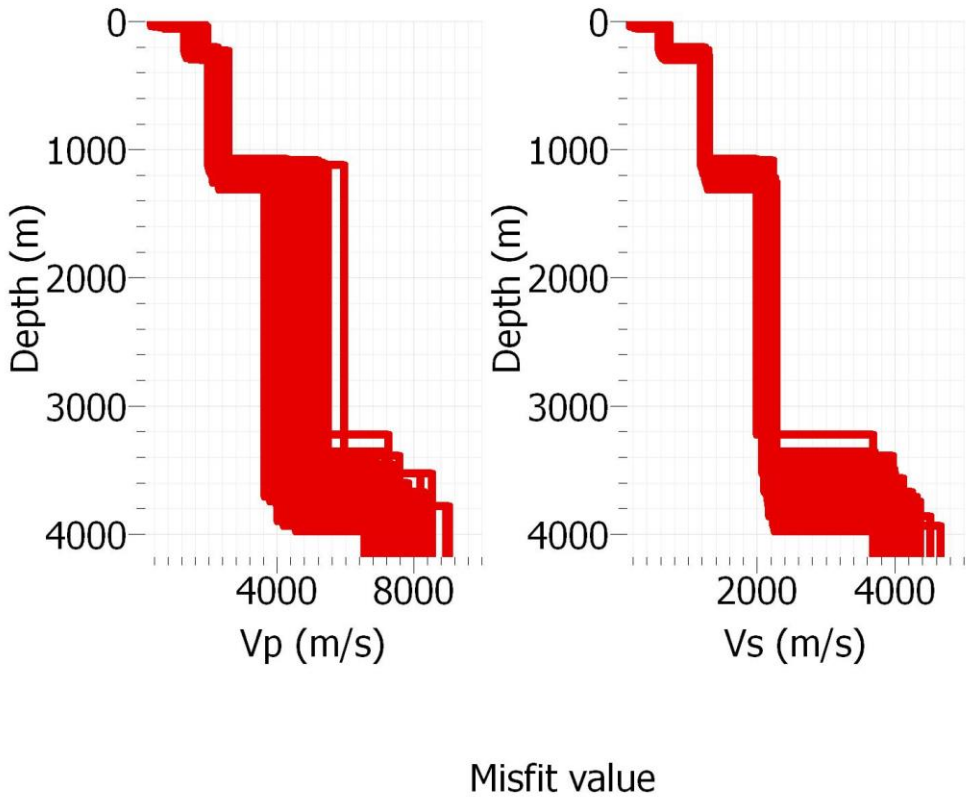

Figure 16 : Vp and Vs profiles produced by joint inversion for station 6991

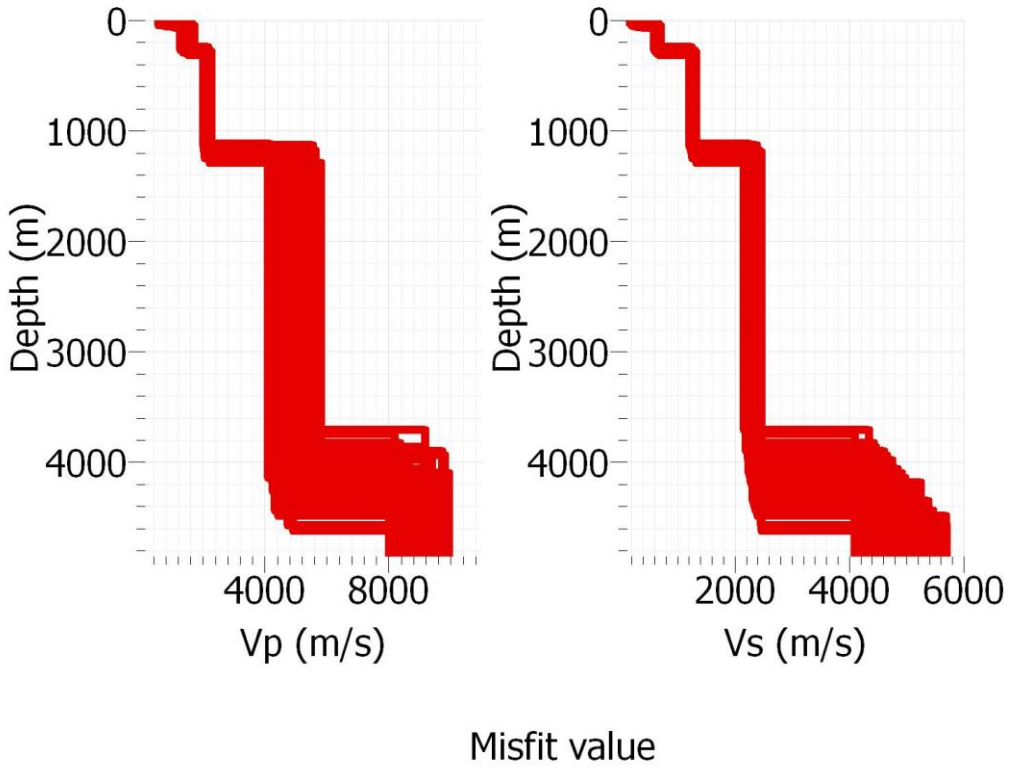

Figure 17 : Vp and Vs profiles produced by joint inversion for station 6992

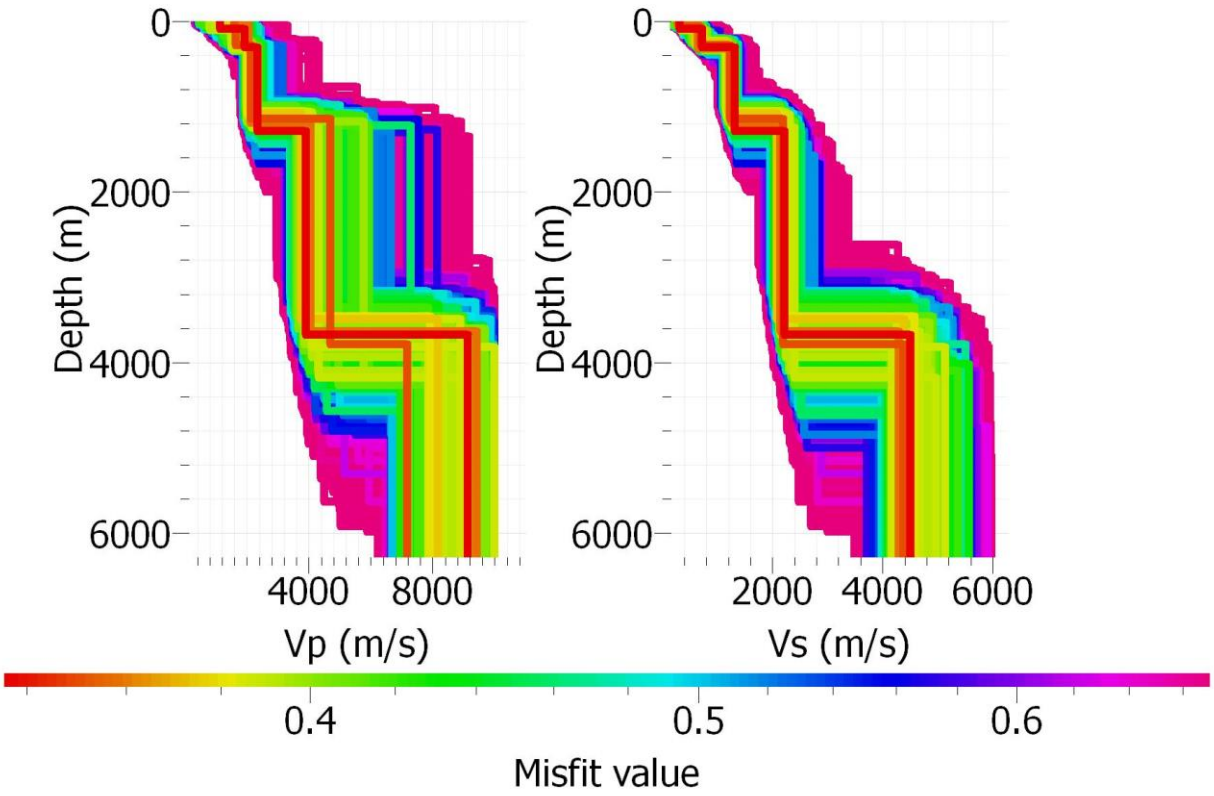

Figure 18 : Vp and Vs profiles produced by joint inversion for station 6993

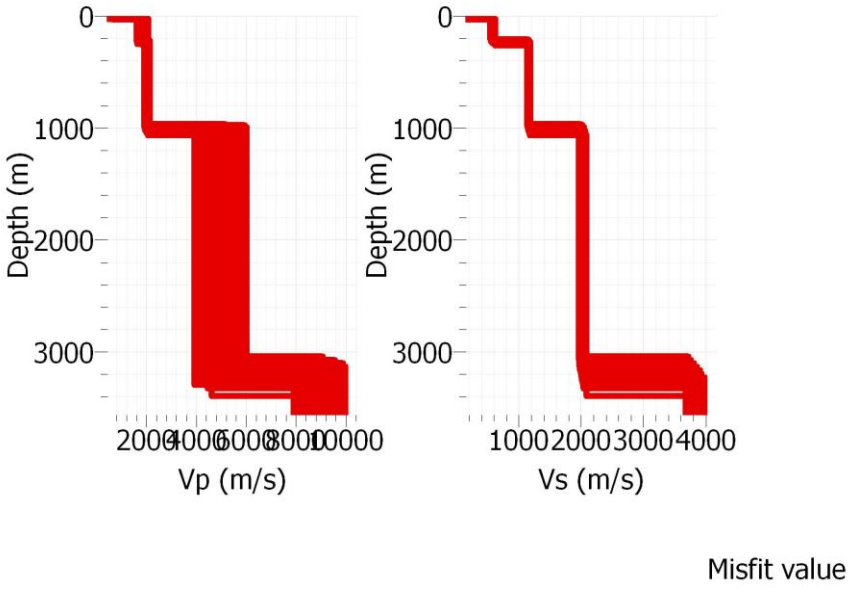

Figure 19 : Vp and Vs profiles produced by joint inversion for station 6994

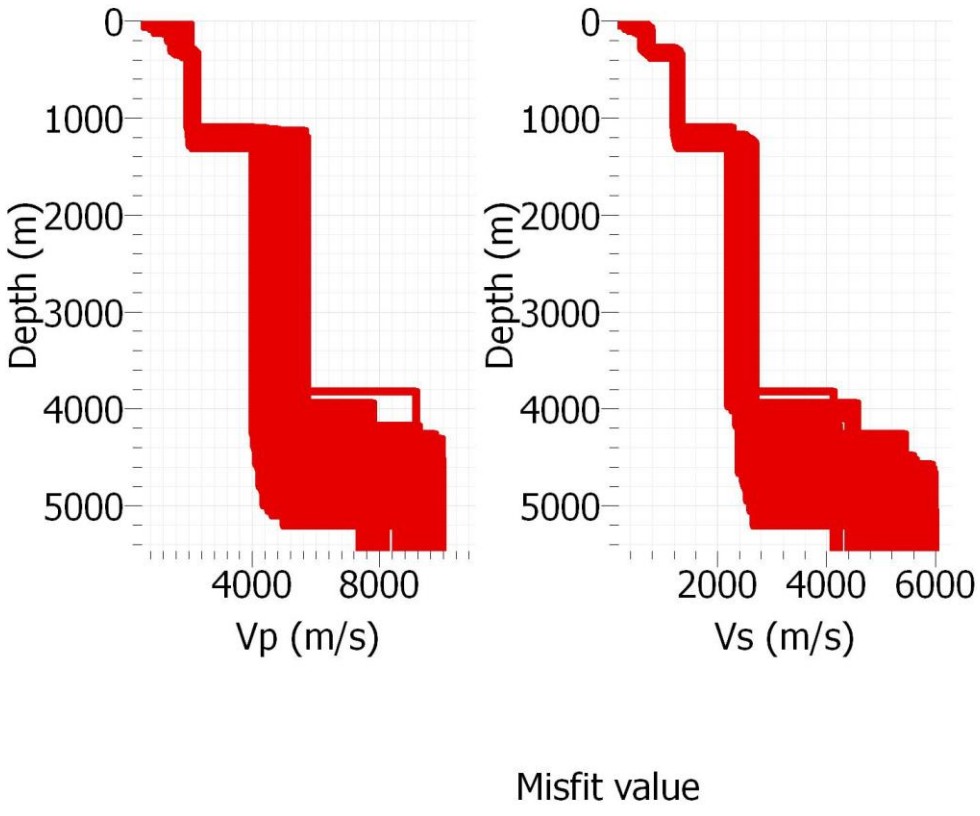

Figure 20 : Vp and Vs profiles produced by joint inversion for station T3602
Figure 21 : Vp and Vs profiles produced by joint inversion for station 6995

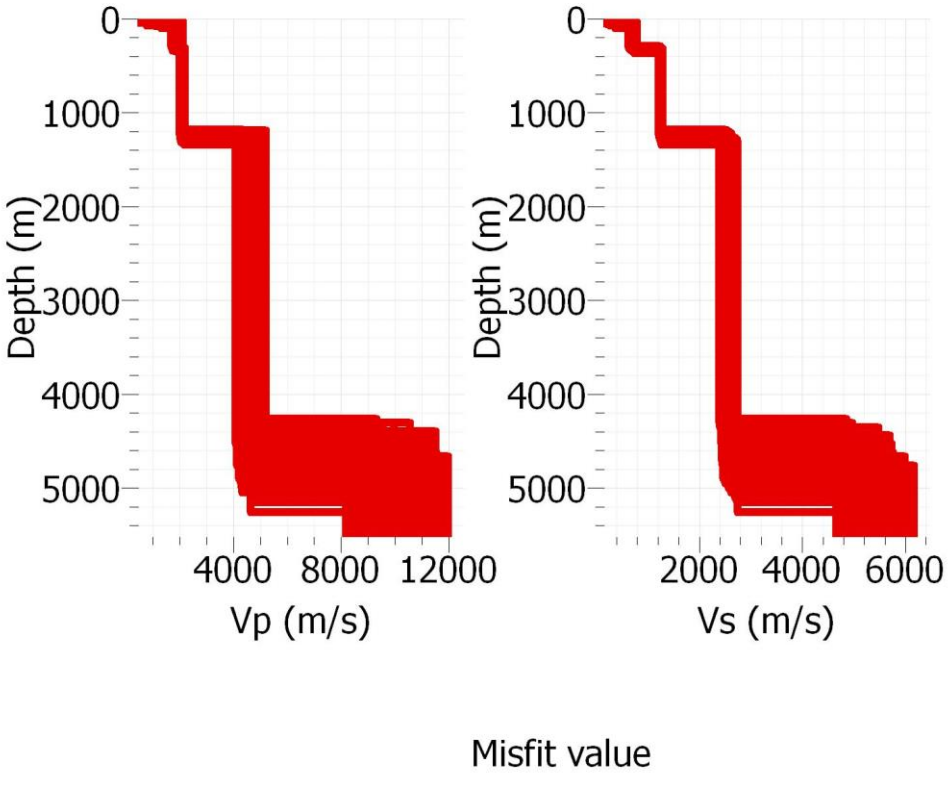

Figure 22 : Vp and Vs profiles produced by joint inversion for station T3602

We obtain the following depths of the sediment-bedrock interface for each station :

Station name	Estimated depth (m) + error bar (m)
6986	3910+-600
6988	3950+-600
6991	3675+-325
6992	4160+-480
6993	3875+-725
6994	3205+-200
6995	4530+-700
T3602	4765+-485

These results were compared to the geological models realised in the Interreg GeorG framework, in particular the modelled top of the Hercynian layer, as shown on the map below :

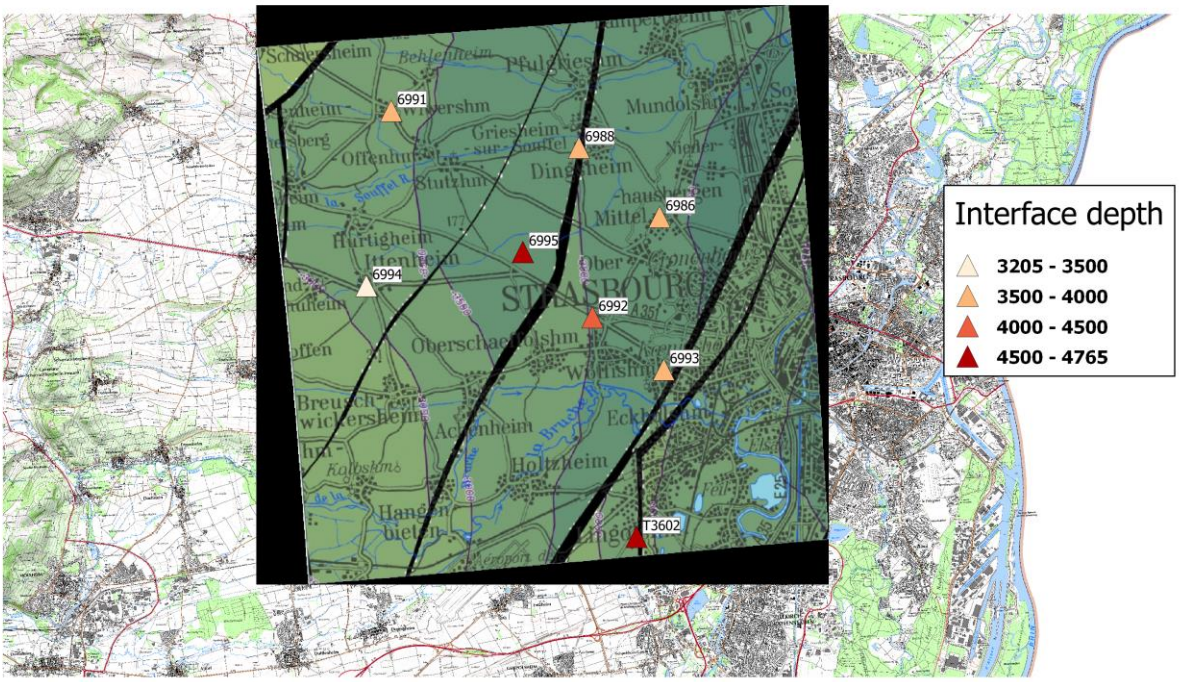

Figure 23 : map (RGF93 Lambert 93 coordinates) of the studied area, projected map of modelled Hercynian top depth and computed depths derived from velocity profiles at each station

Datas derived from the joint inversion are in overall good agreement with the modelled geological map which used seismic lines and well logs. 6992 gives a depth slightly greater than the model but is within the error bar, while 6995 and T3602 give depths greater than geological models even if one takes into account the error bar ; in particular, T3602 gives a far greater depth than previously expected, indicating that this segment should be put deeper than previously thought.

2.2.2.4 Methodological conclusions from this study

We have shown that joint inverting dispersion of Rayleigh waves and H/V curves for sedimentary basins susceptible to site effects (which is the case for the geothermal sedimentary targets examined

by IMAGE project) can give estimates of the sediment-bedrock interface with a 10% to 20% error bar. For less known sites, it is believed that this approach can therefore bring useful estimates for the target interface with a cost far lower than active seismic lines or well logs previously used to get this image.

This approach can of course be improved in order to be fully operational :

- As the initial goal of the network was not to do H/V surveys, only a few H/V curve were done. Since H/V method requires only a short amount of data (one night is more than enough even for deep basins) and can be done at any time, one can imagine doing a full H/V survey with a denser and more regular grid as it is already done for microzonation surveys ; since each point is independent to the others, such a study can be realised with limited manpower and equipment if time is given
- Error bars are still high, it is likely that it is mainly due to the limited precision of the dispersion obtained through long-range noise correlation. In order to improve the precision, one can experiment combining together several long-range noise correlations in order to improve the average through high number statistics ; another possibility is to switch to FK or MSPAC methods that will give an average velocity profile

2.2.3 Receiver functions

2.2.3.1 Introduction

The geothermal reservoirs, featuring permeable zones of sufficiently high temperature and fluid movement, are generally found at depths of at least a few kilometers in the Earth's crust. However, the uncertainty involved in efficiently localizing the resource at such depth has been a significant impediment in the exploitation of potential geothermal energy. Hence, more research is needed to explore different subsurface imaging tools in order to identify and characterize geothermal reservoirs in detail. In this context, the 2013-2017 IMAGE (Integrated Methods for Advanced Geothermal Exploration) project, co-funded by the European Commission (EC) within the 7th Framework Program for Research and Technological Development (FP7), sets out to develop an integrated geothermal exploration approach based on state-of-the-art scientific methods. One of the work packages of this project involves assessing the ability of teleseismic earthquake data and, hence, the value added in a multidisciplinary approach, in characterizing a continental sedimentary site.

Generally, the target geothermal zones are mostly controlled by faults and fractures. Hence, the focus in seismic geothermal exploration is mapping deep sedimentary and basement structures with such features. Comparing tomographic images of seismic body waves speeds (Vp and Vs) from the analysis of multicomponent ground motion records offer good insights into the underground fracturation level. In recent years, due to the increase in the amount of broadband seismic data available, many new approaches of exploiting large teleseismic datasets in computationally efficient ways have emerged. Receiver function (RF) studies have been one of them. Initially, they were focused on tectonic and geodynamic questions on regional scales of a few hundred square kilometers. Since the work of Langston (1979), the RF method is widely applied to study the discontinuities of Earth crust and mantle structure beneath seismic stations, particularly for imaging deeper interfaces (e.g., moho). Despite the relatively low-frequency range of teleseismic body waves, recent applications showed that RFs can provide information on shallow structure (e.g. depth <10 km : Leahy et al. 2012; Schmedes et al. 2012; Licciardi and Agostinetti 2014, 2017). Hence, the present work discusses the applicability of this method to three-component passive source data to investigate seismic discontinuities in the shallow crust for a peri-urban geothermal site.

2.2.3.2 Methodology

RF method is based on the idea that the recorded teleseismic long-period body waves, including direct P- and converted P-to-S wave, contains the information of the crustal structure near the receiver. These waveforms arriving at the recording stations generally carry the effects of earthquake source, the earth's structure in the vicinity of both the source and station and mantle propagation effects. The incident P-wave on the vertical component that carries out the source, path and instrument effects is deconvolved from the radial and tangential components. The resulting series of pulses, which represent the direct P-wave, the direct P-to-S conversions (Ps), several multiples (PpPs, PpSs, PsPs), and reverberations in the structure close to the recording stations, are known as the receiver functions (Langston 1979). As RFs are supposed to be sensitive to the impedance contrasts associated with major discontinuities in the crust (e.g., shallow low velocity layers in the sediment) as well as the Moho gradient, they exhibit the response of the crust and upper mantle.

The regular deconvolution methods for RF calculation are often limited to the relatively fewer observations from large seismic events, mainly because of the required high signal-to-noise ratio to extract good receiver functions, especially at temporary deployments. Several frequency (Clayton and Wiggins 1976; Park and Levin 2000) and time domain (Abers et al. 1995; Gurrola et al. 1995; Sheehan et al. 1995; Ligorria and Ammon 1999) deconvolution methods with different noise stabilization processes have been developed to deal with this issue. Based on Kikuchi and Kanamori (1982) iterative deconvolution methods in time domain, Ligorria and Ammon (1999) provided a new approach to solve this problem. It is characterized as a predictive convolution method which is supposed to produce truly causal signals with little or no loss of spectral information. The advantage of this method is that it is effective in estimating RFs not only from large events but also from moderate or noisy observations. It also simplifies the calculations by leaving the parameters, such as, water-level, time-domain smoothing and damping out of consideration. Since our objective is to characterize the capacity of RFs to constrain the interfaces (sediments/bedrock) at a relatively shallow depth (few km) and the target site is located near an urban area, this method is deemed as suitable for its capacity to remove anthropic noise.

2.2.3.2.1 Teleseismic Waves to probe Earth's Interior

The paths of the waves propagating through the Earth are affected by two main discontinuities at depths 30-60 km (Moho) and 2900 km (Gutenberg discontinuity). The Moho divides the Earth internally into an outer shell, called the crust, and an intermediate shell, called the mantle. For the seismic waves arriving from a distance between about 30° and 100°, the P and S waves travel through the lower mantle that is characterized by a rather smooth positive velocity and density gradient. The basic aspect of RF method is that part of the P waves signals from such distant events incident to a discontinuity in the crust or upper mantle will be converted to S waves (Ps) accompanied by possible reverberations and multiples (PpPs, PpSs, PsPs). These arrivals will be registered within the P wave coda within the first few seconds directly after the direct P wave arrival at the seismic station under consideration. The Ps conversions are sensitive to shear velocity contrasts and have much stronger amplitude on the horizontal component than on the vertical. By performing the deconvolution of vertical seismogram from the rotated horizontals, these phases are made identifiable on the Radial (R) and the Transverse (T) receiver functions. The delay time of each conversion is a function of the depth of the interface that generates it, while the amplitude is proportional to the size of the velocity contrast at depth. As the S waves travel slower than the P waves, the time difference in the arrival of the direct P wave and the converted phase (Ps) could be exploited to measure the depth of the discontinuity, provided the velocity model is known. In addition, the multiples resulting from the discontinuity and free surface could also be identified on the receiver function traces and used for exploring the relevant depths. In a medium that is horizontally isotropic, all the conversions due to impedance contrasts at depth are observed in the RRF while no energy should be present on the TRF (Agostinetti and Licciardi 2015). The presence of anisotropy or dipping interfaces in the subsurface causes the energy to rotate out of the plane of the incoming wave field

and gives a contribution to the TRF with known pattern of variations as a function of the backazimuth (Levin and Park 1998; Savage 1998).
Figure 24 shows the major Ps converted phases and the following two types of multiples, PpPs and PpSs, for a layer over a half space model as well as the corresponding receiver function trace. The converted Ps as well as the first multiple (PpPs) has a positive polarity, while the second multiple (PpSs) has a negative polarity.

RF functions are traditionally inverted to develop an estimation of shear wave velocity (Vs) structure under the recording station. It involves a non-linear inversion scheme, which requires an initial velocity and depth, generally taken from existing knowledge or reflection/refraction studies, and then iteratively improves the model by splitting it in a sequence of relatively thin layers with a gradual increase or decrease of the velocity. Figure 25 shows an example of the results of the receiver function inversion taken from the (Mohsen 2004).

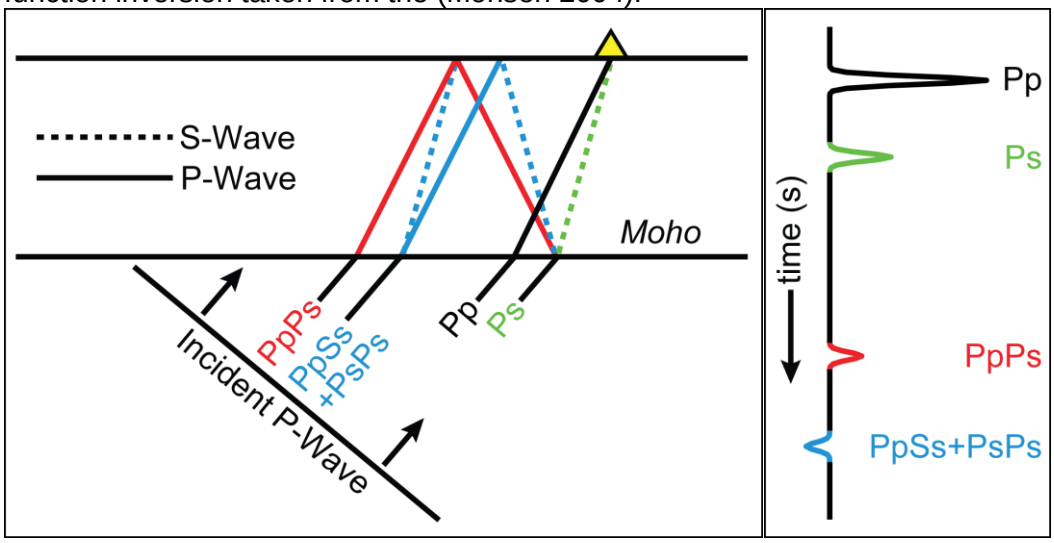

Figure 24: Left: Schematic representation of the major Ps converted phases for a layer over a half space model. Right: Simplified radial receiver function corresponding to the model showing the direct P and the Ps conversions from the Moho and its multiples (Mohsen 2004; Frassetto 2013). Upgoing travel paths are labelled with lower case letters, downgoing travel paths with upper case letters.

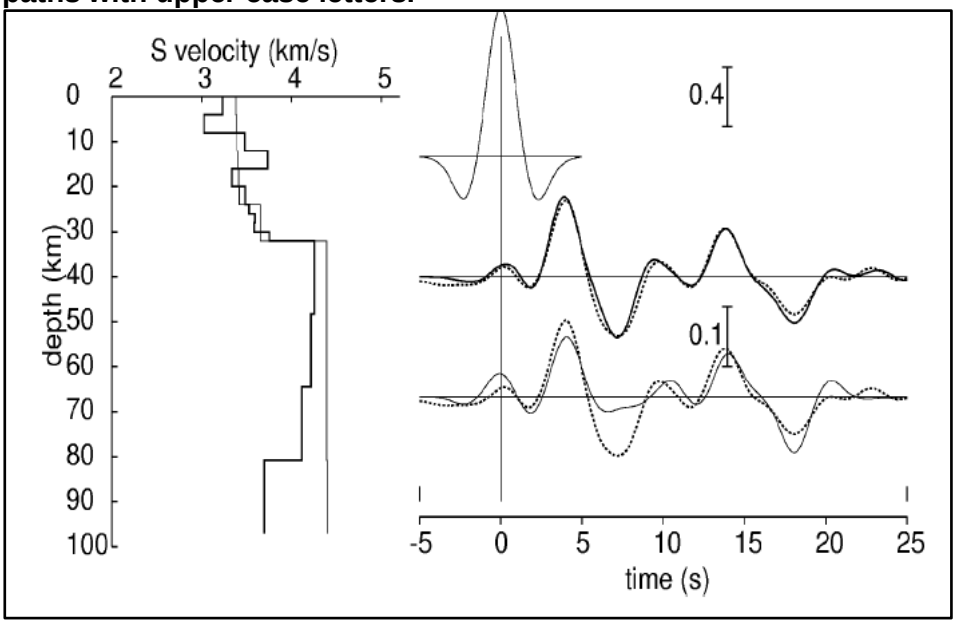

Figure 25: Receiver function inversion of a station (Mohsen 2004). Starting and final models are shown by thin and thick lines in the left, respectively. The dashed line in the right is the

observed receiver function, solid lines are synthetic receiver functions for the starting model (thin line at the bottom) and for the final model (thick line of the middle trace) after 4 iterations. The top trace on the right is the input P signal.

RF functions are also exploited to determine the crustal thickness and Vp/Vs ratio as the converted phase Ps and the crustal multiples PpPs and PpSs+PsPs contain important relevant information. The delay time of the direct Ps conversion from the Moho and the crustal multiples can be used to estimate the crustal thickness by a given average crustal P velocity.

H-κ stacking is a commonly used method to facilitate such RF analysis. It is a grid searching method that stacks receiver function amplitudes for a given seismic station at predicted arrival times of crustal phases based on the Moho depth (H) and Vp/Vs ratio (κ) of the crust (Zhu and Kanamori 2000). The P-to-S conversion at the Moho (Ps) and reverberations within the crust (PpPs and PpSs+PsPs) are used to reduce the inherent tradeoffs between H and κ (Zandt and Ammon 1995). The advantage of this method is that it does not require arrival-time pickings. Figure 26 shows an example of relation between crustal thickness and Vp/Vs curves representing the contributions of Ps and the crustal multiples to the stacked amplitudes as a function of crustal thickness and Vp/Vs.

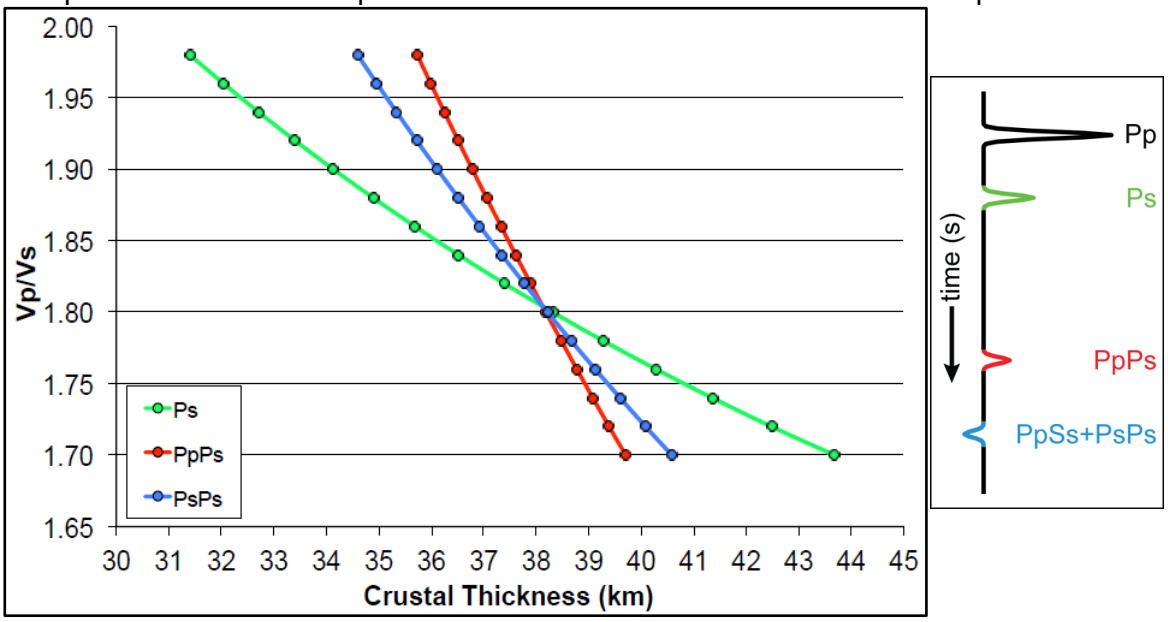

Figure 26: Curves showing the contributions of Ps and its two major crustal multiples (PpPs and PpSs+PsPs) to the stacked amplitude as a function of crustal thickness and Vp/Vs ratio (Mohsen 2004; Frassetto 2013).

The principle steps of this process are described here from Mohsen (2004). From the arrivals of the phases, the delay time of Ps converted wave can be calculated (Kind and Vinnik 1988) as follow:

$$\mathbf{TPs = H\left((Vs^{-2} - p^2)^{1/2} - (Vp^{-2} - p^2)^{1/2}\right)} \qquad \textbf{Eq. 1}$$

Similarly, delay travel times for crustal reverberations can be given as:

For the PpPs that has two P legs and one S leg is

$$TPpPs = H\left((Vs^{-2} - p^2)^{1/2} + (Vp^{-2} - p^2)^{1/2}\right) \qquad \text{Eq. 2}$$

Eq. 2

For PpSs and PsPs composed of the sum of reverberations with two S legs and one P leg, and has two contributions with final S leg is

$$\mathbf{TPpSs/PsPs = 2H(Vs^{-2} - p^2)^{1/2}} \qquad \textbf{Eq. 3}$$

Finally, for PsSs that has three S legs is

$$\mathbf{TPsSs = H\left(3(Vs^{-2} - p^2)^{1/2} + (Vp^{-2} - p^2)^{1/2}\right)} \qquad \textbf{Eq. 4}$$

where p is the ray parameter of the direct P wave, H is the depth of the discontinuity, Vs is the S velocity and Vp is the P velocity in the layer.

For the final estimation of Moho depth, P-to-S converted phases of receiver functions (radial component) from a large number of events (from different azimuths and epicentral distances) are stacked in order to increase the signal to noise ratio. Thus a mean RF of the dataset, representing the subsurface sampled by the incoming rays underneath the station, is determined.
The phases are stacked and weighted as follows:

$$S(H,Vp,Vs) = w1Q(t1)+w2Q(t2)-w3Q(t3) \quad \textbf{Eq. 5}$$

and Vp/Vs ratio as follows:

$$Vp/Vs = ((1-p^2\,Vp^2)[2(Ps/PpPs-Ps)+1]^2 + p^2\,Vp^2)^{1/2} \quad \textbf{Eq. 6}$$

where Q(ti) are the receiver function amplitudes, t1, t2 and t3 are the predicted travel times for Ps, PpPs and PpSs+PsPs corresponding to crustal thickness H and Vp/Vs ratio, wi's are the weighting factors for the direct conversion from the Moho and the multiples. The highest value is given to the direct conversion (w1>w2+w3), as the slopes of crustal multiples are very similar. The S(H,Vp,Vs) reaches a maximum when all three phases (Ps,PpPs and PpSs+PsPs) are stacked coherently. An example of the results from multiple receiver function staacking is shown in Figure 27 for a seismic station with clear Ps conversion and crustal multiples.

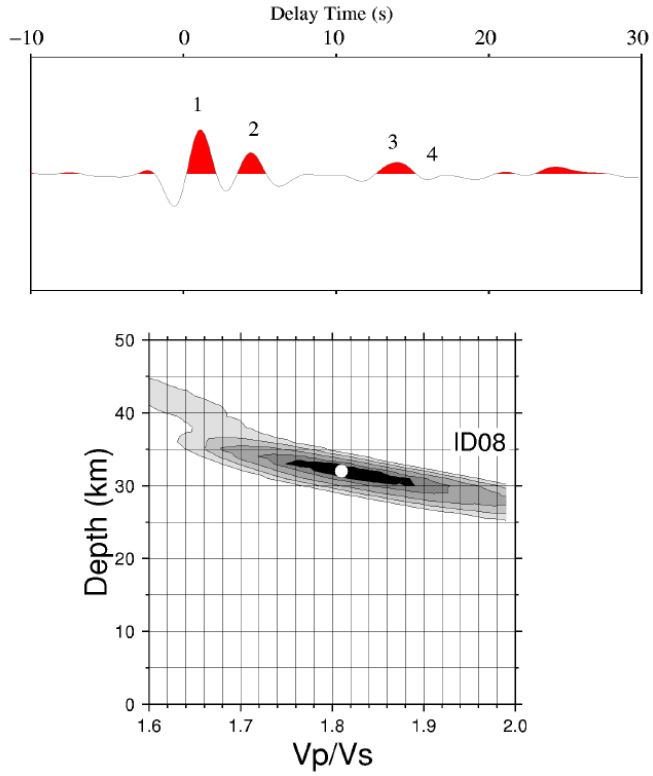

Figure 27: An example to show the application of the Zhu and Kanamori method of stacking for one seismic station (Mohsen 2004). The crustal thickness of 32 km and Vp/Vs ratio of 1.81 are obtained. Labels (1) and (2) at the second panel represent direct conversion within the crust and from the Moho, respectively. (3) and (4) represent the crustal multiples, PpPs and PpSs+PsPs, respectively.

2.2.3.3 The Current Study: Site and Dataset

The present study takes place in the Upper Rhine Graben, located between Strasbourg and Obernai in Alsace in north-eastern France, created during the Oligocene and the Miocene with the African and Eurasian plate collision and filled with thick (>4km) tertiary to quaternary deposits. These sediments cover the Mesozoic series from the Jurassic to the Triassic, resting on a paleozoic basement. The main formations of geothermal interest are found in these Mesozoic formations. The geological setup of this site is well-studied (Dezayes et al. 2010) and the existing geothermal

anomaly of the area has led to an increased industrial interest with the kicking off some exploitation projects in the vicinity. It is very close to the city of Strasbourg and has a deep sediment-basement interface, exposing it to the expected conditions of future geothermal projects for major European cities. Therefore, it is very suitable to be considered as a test site. A 10km X 10 km area to the western outskirt of Strasbourg is set as the experimentation site. A temporary network (Figure 28) was deployed for about 6 months, from November 2015 to May 2016, with the goal of testing the seismic noise tomographic methods in the area. The network was equipped with 7, three-component (3C) Guralp broadband velocimeters CMG-6TD (0.1-100 Hz) and one Guralp CMG-3TD broadband velocimeter coupled with a CMG-EAM Guralp data logger (0.017-100 Hz). Additionally, the data from a nearby broadband permanent station belonging to the French national network RESIF (STR station, located in Strasbourg) was used. Taking advantage of the available teleseismic events recorded by this network of 9 stations as well as the currently available codes and software, the RF method seems to be reasonably applicable on this site.

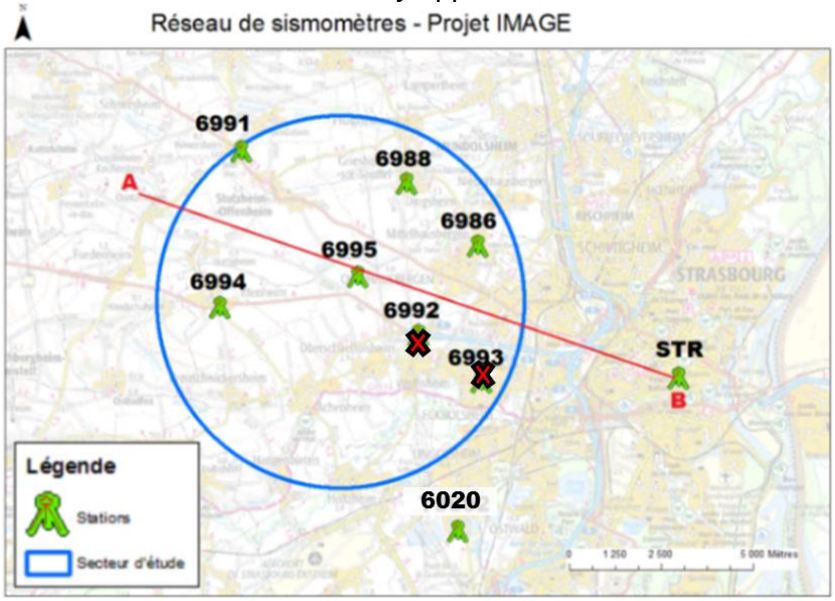

From¤	To¤	Distance (km)¤
STR¤	6986¤	6.41¤
STR¤	6988¤	8.96¤
STR¤	6991¤	13.28¤
STR¤	6992¤	7.10¤
STR¤	6993¤	5.30¤
STR¤	6994¤	12.56¤
STR¤	6995¤	9.15¤
STR¤	6020¤	7.29¤

Figure 28: The network of seismometers in the study area. The CMG-6TD stations are marked by the numbers from 6986 to 6995, the CMG-3TD by 6020 and the RESIF permanent station by STR. The stations marked by the red cross mark are not considered in the final analysis because of the noise and lack of records. Distance between the STR and other stations are shown in the right.

To estimate the receiver functions, seismograms from teleseismic earthquakes of magnitude Mw>5.5 with epicentral distances between 30° and 90° are used. Our recorded data are generally noisy; hence, a visual quality control was performed and only the seismograms that have clear direct-P arrivals are used. This operation reduced the number of exploitable events and stations in the dataset. As a preliminary step, 14 good quality, Mw 6-8, events and 7 stations, resulting in 2 to 14 events per station, have been selected for the analysis. Furthermore, some stations were installed underground, not isolated from the surrounding building noise. The characteristics of the selected events are provided in Table 1 and their locations are shown in Figure 29. Examples of recorded signals by the stations and their signal-to-noise ratios (SNRs) have been presented in Figure 30. It seems that on an average, the signals are exploitable (SNR> 1) within the frequency band 0.1-2.0 Hz. Compared to a quasi-equivalent station deployment with an equivalent objective (e.g. Licciardi and Agostinetti 2017), our database of exploitable waveforms seems to be quite poor. Our stations were deployed in a noisy suburban context, at a basin filled with thick deposits, designed to be compatible for performing noise correlation methods.

Table 1: Characteristics of the selected teleseismic events

Event No.	Date-Time (YYYY.MM.DD-hh.mm.ss)	Depth (km)	Magnitude (Mw)	Distance (°) from the station 6992	Region
1	2015.11.13-20.51.35	10	6.7	84.79	Kyushu, Japan
2	2015.11.24-22.45.40	636	7.6	90.67	Central Peru
3	2015.11.24-22.50.54	63	7.6	90.18	Central Peru
4	2015.12.07-07.50.07	30	7.2	47.05	Tajikistan
5	2015.12.25-19.14.47	212	6.3	46.95	Hindukush Region, Afghanistan
6	2016.01.03-23.05.21	50	6.7	69.07	Manipur, India
7	2016.01.24-10.30.30	128	7.1	70.66	Southern Alaska
8	2016.01.30-03.25.09	159	7.2	74.48	Kamchatka Peninsula, Russia
9	2016.03.19-01.35.10	10	6.1	79.87	Andreanof Islands
10	2016.03.20-22.50.20	30	6.4	75.03	Near East Coast of Kamchatka
11	2016.04.10-10.28.58	221	6.6	46.95	Hindukush Region, Afghanistan
12	2016.04.13-13.55.17	137	6.9	71.11	Myanmar
13	2016.04.15-16.25.07	10	7.0	83.97	Kyushu, Japan
14	2016.04.16-23.58.37	20	7.8	88.09	Near Coast of Ecuador

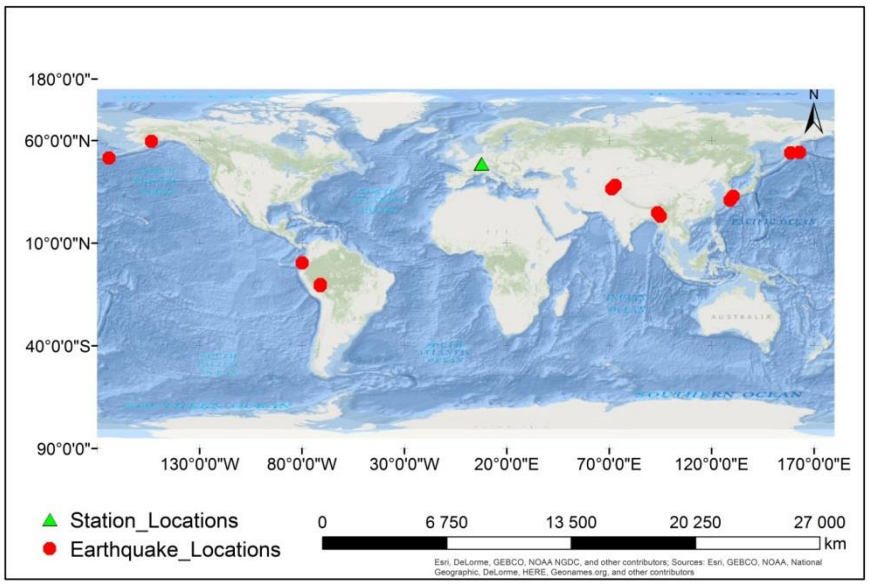

Figure 29: Location of the selected teleseismic events

(a) Event no. 3 (b) Event no. 5 (c) Event no. 14

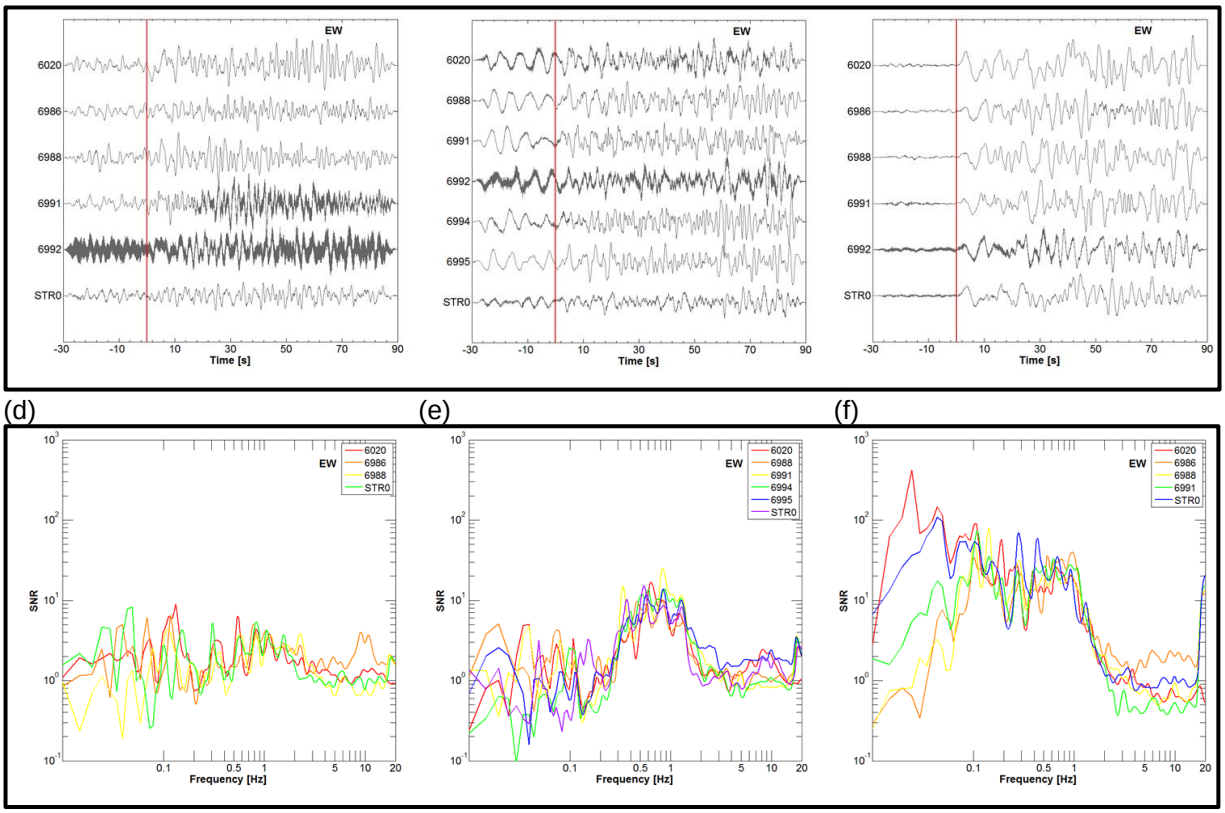

Figure 30: Examples of (a)-(c) EW component signals recorded by different stations and their (d)-(e) signal-to-noise ratio for the event no. 3, 5 and 14 (Table 1)

2.2.3.4 Data Processing

The iterative time domain deconvolution approach (Ligorria and Ammon 1999) has been used in this study. We summarize the basic steps of the algorithm here according to Eagar (2011). “It first computes an RF by performing a cross-correlation on the vertical and radial seismograms. Then, a spike train is convolved, based on the lag time, which represents that lag time with a Gaussian function. The Gaussian parameter determines the width of the Gaussian wavelet and essentially acts as a low-pass filter for the RF. After the first pulse is generated on the predicted RF, the RF is convolved with the vertical seismogram to get a predicted radial seismogram. The difference between the predicted radial and the data is then computed to get a residual. As long as the residual is greater than a given threshold, the process continues. The first pulse is stripped and the next pulse is generated, again by the process of cross-correlation, convolution with a Gaussian wavelet to produce a predicted RF, and convolution of the RF with the vertical seismogram.”

In the present study, a two-point second order Butterworth filter with corner frequencies of 0.01 and 5 Hz was applied prior to the RF computation. The program code ‘saciterd’, written by Dr. Charles J. Ammon, provided in Computer Programs in Seismology (CPS) package Herrmann (2013) was used. In this program, the deconvolution is expressed as a sequence of Gaussian filtered impulses, where a parameter called ‘alpha (α)’ controls the frequency content by acting as a low pass filter of the receiver functions (e.g., α =1 corresponds to a frequency of about 0.3 Hz). This study uses three Gaussian filter parameters, α=0.5, α=1.0 and α=2.5 for the calculation.

The processing of the resulting RFs has been done on the Matlab software (version R2013a) using an interactive toolbox, ‘Funclab’, developed by Eagar and Fouch (2012). The final results are analyzed and interpreted to identify the probable impedance contrasts in the underlying structure, and to compare with the observations coming from other site characterization approaches.

2.2.3.5 Results

We present the resulting radial component receiver functions (RRFs) computed from each event recorded by the station STR in Figure 31 (along the respective event no.) and Figure 32 (along the respective event backazimuths). Calculated RFs from our dataset show different characteristics in quality, from one station to another. After the direct arrival, some common patterns can be identified. The positive pulse at 0 s corresponds to the direct P wave arrival, while all the following pulses could be either conversions at a true velocity discontinuity or reverberatory phases. For example, the RFs at the STR station show a clear direct P arrival (at around 0 s) and a rather coherent Ps arrival, even though a bit ambiguous at times, at around 4 s delay time. We probably observe a PpPs reverberation at around 15-16 s. On the other hand, PsPs phase is not observed clearly. The positive pulses indicate a positive jump in velocity and the negative arrivals may indicate decreasing velocity with increasing depth.

Figure 33 shows the RRFs from STR, plotted only for the first 10 s of the traces and presented along the event backazimuth as well as the ray parameter. This zoomed view of the traces show that the largest pulse arrives at around 0.5 s. It is then immediately followed by some high-amplitude arrivals at around 1 to 2 s. This reverberation might be indicative of some shallow intracrustal converters. We also observe a negative arrival around 2.5 s, before the Ps (close to 4 s). This might be indicative of a low-velocity layer just above the Moho. An example of the H-κ stacking results and corresponding summation of all RRFs for the same station are presented in Figure 34 and Figure 35. Summation of stacked RRFs (in red) for the stations aligned in the NW-SE direction (6991, 6986, 6988 and STR) are presented in Figure 36. More disperse train of arrivals is seen at other stations compared to the STR. Note that the RFs have not been sorted by quality, hence these results are very crude and not well-constrained - they serve only as examples. A more careful signal processing and analysis of the results are required to extract meaningful information from this dataset.

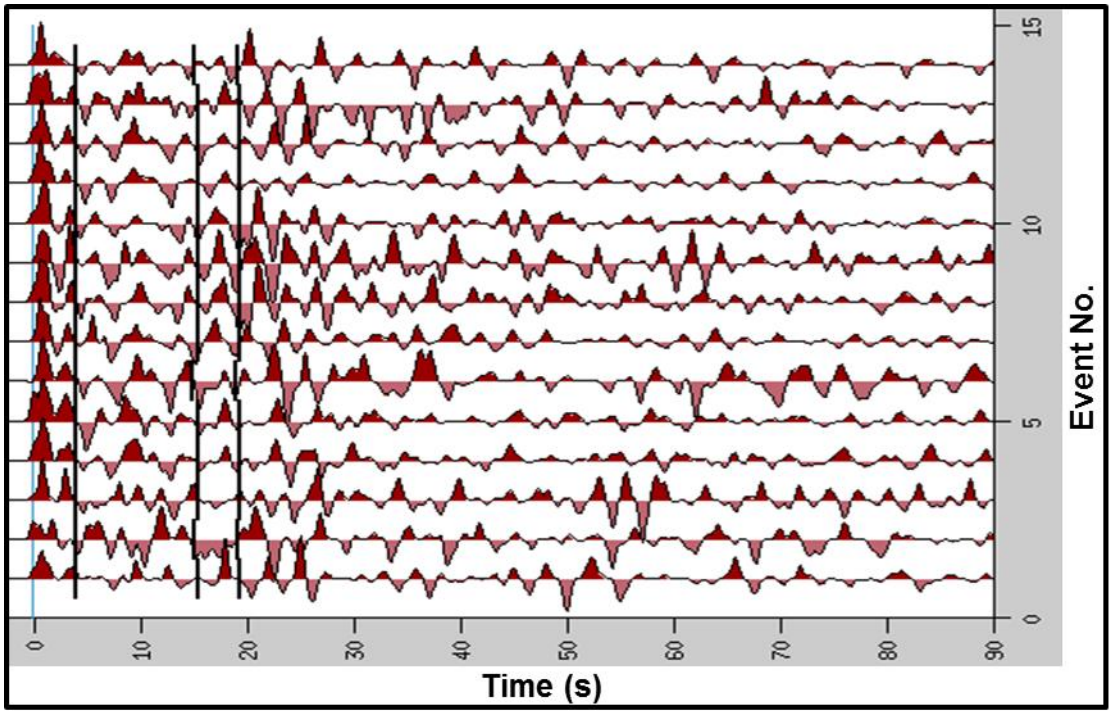

Figure 31: RRFs computed from the events recorded by the station STR (α=2.5). The thick black vertical lines show the theoretical phase arrivals Ps, PpPs, PsPs, consecutively, considering the AK135 (Kennett et al. 1995) travel-time model.

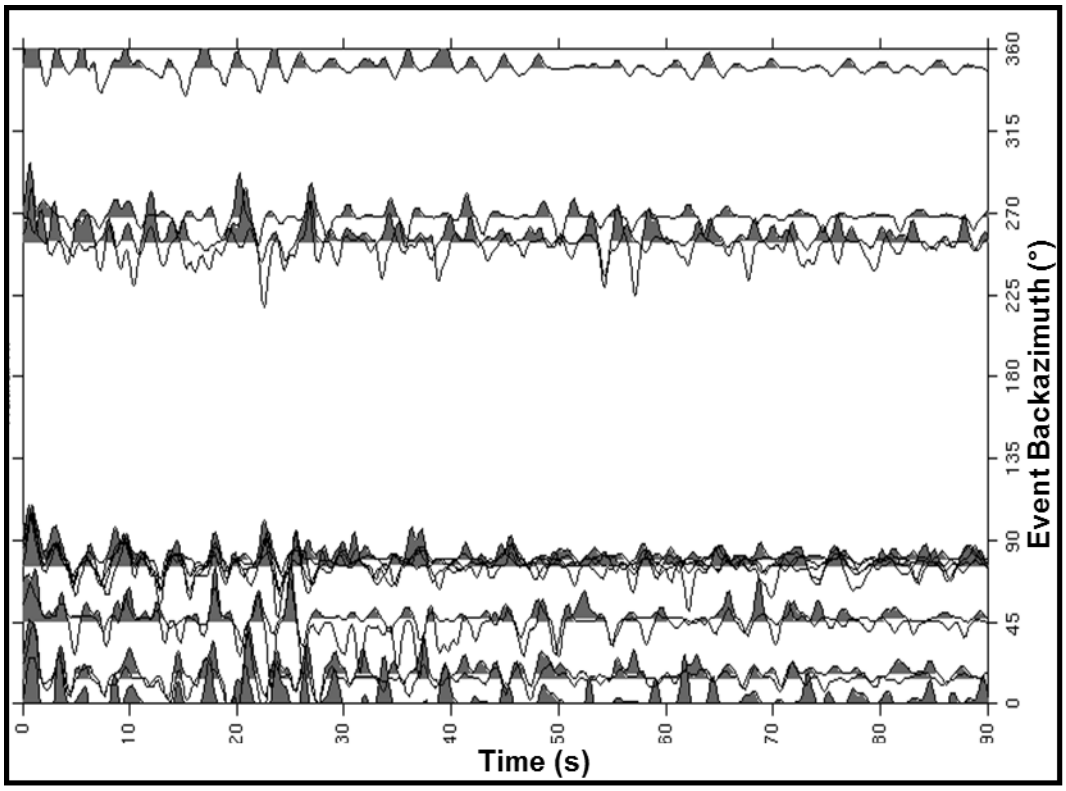

Figure 32: RRFs computed from the events recorded by the station STR along the respective event backazimuths.

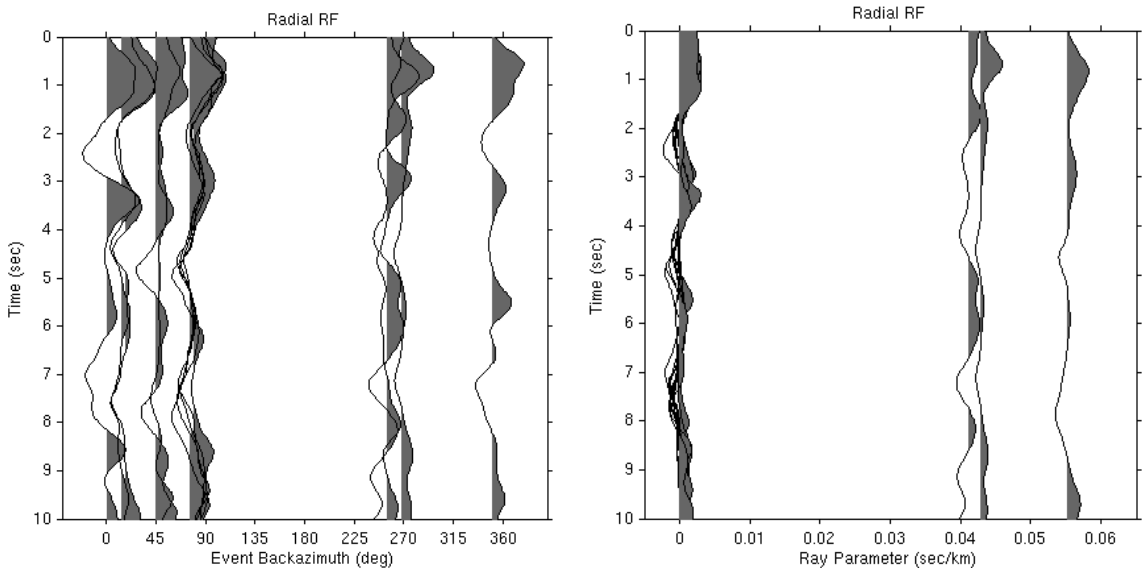

Figure 33: RRFs computed from the events recorded by the station STR, plotted for the first 10 s, along the respective (a) event backazimuths and (b) ray parameter.

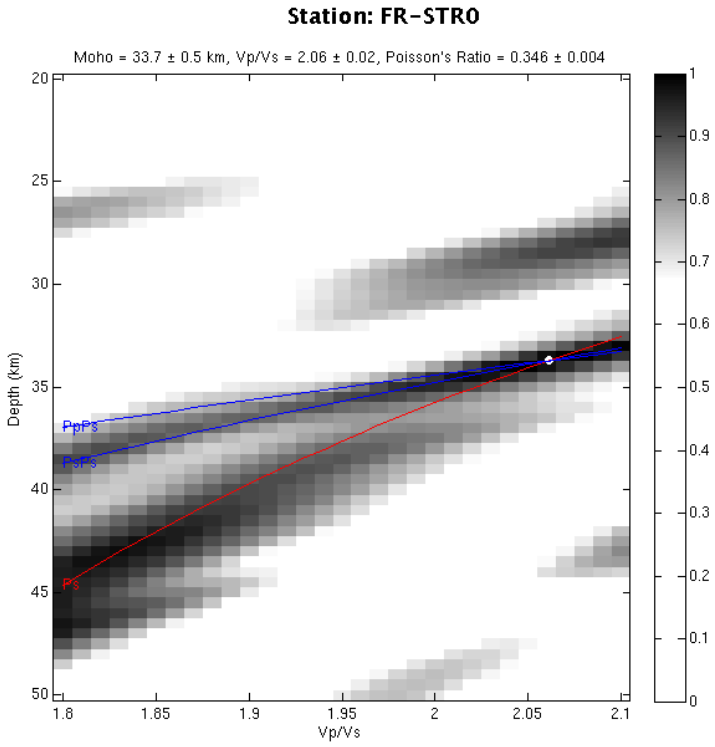

Figure 34: H-κ stacking results showing the contributions of Ps and its two major crustal multiples (PpPs and PsPs) to the stacked amplitude as a function of crustal thickness and Vp/Vs ratio for the station STR.

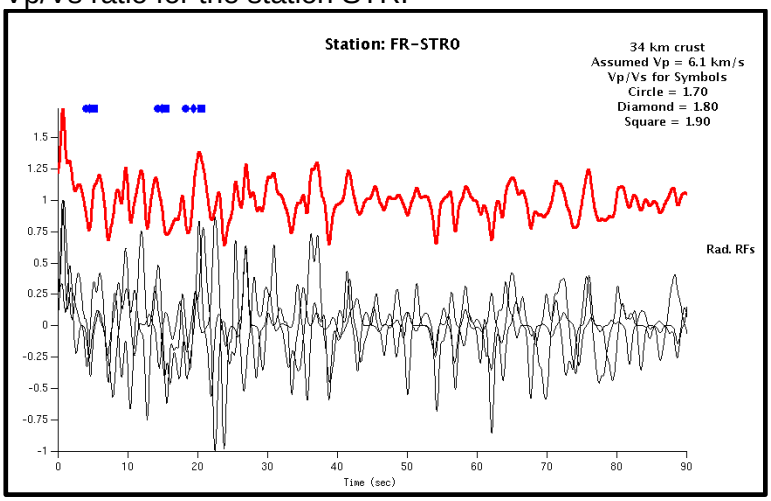

Figure 35: Stacked radial component RF (in red) for the station STR.

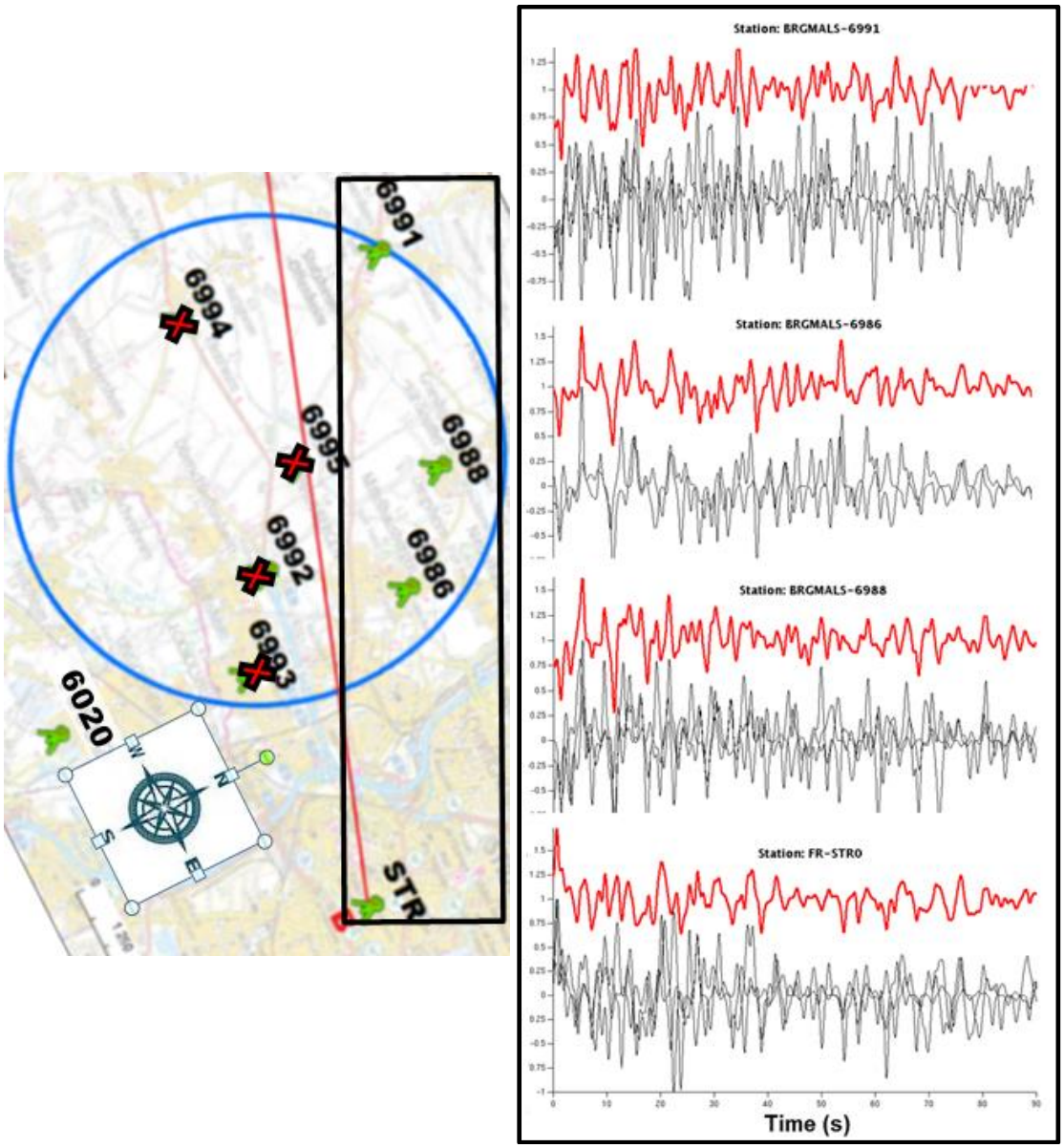

Figure 36: Stacked RRFs (in red) for the stations aligned in the NW-SE direction (6991, 6986, 6988 and STR) enclosed by the black rectangle on the station map.

2.2.3.6 Discussion

The objective of this work was to explore the capacity of RF method in determining shallow, intracrustal interfaces. As the station network used in this study was not suited for such investigation and the recorded dataset was not sufficient, our research was rather limited to the exploration of the applied method and tools. Evidently, this study does not mean to provide any definitive conclusions. However, the preliminary results look promising enough to continue our research through improving the data quality. Hence, it seems relevant to discuss some results from some of the existing research works in this domain and demonstrate the further scopes of our study.

Eagar et al. (2011) successfully analyzed teleseismic receiver functions to image the crustal structure beneath the High Lava Plain of eastern Oregon by using the iterative time deconvolution method and H-κ stacking. We present an example RF analysis from a station and the corresponding H-κ stacking results in Figure 37. It shows how a selection of quality RFs, and better constrained H and κ could help exploring the complex crustal structure.

Leahy et al. (2012) showed, thanks to a large passive experiment and to a dense array, that earthquake waveforms permit to image the shallow crust with a vertical resolution of 500m, and a lateral resolution depending on the stations spacing. The authors followed a noise-damped frequency domain method to estimate the RFs, which allowed them to investigate the resolution of the geological structure as a function of increasing frequency content. Figure 38 shows an example of the RFs at 2 Hz and Figure 39 show the results at increasing frequency content. The results using the 2 Hz filter do not suggest much shallow structure because the direct P arrival contains energy on both the horizontal and vertical component of the seismogram, RFs have a large correlation pulse centred at zero time, .effectively hiding near-surface conversions. At higher frequencies, the direct P arrival is narrowed, revealing possible Ps conversions from the near-surface. With the increase of frequency content, the sharpening of the pulse (at 0.8s in Figure 39) that remains essentially stationary in time indicates the potential resolving power of the data at higher frequencies. Schmedes et al. (2012) performed inversion of shallow velocity model that showed the lateral resolution being at the order of station spacing whereas poor vertical resolution due to steep incidence.

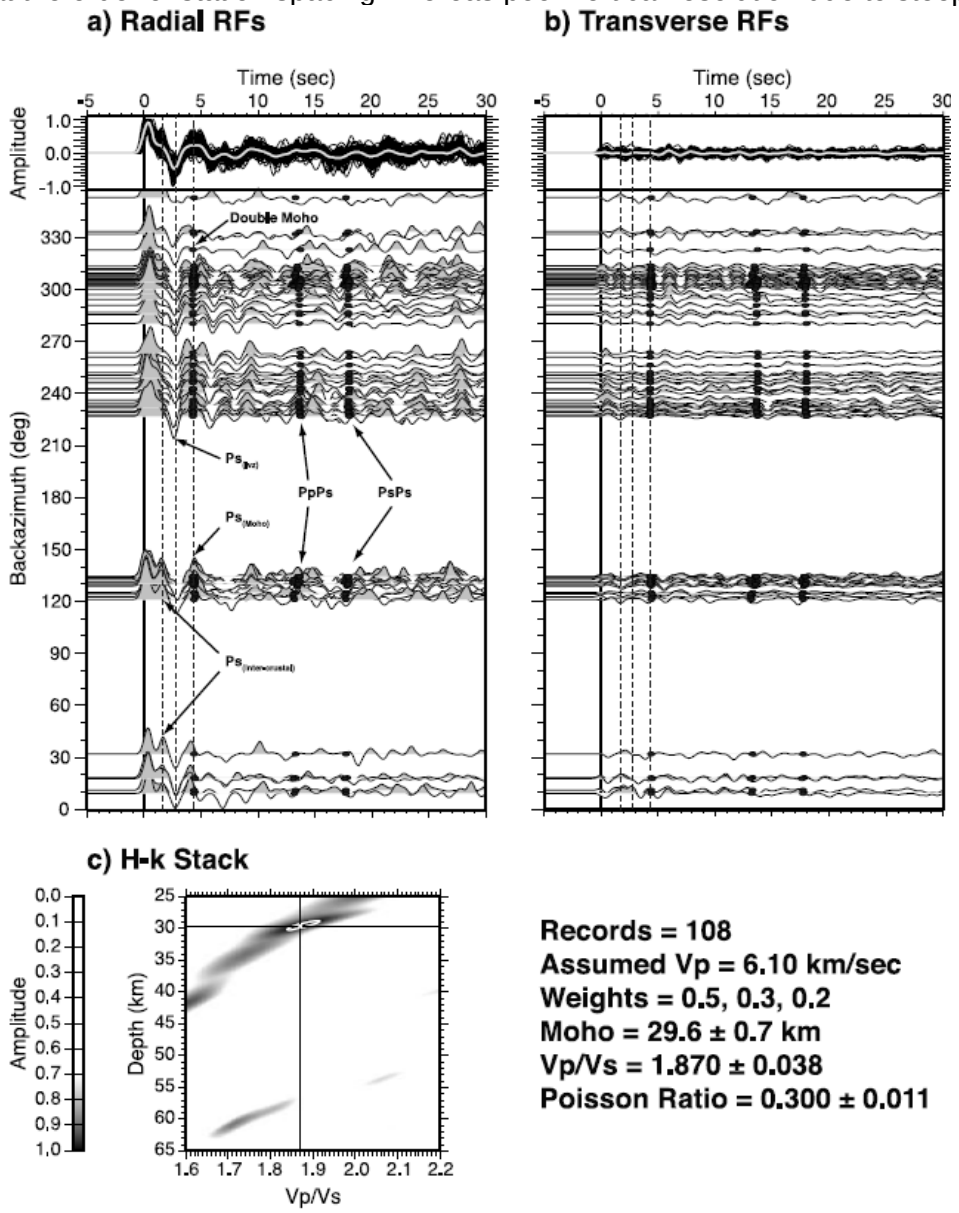

Figure 37: (a) Radial and (b) transverse receiver functions as a function of backazimuth and (c) H–κ stack from station a station (Figure 7 from Eagar et al. 2011). On top of (a) and (b), the normalized receiver functions are shown in black and linear stack in gray. Radial receiver functions show back azimuthal variations in an intracrustal positive; a strong, persistent

intracrustal negative; and a double Ps for events from the NW. The transverse receiver functions show similar energy from the intracrustal positive, as well as sub - Moho energy for events from the NW. In (c), the H–κ stacking grid shows a broad zone of energy associated with the Ps conversion. White circles denote one standard deviation contour from maximum normalized amplitude. The H–κ stacking result has large tradeoffs and is not well constrained.

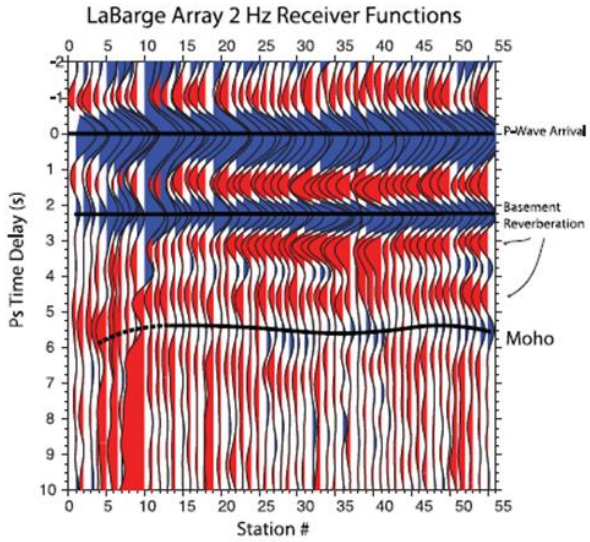

Figure 38: Stacked RFs at 2 Hz (Figure 5 from Leahy et al. 2012). The direct P arrival is seen at 0 s. Two reverberation candidates associated to basement and Moho are shown at ~2 sand ~6 s, respectively.

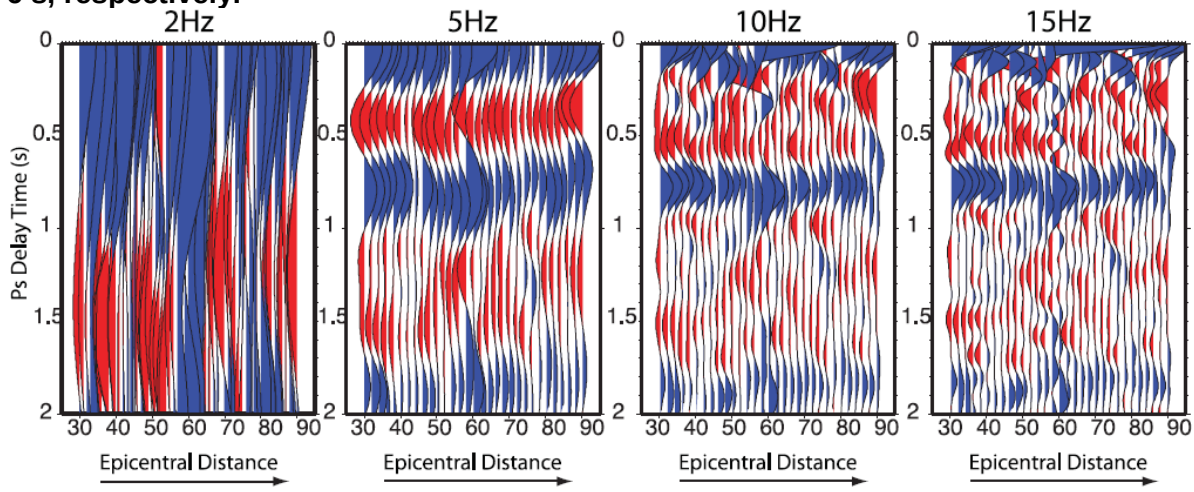

Figure 39: Epicentral distance stacks of receiver functions for a station (Figure 6 from Leahy et al. 2012). Increasing the frequency content of the receiver functions increases the resolution of geological structure and helps to determine which conversions are real. Positive (blue) amplitude represents increasing impedance with depth.

Licciardi and Agostinetti (2017) applied RFs technique in order to characterize the Dublin sedimentary basin. Use of high frequency RFs (up to 8Hz) permitted them to identify a discontinuity associated to the main basin bounding fault and to constrain a velocity model associated with a vertical resolution of 500m. Figure 40 shows an example of the stacked RRFs they obtained from a station for multiple values of the cut-off frequency (Agostinetti and Licciardi 2015). Again, some consistent pulses are observed at even higher frequencies, indicating the reliability of the RFs. Figure 41 shows an example how the observations from the RFs at high frequencies along the length of the array could be interpreted to examine the lateral variations of the pulses and, tentatively, to constrain

the structural setting of the basin. Therefore, the ability of RF method to characterize shallow structure (<10km) from high frequency signal associated to appropriate processing tools seem promising.

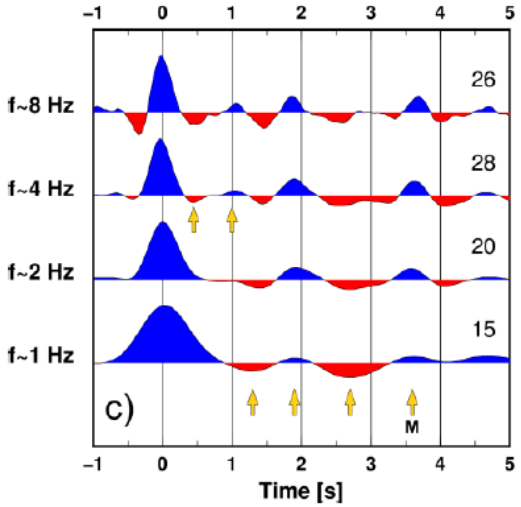

Figure 40: Stacks of RRFs at a station for 4 different progressively increasing cutoff frequencies (Figure 8 from Agostinetti and Licciardi, 2015). The number of RFs used in each stack is indicated over the trace. Each arrow marks the onset of a particular pulse at the corresponding frequency. The presence of signal in the first second after the direct P-wave arrival is revealed for frequencies cut-off greater than 2 Hz.

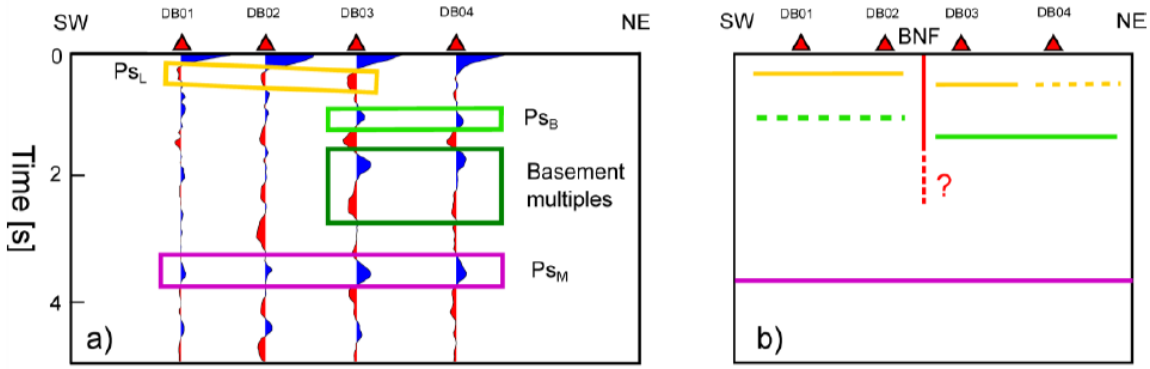

Figure 41: (a) Profile of time-stacked RRF (8Hz) along the length of the array and (b) possible interpretation of the structural setting of the SW margin of the Dublin basin (Figure 9 from Agostinetti and Licciardi, 2015). PsL: conversion at a negative velocity jump in the sediment pile; PsB: conversion at the sediment-basement interface; PsM: conversion from the Moho. Major changes in the pulses amplitudes are related to the presence of the BNF.

2.2.3.7 Conclusions and Perspectives

The results of the preliminary RF analysis from a set of only 14 events recorded by our station network at Strasbourg have been presented in this work. It is worth mentioning that the geometry of the station network is not ideal for RF estimation, and the data are noisy even for moderate earthquakes. Because of the suburban site conditions and the nature of deployment, the SNR of the recorded teleseismic signals do not seem to be sufficient in the workable frequency domain for exploring only few kilometers' resolution at depth. Despite the limitations, some promising indications have been observed in the results. The frequency content of the estimated RFs contain frequencies as high as 5 Hz. Yet, some consistent arrivals have been observed at the permanent station. The estimated RFs seem to be good enough for shallow crust imaging (determining Moho depth), therefore, implicating a possibility of deeper resolution compared to that from other passive methods.

The results from the temporary stations seem slightly inconsistent, presumably, due to the higher level of noise. A complex ensemble of pulses has been observed right after the direct P arrival and much before the Ps. However, this feature is expected in a basin where the reverberations in the sediment strongly complicate the observed waveforms. Obviously, more data and good quality RFs are essential in interpreting these results.

As a perspective, data from more events is suggested to be added to improve the resolution of the results. In order to enlarge the database and to enhance vertical resolution, regional earthquakes could be added in the analysis (Schemdes et al., 2012). Depending on the quality of the final dataset, a forward synthetic modeling and/or an RF inversion could also be performed. The RFs could also be processed by using various stacking techniques, such as, Common-Conversion-Point (CCP) (Zhu, 2000) and H-κ stacking (Zhu and Kanamori, 2000) to estimate the Moho depth (H) and the bulk crust ratio Vp/Vs (κ). Frequency dependence of the shallow converters at each station could be investigated, by applying the RF technique at increasingly higher frequency bands, and focusing on the first 5 s of the RFs. The observations could be compared with those obtained from the other approaches/research works undertaken in the framework of the IMAGE project.

2.3 Electromagnetics

The following sections will describe

1) the motivations behind the acquisition of electro-magnetic data for the characterization of deep geothermal resources in the Strasbourg area
2) the results of the CSEM and MT feasibility study
3) how the CSEM and MT surveys have been designed
4) the obtained data quality and coverage from the CSEM and MT field trials
5) the results of CSEM and MT imaging
6) conclusions and recommendations with respect to the applicability of CSEM and MT techniques for deep geothermal exploration in such context

2.3.1 Feasibility study and survey design

2.3.1.1 Feasibility study

2.3.1.1.1 Generic geo-electrical model for the Strasbourg Area

The basis for the CSEM and MT feasibility study is a representative geo-electric model of the survey area. For this purpose, we used the structural information from the existing 3D geological models as well as resistivity logs from oil exploration wells in the vicinity of the survey area and geothermal wells from the Soultz-sous-Forêts geothermal plant. The resulting geo-electric model is shown on Figure 42. It mainly consists in a thick (~4km) conductive (<100 Ω.m) sedimentary cover over a resistive (1000 Ω.m) crystalline basement. The sedimentary cover is pretty heterogeneous with multiple conductive (marls) and less conductive (limestone, salt) layers. In order to perform a resolution study, we have subsequently simplified this model into a four layer model (Figure 43).

The main geothermal targets in the Upper Rhine Graben are fractured zones within the basement or at the transition zone between the basement and the sedimentary cover. We have therefore modelled these as alteration/fractured zones at the top of the basement and along major faults. The resistivity and thickness of these zones have been defined using the Soultz-sous-Forêts wells logs as analogues (Figure 44). In the EPS1 well, the fractured/alteration zones show pronounced resistivity decreases from more than 1000 Ω.m for the unaltered granite to less than 100 Ω.m (down to 10 Ω.m). Their cumulative thickness observed over this 600m long section is about 100m. As this well is not necessarily representative of a well-developed alteration/fractured zone but also because the alteration/fractured zone is likely to extend both in the basement and sedimentary cover, we modelled the geothermal targets as 500m thick 10 Ω.m layer (Figure 45).

Depth (m)	Interface	Thickness (m)	Resistivity (Ω.m)	Rock Type
0m	Air	200m	10 Ω.m	Gravel Sand
200m	Base Quaternaire = Top Tertiaire	700m	1.5 Ω.m	Silteous Marls
900m	Upper Sannoisian	600m	20 Ω.m	Salty Marls + Anhydrite
1400m	Lower Sannoisian	500m	1 Ω.m	Salty Marls
1900m	Lower Sannoisian	500m	100 Ω.m	Massif salt
2400m	Base Tertiaire = Top Jurassique	500m	2 Ω.m	Marnes
2900m	Base Trias Superieur = Top Muschelkalk	500m	100 Ω.m	Calcaires/Anhydrites
3250m	Base Muschelkalk=Top Bundsandstein	750m	20 Ω.m	Grès
4000m	Base Bundsandstein = Socle	∞	1000 Ω.m	Granite

Figure 42: Geo-electric model of the Strasbourg area

Depth (m)	Interface	Thickness (m)	Resistivity (Ω.m)	Rock Type
0m	Ground surface	2000m	5 Ω.m	Young sediments
2000m	Tertiary Base	500m	100 Ω.m	Older sediments (salt/limestones)
2500m		1500m	20 Ω.m	Sandstones claystones
4000m	Basement	∞	1000 Ω.m	Granite

Figure 43: Simplified geo-electric model of the Strasbourg area

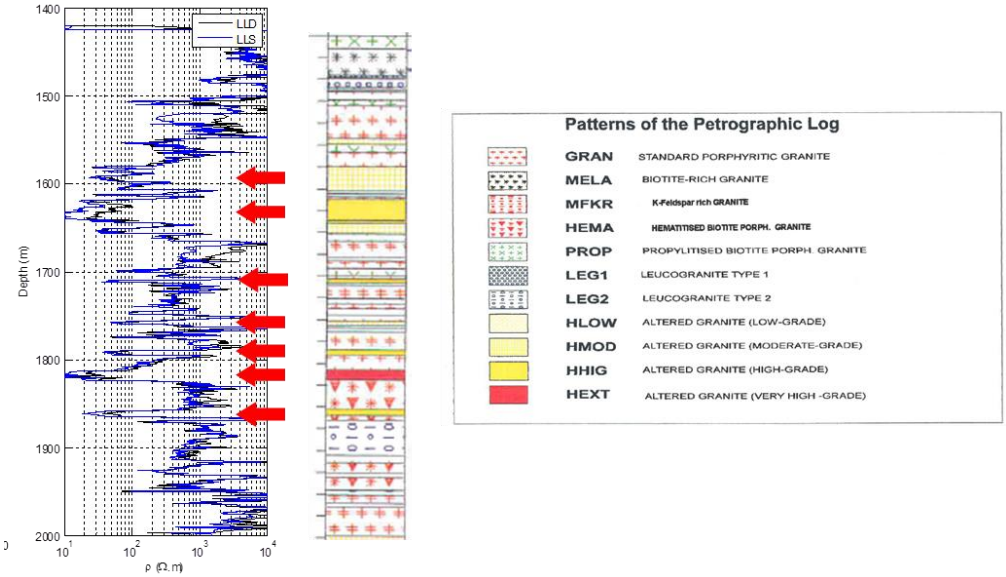

Figure 44: Resistivity log in the EPS-1 well from the Soulz-sous-Forêts geothermal plant. Please note the strong resistivity decrease while crossing the main alteration zones.

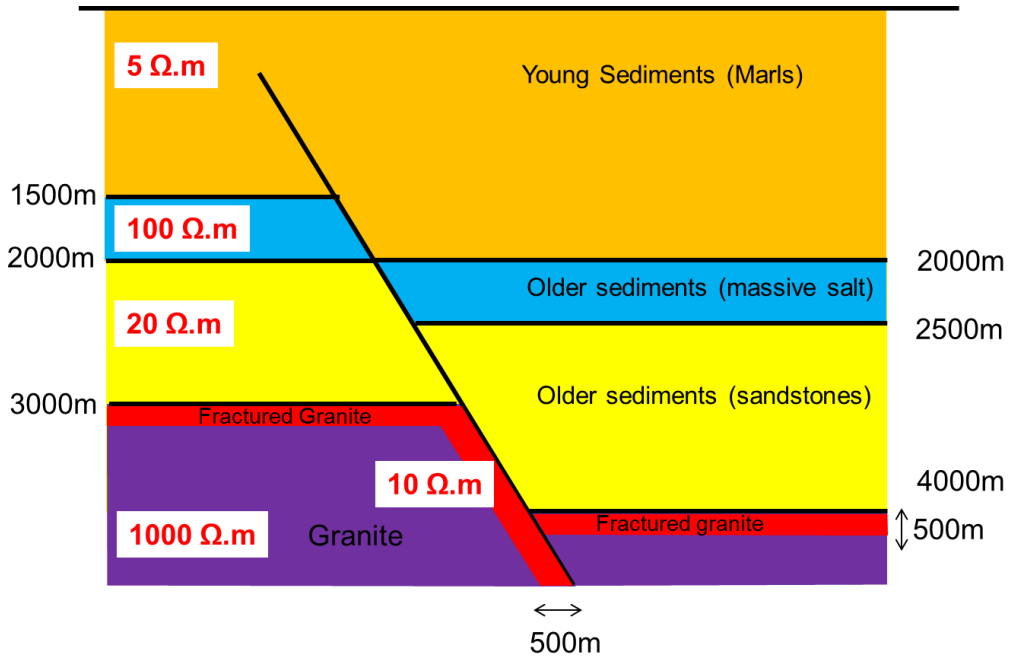

Figure 45: Conceptual 2D geo-electric model of the geothermal targets in the Strasbourg area.

2.3.1.1.2 Controlled Source Electro-Magnetic Imaging

2.3.1.1.2.1 1D CSEM Modelling

The first step of feasibility study consists in defining the geometry and frequencies of the CSEM transmitter/receivers. The CSEM transmitters have been chosen as two 1km-long orthogonal electric dipoles while the CSEM receivers consist in orthogonal horizontal electric and magnetic sensors. The CSEM frequencies and geometries have been selected by calculating the 1D CSEM responses with/without the geothermal target of the simplified geo-electric model (Figure 43) as a function of source-receiver offsets, frequencies and transmitter polarizations. To assess the CSEM response, we looked into the absolute electric fields (Figure 46 and Figure 49), the scattered fields (Figure 47 and Figure 50) and the normalized fields (Figure 48 and Figure 51) for each transmitter polarization: inline = transmitter aligned with the receivers and broadside = transmitter orthogonal to the transmitter/receiver lines. We also computed the apparent resistivity and phase (Figure 52) and anomalies (Figure 53) of the impedance tensor (Zonge and Hughes, 1991) to allow a thorough comparison with the MT modelling results.

For a broadside transmitter, the maximum amplitude anomaly associated with the geothermal target is about 10% and 3.10^{-13} V/A.m^2 at 10km offset and for frequencies lower than 1Hz. For an inline transmitter, the maximum amplitude anomaly associated with the geothermal target is about 4% and 10^{-13} V/A.m^2 at 10km offset and for frequencies lower than 1Hz. As the geothermal target is more conductive than the background model, the best coupling is with Transverse Electric coupling i.e. a broadside configuration. When comparing the amplitudes of the CSEM anomalies with background noise estimates in different CSEM noise conditions (Figure 47) and typical measurement errors (usually a few percent of the total field, Figure 48), it is clear that the CSEM anomalies associated the geothermal target are close to the noise levels and require either low ambient noise conditions or high power CSEM transmitters (>20kVA). If such conditions are met, the frequency band of interest is between 0.01 Hz and 1Hz and long transmitter/receiver offsets are necessary (>5 km).

Similar conclusions can be drawn on the impedance tensors, except that we cannot easily define the frequency band of interest as it requires both electric and magnetic noise estimates. We can however conclude from the shape of the apparent resistivity and phase curves that at the frequency band of interest for the geothermal target (0.01 Hz and 1Hz) and at 10km offset, we are working in the transition zone between the audio-magnetic band (>1Hz with phases close to 45°) and the near-field band (< 0.01Hz with phases close to zero and an asymptotic behaviour of the apparent resistivity).

As a result from this 1D analysis, the next step of the feasibility study was to perform a 3D modelling exercise built from the 2D geoelectric model and based on a 8km x 8km grid of 500m-spaced receivers and using three transmitters at 4km offset from the first receivers along the strike and at 90° degrees from the fault zone to ensure enough offsets to sense the deep targets but also diversity of the illumination of the fault zone (Figure 54). The transmission frequencies were logarithmically selected from 0.01 Hz to 100Hz as follows: 0.03125, 0.044, 0.0625, 0.088, 0.125, 0.18, 0.25, 0.35, 0.5, 0.7, 1, 1.4, 2, 2.8, 4, 5.7, 8, 11.3, 16 and 32Hz.

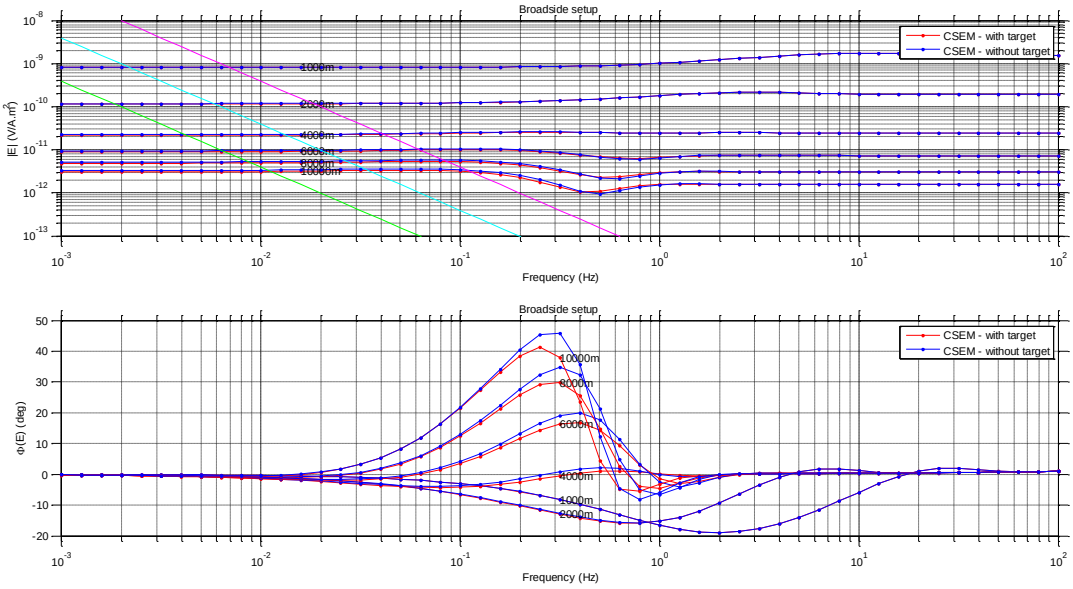

Figure 46: Top: Amplitude of the broadside horizontal electric field with (red) and without (blue) the geothermal target of the simplified geo-electric model of the Strasbourg area as function of transmitter frequency and offset. The magenta, cyan and green lines corresponds to modelled noise spectra using a 20kWA transmitter in a noisy and quiet EM noise environment and a 200 kVA in a quiet EM noise environment, respectively. Bottom: Phase of the broadside horizontal electric field with (red) and without (blue) the geothermal target of the simplified geo-electric model of the Strasbourg area as function of transmitter frequency and offset.

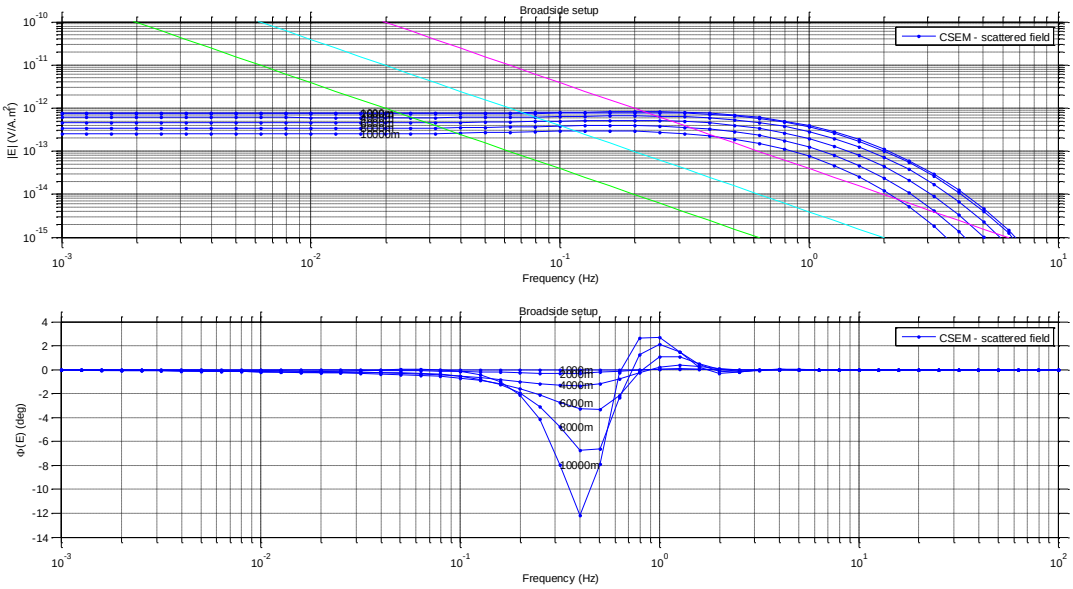

Figure 47: Top: Amplitude difference between the broadside horizontal electric field with (red) and without (blue) the geothermal target of the simplified geo-electric model of the Strasbourg area as function of transmitter frequency and offset. The magenta, cyan and green lines corresponds to modelled noise spectra using a 20kWA transmitter in a noisy and quiet EM noise environment and a 200 kVA in a quiet EM noise environment, respectively. Bottom: Phase difference between the broadside horizontal electric field with (red) and without (blue) the geothermal target of the simplified geo-electric model of the Strasbourg area as function of transmitter frequency and offset.

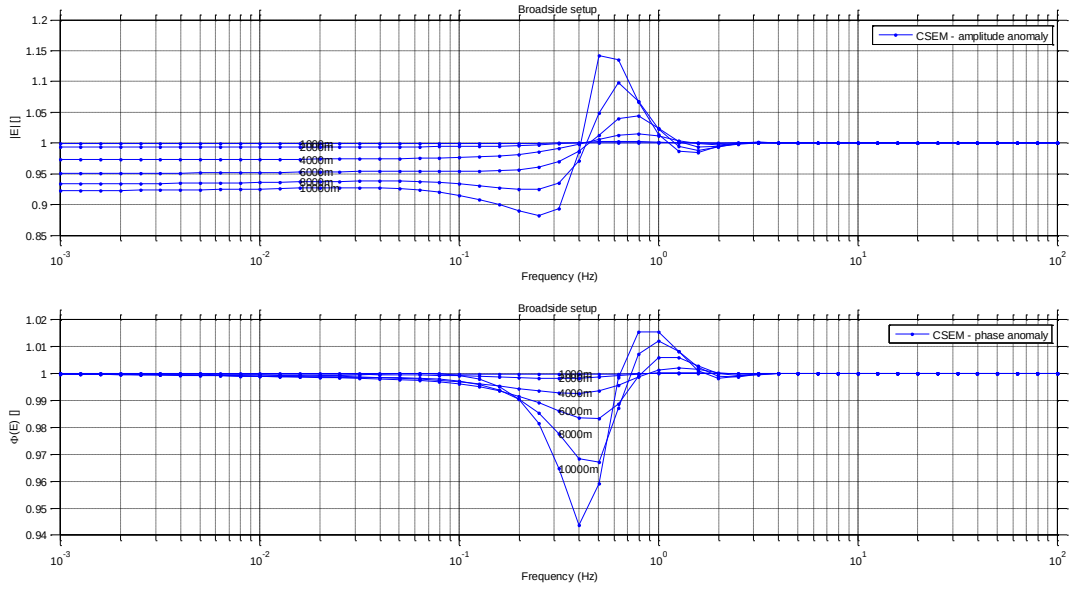

Figure 48: Top: Amplitude ratio between the broadside horizontal electric field with (red) and without (blue) the geothermal target of the simplified geo-electric model of the Strasbourg area as function of transmitter frequency and offset. The magenta, cyan and green lines corresponds to modelled noise spectra using a 20kWA transmitter in a noisy and quiet EM noise environment and a 200 kVA in a quiet EM noise environment, respectively. Bottom: Phase ratio between the broadside horizontal electric field with (red) and without (blue) the geothermal target of the simplified geo-electric model of the Strasbourg area as function of transmitter frequency and offset.

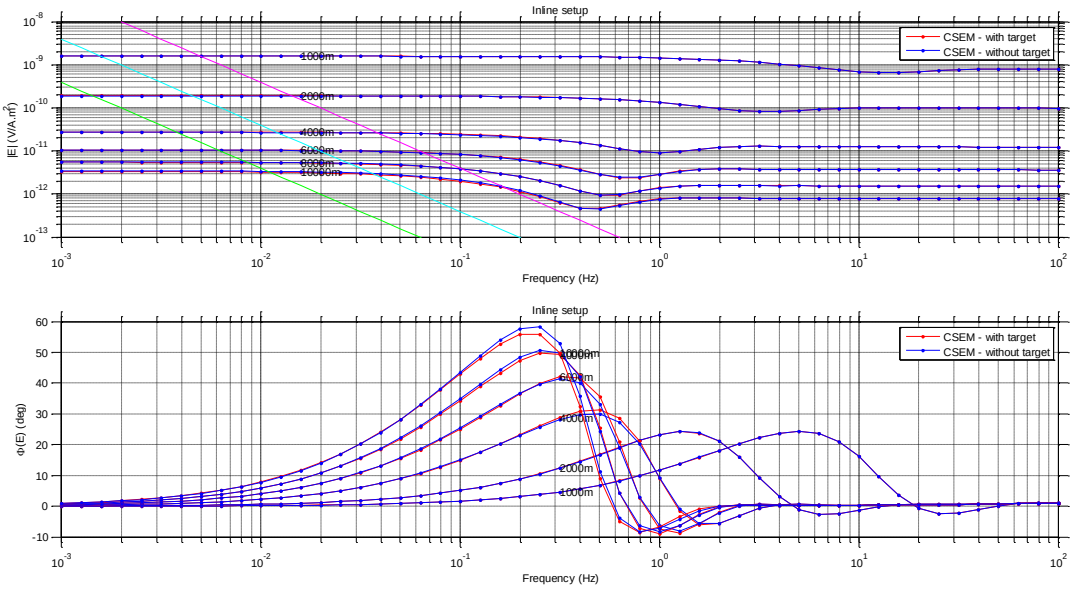

Figure 49: Top: Amplitude of the inline horizontal electric field with (red) and without (blue) the geothermal target of the simplified geo-electric model of the Strasbourg area as function of transmitter frequency and offset. The magenta, cyan and green lines corresponds to modelled noise spectra using a 20kWA transmitter in a noisy and quiet EM noise environment and a 200 kVA in a quiet EM noise environment, respectively. Bottom: Phase of the inline horizontal electric field with (red) and without (blue) the geothermal target of the simplified geo-electric model of the Strasbourg area as function of transmitter frequency and offset.

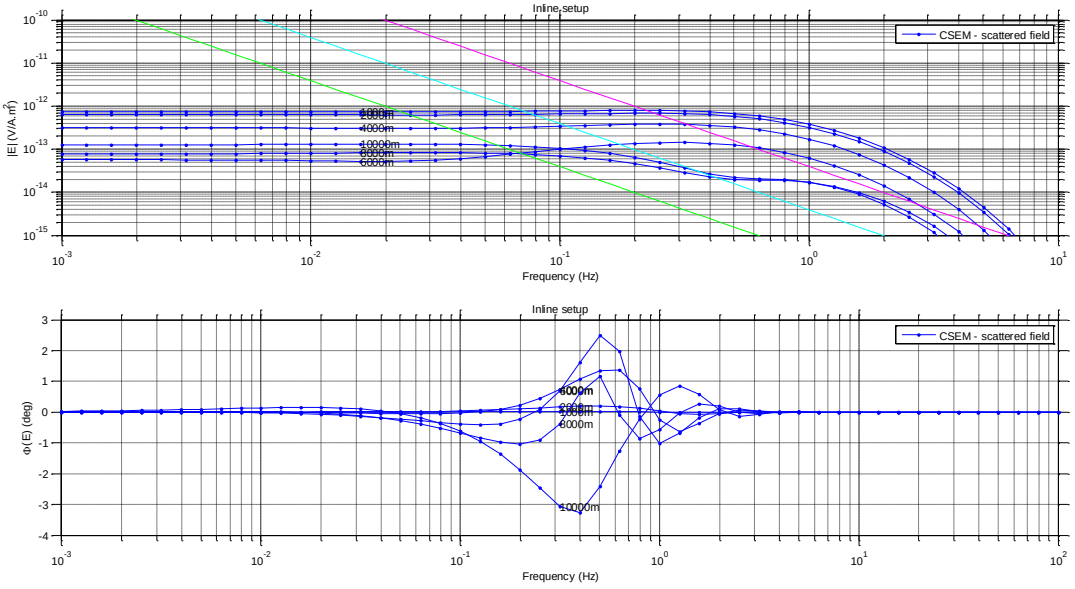

Figure 50: Top: Amplitude difference between the inline horizontal electric field with (red) and without (blue) the geothermal target of the simplified geo-electric model of the Strasbourg area as function of transmitter frequency and offset. The magenta, cyan and green lines corresponds to modelled noise spectra using a 20kWA transmitter in a noisy and quiet EM noise environment and a 200 kVA in a quiet EM noise environment, respectively. Bottom: Phase difference between the inline horizontal electric field with (red) and without (blue) the geothermal target of the simplified geo-electric model of the Strasbourg area as function of transmitter frequency and offset.

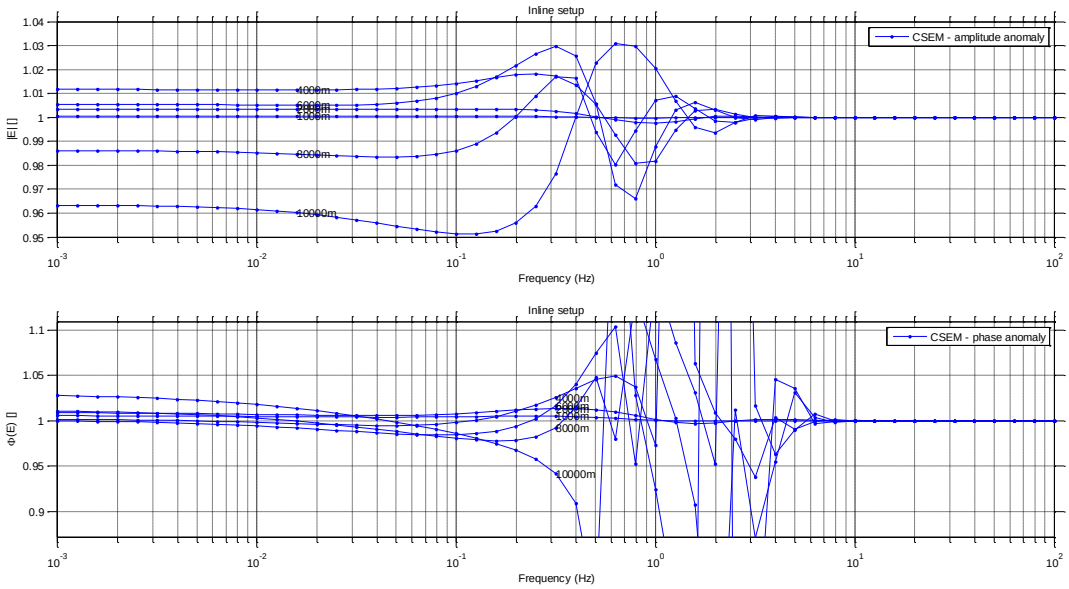

Figure 51: Top: Amplitude ratio between the inline horizontal electric field with (red) and without (blue) the geothermal target of the simplified geo-electric model of the Strasbourg area as function of transmitter frequency and offset. The magenta, cyan and green lines corresponds to modelled noise spectra using a 20kWA transmitter in a noisy and quiet EM noise environment and a 200 kVA in a quiet EM noise environment, respectively. Bottom: Phase ratio between the inline horizontal electric field with (red) and without (blue) the geothermal target of the simplified geo-electric model of the Strasbourg area as function of transmitter frequency and offset.

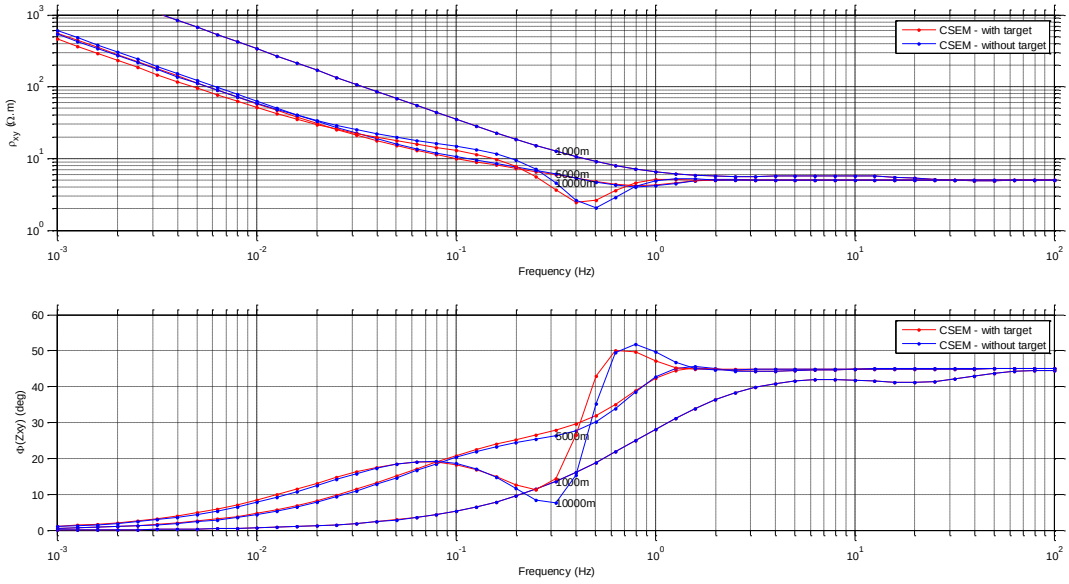

Figure 52: Top: Apparent resistivity with (red) and without (blue) the geothermal target of the simplified geo-electric model of the Strasbourg area as function of transmitter frequency and offset. The magenta, cyan and green lines corresponds to modelled noise spectra using a 20kWA transmitter in a noisy and quiet EM noise environment and a 200 kVA in a quiet EM noise environment, respectively. Bottom: Phase ratio between the inline horizontal electric field with (red) and without (blue) the geothermal target of the simplified geo-electric model of the Strasbourg area as function of transmitter frequency and offset.

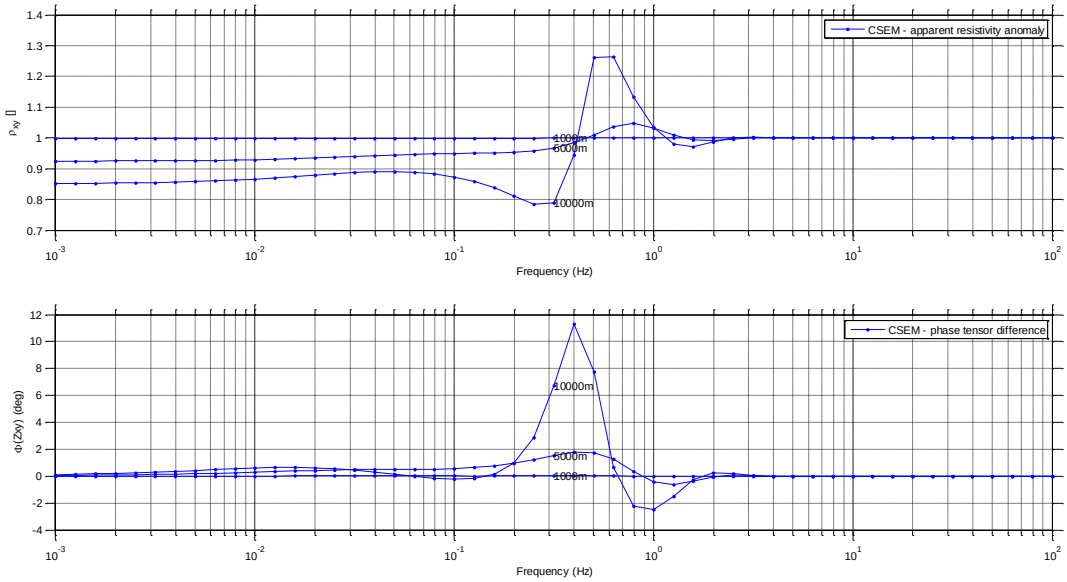

Figure 53: Top: Ratio between the apparent resistivity ratio with (red) and without (blue) the geothermal target of the simplified geo-electric model of the Strasbourg area as function of transmitter frequency and offset. Bottom: Phase difference between the inline horizontal electric field with (red) and without (blue) the geothermal target of the simplified geo-electric model of the Strasbourg area as function of transmitter frequency and offset.

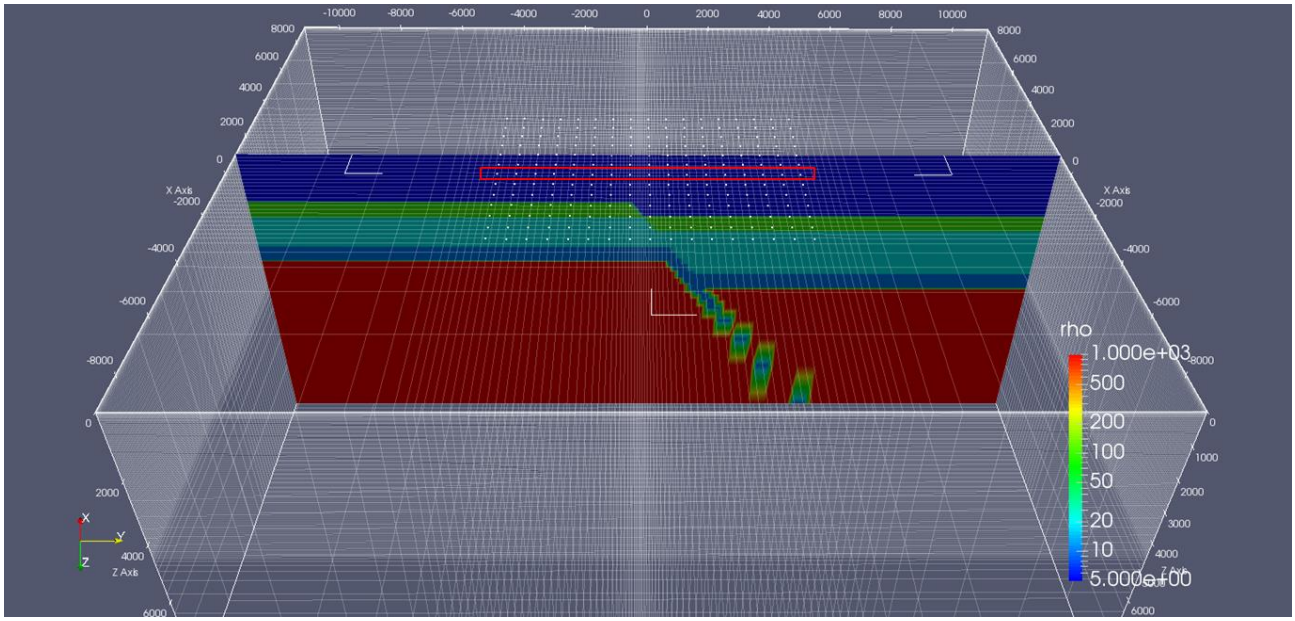

Figure 54: 3D geo-electric model of the geothermal targets in the Strasbourg area. The white dots represent CSEM and MT stations while the L-shape white lines represent the CSEM transmitters.

2.3.1.1.2.2 3D CSEM Modelling

The 3D CSEM response was computed using BRGM's proprietary 3D electromagnetic modelling code POLYEM3D. To interpret the modelling results, we have selected a subset of receivers along a profile crossing two transmitters and orthogonal to the strike to the fault (red box on Figure 54). To highlight the CSEM response of the different geological objects, we have calculated the scattered fields by normalizing the 3D modelling results with different 1D modelling responses.

The first normalization is against a homogeneous half-space (here, 5 Ω.m). We have displayed the ratio and difference between the amplitudes of the horizontal electric fields from the 3D model and homogeneous half-space for both inline (Figure 55) and broadside (Figure 60) configurations, but only for the transmitter at -8000m offset from the fault. Whatever the transmitter polarization, amplitude ratios show a significant anomaly (>100%, > $10^{-11.5}$ V/A.m^2) at low frequency (<1 Hz) and for all receiver positions i.e. easy measurable with a conventional transmitter even in noisy EM environment. This anomaly is the signature of the deep resistivity variations that are anomalous to the 5 Ω.m background resistivity. Here, we believe most of the signal comes from the 100 Ω.m 500m thick resistive layer. This hypothesis is reinforced by the fact that the inline response (max 4) is larger than the broadside response (max 2.5). Indeed, deep resistive layers are better coupled in a TM-mode (inline configuration) than TE-mode (broadside configuration) (Constable, 2010).

The second normalization is against a two-layer model (5 – 100 Ω.m, 1500m) to remove as much as possible the effect of the 100 Ω.m resistive layer at 1500m/2000m (Figure 45). Again, we have displayed the ratio and difference between the amplitudes of the horizontal electric fields from the 3D model and the two-layer model for both inline (Figure 55) and broadside (Figure 61) configurations. At negative offsets from the fault and for both transmitter polarizations, the amplitude anomaly is a lot more subtle (+/- 10%, max 10^{-12} V/A.m^2) at low frequency (<1 Hz) i.e. challenging to measure with a conventional transmitter in a noisy EM environment but measurable in other conditions. This anomaly is the signature of the deep resistivity variations underneath the 100 Ω.m resistive layer at 1500m i.e. mainly the conductive 20 Ω.m older sediments. Contrary to the resistive layer, the inline response (max 10% at <1Hz) is smaller than the broadside response (max +/-20% at <1Hz). Indeed, deep conductive layers are better coupled in a TE-mode (broadside configuration) than TE-mode (inline configuration) (Constable, 2010). At positive offsets from the fault, the anomalies are larger, simply because the 100 Ω.m resistive layer is deeper than in the 1D normalization model and hence its effect is only partially removed. From now, we will therefore only focus on the negative offsets.

The third normalization is against a three-layer model (5 – 100 – 20 Ω.m, 1500 - 2000m) to remove as much as possible the effect of the overburden layers and highlight the basement response. Again, we have displayed the ratio and difference between the amplitudes of the horizontal electric fields from the 3D model and the three-layer model for both inline (Figure 57) and broadside (Figure 62) configurations. At negative offsets from the fault and for both transmitter polarizations, the amplitude anomaly is small (+/- 5%, max $10^{-12.5}$ V/A.m^2) at low frequency (<1 Hz) i.e. challenging to measure with a conventional transmitter even in a quiet EM environment, only a powerful transmitter will give rise a significant signal to ratio. This highlights the fact that deep resistive basements are challenging targets for the CSEM technology, even if good S/N ratio is achieved.

The fourth normalization is against a four-layer model (5 – 100 – 20 – 1000Ω.m; 1500 – 2000 – 3000m) to remove as much as possible the effect of the overburden layers and basement and highlight the response of the conductive (10Ω.m) alteration zone at the top of the basement. Again, we have displayed the ratio and difference between the amplitudes of the horizontal electric fields from the 3D model and the three-layer model for both inline (Figure 58) and broadside (Figure 63) configurations. At negative offsets from the fault and for both transmitter polarizations, the amplitude anomaly is very small (a few %, <10^{-13} V/A.m^2) at low frequency (<1 Hz) i.e. very challenging to

measure with any type of transmitter, even in a quiet EM environment. Deep thin (<500m) conductive (10Ω.m) alteration zones are therefore very challenging targets for the CSEM technology.

The fifth normalization is against a five-layer model (5 – 100 – 20 – 10 – 1000Ω.m; 1500 – 2000 – 3000 – 3500m) to remove as much as possible the effect of the overburden layers, basement and alteration zone at the top of the basement and define with which lateral resolution the technique can image the fault. Again, we have displayed the ratio and difference between the amplitudes of the horizontal electric fields from the 3D model and the three-layer model for both inline (Figure 59) and broadside (Figure 64Figure 63) configurations. The amplitude anomalies at negative offsets are the signature of the fault and show that with an inline configuration, the accuracy of the fault position is a few 100's of meters and about 1km for the broadside configuration.

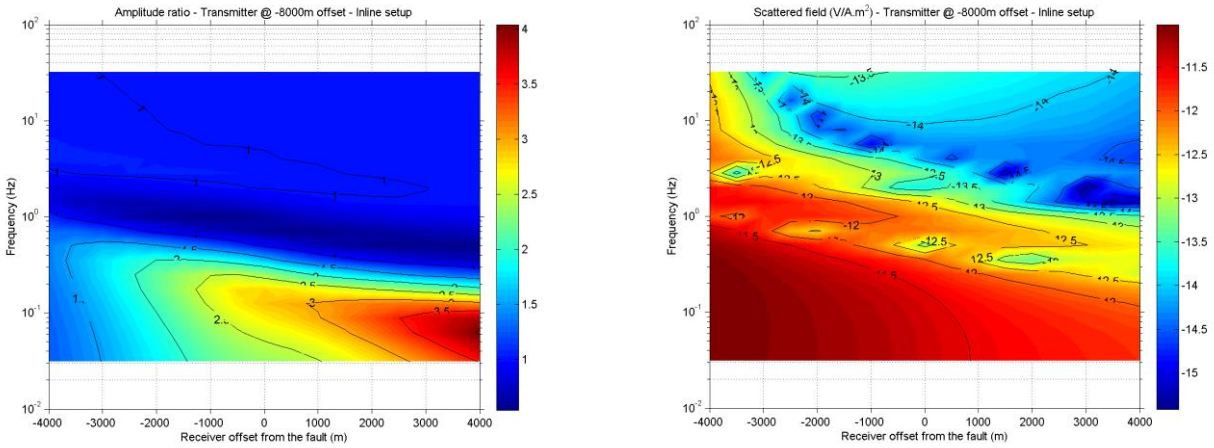

Figure 55: <u>Left:</u> Ratio between the amplitude of the inline horizontal electric field calculated from the 3D geo-electric model of Figure 54 and from a 5 Ω.m half-space model for the transmitter located at -8000m offset from the main fault. <u>Right:</u> Difference between the amplitude of the inline horizontal electric field calculated from the 3D geo-electric model of Figure 54 and from a 5 Ω.m half-space model for the transmitter located at -8000m offset from the main fault.

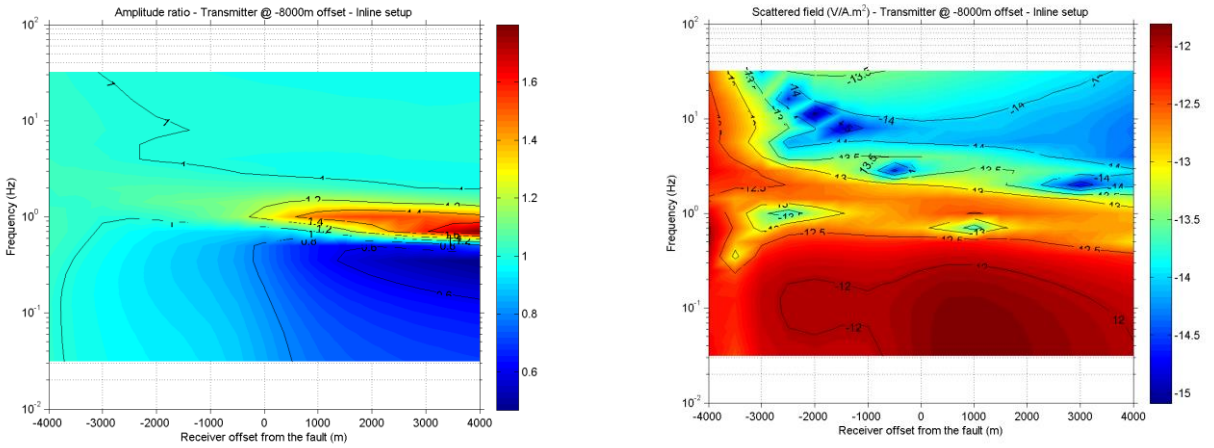

Figure 56: <u>Left:</u> Ratio between the amplitude of the inline horizontal electric field calculated from the 3D geo-electric model of Figure 54 and from a two-layer model [5 – 100 Ω.m; 1500m] for the transmitter located at -8000m offset from the main fault. <u>Right:</u> Difference between the amplitude of the inline horizontal electric field calculated from the 3D geo-electric model of Figure 54 and from a two-layer model [5 – 100 Ω.m; 1500m] for the transmitter located at -8000m offset from the main fault.

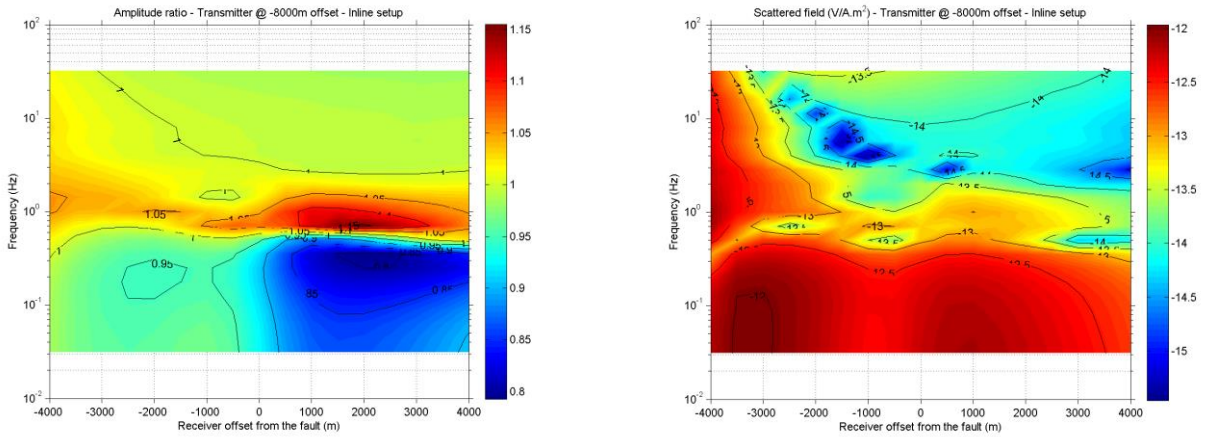

Figure 57: Left: Ratio between the amplitude of the inline horizontal electric field calculated from the 3D geo-electric model of Figure 54 and from a three-layer model [5 – 100 – 20 Ω.m; 1500 – 2000m] for the transmitter located at -8000m offset from the main fault. Right: Difference between the amplitude of the inline horizontal electric field calculated from the 3D geo-electric model of Figure 54 and from a three-layer model [5 – 100 – 20 Ω.m; 1500 – 2000m] for the transmitter located at -8000m offset from the main fault.

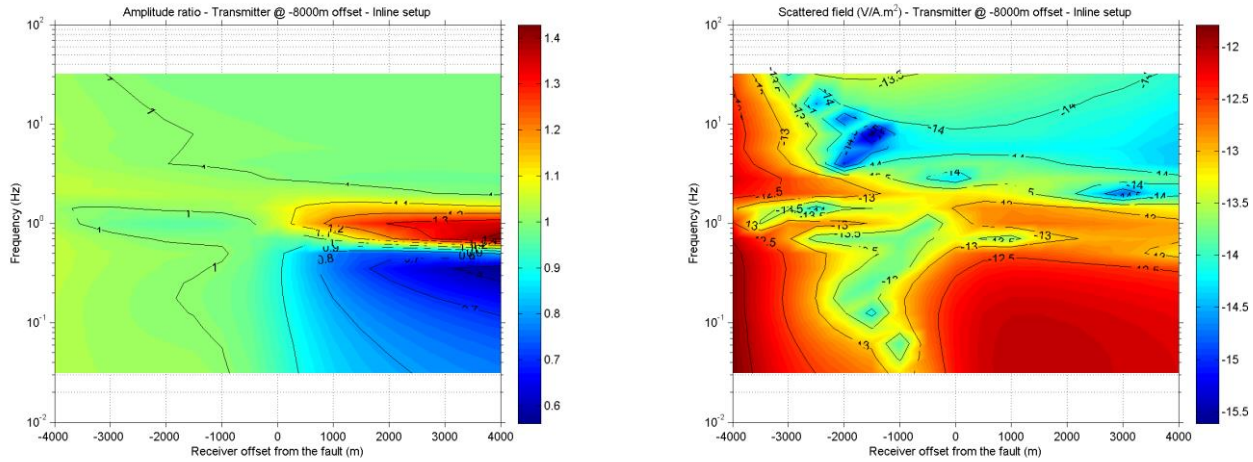

Figure 58: Left: Ratio between the amplitude of the inline horizontal electric field calculated from the 3D geo-electric model of Figure 54 and from a four-layer model [5 – 100 – 20 – 1000Ω.m; 1500 – 2000 – 3000m] for the transmitter located at -8000m offset from the main fault. Right: Difference between the amplitude of the inline horizontal electric field calculated from the 3D geo-electric model of Figure 54 and from a four-layer model [5 – 100 – 20 – 1000Ω.m; 1500 – 2000 – 3000m] for the transmitter located at -8000m offset from the main fault.

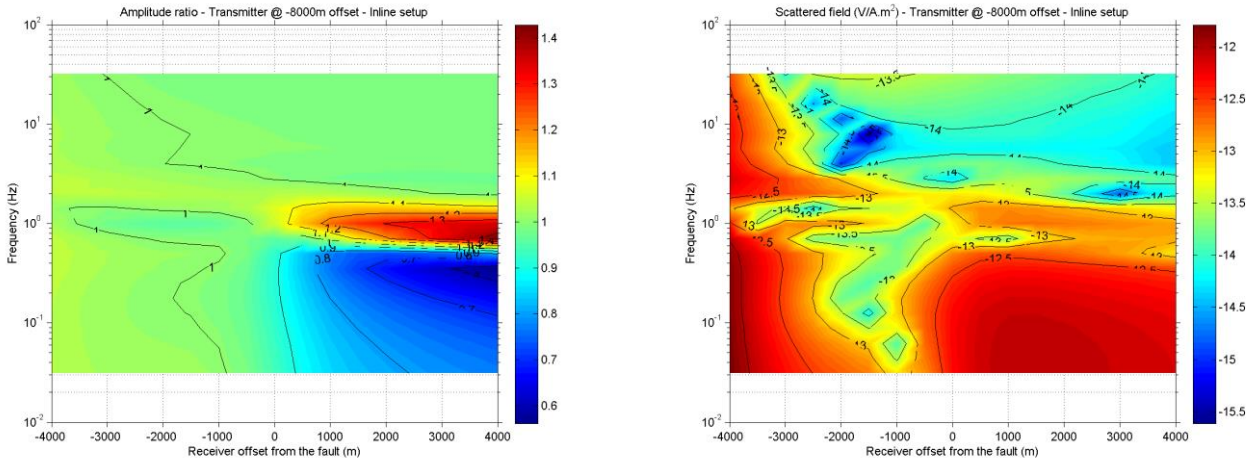

Figure 59: <u>Left:</u> Ratio between the amplitude of the inline horizontal electric field calculated from the 3D geo-electric model of Figure 54 and from a five-layer model [5 – 100 – 20 – 10 – 1000Ω.m; 1500 – 2000 – 3000 – 3500m] for the transmitter located at -8000m offset from the main fault. <u>Right:</u> Difference between the amplitude of the inline horizontal electric field calculated from the 3D geo-electric model of Figure 54 and from a five-layer model [5 – 100 – 20 – 10 – 1000Ω.m; 1500 – 2000 – 3000 – 3500m] for the transmitter located at -8000m offset from the main fault.

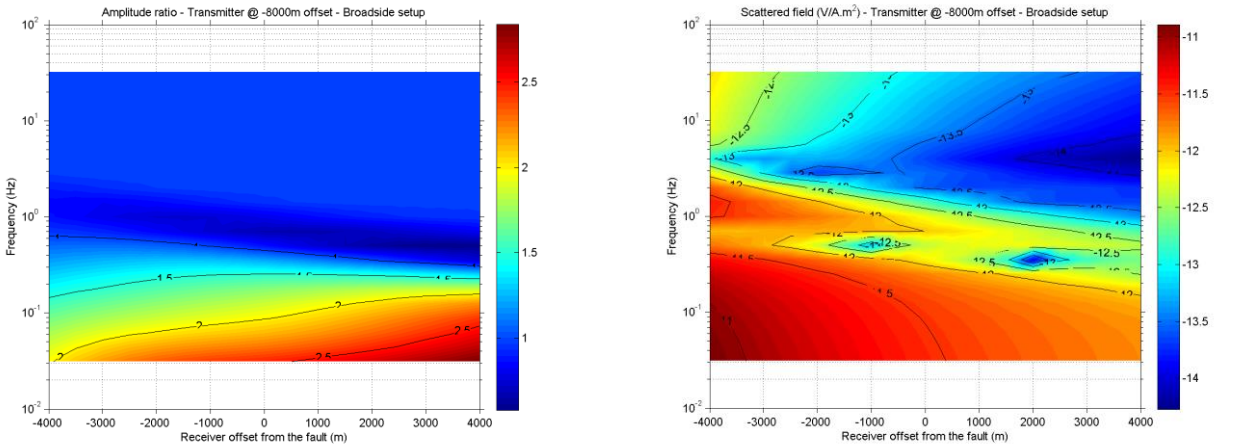

Figure 60: <u>Left:</u> Ratio between the amplitude of the broadside horizontal electric field calculated from the 3D geo-electric model of Figure 54 and from a 5 Ω.m half-space model for the transmitter located at -8000m offset from the main fault. <u>Right:</u> Difference between the amplitude of the broadside horizontal electric field calculated from the 3D geo-electric model of Figure 54 and from a 5 Ω.m half-space model for the transmitter located at -8000m offset from the main fault.

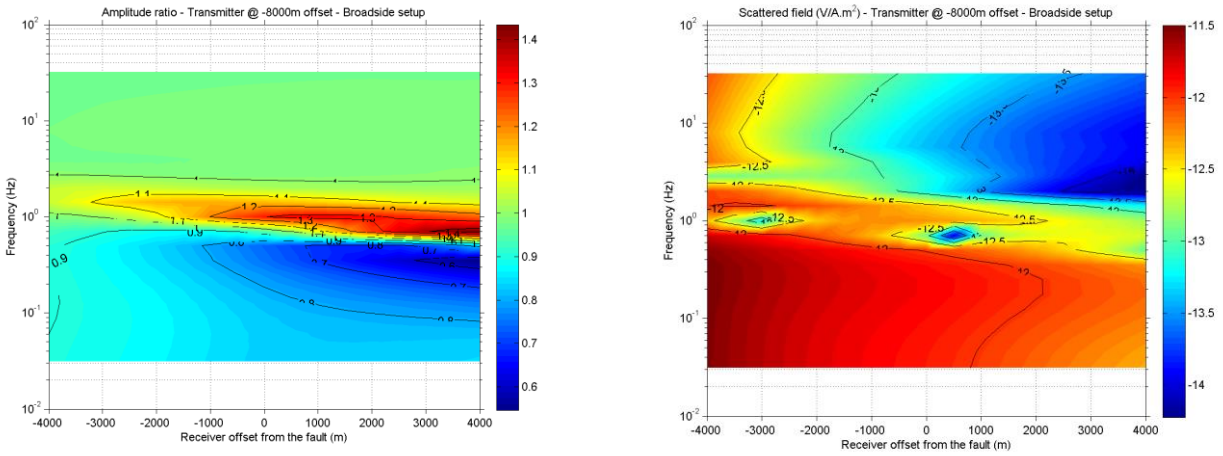

Figure 61: <u>Left:</u> Ratio between the amplitude of the broadside horizontal electric field calculated from the 3D geo-electric model of Figure 54 and from a two-layer model [5 – 100 Ω.m; 1500m] for the transmitter located at -8000m offset from the main fault. <u>Right:</u> Difference between the amplitude of the broadside horizontal electric field calculated from the 3D geo-electric model of Figure 54 and from a two-layer model [5 – 100 Ω.m; 1500m] for the transmitter located at -8000m offset from the main fault.

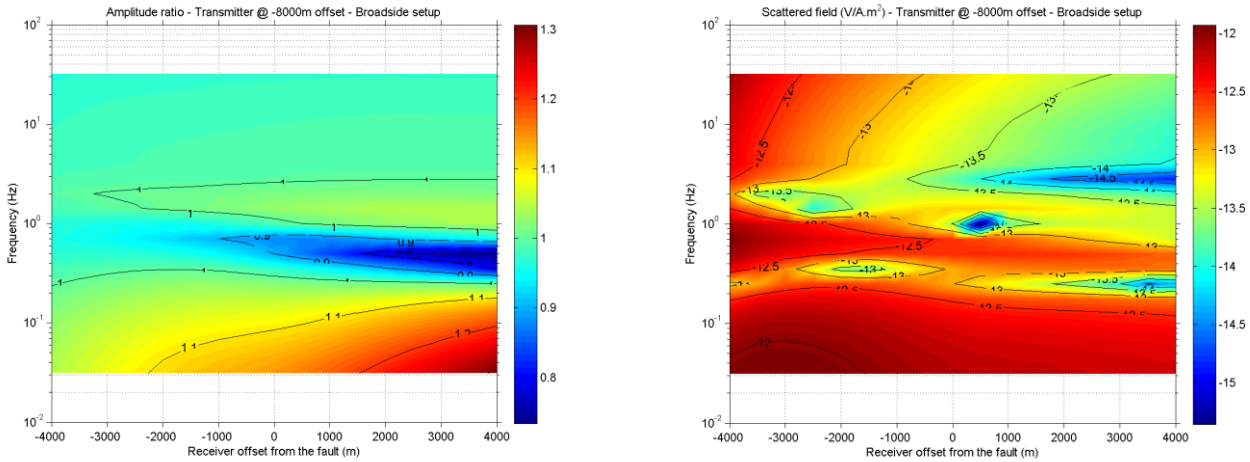

Figure 62: <u>Left:</u> Ratio between the amplitude of the broadside horizontal electric field calculated from the 3D geo-electric model of Figure 54 and from a three-layer model [5 – 100 – 20 Ω.m; 1500 – 2000m] for the transmitter located at -8000m offset from the main fault. <u>Right:</u> Difference between the amplitude of the broadside horizontal electric field calculated from the 3D geo-electric model of Figure 54 and from a three-layer model [5 – 100 – 20 Ω.m; 1500 – 2000m] for the transmitter located at -8000m offset from the main fault.

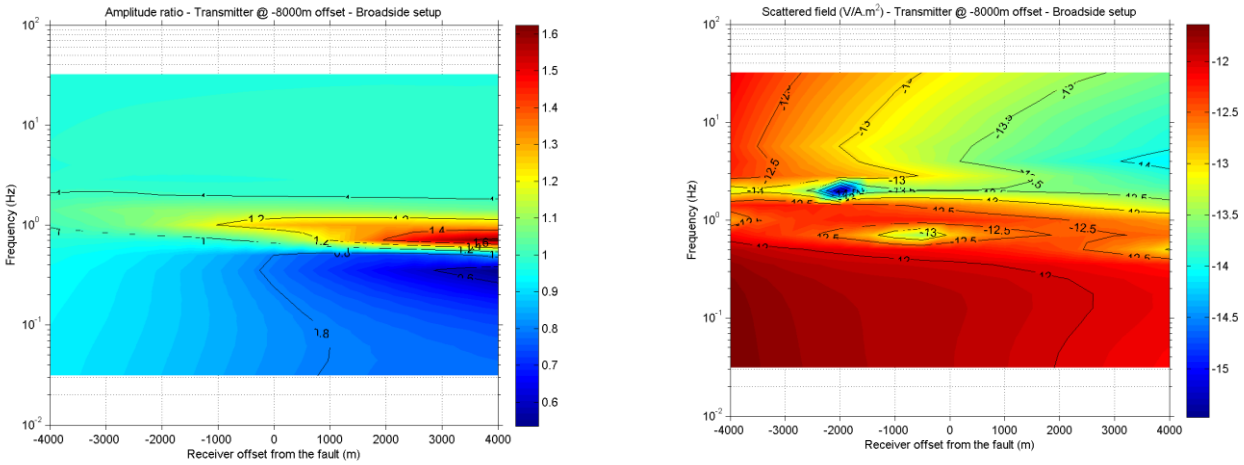

Figure 63: Left: Ratio between the amplitude of the broadside horizontal electric field calculated from the 3D geo-electric model of Figure 54 and from a four-layer model [5 – 100 – 20 – 1000Ω.m; 1500 – 2000 – 3000m] for the transmitter located at -8000m offset from the main fault. Right: Difference between the amplitude of the broadside horizontal electric field calculated from the 3D geo-electric model of Figure 54 and from a four-layer model [5 – 100 – 20 – 1000Ω.m; 1500 – 2000 – 3000m] for the transmitter located at -8000m offset from the main fault.

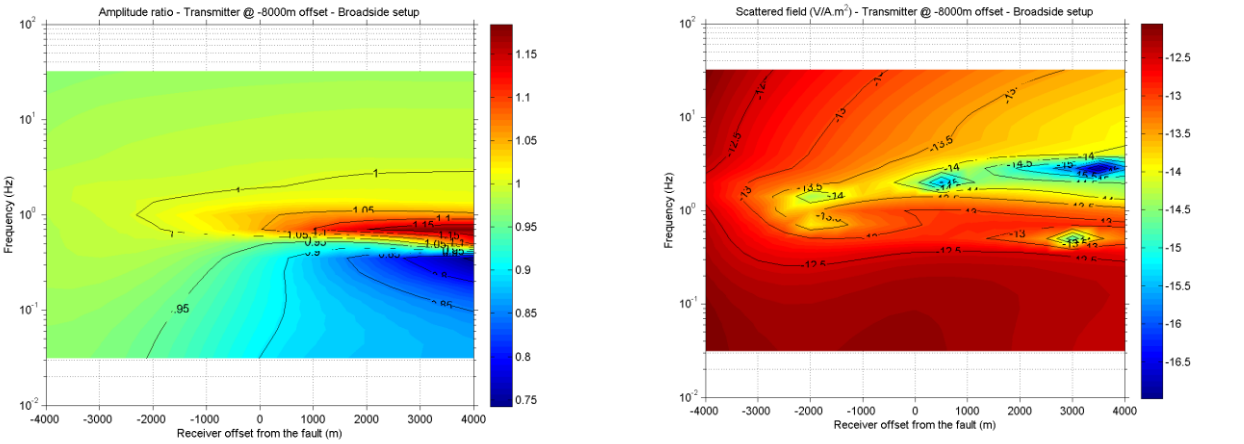

Figure 64: Left: Ratio between the amplitude of the broadside horizontal electric field calculated from the 3D geo-electric model of Figure 54 and from a five-layer model [5 – 100 – 20 – 10 – 1000Ω.m; 1500 – 2000 – 3000 – 3500m] for the transmitter located at -8000m offset from the main fault. Right: Difference between the amplitude of the broadside horizontal electric field calculated from the 3D geo-electric model of Figure 54 and from a four-layer model [5 – 100 – 20 – 10 – 1000Ω.m; 1500 – 2000 – 3000 – 3500m] for the transmitter located at -8000m offset from the main fault.

2.3.1.1.2.3 CSEM imaging

The final step of the CSEM feasibility study consisted in performing 1D inversion of the 3D CSEM datasets in order to quantify the resolution at which the geological targets can be resolved. For this purpose, we used the smooth 1D inversion code designed by Constable et al. (1987) and Key (2009) called OCCAM1D. We inverted all CSEM stations along a 2D profile crossing the fault and passing through the transmitter located at -8000m offset. One example is shown on Figure 65 for CSEM receiver located at -4000m offset (i.e. 4km from the fault and 4km from the transmitter). Data fit is good and the recovered resistivity profile shows that the sediments are well imaged (resistivity and position of the interfaces are correct) while the depth and resistivity of the basement not so well. This illustrates again the fact that even though the dataset is noise free, the CSEM technique struggles to recover deep resistive variations. After inversion of all CSEM stations (Figure 66), we can observe that the sediments are well imaged (resistivity of layers and depth of interfaces) but also that the fault can easily be identified (although a small error in position exists due to the 1D assumption in the inversion process). As expected from the sensitivity analysis, the depth and resistivity of the basement is not so well imaged, at best it recovers the presence of a deep resistive body.

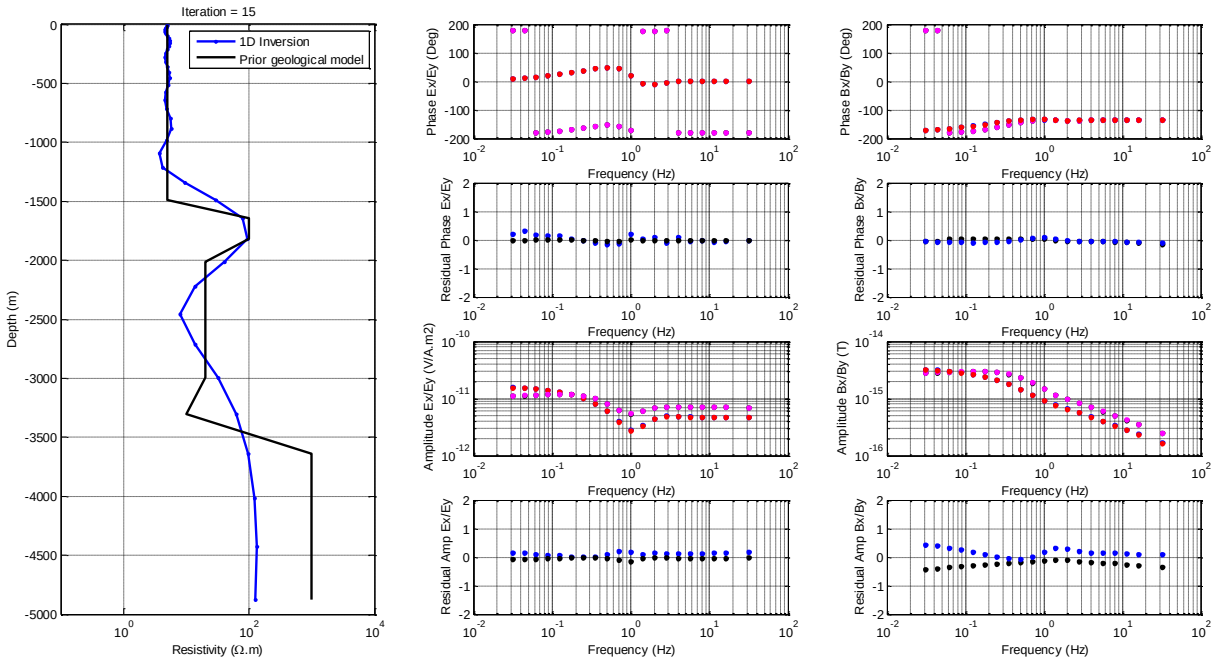

Figure 65: <u>Left:</u> Resistivity profile after inversion of the CSEM data (blue) and true (black). <u>Middle:</u> true (blue: inline transmitter, black: broadside transmitter) and inverted (black: inline transmitter, magenta: broadside transmitter) phase (top) and amplitude (bottom) of the electric field as a function frequency. <u>Right:</u> true (blue: inline transmitter, black: broadside transmitter) and inverted (black: inline transmitter, magenta: broadside transmitter) phase (top) and amplitude (bottom) of the magnetic field as a function frequency.

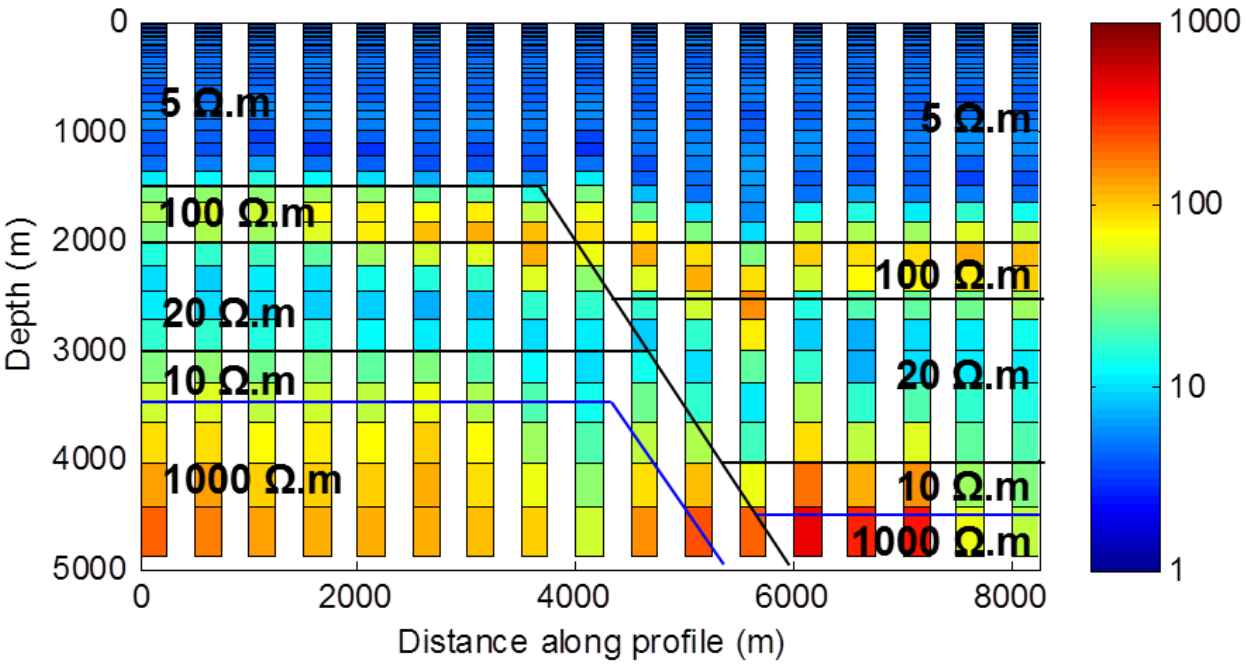

Figure 66: Resistivity profile (log10) after 1D inversion of the CSEM dataset calculated from the 3D geo-electric model of Figure 54 and the transmitter at -8000m from the fault.

2.3.1.1.3 Magneto-Telluric Imaging

To assess the benefits and limitations of MT data in this area, we performed a similar sensitivity analysis on the MT data calculated from 3D geo-electric model of Figure 54 and performed a smooth 1D inversion using Constable et al. (1987) code. Here also, we inverted all MT stations along a 2D profile crossing the fault and passing through the transmitter located at -8000m offset. One example is shown on Figure 65 for MT receiver located at -4000m offset (i.e. 4km from the fault and 4km from the transmitter). Data fit is excellent but the recovered resistivity profile shows that the shallow conductive sediments are well imaged (resistivity/thickness of the first layer) but the first resistive layer is not imaged (the MT technique is not sensitive to it because it too thin). A smooth increase related to the presence of the basement is recovered at depth but the position of the interfaces and resistivities are not well defined. This illustrates again the fact that even though the dataset is noise free, the MT technique struggles to recover the geometry of deep resistive bodies but rather highlights the presence of conductive layers. Similar conclusions can be drawn from the inversion of all MT stations (Figure 68).

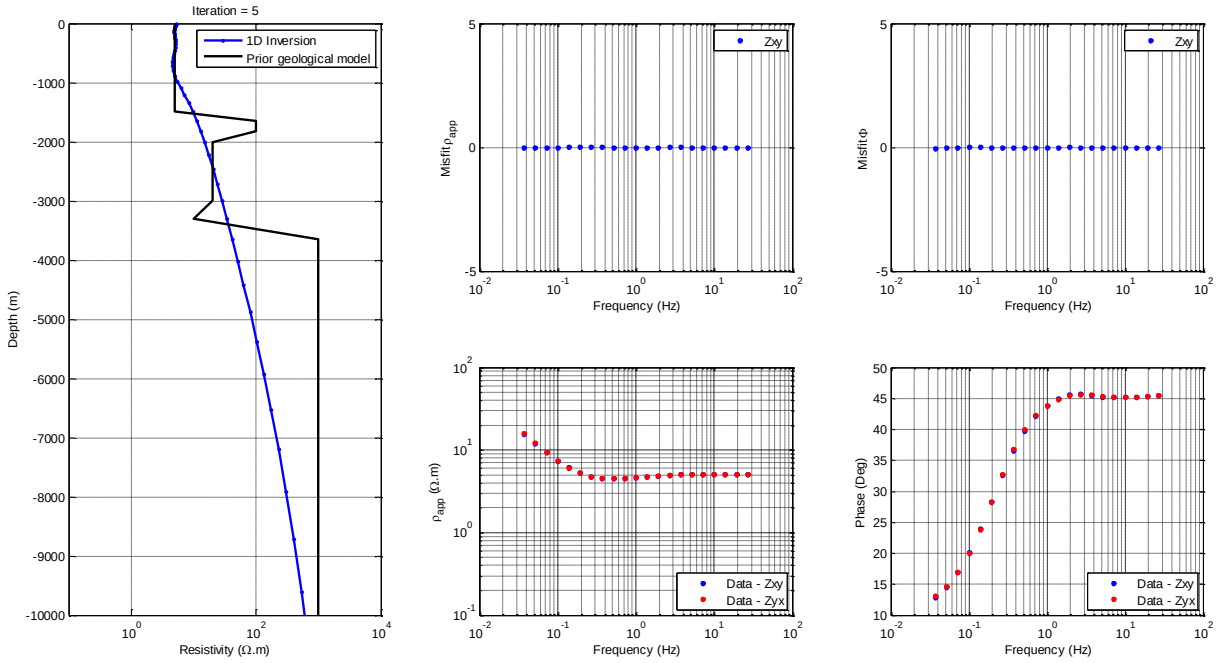

Figure 67: <u>Left:</u> Resistivity profile after inversion of the MT data (blue) and true (black). <u>Middle:</u> true (blue) and inverted (red) apparent resistivity (bottom) and residuals (top) as a function frequency. <u>Right:</u> true (blue) and inverted (red) phase (bottom) and residuals (top) as a function frequency.

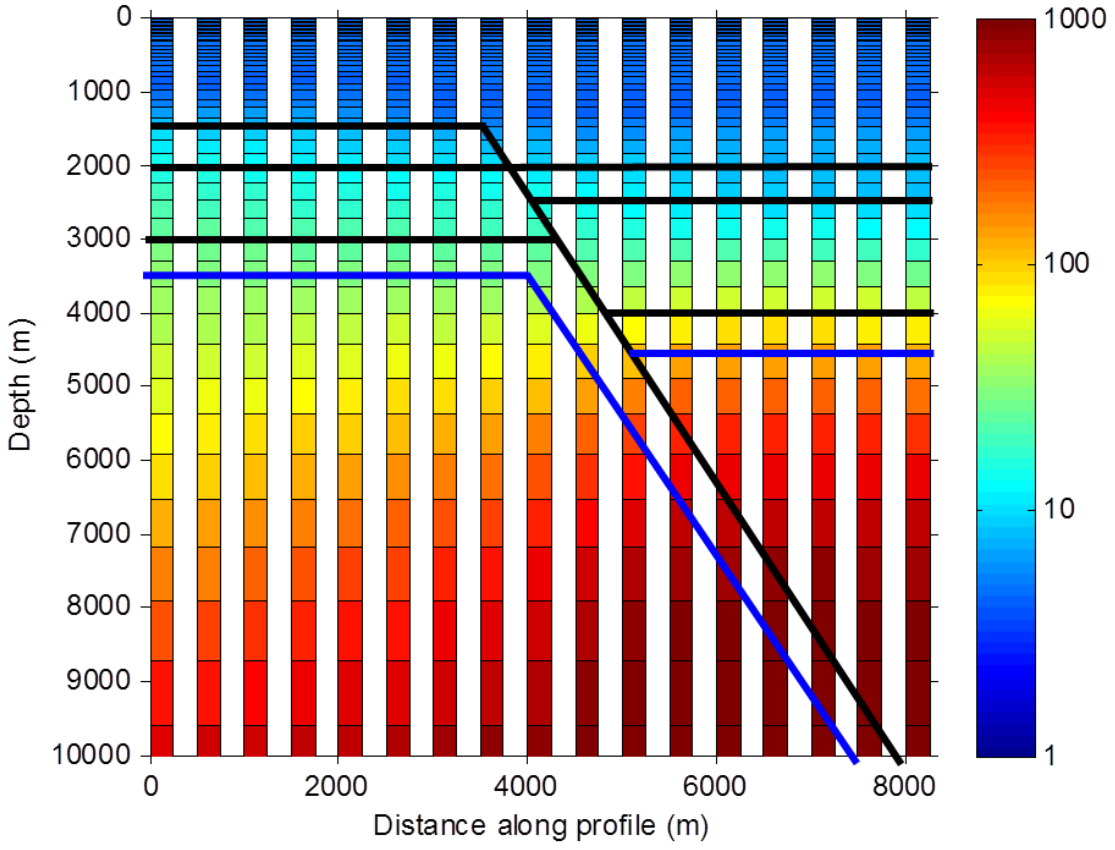

Figure 68: Resistivity profile (log10) after 1D inversion of the MT dataset calculated from the 3D geo-electric model of Figure 54.

2.3.1.1.4 Joint Controlled Electro-Magnetic and Magneto-Telluric Imaging

To take advantage of the different sensitivities of the CSEM and MT techniques for increased resolution, we performed a joint smooth 1D inversion of the MT and CSEM datasets calculated from 3D geo-electric model of Figure 54. Here also, we inverted all CSEM and MT stations along a 2D profile crossing the fault and passing through the transmitter located at -8000m offset. One example is shown on Figure 69 for the CSEM/MT receiver located at -4000m offset (i.e. 4km from the fault and 4km from the transmitter). Data fit is good but not as good as with MT or CSEM data alone. The recovered resistivity profile shows that the sediments are well imaged (resistivity/thickness of the first layer) but also the resistivity of the basement is better recovered than with CSEM data only (Figure 65) due to the additional constraints on the basement from the MT dataset. This illustrates the benefit of the joint inversion as it allows the CSEM and MT datasets to complement each other when one fails to recover a structure. Similar conclusions can be drawn from the joint inversion of all CSEM/MT stations along the 2D profile (Figure 70). Indeed, the resistivity and depth of the interfaces in the sedimentary cover are better recovered than with CSEM data only (Figure 66) or MT only (Figure 68) but also the position of the fault is more correct. The resistivity of the basement is now also properly recovered but the position of the top of the basement is not so well defined, most likely due to the smooth nature of the inversion. To compensate for this effect and increase even more the vertical resolution of the final image, we performed a joint sharp inversion structurally constrained by depth horizons. To do so, we introduced breaks in the smoothing function at the depth of the main resistivity contrasts (base of young sediments, top of old sediments and top basement) during the inversion process. The resulting resistivity profile (Figure 71) is now obviously structurally correct but we also manage to recover a conductive anomaly at the fault position and depth of the basement, which is very likely associated to the conductive fault zone in geo-electric model. This demonstrates that the only way to recover subtle deep resistivity variations associated to conductive fault zone is by performing a joint inversion of CSEM and MT datasets structurally constrained by depth horizons (e.g. from seismic/gravity data or geological models).

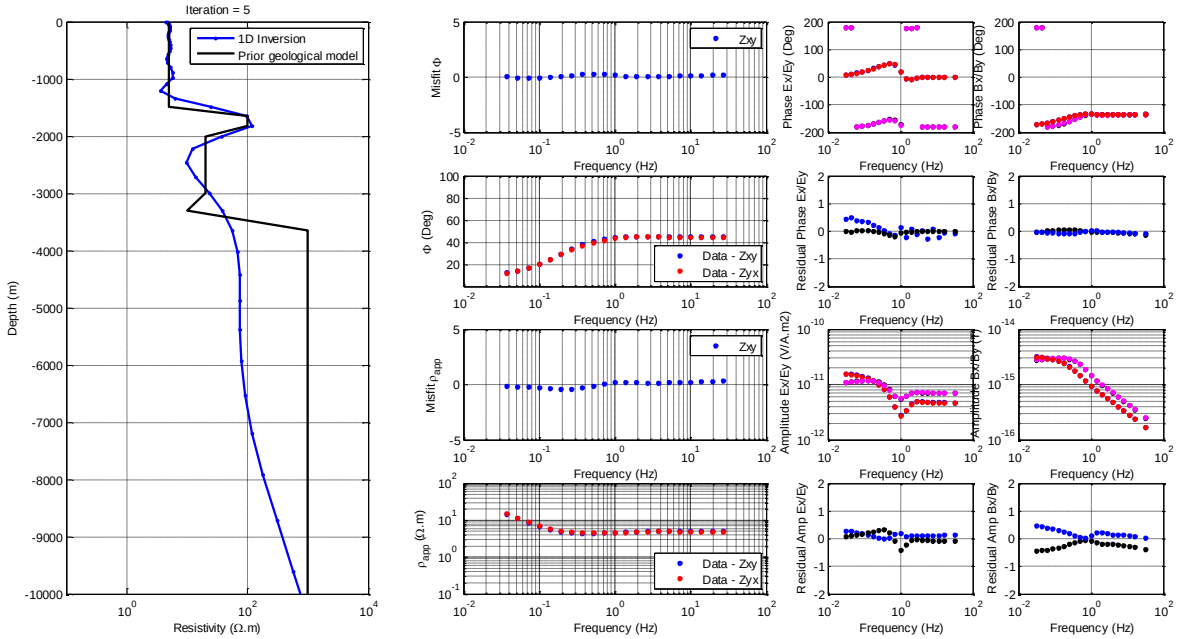

Figure 69: <u>Left:</u> Resistivity profile after the joint inversion of the CSEM and MT data (blue) and true (black). <u>Middle:</u> true (blue) and inverted (red) apparent resistivity (bottom) and phase (top) as a function frequency. <u>Right:</u> true (blue: inline transmitter, black: broadside transmitter) and inverted (black: inline transmitter, magenta: broadside transmitter) phase (top) and amplitude (bottom) of the electric and magnetic field as a function frequency.

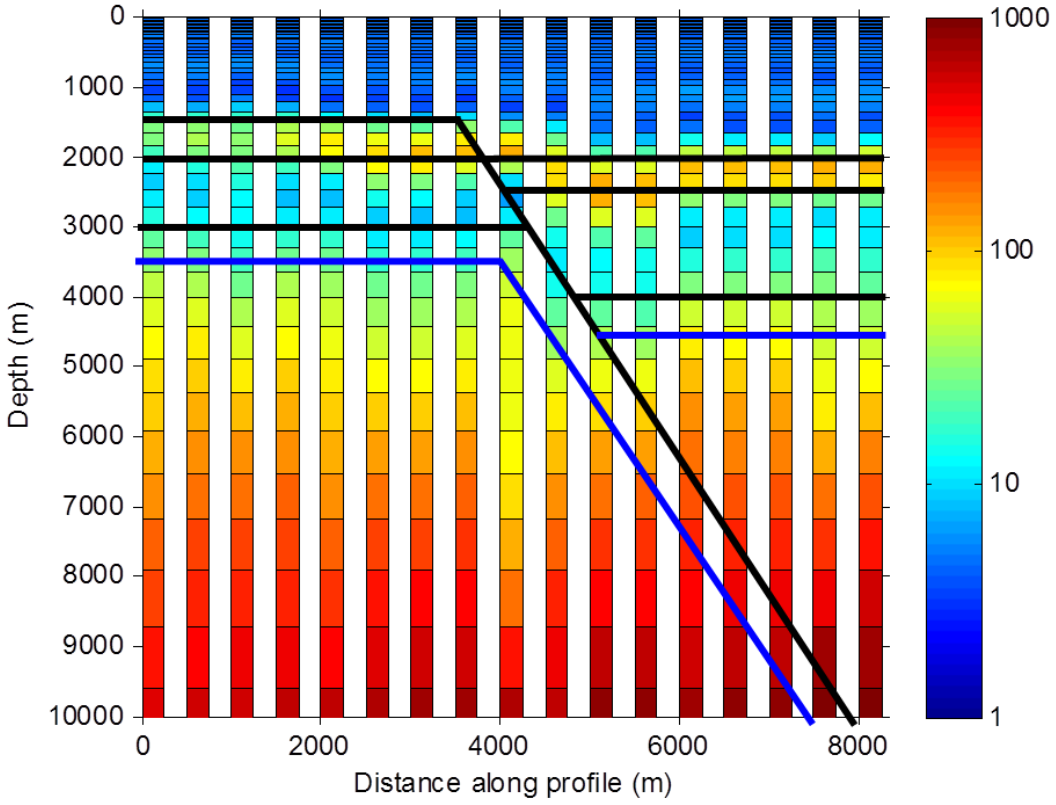

Figure 70: Resistivity profile (log10) after unconstrained joint 1D inversion of the CSEM and MT dataset calculated from the 3D geo-electric model of Figure 54.

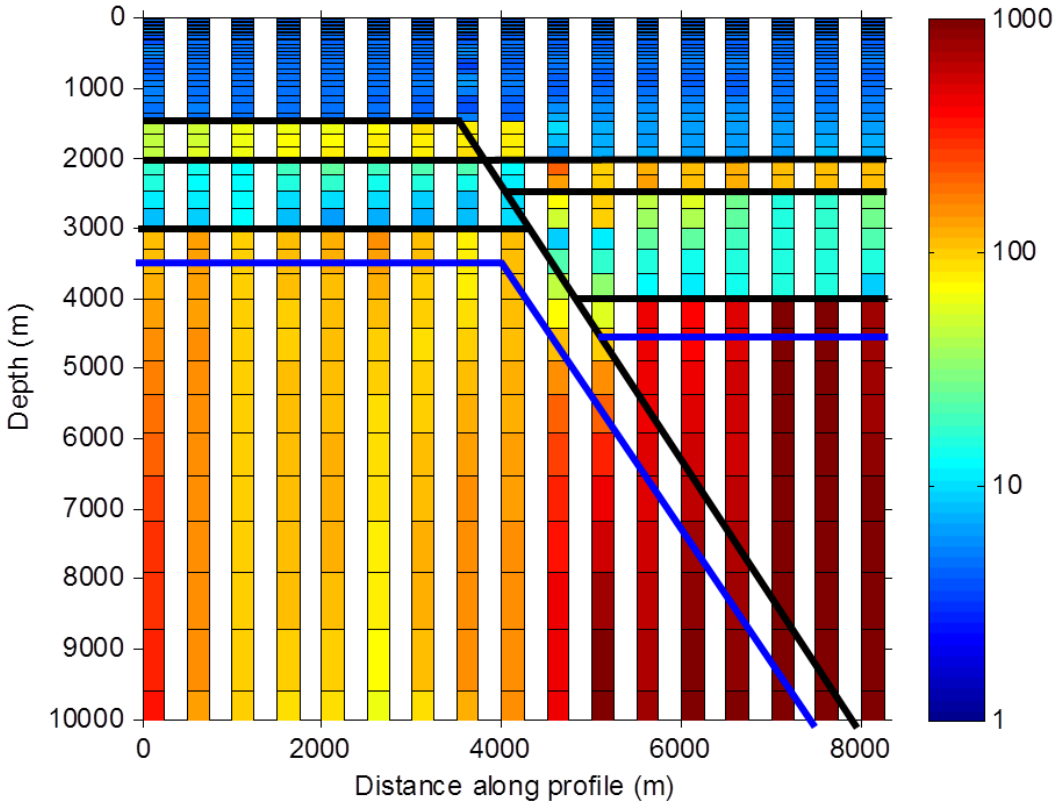

Figure 71: Resistivity profile (log10) after constrained joint 1D inversion of the CSEM and MT dataset calculated from the 3D geo-electric model of Figure 54.

2.3.1.2 Survey Design

The feasibility study based on 1D & 3D modelling showed that expected CSEM anomalies related to deep conductive bodies associated to hydrothermally altered zones are likely to be small, at low frequencies (<1Hz) and close the noise level with conventional CSEM sources. We therefore decided to acquire as low as possible CSEM frequencies during the survey. The level of EM noise at low frequency (<1Hz) is however increasing roughly by a factor 10 over one decade (Figure 72) while the scattered field due to geological target (here, a 100 Ω.m half-space compared to a 1000 Ω.m half-space) does not increase as steeply (red line on Figure 72). There is therefore a frequency window for which the signal to noise is optimal. For this particular target, the optimal period is 16s (signal to noise ratio close to 3) while a 32s period would lead to a poor signal to noise ratio (close to 1). As the response from a half-space is the maximal response we can expect, we decided to use this calculation to define the survey frequencies i.e. starting with a square wave of fundamental period 16s (0.0625Hz) and subsequent higher fundamental periods decreasing with a factor 4 (8s, 2s, 0.5s, 0.125s, 0.03125s etc…, see Table 2). We also looked into the possibility of increasing the recording time in order to stack out as much as possible random EM noise (Figure 73). We can observe that recording times larger than 15min (i.e. 50 cycles) do not lead to lower noise levels, probably due to the presence of coherent sources of noise. We therefore decided to limit the recording times at 16s to 22 min (i.e. 82.5 cycles). In terms of transmitter-receiver offsets, it is clear that long offset are required to image deep resistivity variations and that short-offset do not contribute much (<2 km; see 3D modelling paragraph). We therefore decided to place CSEM receivers at least 2km away from the transmitter. In terms of source polarization, as shown in the previous paragraph, inline and broadside configurations respond differently to deep resistivity contrasts and therefore needs to be measured to recover the true resistivity.

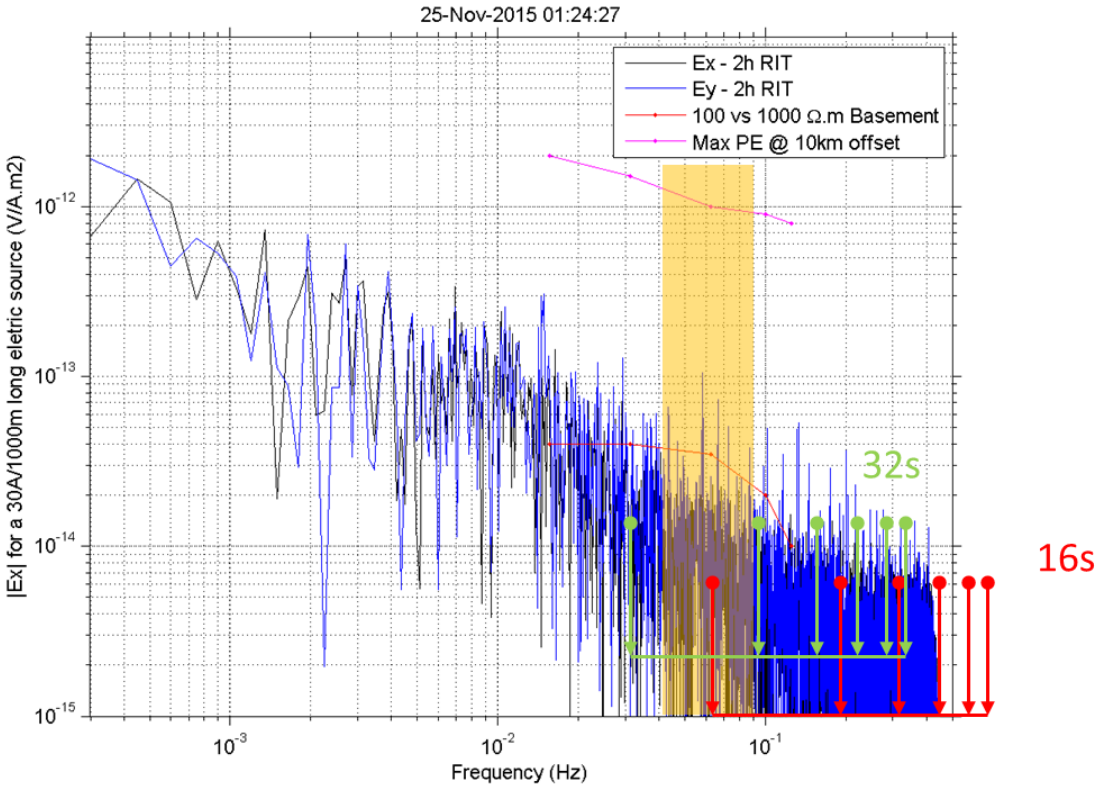

Figure 72: Amplitude of the EM noise recorded over a 2h period in the Upper Rhine Graben.

FREQ (Hz)	PERIOD (s)	LENGTH (min)	Nb Stack
0.0625	16	22	82.5
0.125	8	10	75
0.5	2	5	150
2	0.5	2	240
8	0.125	1	480
32	0.03125	0.5	960
128	0.0078125	0.5	3840
256	0.00390625	0.5	7680
512	0.00195313	0.5	15360
	TOTAL	42	

Table 2: Fundamental frequencies and durations of the selected square waves to be transmitted during the CSEM survey.

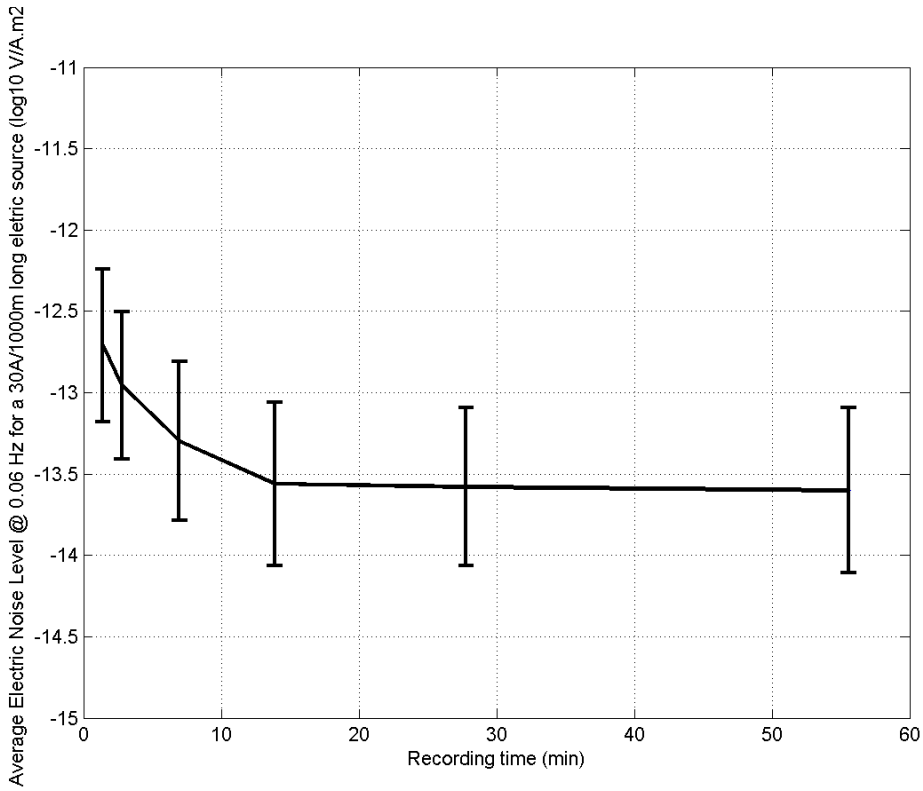

Figure 73: Average amplitude of the EM noise at 16s recorded over a period of variable length (x-axis) in the Upper Rhine Graben.

2.3.2 CSEM data acquisition and processing

2.3.2.1 Data Acquisition

The survey took place in May 2016 in the western side of Strasbourg city (France, see Figure 74). 2km of cables were installed in order to link a northern (black line) and eastern (red line) patches of 15 metallic electrodes to the transmitter (a TXM22 source, made by Metronix), a third cluster of 15 electrodes was installed in the vicinity of the source (light green line). The North and central cluster forms an electric dipole called polarization 1, the Eastern and central cluster defines polarization 2.

A total number of 25 Rx stations (ADU07 MT stations, Metronix) were installed along two parallel NW-SE profiles and one transverse SW-NE profile. All stations made CSEM measurements. 10 stations recorded magnetotelluric (hereafter MT) signals during the nights and week-ends.

For CSEM, the injected signals were consecutive squared signals of fixed frequencies. Corresponding duration and frequencies are given in Table 1 during a sequence of 45 minutes. This process is repeated continuously all day along in polarisation 1 and 2. It allows Rx teams to increase their efficiency. Injected signal intensity was of 35 Amperes for the lowest frequencies and about 29 A for the highest frequencies for both polarisations 1 and 2.

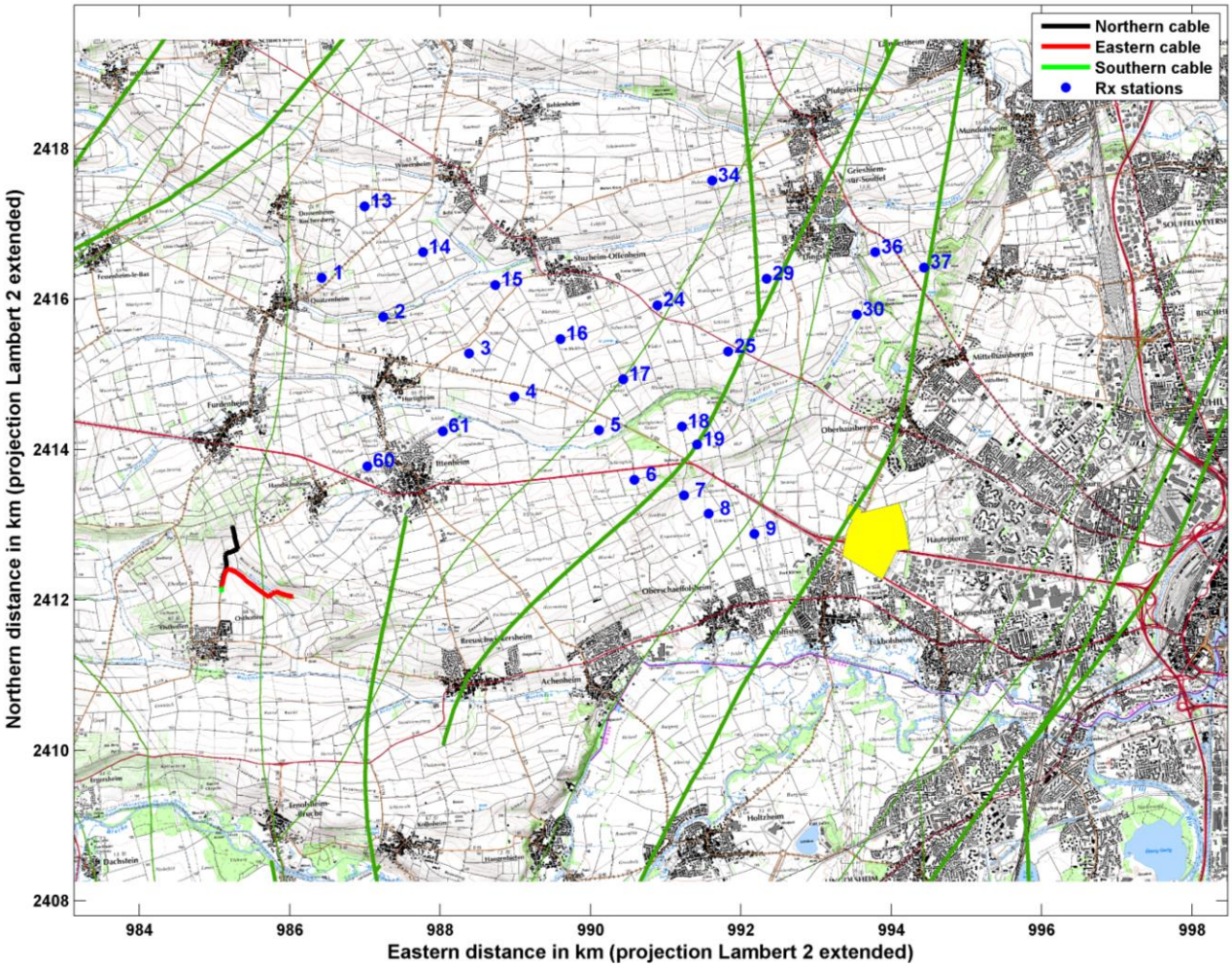

Figure 74: Map of the Strasbourg Region survey. Large green lines show the major accidents of the region. The yellow area represents Fonroche prospect area for the building of a geothermal doublet (beginning in 2017). The source cables for Tx dipoles are shown in b black red and green. Receiver positions are blue points.

.

Tx Emitted period in seconds(T>1s)/Hz (T<1s)	Duration (min s)	Emission TimeTable from starting hour H	fTx sampling frequency in Hz	fRx sampling frequency
16 s	20 min	H	128	128

8 s	9 min	H+21 min	128	128
2 s	4 min	H+31 min	128	128
2 Hz	2 min	H+36 min	128	128
8 Hz	1 min	H+39 min	4096	4096
32 Hz	30 sec	H+41 min	4096	4096
128 Hz	30 sec	H+42 min 30 sec	4096	4096

Tableau 1: Table of emitted squared signal frequencies, duration, time table and Rx an Tx sampling frequencies

2.3.2.2 Robust Processing of CSEM data

At each station, the horizontal electric $(e_x(t),e_y(t))$ and horizontal and vertical $(h_x(t),h_y(t),h_z(t))$ (when possible) magnetic field are recorded in time domain. Measurements are synchronous to the source injection current i(t).

For each polarization and injected fundamental frequency f_{TX}, the spectral domain transfer function (hereafter) between each components of e or h and I is estimated using direct Fourier transform ratio, classical weighted least square (Streich et al.,2013) and robust algorithm like M-estimator and bounded influence estimator (theory derivated from magnetotelluric TF procedures available in Chave and Jones, 2012). The estimates are realised on all even harmonics of the injected frequency. Weighted least square and robust procedures allows to reject contaminated data in the processed populations using regression residual robust statistics.

From then the user can pick the processed TF ($E_x(f)$, $E_y(f)$, $H_x(f)$, $H_y(f)$, $H_z(f)$) of electric and magnetic fields that display the highest quality. To evaluate the quality of the TFs, one can compare horizontal electric and magnetic TF vectors with modelled data.

Those modelled data are associated with a homogeneous half space in which the exact position of the grounded electrodes for polarization 1 and 2 are implemented. Modelling is performed using the EM3DS code (Newman and Hohmann, 1988). First, the code uses an analytic formulation to compute the components of the EM fields generated by a surface injection setup on a layered medium (stratified earth, flat soil surface). The EM source is modelled as a polygonal electrical wire, which extremities are grounded (galvanic injection); the EM fields generated are called the primary fields. In our case modelling is performed using a simple layered medium. The resistivity of the half space is deduced the conceptual model showed in Figure 43.

Vectors of in-phase (the real part) electric field TFs $[E_x(f), E_y(f)]$ from the data set are compared with modelled values. All transfer method estimation method is shown: classical TF ratio, weighted least-square, M-estimator and bounded influence estimator. The purpose of this quality check is to compare the orientation of Ep vectors to modelled ones, and to assess the dispersion of estimation procedure methods. Figure 75 and Figure 76 display results obtained for fundamental frequencies of injection 0.125Hz and 32 Hz. One can see that the fit between modelled data and observed ones is good for stations associated with easting coordinates under 991km, which have been identified as stations with high signal to noise ratio. Above 991km easting, anthropic noise sources overwhelm the Tx source signal. Consequently, the angular fit is poor and estimation procedure results diverge.

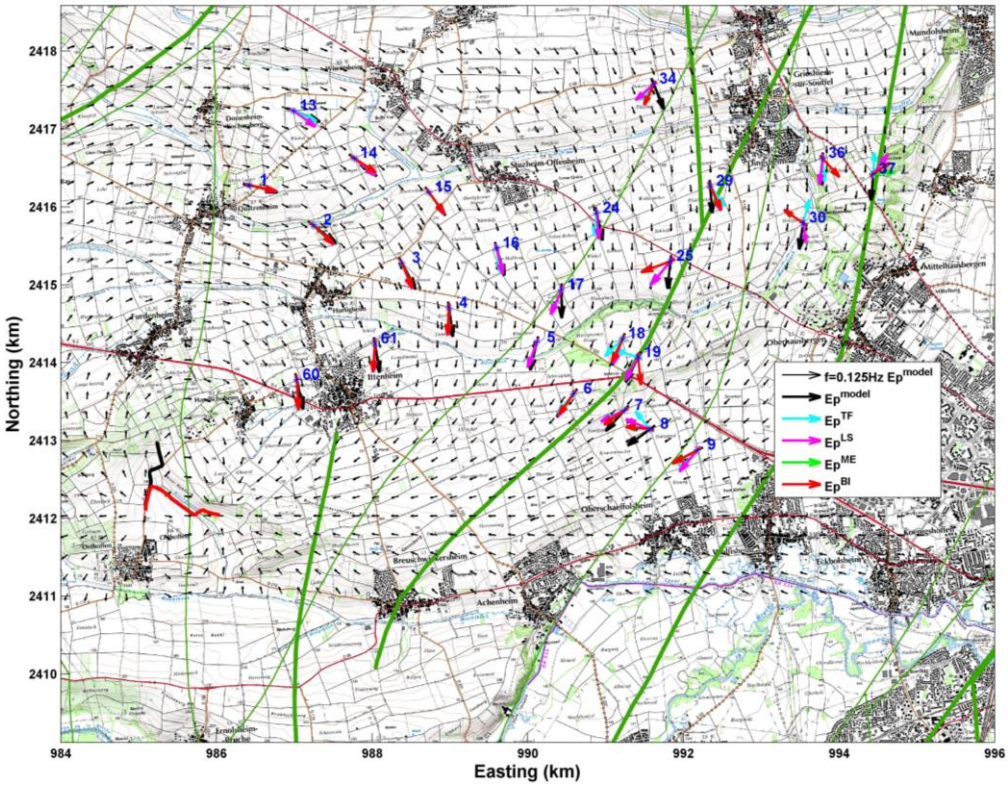

Figure 75: f=0.125 Hz. Map of in phase electric field vectors data compared to modelled data: a) classical TF ratio (blue), b) Weighted least square, c) M-estimator, d) Bounded influence, e) black: Modelled data.

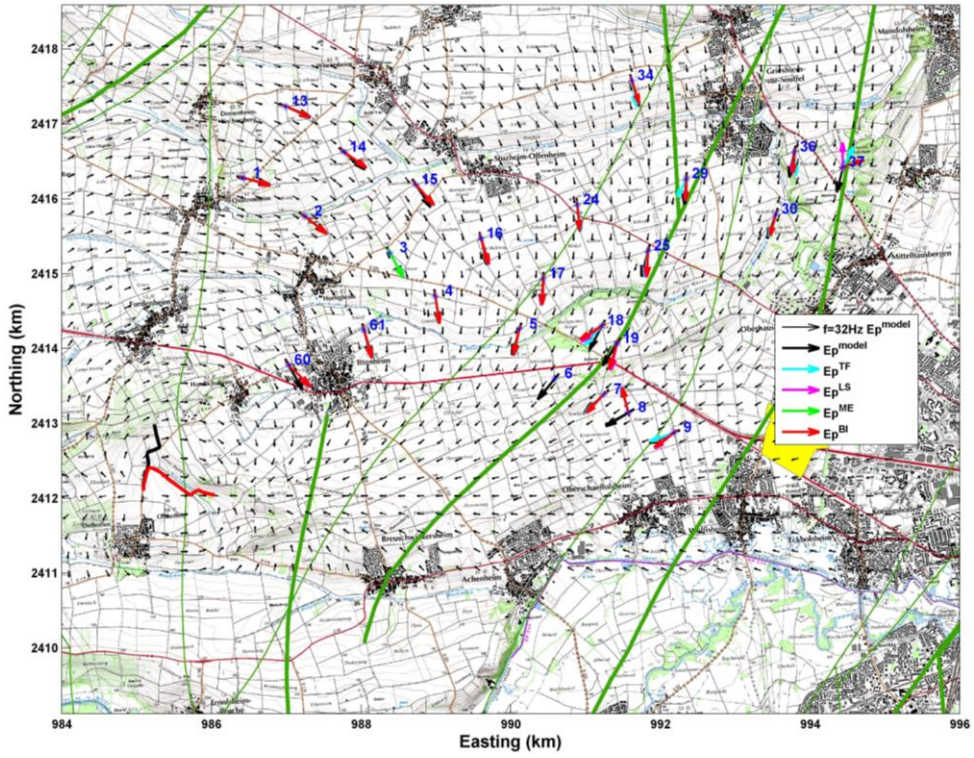

Figure 76: f=32 Hz. Map of in phase electric field vectors data compared to modelled data: a) classical TF ratio (blue), b) Weighted least square, c) M-estimator, d) Bounded influence, e) black: Modelled data.

Other quality check procedures are implemented such as spectral continuity of modulus and phases for the TFs and polarization diagrams of in phase and quadrature components of the TFs. Consequently, detailed analysis of the processed CSEM and noise attributes (e.g. noise estimates, power spectra, Argan diagrams, polarization diagrams) showed that the maximum usable offset for the CSEM survey is about 7km (Figure 81). All data further than 7km from the transmitter suffers from a high level of noise due to the proximity of the Strasbourg city or the low level of CSEM signal. As a consequence, the eastern part of the survey area was not successfully covered (Figure 77).

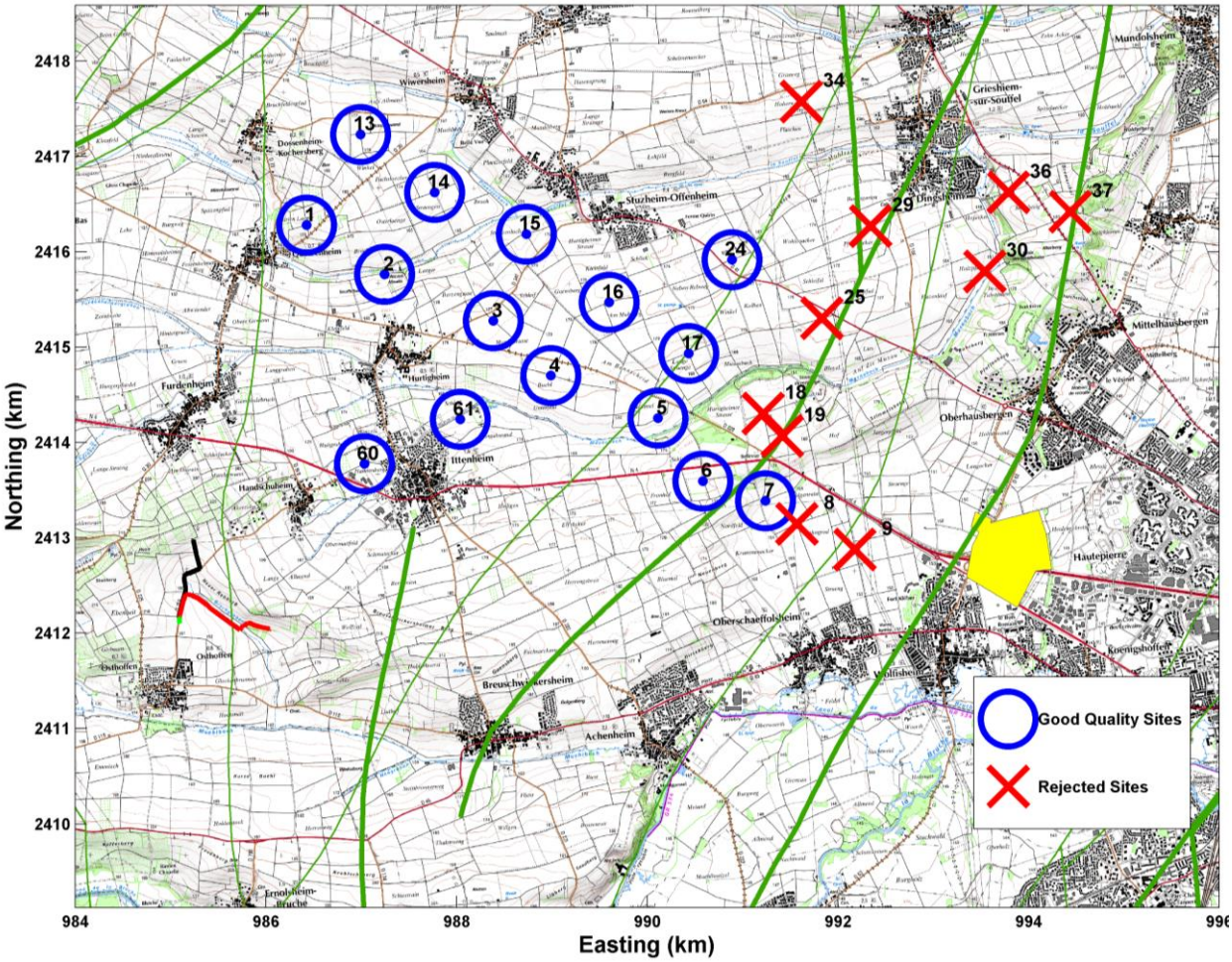

Figure 77: Distribution of the CSEM receivers (blue circles) with sufficient signal to noise and noisy receivers (red crossed). For other legend elements, see
Figure 74: Map of the Strasbourg Region survey. Large green lines show the major accidents of the region. The yellow area represents Fonroche prospect area for the building of a geothermal doublet (beginning in 2017). The source cables for Tx dipoles are shown in b black red and green. Receiver positions are blue points.
.

2.3.3 Magnetotelluric data acquisition and processing

2.3.3.1 MT dataset

Magnetotelluric soundings have been performed in complement of the CSEM measurements in order to add deep geo-electrical information/constrains to the CSEM dataset. It is well known that MT measurements are highly sensitive to anthropic noise, so that MT soundings can be significantly biased and/or distorted by noise sources. The survey area is crossed by several powerlines (inducing 50Hz pollution of the EM signals) features a city on its eastern extent, including factories and train rails, known for biasing low frequency domains of MT soundings curves. In order to overcome such predictable bias in our data sets and especially in the low frequency band (f<1Hz), critical to investigate at depth above 1km, synchronous measurements have been performed by at least two MT stations on the area and the survey.

Thanks to the Ecole and Observatoire des Science de La Terre (EOST, Strasbourg France), we also benefit of two mid distant remote reference stations located at the Welschbruch observatory and Schwabwiller (a MT station installed for geothermal monitoring). Both stations are recording the horizontal magnetic field with a 512 Hz sampling rate. On the 25 CSEM stations, 10 were used as MT stations.

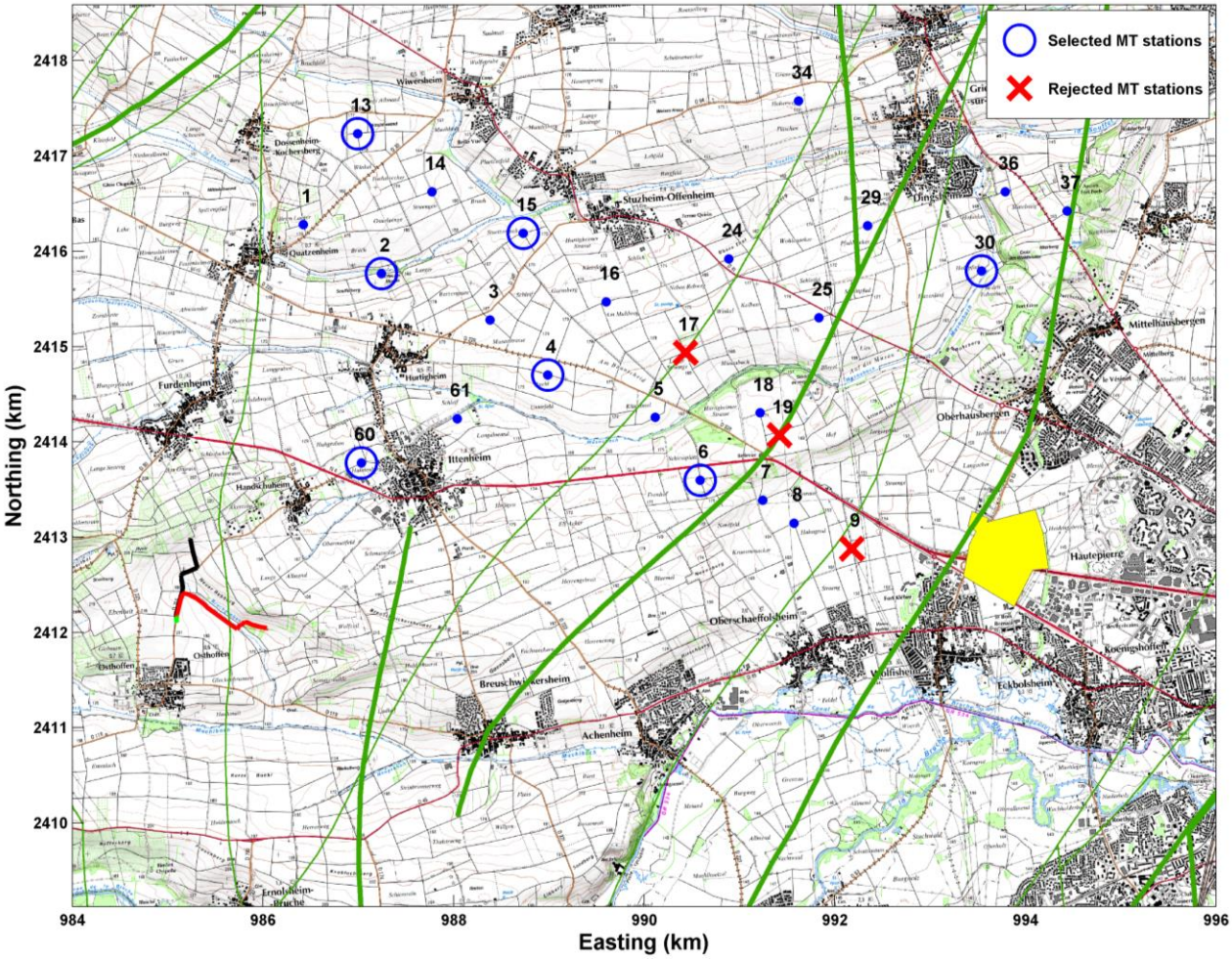

Figure 78: Map of the MT stations. Blue circles: selected MT stations after QC. Red crosses: Rejected MT stations.

2.3.3.2 Robust remote reference processing

Using a BRGM own code named RAZORBACK, based on classical MT robust processing theory (Chave and Jones.,2012), data were processed using all possible combinations of local and distant remote reference stations (hereafter RR). The specific method used in this study for TF estimates is bounded influence estimator (Chave et al., 2004). Testing all possible combination of RR and comparing divergence of associated estimates is a method that has been used in the past (Varenstov., 2006) for large EM arrays. In the framework of the IMAGE project we experimented it in the highly anthropized peri-urban area of Strasbourg Western region. Comparison between single site (hereafter SS) and combined RR soundings allows identifying biased data. Moreover, this method is useful to detect correlated noise between local MT soundings.

Folllowing D7.2 guidelines on noise reduction practices, noisy MT soundings have been identified using several criterions:

- Low frequency asymptotic behaviour: apparent resistivity increasing with periods with a one decade per decade steep, phases tending to 0°. This trend is a clue for identifying local EM noise sources, like railways.
- Unsmooth curves with random jumps of several decades on resistivity and tens of degrees on phases. This can be linked to a bad electrical coupling to the medium under the station and/or transient noise sources.
- Important difference between RR and SS soundings.

From those observations, one must choose the best processing sounding and/or reject some stations. On the whole survey and for any combination of RR, low frequencies (f<0.1Hz) of MT quantities associated with the xy component (EW electric field and NS magnetic field) is of lower quality than yx.

Results from Sites 2 and 15 are shown on Figure 79 and Figure 80. A quick analysis of the results shows that SS estimates are discontinuous and biased. Soundings obtained from using as only RR distant station Welschbruch and Schwabwiller are slightly more robust but can show significant random statistical noise (Pederson, 1982). Soundings obtained from local RR only are less noisy than SS and distant RR soundings but still show significant bias, due to locally correlated noise on the magnetic field, which is a limitation of the method (Gamble et al., 1979). The smoothest soundings are obtained for combinations of RR including the 2 distant RR stations and at least one local RR. This behaviour is frequency dependant: some combination might give a better sounding for high frequencies while another one would yield more robust low frequency components. This is why we selected the 4 or 5 best soundings for each investigated site. Those data (apparent resistivity and phase for each component of the tensor and selected combination of RR) are given as input to the inversion.

On the 10 stations originally recorded, 7 were kept for further analysis and 3 stations were discarded because of noise to signal conditions. One can note that those stations are close to Strasbourg city. Another important point is that, the greater the distance to the city, the better the soundings quality.

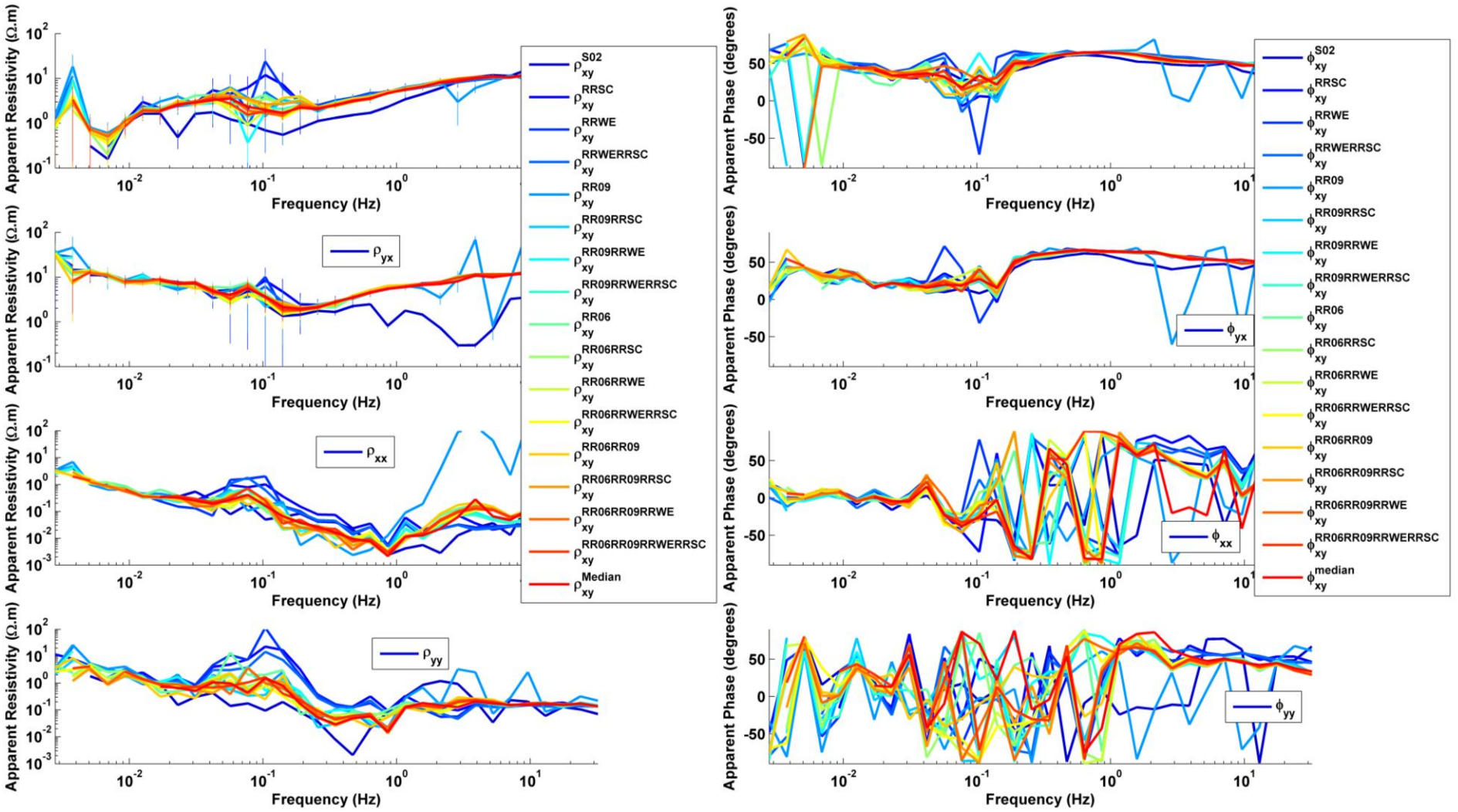

Figure 79: SITE 02 with local RR 4, 6, 9 and distant RR Welschbruch and Schwabwiller. Robust MT transfer function estimates for all possible combination of Remote Reference station. Left side: Apparent resistivity for xy, yx, xx and yy (from top to down). Right side: phase in degrees for xy, yx, xx and yy (from top to down).

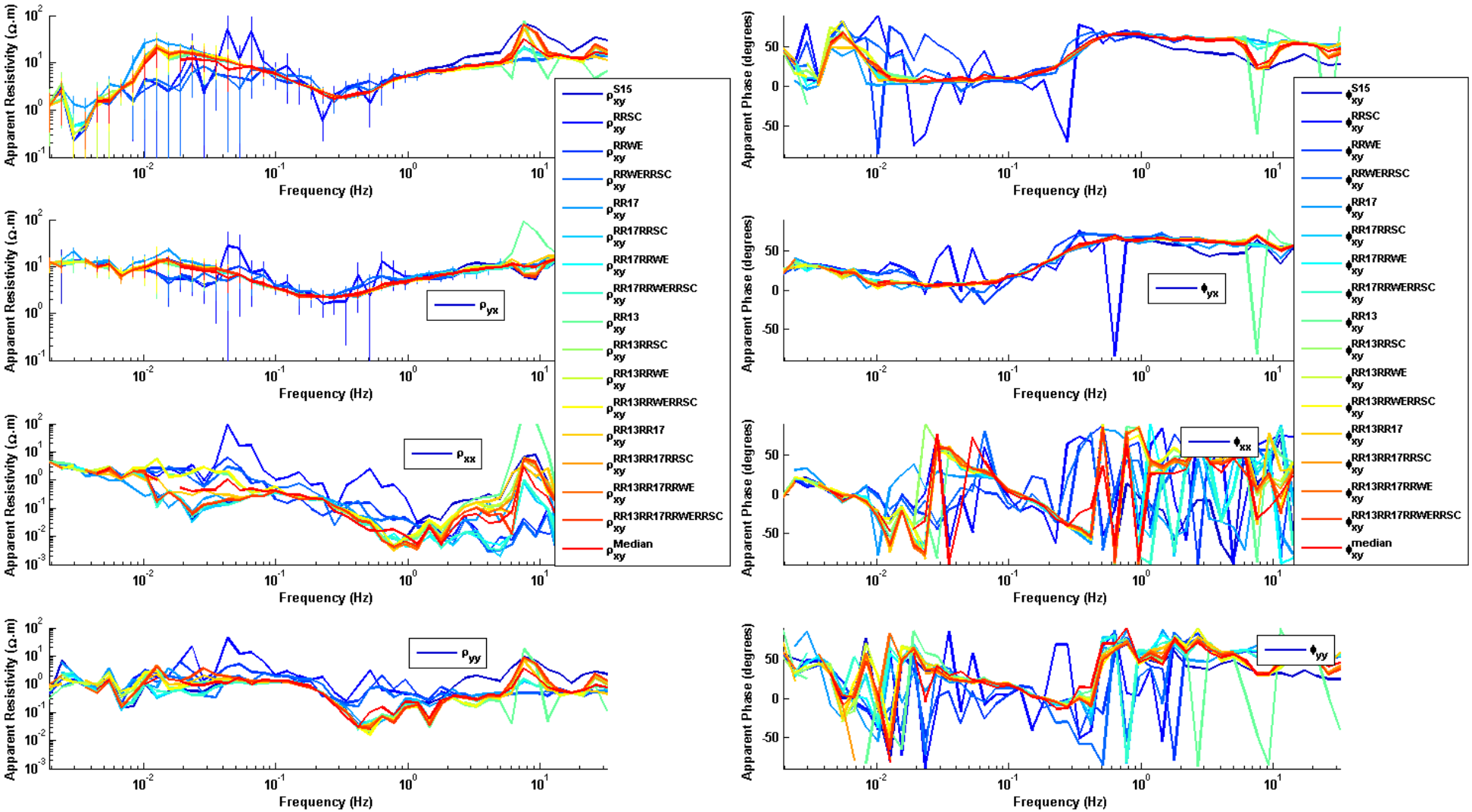

Figure 80: SITE 15 with local RR 13, 17 and distant RR Welschbruch and Schwabwiller. Robust MT transfer function estimates for all possible combination of Remote Reference station. Left side: Apparent resistivity for xy, yx, xx and yy (from top to down). Right side: phase in degrees for xy, yx, xx and yy (from top to down).

2.3.4 CSEM and MT inversion

We first performed a smooth unconstrained 1D inversion of the CSEM dataset to image the main resistivity contrasts. For this purpose, we only inverted the maximum of the polarization ellipse of the electric field. One example for station 04 is shown on Figure 82. The obtained data fit is good showing that the inversion has well converged. The inverted resistivity profile shows a shallow resistive layer (10 Ω.m a few 100's meter thick) followed by a thick conductive layer (1 Ω.m over a few 100's meter) and then resistivity increases monotonously with depth to reach 10 Ω.m at 2.5km depth and 100 Ω.m at 5km depth. This pattern is observed consistently on all CSEM stations in the survey area. To illustrate this, we have extracted two profiles from the dataset (P1 and P2, see Figure 83) crossing the main regional faults of the area (Figure 84 and Figure 85). We can therefore conclude that there is no major resistivity contrast in the survey area related to the main structural elements of the area (faulting, basin thickness variations).

To constrain the resistivity variations at depth even further, we subsequently performed constrained 1D inversion of the dataset. To do so, we used the depth horizons of the main geological units derived from the 3D geological of the area. To improve the resistivity definition even further, we now inverted the amplitude and phase of the maximum of the polarization ellipse. One example for station 04 is shown on Figure 86. Here also, the obtained data fit is good showing that the inversion has well converged. We managed to fit the data with a three-layer model equivalent to the smooth model of Figure 82, illustrating the non-uniqueness of solutions of the CSEM inversion problem and hence the need of additional constraints to find the most geologically plausible model. Comparison with resistivity logs from a neighbouring oil exploratory well (Figure 87) shows that the first 500m thick resistive layer (8 Ω.m) corresponds to recent sediments (sand, gravel and marls). The second 1km thick conductive layer (1 Ω.m) corresponds to Tertiary marls. The deeper resistive layer (50 Ω.m) corresponds to the mix of Tertiary massive salt and marl (500m thick in the well). Unfortunately, as expected from the feasibility study, a sensitivity analysis showed that the thick 50 Ω.m resistive layer obliterates any deeper resistivity variations (i.e. any deeper change of resistivity does not change significantly the data misfit). Figure 88, Figure 89 and Figure 90 represent the results of the constrained 1D inversions along the P1, P2 and P3 profiles, respectively. All models shows similar resistivity variations at depth and consistently with the a-priori geological model demonstrating that reliable resistivity measurements are been achieved down to the base of the Tertiary sediments but not deeper due to the limited transmitter/receiver offsets.

In an attempt to image deeper resistivity variations, we performed a joint constrained 1D inversion of the MT and CSEM datasets. Due to the poor quality of the MT soundings, we only managed to jointly invert a few stations. One example for station 02 is shown on Figure 91, for which data fit is acceptable for the CSEM data and high frequency MT data (>0.1 Hz). In this five-layer model, we managed to recover a deep resistive basement at 4km depth. We however explored the space of possible solutions of the inversion problem and found an alternative three-layer model (Figure 92) that fits equally well the CSEM and high-frequency MT data. The only discrepancy in data misfit between the two models is for the low frequencies of the MT data but due to the poor MT data quality at low frequencies (<0.1Hz), these two models cannot be discriminated.

To put it in a nutshell, we conclude that:

1. Anthropic noise has severely affected the quality of the CSEM and MT data in the vicinity of Strasbourg city. Only 15 out of 25 CSEM recording sites (60%) are of sufficient quality
2. Reliable resistivity measurements have been obtained down to the base of Tertiary sediments (about 2.5 km depth) but deeper measurements are not possible due the high level of noise on CSEM and MT and complexity of geology (thick Tertiary salt layer obliterates deeper layers)

3. With better EM noise conditions and/or stronger CSEM transmitters, longer maximum usable offset (> 7km) could be achieved and hence deeper resistivity measurements obtained by joint constrained inversion of CSEM and MT data

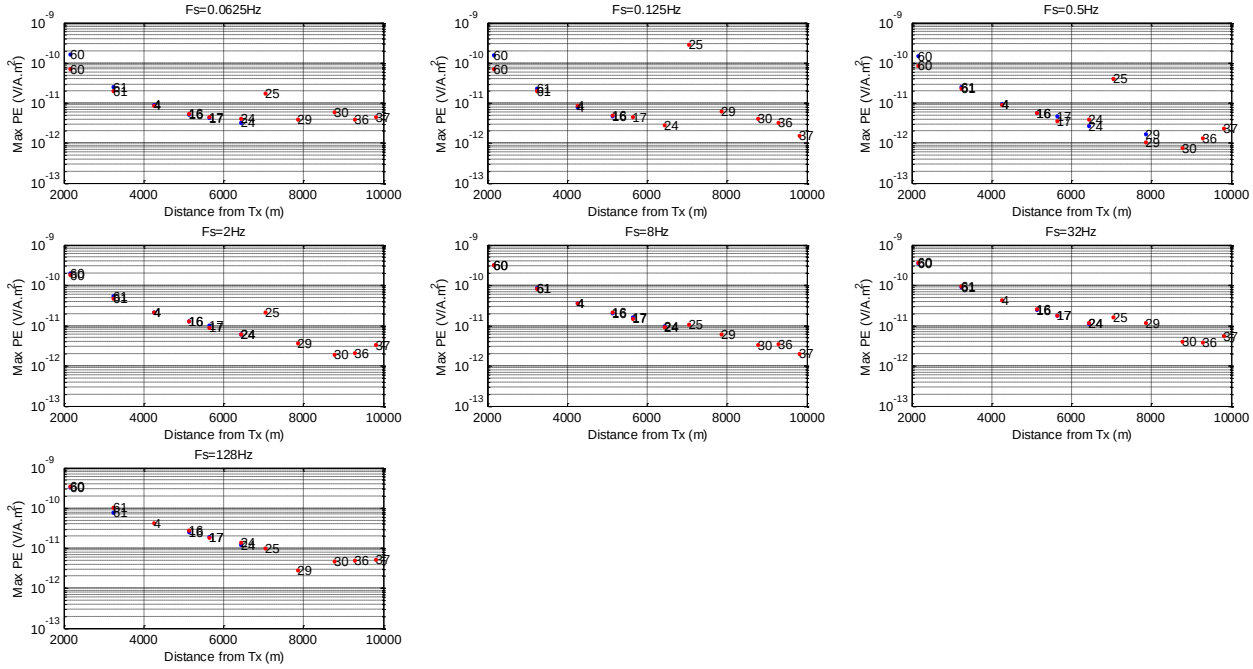

Figure 81: Maximum of the polarization ellipses of the electric fields for all CSEM stations and the two transmitter polarizations as function of transmitter-receiver offset (x-axis) and frequency (panels).

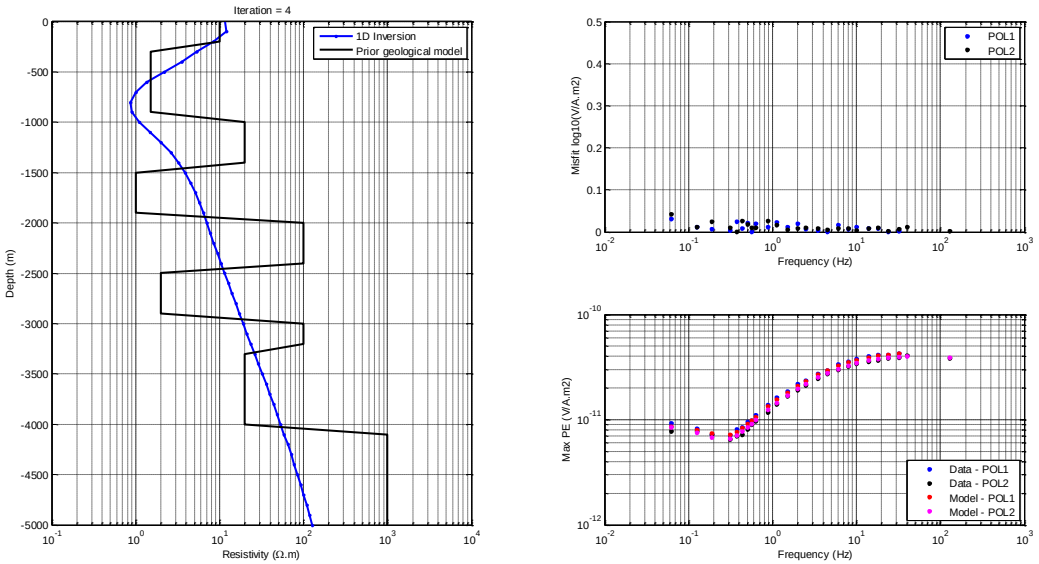

Figure 82: <u>Left:</u> Resistivity profile after unconstrained 1D inversion of the CSEM data (blue) and a-priori from the geological model of the area (black). <u>Right:</u> observed (blue and black, for transmitter POL1 and 2, respectively) and modelled (red and magenta, for transmitter POL1 and 2, respectively) maximum of the polarization ellipse of the electric field as a function of frequency.

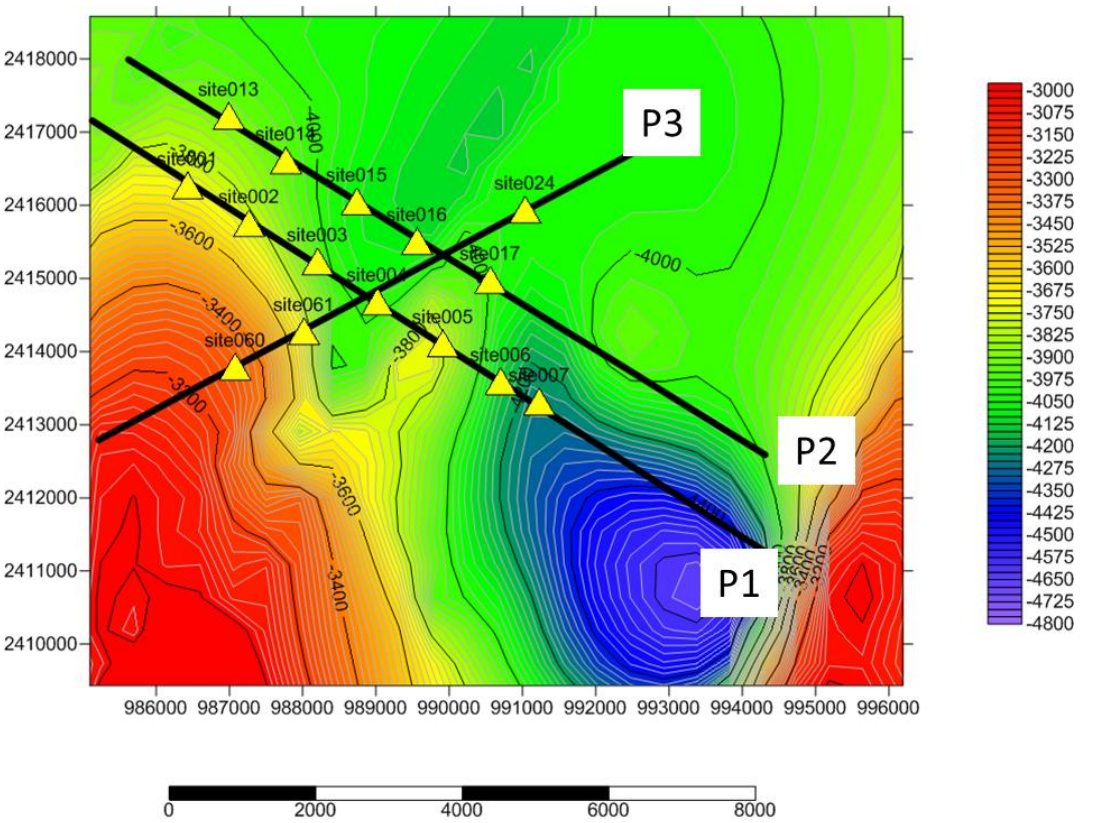

Figure 83: Top depth map of the Bundsandstein together with the location of the CSEM receivers and profiles (P1, P2 and P3) extracted for CSEM interpretation.

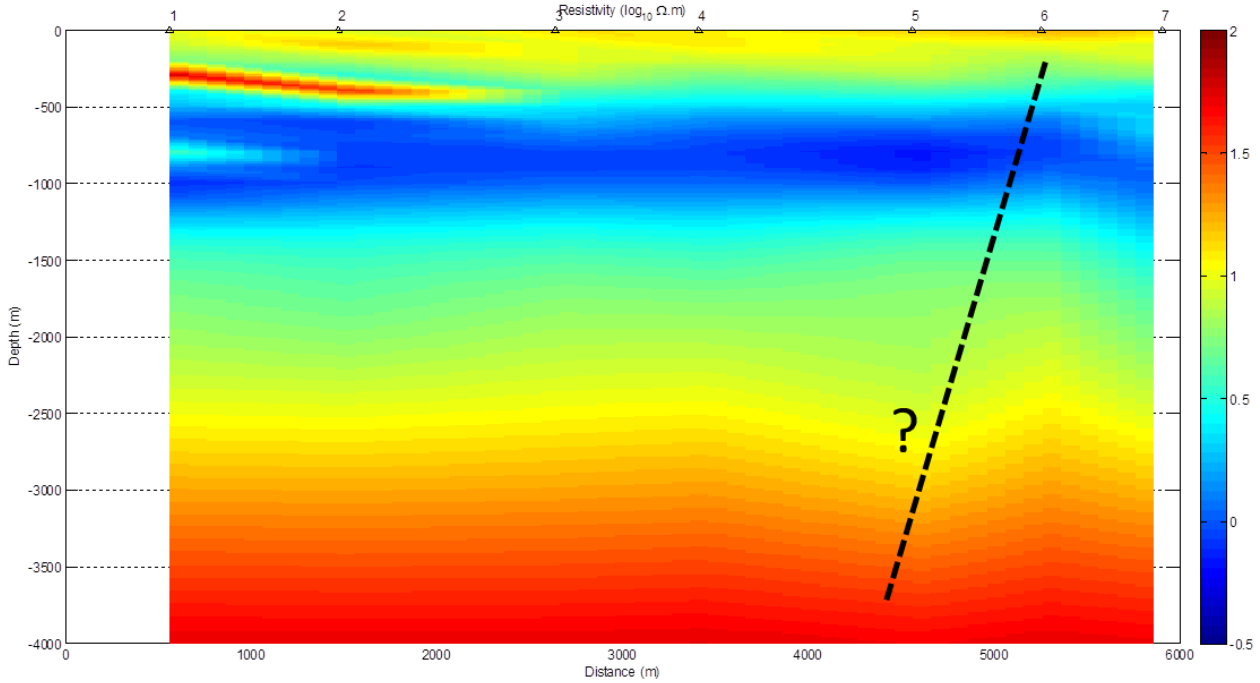

Figure 84: Interpolated resistivity (log10) cross-section after 1D unconstrained inversion of CSEM data along profile P1

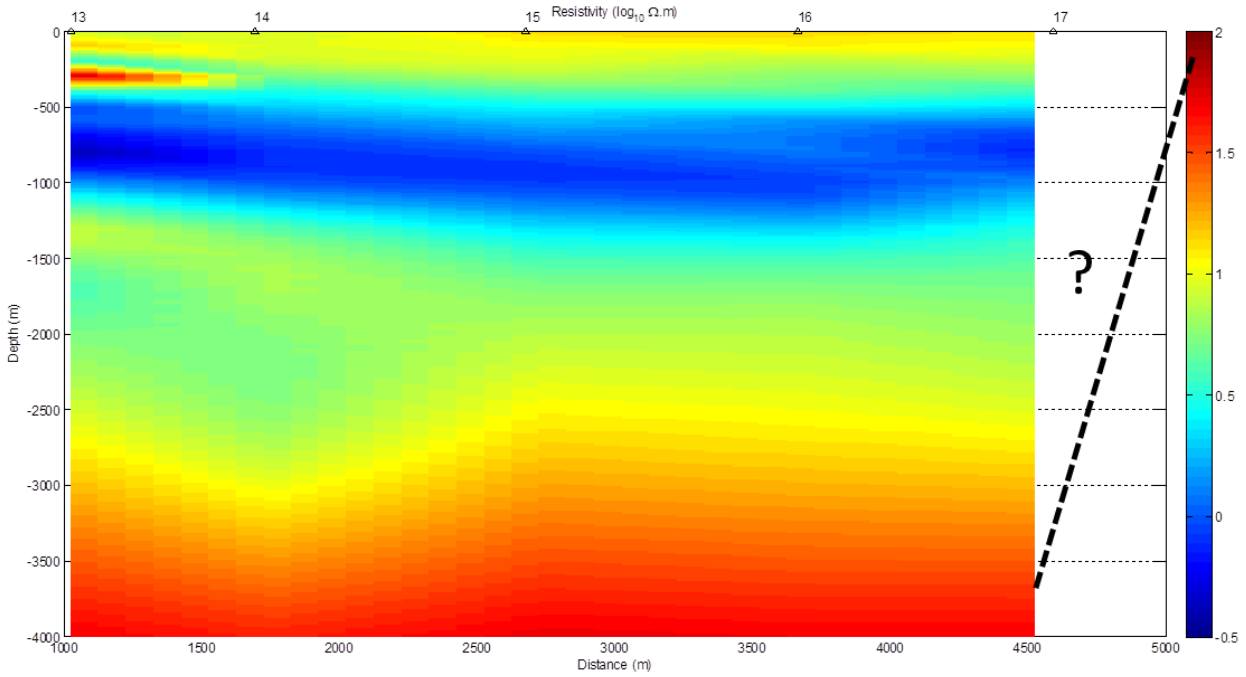

Figure 85: Interpolated resistivity (log10) cross-section after 1D unconstrained inversion of CSEM data along profile P2.

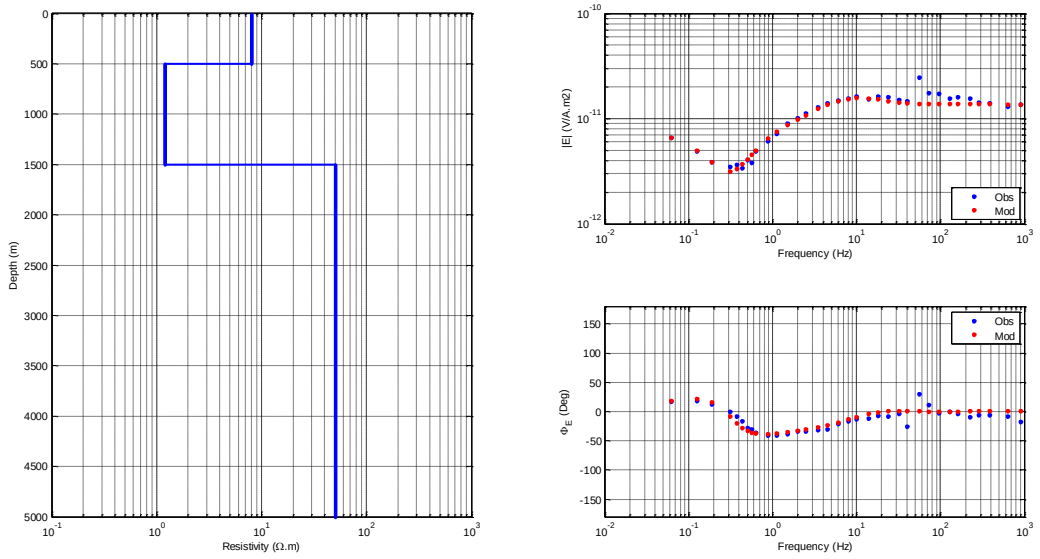

Figure 86: <u>Left:</u> Resistivity profile after constrained 1D inversion of the CSEM data. <u>Right: Top:</u> observed (blue) and modelled (red) maximum of the polarization ellipse of the electric field as a function of frequency for POL1 transmitter. <u>Bottom:</u> observed (blue) and modelled (red) phase of the polarization ellipse of the electric field as a function of frequency for POL1 transmitter.

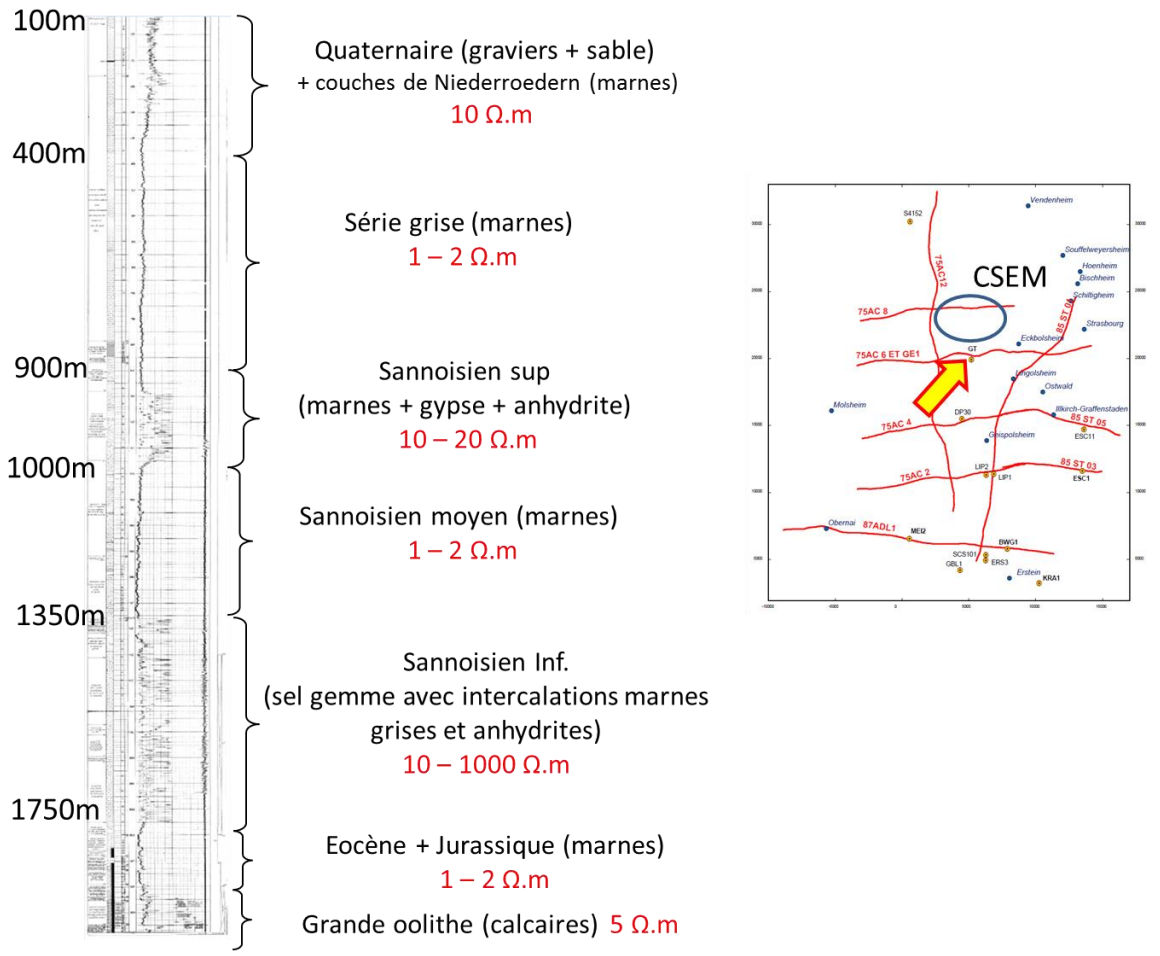

Figure 87: Resistivity logs (Laterolog) from the Holtzheim oil exploratory well.

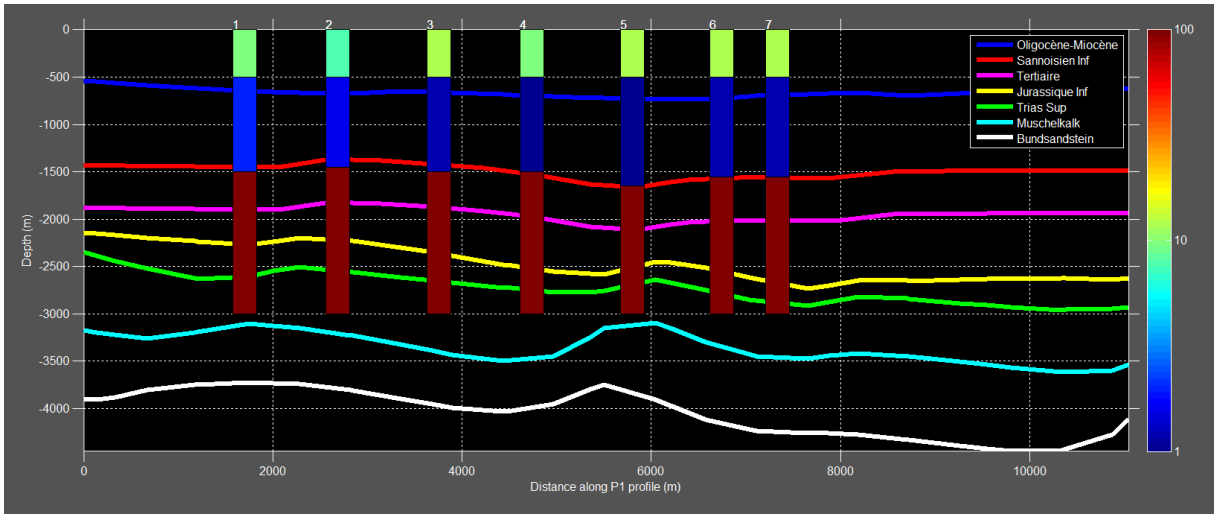

Figure 88: Resistivity (log10) cross-section after 1D constrained inversion of CSEM data along profile P1. The coloured lines represent the main geological interfaces from the 3D geological model of the area.

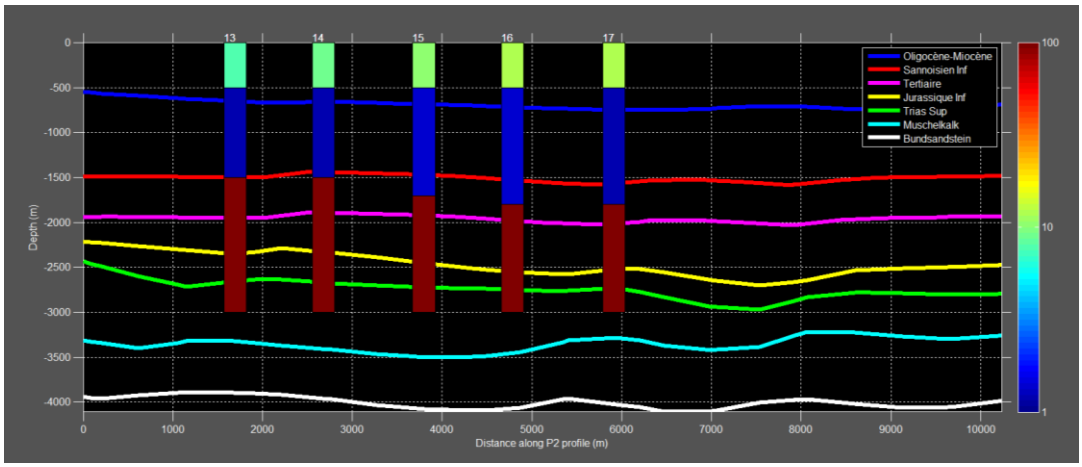

Figure 89: Resistivity (log10) cross-section after 1D constrained inversion of CSEM data along profile P2. The coloured lines represent the main geological interfaces from the 3D geological model of the area.

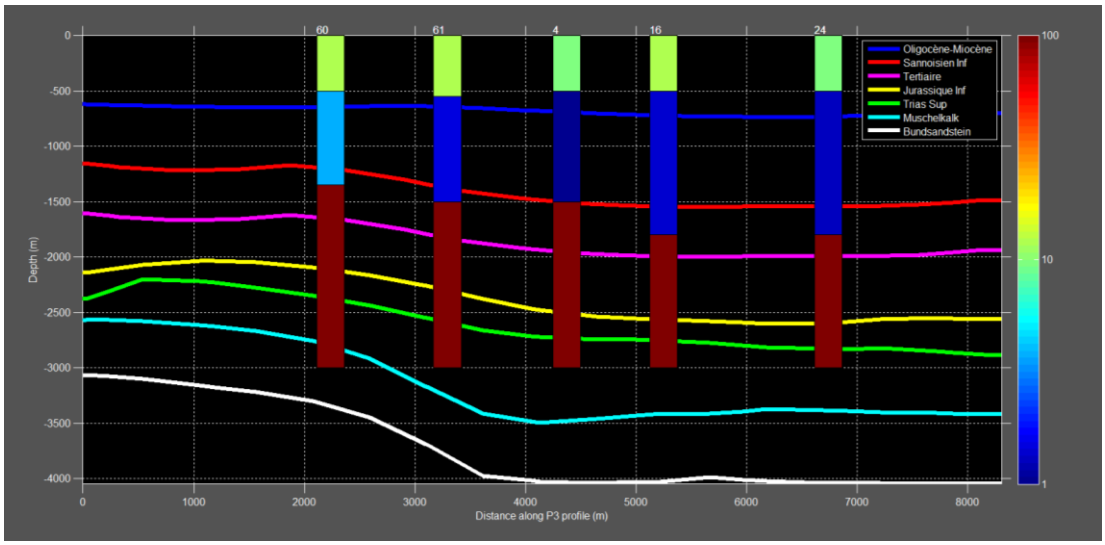

Figure 90: Resistivity (log10) cross-section after 1D constrained inversion of CSEM data along profile P3. The coloured lines represent the main geological interfaces from the 3D geological model of the area.

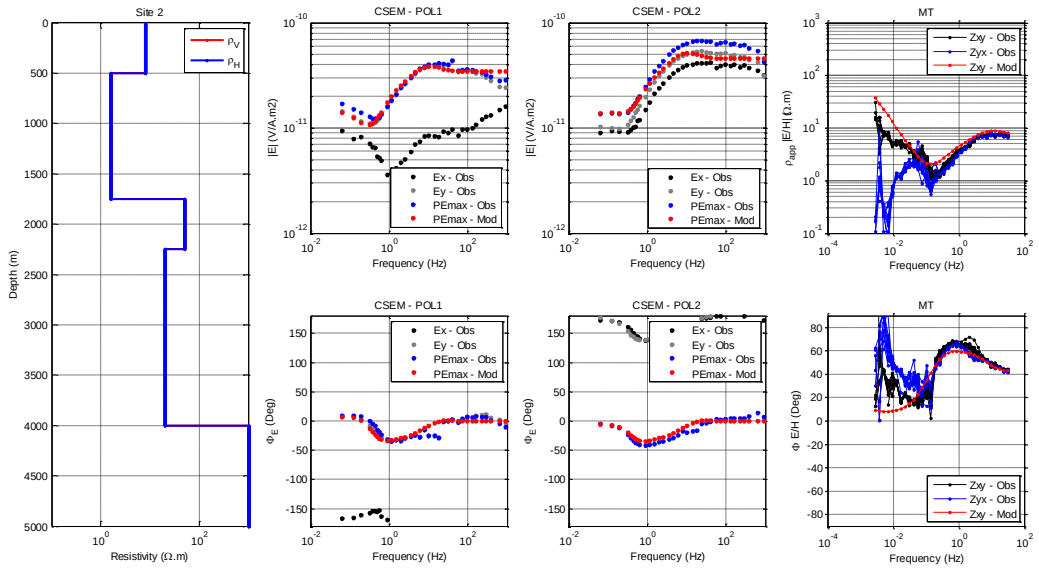

Figure 91: <u>Left:</u> Resistivity profile after the joint constrained inversion of the CSEM and MT data (blue) for station 02 with a five-layer model. <u>Middle:</u> observed (blue Ex, black Ey) and inverted (red) maximum (top) and phase (bottom) of the polarization ellipse of the electric field as a function frequency for POL1 and POL2 transmitter. <u>Right:</u> observed (blue Zxy and black Zyx) and inverted (red) apparent resistivity (top) and phase (bottom) of the MT impedance tensor as a function frequency.

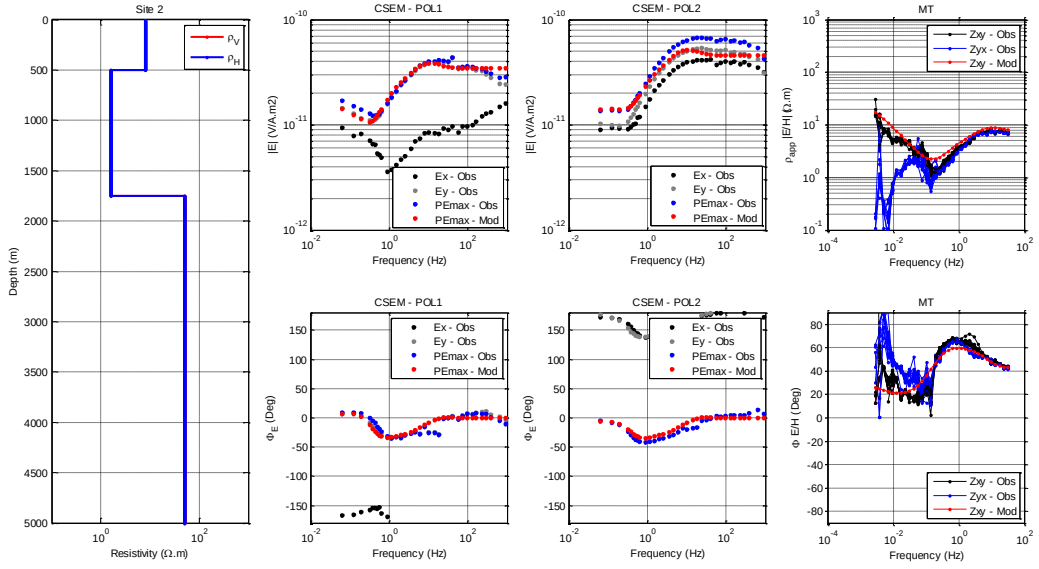

Figure 92: <u>Left:</u> Resistivity profile after the joint constrained inversion of the CSEM and MT data (blue) for station 02 with a three-layer model. <u>Middle:</u> observed (blue Ex, black Ey) and inverted (red) maximum (top) and phase (bottom) of the polarization ellipse of the electric field as a function frequency for POL1 and POL2 transmitter. <u>Right:</u> observed (blue Zxy and black Zyx) and inverted (red) apparent resistivity (top) and phase (bottom) of the MT impedance tensor as a function frequency.

3 Reservoir characterisation based on fractal parameters of fracturing, stress and micro-seismicity applied to Basel and Soultz sites

3.1 Introduction

Enhanced Geothermal System (EGS) reservoirs aim to extract the heat from the Earth by circulating fluids (e.g. water) between injections and productions wells in deep underground, where high temperatures are present. Since the target reservoirs are mainly located in low-porosity basement rocks, the flow develops primarily through the fracture network (Genter *et al.*, 2010). The natural fracture transmissivity is, however, typically not sufficient for economical flow rates. In order to increase the ~~possible~~ flow rates, massive fluid injections, referred as hydraulic stimulations, are performed to increase the permeability of the fractured media. Experience has shown such treatments to be effective, but the mechanisms underlying the permeability increase are not completely understood. Massive fluid injection changes the stress conditions by elevating the pore pressure and is expected to increase the permeability by shearing rough fracture surfaces and/or generating new fractures (Evans, 2005, Evans *et al.*, 2005). The process of stimulation is accompanied by microseismicity, and in some cases like at Basel and St. Gallen in Switzerland felt earthquake led to project abandonment. A major challenge of EGS is thus to increase the permeability of the fractured media without inducing damaging seismicity.
In order to design and assess EGS development strategies, a geological model of the target rock mass is required. This geological model should be representative of the whole reservoir with a realistic distribution of geological features such as the fracture network from small to large scales. However, the characterization of the fracture network is difficult, particularly at the early project stage when only a single exploration well may be available. Particularly problematic is the characterization of the fracture length distribution – a key parameter for assessing the connectivity of the fracture network – with data from a single well.
The characteristics of facture networks have been studied from outcrops and multi-well study sites where a more complete characterization of the fractures is possible (Cowie *et al.*, 1996). In such situations, it has been observed that fractures exhibit self-similar patterns referred as fractal organization (Barton, 1995, Bonnet *et al.*, 2001). Thus, power-laws have been widely utilized to interpret the scaling phenomena in fracture networks (Davy *et al.*, 1990, Odling *et al.*, 1999, de Dreuzy *et al.*, 2001, Bour *et al.*, 2002, de Dreuzy *et al.*, 2002, Lei *et al.*, 2015). Specifically, power-law scaling has been applied to characterize different fracture attributes, such as spatial distribution, trace length, spacing, RQD (Rock Quality Designation, Deere and Deere (1988)), aperture, surface roughness etc. (Power & Tullis, 1991, Barton & Zoback, 1992, Boadu & Long, 1994, Bonnet *et al.*, 2001). The origin of power-law scaling in nature isn't entirely clear, but some researchers have related the statistics of large scale structures to smaller ones using complex self-organized critical dynamics (Allegre *et al.*, 1982, Bak *et al.*, 1988, Sornette *et al.*, 1990, Sornette, 2006). The stress interactions between fractures in an growing fracture population could also lead to power-law distributions (Spyropoulos *et al.*, 2002, Davy *et al.*, 2010). This suggests that some relation exist between the characteristics of the fracture network and the stress variability within this fractured rock mass. This interdependence can be anticipated by considering that the size of the stress perturbation about a single fracture after dislocation scales linearly to the size of the fracture inducing the perturbation (Eshelby, 1957, Pollard & Segall, 1987). However, in a fracture network, the interrelation becomes non-trivial (Valley *et al.*, 2014). Nevertheless, fluctuations in stress orientation along boreholes have been shown to be characterized by power-law scaling (Shamir & Zoback, 1992, Day-Lewis, 2007, Valley & Evans, 2014). The relations between the power-law observed in fracture network and stress fluctuation are, however, not well understood, and this is precisely the motivation of the current research. Clarifying this relation could have important practical implications if one can use scaling information of stress fluctuations derived from wellbore failure observations to constrain characteristics of the fracture network like fracture length distribution that cannot be quantified otherwise. Further applications could also be envisaged if relationships to seismogenic scaling

parameters, such as b-value can be established. B-value relates earthquake frequency to magnitude through a power law. Intuitively, one can assume that the magnitude distribution of earthquake is at least partly controlled by the fracture size distribution and the stress state in the reservoir. If the details of these inter-relationships were better understood, it could be possible to use observation at the borehole wall of natural fracture and stress-induced failure to better anticipate reservoir response to stimulation operations.
The starting point of this research is thus the observation that some key reservoir characteristics like fracture network organization, stress fluctuation and seismic magnitude distribution present power-law scaling and that these scaling could be related. A necessary preliminary work to study these potential relationships is to fully understand the characteristics and limitation of the scaling law of each parameter separately. In the following sections we investigate these the scaling relationships of natural fracture, stress and induced seismicity in the geothermal reservoirs of Basel and Soultz-sous-Forêts.

3.2 Fractal characteristics of stress variations

The topic of fractal characterisation of stress variations has been discussed extensively in the image report D6.03, Section 3.3 and only a summary of the results obtained in terms of characterising the sites of Basel and Soultz-sous- Forêts are recalled here.

3.2.1 Methodology

Various methodologies to estimate the fractal dimension of fluctuations in stress orientation along boreholes including the effects of noise and gaps in the data have been reviewed and tested. The most robust approach was the one based the Fourier transform of the data after pre-filtering with a Hanning window. In order to reduce the effects of noise in the data on the power spectrum estimate we used the technique of section averaging, which averages the spectra obtained on segments of the complete signal. The noise reduction is obtained at the expense of frequency resolution. In our analyses we split the signal into 15 segments with a 50% overlap (i.e. Welch's method). The fractal dimension is then estimated from the power spectral density (PSD). For a fractal series, the PSD spectrum has a slope of $1/f^{\beta}$, and thus declines linearly with frequency with a slope of $-\beta$ in a log $Sv(f)$ vs. log f plot. The slope β is referred as the spectral index. For a one-dimensional fractal signal, β lies in the range $1 < \beta < 3$, and is related to the fractal dimension by Equation 1:

Equation 1

$$D = \frac{5-\beta}{2}$$

3.2.2 Application to Basel and Soultz stress data

In this section, we present the estimation of fractal dimension for datasets from Basel and Soultz. The datasets stem from three deep boreholes: GPK3 and GPK4 located at the Soultz-sous-Forêts EGS site in France, and borehole BS1 at Basel in Switzerland. The original data for Soultz-sous-Forêts are presented in Valley and Evans (2010) and for Basel in Valley and Evans (2009). The data sets consist of profiles of SHmax-orientation derived from wellbore failure indicators.

In the case of the Soultz-sous-Forêts data, the SHmax-orientation estimates from breakouts and/or Drilling Induced Tension Fractures (DITFs) were determined over successive 0.5 m windows, whereas for the Basel data, the orientation of the features were determined every 0.4 m. For each well, the mean SHmax-orientation was subtracted from the data in order to keep only the variation from the mean. The data were prepared for the analyses by resampling at a uniform spacing of 0.1 m. Only subsections of the datasets where the SHmax-orientation estimates are relatively continuous are considered for the analyses performed in this paper.

The prepared datasets are presented in Figure 93, and a summary of their key characteristics is given in Table 3 For the GPK3 and GPK4 datasets, the SHmax-estimates in the selected intervals are derived largely from drilling induced tension fractures, whereas for BS1 data they stem principally from borehole breakouts.

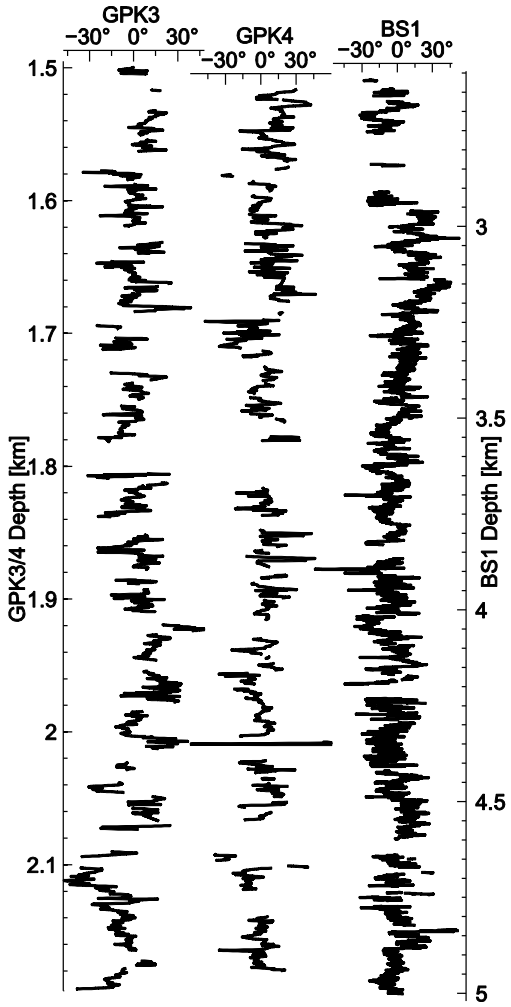

Figure 93 - Sections of the GPK3, GPK4 and BS1 data sets used in this paper.

Table 3 - Summary of key characteristics of the prepared data

Hole	GPK3	GPK4	BS1
Interval	1495 – 2195 m	1511 – 2186 m	2618 – 5000 m
Length	700 m	675 m	2382 m
Number of data point	7001	6751	23820
% of missing data	36%	35%	19%
Number of gaps	41	43	115
Longest continuous data section	63 m	44 m	99 m
Longest gap	24 m	35 m	80 m

Based on the evaluation summarized above, the best estimate of *D* is obtained using the FFT approach. The obtained fractal dimensions D = 1.75 for GPK4, *D* = 1.74 for BS1 and *D* = 1.68 for GPK3. The important conclusion is that there is more similarity in the range of *D*-estimates between GPK4 and BS1 than there is between GPK3 and 4, despite the fact that the latter two sample essentially the same rock volume.

A more detailed analysis of the BS1 dataset was performed using the FFT approach in order to clarify the form of the power spectrum at long wavelengths. Power Spectral Density (PSD) estimates were derived in a similar manner than explained in Section 3.2.1 but with 20-30% overlap of adjacent

series segments. The results are presented in Figure 94 for two analyses in which gaps in the original series shorter than 15 m and 41 m were filled with linear trends. Including longer filled gaps in the analysis serves to increase the length of continuous sections, thereby allowing PSD estimates to be derived for longer wavelength variations. Filling all gaps with length less than 41 m yielded 4 sections of 650 m length to be formed with 27% overlap.

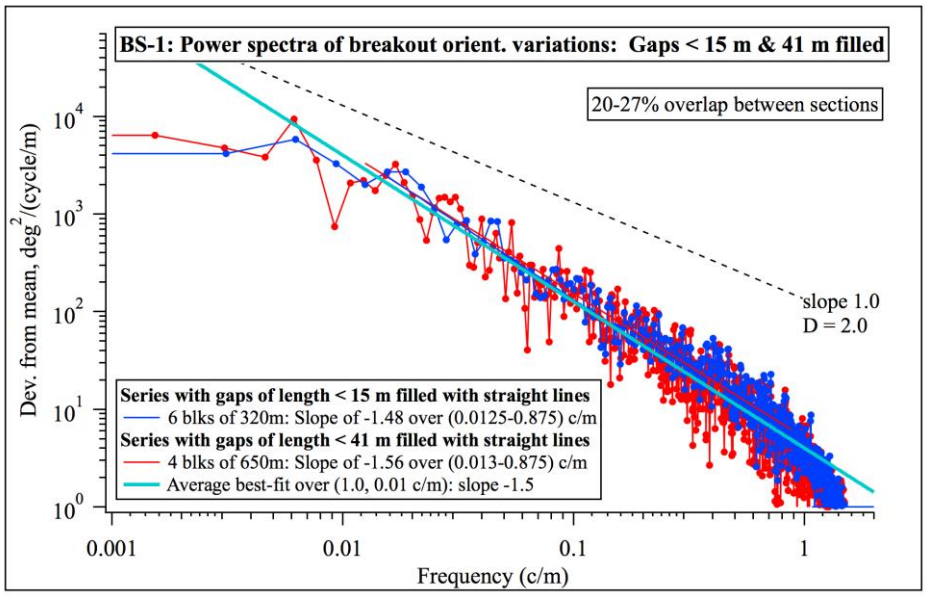

Figure 94 - PSD functions derived from the BS-1 data for two series which differ in the maximum gap length that was filled with linear trends. Both curves define a slope of about -1.5 extending from 1 c/m to 0.01 c/m, and become flat at frequencies less than 0.01 c/m.

The analysis yielded the following results:

- The log-log plot of PSD vs frequency is linear between 1 and 0.006 c/m (wavelengths of 1 and 166 m) and has a slope of -1.5, implying a fractal dimension D = 1.75. This is in agreement with the results presented above using Welch's method to compute the PSD.
- At frequencies above 1 c/m, the power decreases faster than for the linear trend. Fluctuations at such short wavelengths are expected to be small, and approach the scale of the borehole itself.
- At frequencies lower than 0.006 c/m (wavelengths longer than 166 m), the spectra become flat and remain so out to the longest wavelength of 650 m at which PSD could be estimated. This flattening is also evident in the spectra from the higher-quality series with gaps up to 15 m filled, from which 6 sections of length 320 m could be formed. Consequently, the flattening is possibly real and not an artifact of the uncertainty in the spectra at the longest wavelengths resolved.

3.3 Fracture network fractal characterisation

Fractal geometry has been widely utilized to quantify the scale invariant pattern of DFNs. Since fracture network data from a deep geothermal reservoir is often limited to the data obtained from one borehole, we must extract as much information from this data as is possible that is relevant to creating a reliable geologic model of the reservoir. We need to extend the 1-D line sample of the spatial distribution of fractures from the borehole to a three-dimensional model. Therefore, this model must incorporate valid stereological relationships for mapping from one dimension up to three dimensions. According to the literature, the only model with such valid stereological relationships is a first-order fractal model of fracture length and density proposed by Davy et al. (2010). This model is based on a double power-law in the form of Equation 2,

Equation 2 $$\boldsymbol{n(l, L) = c\, L^{D} l^{-a}}$$

where, $n(l,,L)dl$ is the number of fractures whose length is in the range $[l, l + dl]$ and whose center belongs to a volume in three dimensions of size L, c is a constant, D is the correlation dimension of fracture centers and a is the length exponent. Bour et al. (2002) have applied this statistical model to scale the fracture geometry on multiscale fracture maps taken from outcrop in Hornelen basin in Norway. If Equation 2 governs the spatial distribution of fracture centers and length distributions, we would be able to construct a three dimensional probabilistic geological model from borehole observations, according to stereological relationships established by Darcel et al. (2003a).

3.3.1 Application of borehole data to constrain the fracture networks

Stereological relationships relate the geometrical properties of a DFN in different dimensions (e.g. a 2-D trace plane intersecting *3-D* network or a *1-D* scanline intersecting a *2-D* trace plane). A detailed stereological analysis of fractal DFNs is presented by Darcel *et al.* (2003). In this section, we focus on the relationships derived for relating *1-D* scanlines that intersect *2-D* trace planes created by first-order model and its application to the fracture network detected in geothermal wells. For the length distributions, there is a simple relationship between a_{2D} and a_{1D} given by Equation 3 Since the lengths of the fractures intersected by boreholes is not known, this equation is not applicable.

Equation 3

$$a_{1D} = a_{2D} - 1 \qquad ()$$

The spatial distribution of fracture centres in two dimensions (D_{2D}) is related to the spatial distribution of fracture intersections (D_{1D}), if a scanline of length *L* is present in LxL domain. Depending on the length distributions, three different dominant equations are derived from analytical analysis given in Equation 4, Equation 5 and Equation 6.

Equation 4 $\boldsymbol{D_{1D} = 1, \quad a_{2D} \leq D_{2D}}$

Equation 5 $\boldsymbol{D_{1D} = D_{2D} - a_{2D} + 1, \; D_{2D} \leq a_{2D} \leq 2}$

Equation 6 $\boldsymbol{D_{1D} = D_{2D} - 1, \quad a_{2D} \geq 2}$

Darcel *et al.* (2003) have tried to verify the stereological relationships in synthetic DFNs. Here we present another methodology to perform stereological analysis. Figure 95 describes the step-by step details of a sample analysis for a given length exponent a.

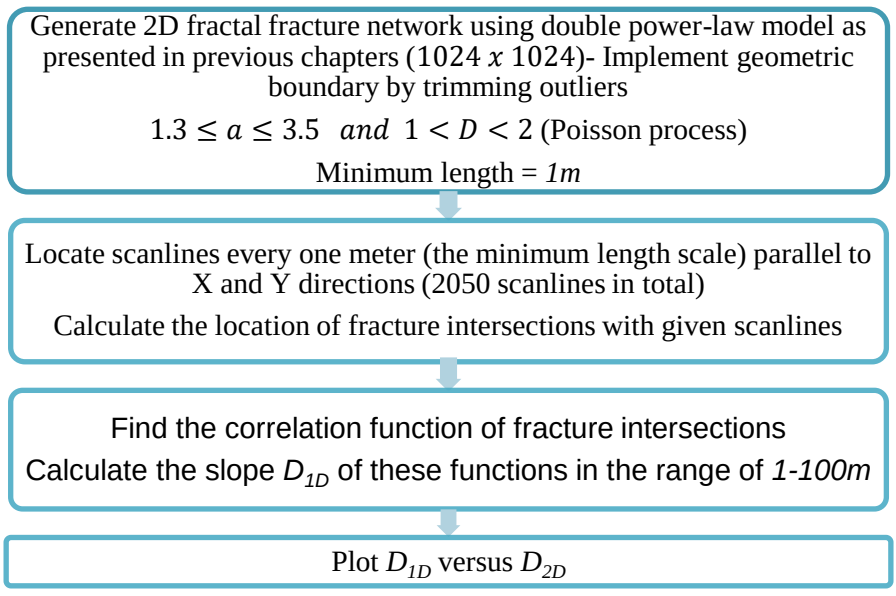

Figure 95: The flowchart of the methodology to do stereological analysis of two dimensional synthetic networks

We do our analysis on two sample length exponents ($a_{2D} = 1.5$ and $a_{2D} = 2.5$). We generate DFNs using the D_{2D} from *1.1* with *0.1* increments ($D_{2D} = 1.1, 1.2, \dots, 1.9$). To remove the effect of number of fractures on the analysis, the number of fractures belonging to every correlation dimension is kept constant and high (*20,000* for the first exponent, $a_{2D} = 1.5$) in order to have enough intersections. Since the length exponent is lower than *2*, we expect higher number of intersection for relatively low number of fractures.

Figure 96 *a* represents the stereological analysis associated to Equation 4 and Equation 5. The analysis shows that, Equation 4 is easily achieved and verified for a length exponent lower than or equal to D_{2D}. In contrast, for $D_{2D} \leq a_{2D} \leq 2$, the stereological relationships do not apply to synthetic DFNs. A similar observation is reported by Darcel *et al.* (2003) who called it the transition regime.

To analyze the stereological relationship of Equation 6, we set $a_{2D} = 2.5$ and generate DFNs using the D_{2D} from *1.1* with *0.1* increments ($D_{2D} = 1.1, 1.2, \dots, 1.9$). The number of fractures belonging to every correlation dimension is kept constant (*200,000* for $a_{2D} = 2.5$). The stereological analysis reveals that resulting D_{1D} is overestimated for any D_{2D}. This overestimation increases for lower D_{2D}. Figure 96 represents the stereological analysis of two length exponents with random orientation of fractures.

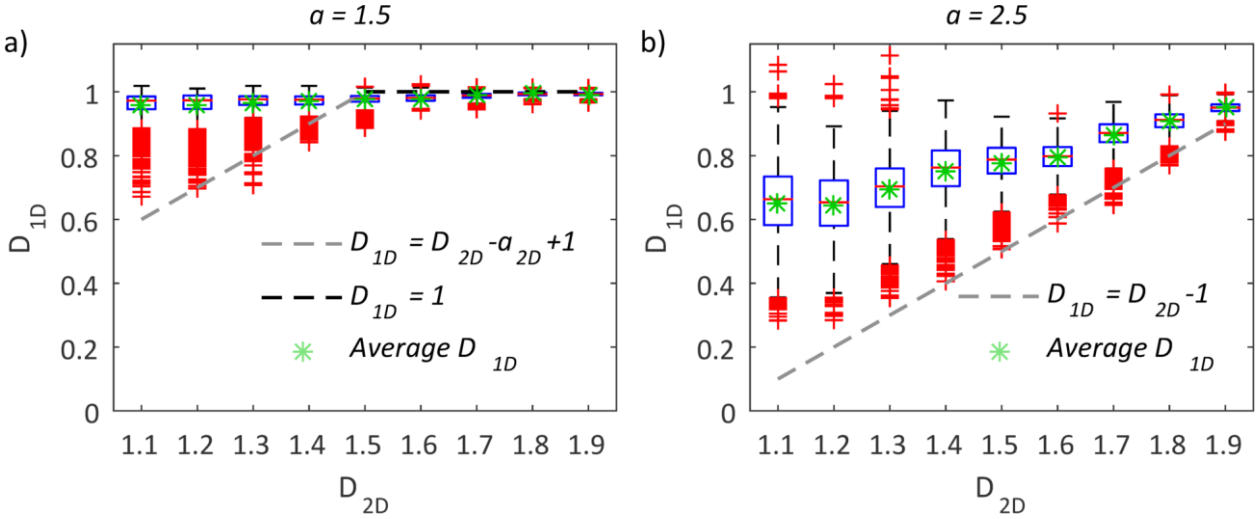

Figure 96 - (a) Two dimensional stereology plot of the length exponent of $a_{2D} = 1.5$ with random orientations. (b) Two dimensional stereology plot of the length exponent of $a_{2D} = 2.5$ with random orientations

Normally, the fractures in boreholes or outcrops belong to families according to their orientation. As an example, Ziegler *et al.* (2015) have characterized the natural fractures in Basel-1 well and have defined fracture sets according to their orientation. If the fractures in *2-D* network belong to two dominant fracture sets (e.g *45*° and *135*° from *x* axis), a stereological analysis similar to random orientations was performed as in Figure 97. Similar to random orientations case, D_{1D} is overestimated for any D_{2D} and this overestimation increases for lower values of D_{2D}.

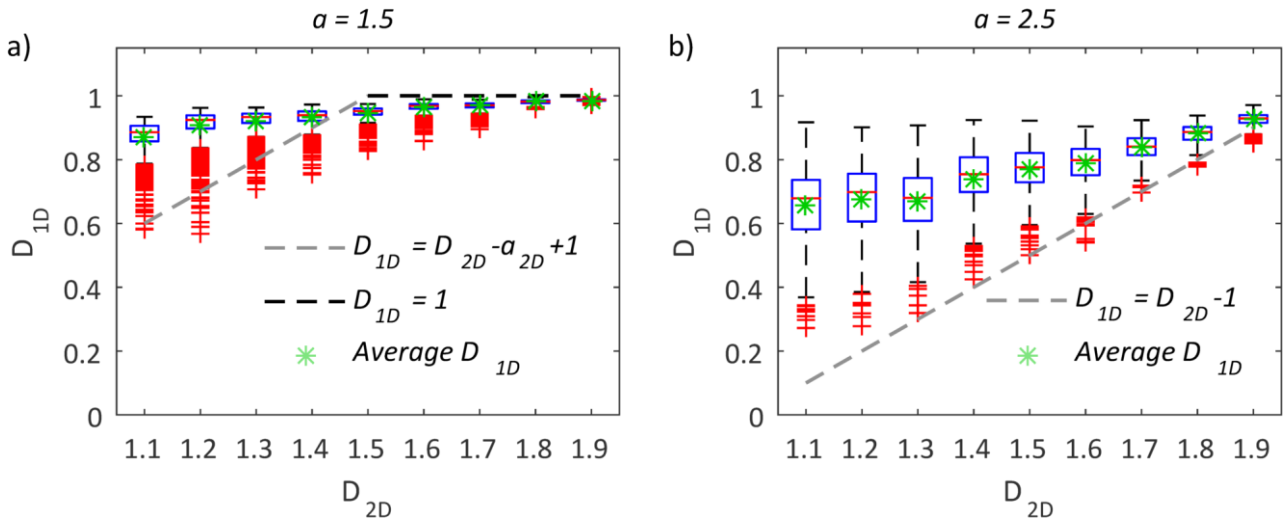

Figure 97 - (a) 2D stereology plot of the length exponent of $a_{2D} = 1.5$ with two perpendicular sets. (b) 2D stereology plot of the length exponent of $a_{2D} = 2.5$ with two perpendicular sets.

An application of the the fractal analysis of fracture patterns in a deep borehole drilled into crystalline basement (Basel-1) is presented on Figure 98. We computed the correlation function of fracture patterns and found the local slope (correlation dimension). Figure 98 shows the fractal patterns of complete fracture dataset and the dominant fracture set. The computed fractal dimension are 0.86 when all mapped fractures are considered and 0.74 when only one dominant set is included in the analyses.

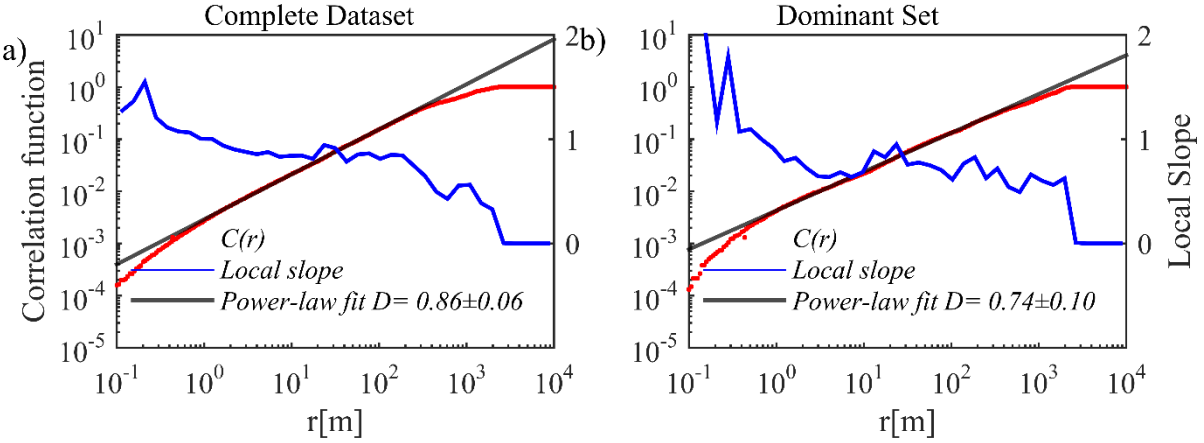

Figure 98 - a) The correlation function of complete fracturing dataset in Base-1 well. b) The correlation function of fractures belonging to the dominant fracture set.

3.3.2 Conclusions

The possible extrapolation of *2-D* and *3-D* spatial distribution of fractures from *1-D* observations such as boreholes, motivated us to perform a critical study on the stereological relationships proposed for fractal DFNs by (Darcel *et al.*, 2003). Figure 96shows a large discrepancy in the analytical predictions and synthetic networks except for the case of $a_{2D} \leq D_{2D}$. As an example if $D_{1D} = 0.7$ and $a_{2D} = 2.5$, D_{2D} could belong to the range of $1.1 \leq D_{2D} \leq 1.8$ (Figure 96*b*). There is no way to determine the exact value of D_{2D} in the given range. If the DFN contains two perpendicular sets (*45°* and *135°* from *x* axis), the resulting stereological analysis shows a similar result (Figure 97). The stereological relationships applied to synthetic networks generated by a first-order model, fails to extrapolate the *2-D* spatial distributions using *1-D* scanlines. The average values of D_{1D} is higher than the analytical predictions (stereological relationships) and the gap between them increases for lower values of

D_{2D}. Estimating *3-D* spatial distribution of discontinuities from *1-D* scanlines involves a large uncertainty associated with estimating D_{2D}. In addition, there is no information about the length distributions of *3-D* fracture planes in the reservoir.

3.4 Microseismic fractal characterisation

The complex nature of discontinuities complicates the hydromechanical behavior of subsurface rock mass during the hydraulic stimulation [Rutqvist and Stephansson, 2003]. The presence of fractures is believed to change the stress field as well as the fluid flow field by introducing highly permeable flow paths [Pollard and Segall, 1987; Sahimi, 2011]. The injection of water into the reservoir rock mass is expected to reduce the effective stress and eventually create a failure on a fracture plane [Zoback, 2010]. The initiation of slip on existing or newly generated fracture planes commonly generates large numbers of microseismic events, the largest of which are occasionally felt by the local community (e.g. M_L=3.4 in Basel geothermal project).

Knowledge of the existing fracture network geometry embedded in a geological model is critical to design and assess EGS development strategies. Until now, the 3-D spatial distribution of centres and the size distribution of the fracture network in a reservoir lying between say 3-5 km depth has been considered uncertain. Since our knowledge from the underlying network in the early stages of EGS development is restricted to the drilled boreholes, it would be very useful if we could calibrate the geological model using the induce microseismicity data. Induced microseismicity has been considered a means to estimate the spatial distribution of the existing fracture network in percolation thresholds [Sahimi et al., 1993; Tafti et al., 2013]. The fractal patterns of micro-earthquake hypocentres are poorly understood and their correlation with the fracture size distribution in not yet clear. On the other hand, the relation between the b-value of induced seismicity and the size distribution of discontinuity planes remains unknown. Clarifying these relations could calibrate our stochastic representation of the existing network (also referred as Discrete Fracture Network DFNs) and possibly ultimately lead to an enhancement of our predictions about the seismogenic response of the reservoir to fluid injection.

The starting step of this research is to understand the fractal patterns of induced microseismicity. Therefore, we generate 3-D synthetic fractal fracture patterns and study the existing relations between the fracture size and spatial distribution. We then use the relation between size distributions and spatial organization to constrain the fracture size in Basel. Performing a Monte-Carlo simulation on the size distribution respecting the uncertainty of hypocentral locations, we will compute the average and standard deviation of the size distribution and induced b-value.

3.4.1 Methodology

Figure 99a represents a *3-D* DFN generated using dual power-law model with the following parameter ($D = 2.7$, $a = 2.8$, $\alpha = 0.02$ and $l_{min} = 10m$). Figure 99b and Figure 99c verify the accuracy of fractal pattern of fracture spatial and size distributions. There is not a direct relation between *a* and *D* in first order model but Bour and Davy (1999) have related a and D through a new scaling law (Equation 7), where *x* is the exponent of a power-law including the average distance (*d*) from a fracture to the closest fractures having a larger size. The exponent of *x* can be computed by Equation 8.

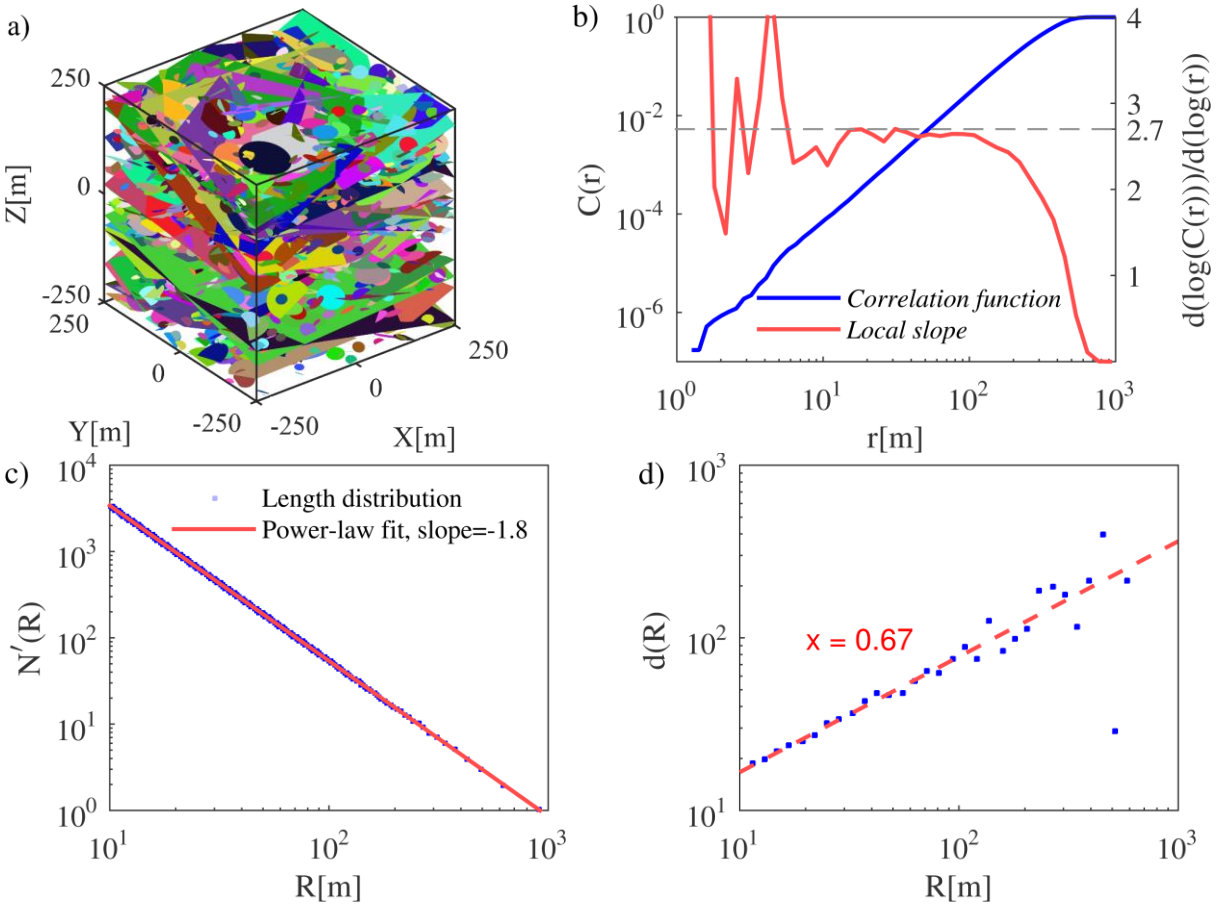

Figure 99 - a) A synthetic network generated using dual power-law model ($D = 2.7$ and $a = 2.8$). b) Correlation function and its local slope of the generated network. c) Complementary cumulative length distribution of the generated network (*N'* is the number of fractures larger than size of *R*). d) Correlation between size and spatial distribution through distance function.

Equation 7 $$d(R) \sim R^x$$

Equation 8 $$x = \frac{a-1}{D}$$

Figure 99d shows the distance function of the example synthetic network in Figure 99a. The estimated *x* of the network (*0.67*) is very close to the computed *x* from analytical definition (*0.667*).

3.4.2 Application to Basel Micro-seismicity

Until now, we have been trying to understand the correlation between fracture size and spatial distribution in *3-D* synthetic fractal fracture networks. In addition, we analyzed the effect of factors deviating the spatial distribution of existing network and induced micro-seismicity. We apply our findings from the synthetic networks and try to understand the spatial distribution of micro-seismicity in Basel geothermal reservoir. For a detailed description of the hydraulic stimulation process, we refer to Häring *et al.* (2008). The initial catalogue of the induced seismicity reports 3560 events. Kraft and Deichmann (2014) have tried to reduce the uncertainty of the initial catalogue by a high-precision relocating the earthquake hypocenters and recycled it to a catalogue containing 1980 events. The correlation function of the relocated catalogue is shown inFigure 99. It is necessary to mention that the uncertainty of micro-earthquakes in the first catalogue is approximately two times of the relocated catalogue.

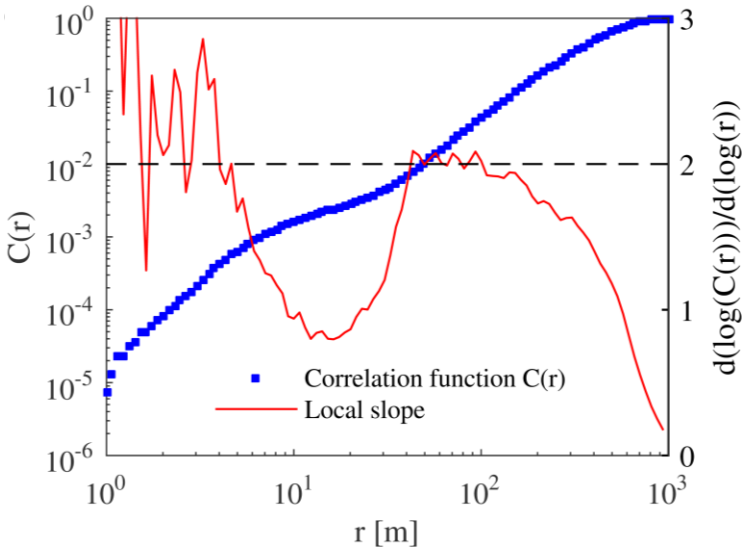

Figure 100 - Spatial distribution of induced micro-seismicity in Basel (1980 relocated events)

To verify the presence of a correlation between rupture size and spatial distribution in Basel, we assign a radius (*R*) to every relocated event through the proportionality of $R \sim 10^{M_w}$. Thus, we can compute the distance function as a function of fracture size. Figure 101a represents the average distance function in every point on the possible range of *cte.R* (*cte* represent the constant of proportionality). If the correlation dimension of spatial distribution (*D*) in the relocated catalogue is approximately *2* (Figure 101d), the b-value of induced seismicity can be computed by equation Figure 101 (Figure 101a. all data). To determine the temporal evolution of b-value, we divided the events into two sub categories; during injection and after bleed off and performed similar computations. We have been able to assign a b-value to the induced micro-seismicity in Basel, applying the concept of distance functions. To verify the computed b-valued, a direct FMD was performed on the relocated catalogue. Figure 101 shows the estimated b-values and its comparison to the b-values computed using the distance function.

The computation of b-values using the distance functions contains an uncertainty that originates from the associated errors of hypocentral locations. According to Kraft and Deichmann (2014), the uncertainty of hypocenters are *74m*, *48m* and *32m* in the direction principal axis of ellipsoids. The corresponding *D* approaches to *3*, similar to what we observed for synthetic fracture networks (Figure 101a). For simplification, we assume the direction of principal axis of ellipsoids correspond to Cartesian coordinates. Figure 101c represents the effect of such an uncertainty on the spatial distribution of hypocenters in a random realization. To analyze the influence of such an uncertainty on size exponent (*a*) and consequently b-value, we performed a Monte-Carlo simulation with *100,000* random realizations. Figure 101d shows the frequency of size exponents (*a*) in Monte Carlo simulations If we try to fit a normal distribution to the results, the mean *a* is *2.08* and standard deviation *0.09*. Furthermore, the resulting b-value could be estimated to be $b = 1.08 \pm 0.09$.

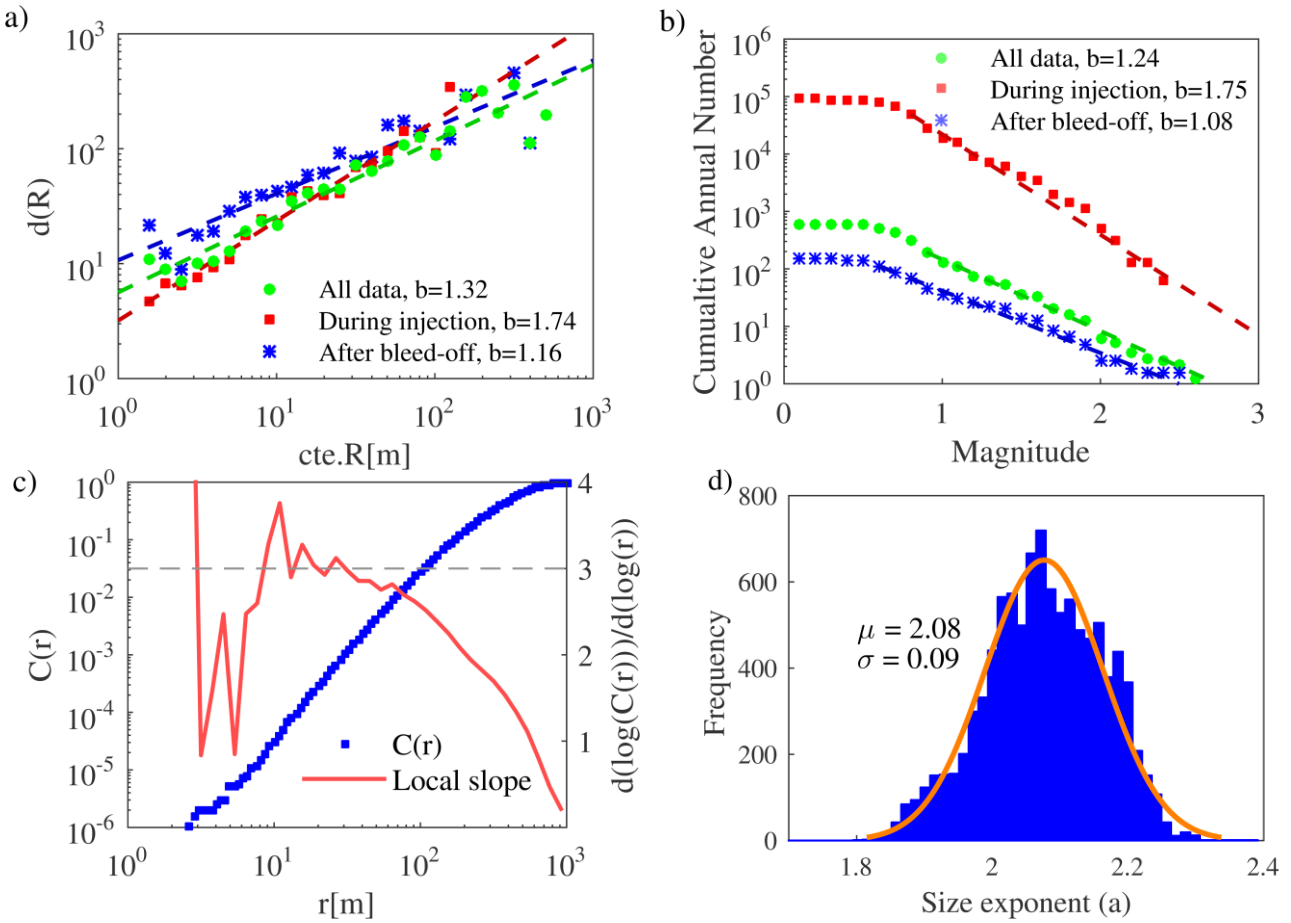

Figure 101 - a) Estimation of b-value using the concept of distance functions applied to the relocated catalogue of Basel micro-seismicity dataset. b) Estimation of b-value using FMDs to the relocated catalogue of Basel micro-seismicity dataset. c) spatial distribution of a random realization respecting the hypocentral uncertainty of 74m, 48m and 32m in XYZ directions. d) Frequency of size exponents (a) in 100,000 random simulations

3.4.3 Conclusions

We applied fractal geometry to relate the existing fracture network to the fractal patterns of induced micro-seismicity (spatial and magnitude distribution). This approach requires some simplifying assumptions and provides a new methodology to estimate the b-value of induced seismicity.
Further analysis confirms the necessity of relocating hypocenters to provide an acceptable schematic distribution of the underlying network. We applied the concept of distance function to the relocated micro-seismicity in Basel and computed the size exponent of existing fractures. The estimated b-values are very close to the estimated values using FMDs. If we include the uncertainty of hypocentral locations in computing distance functions, there will be a large number of possible realizations and different estimations of size exponent and b-value. A probabilistic analysis of the available data reveals a size exponent of $a = 2.08 \pm 0.09$ and b-value of $b = 1.08 \pm 0.09$.

3.5 Perspectives

The performed work presents a systematic analysis of the fractal properties of the deep geothermal reservoirs of Basel and Soultz. Important methodological aspects have been clarified in order to obtain these results. Particularly, the investigation of the stereological relationships for fractal fracture network give insights on the limitations inherent to the interpretation of 1D borehole data for the characterization of fractures network in 2D or 3D.

Research is still on-going with the aim of better understanding the relationships amongst the various fractal indicators. We also aim at deriving practical application for this work. Some of this practical application are hindered by the lack of a 3D numerical model allowing the computation of stresses within a dense embedded discrete fracture network. Nevertheless, the results presented here constitute sound bases for future application in the characterisation of fractal characteristics in deep geothermal reservoirs.

4 Molassic basin – Thonex area

4.1 Introduction

In the framework of the geothermal energy development in Switzerland, the State of Geneva drilled a borehole at Thônex, in country side of Geneva, in 1993, within the Molassic basin between Salève and Jura (Figure 102).

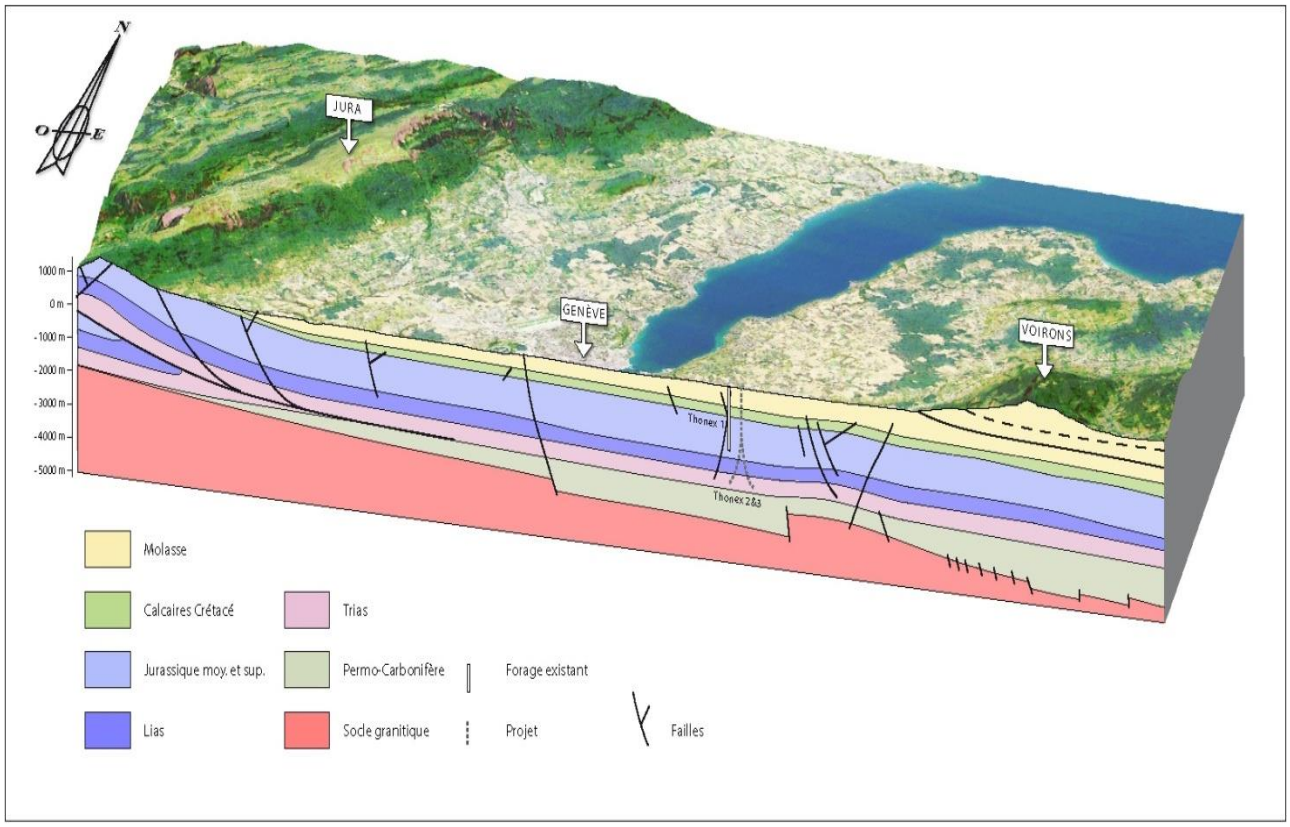

Figure 102 – Location of the THONEX-1 well.

This borehole reached 2530m and 88°C in the limestomes of upper Jurassic (Figure 104). Some fracture zones was cross-cut, but the fluid flow was too weak (<1l/s) and the operation was stopped.

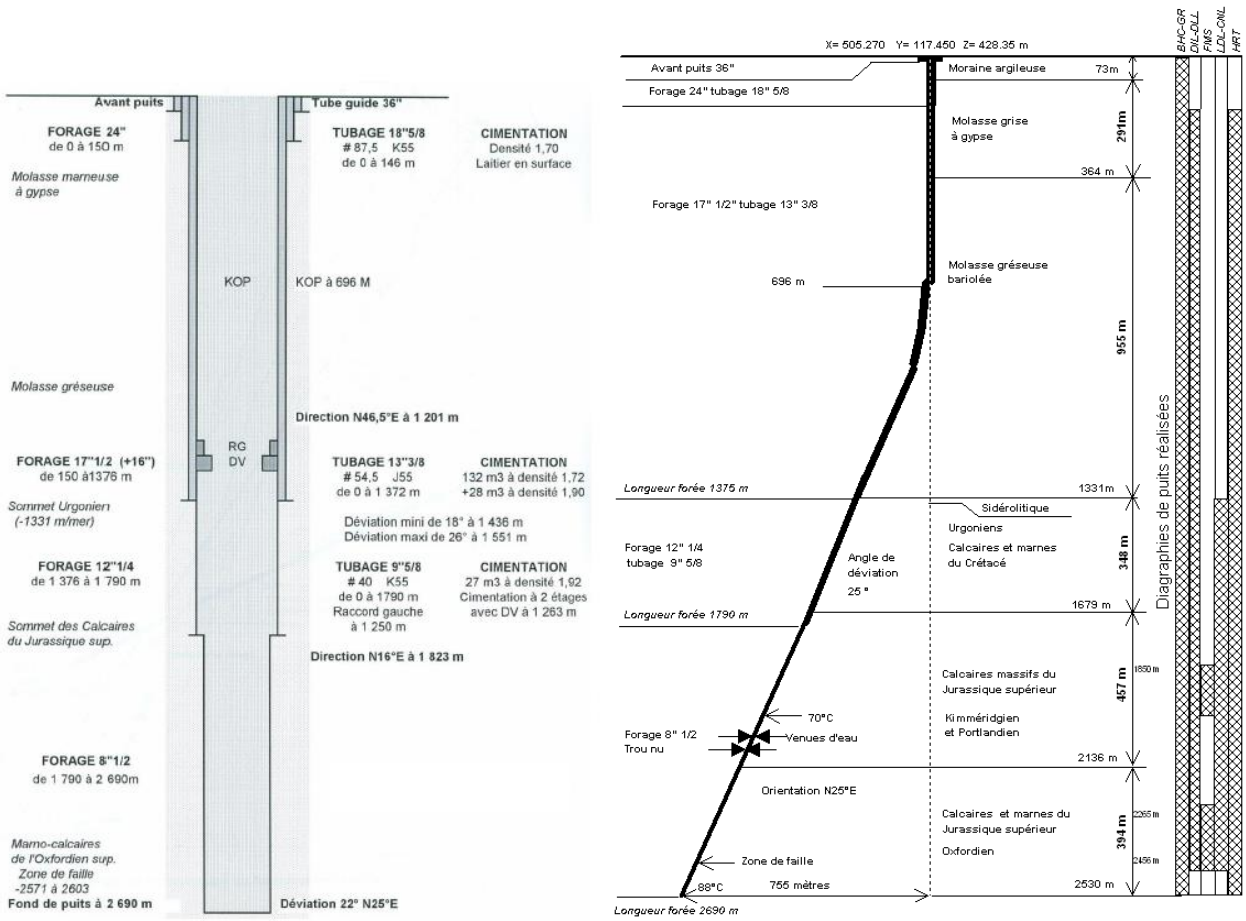

Figure 103 THONEX-1 well design and geological log.

Recently, in 2014, a new geothermal program, namely Geothermie 2020, was launched by the SIG (Service Industriel de Genève) and the State of Geneva. In this framework, the Thônex well has been reconsidered and a partnership between the University of Geneve, SIG and BRGM has been done in the framework of the IMAGE project in oder to performe a VSP survey and a geochemical study of the geothermal fluid.

The well was drilled between April and Septembre 1993, with a deviation of 20° - 26° (Etat de Genève, 1994; Figure 104). The final depth was over 2600 m depth, and the well was cased until 1800 m (Figure 103). In 2007 an inspection found an obstruction at about 1100 m, which was reopened by means of coil-tubing technique. The open hole at this date was already obstructed.

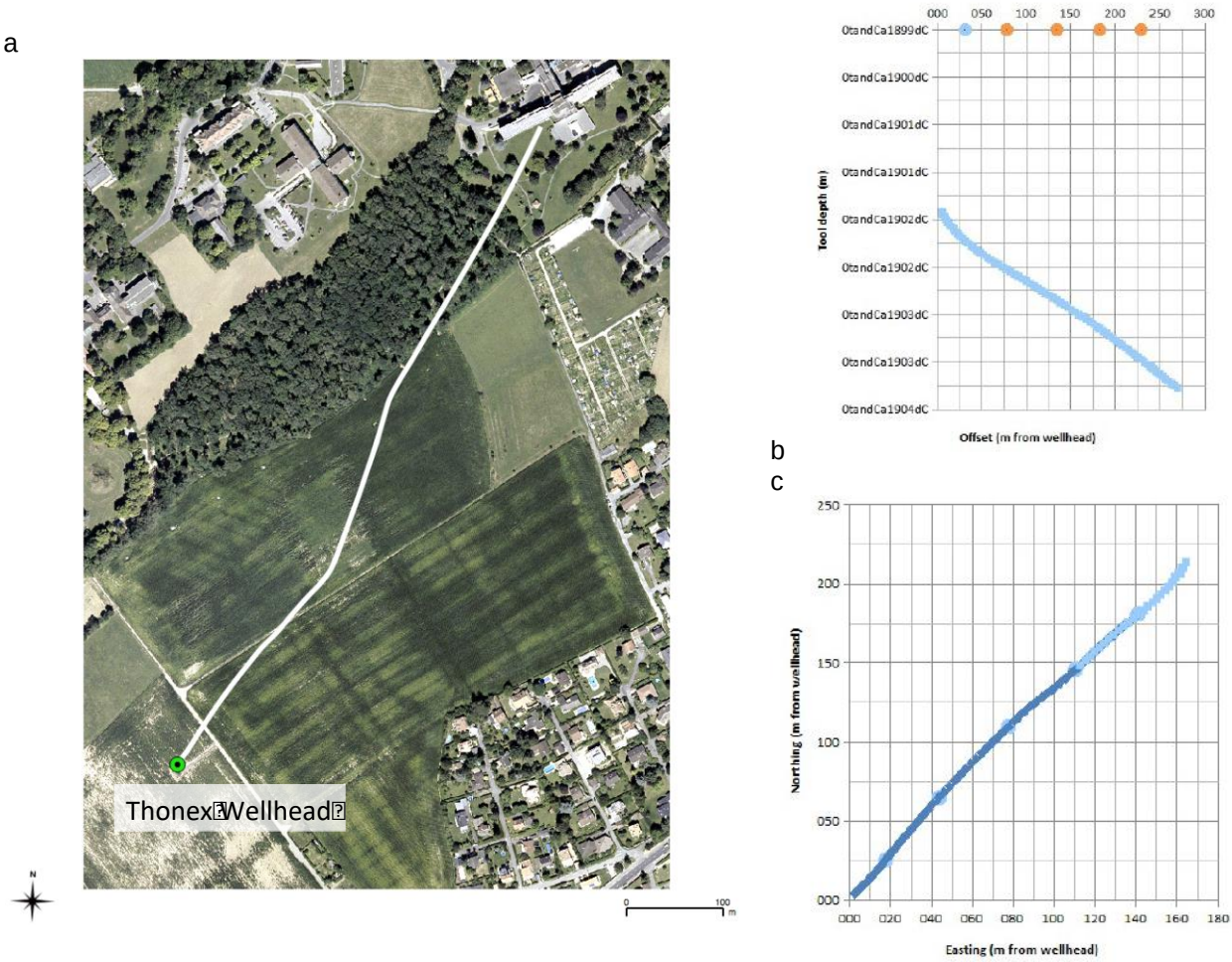

Figure 104 - a. Well Map and well deviation line, b. deviation on vertical section and c. projection over horizontal section

4.2 Geological context of the Geneva Basin

The Greater Geneva area has been extensively studied, both through surface geology (see existing geological maps of the French and Swiss geological surveys) and through several reflection seismic surveys related to hydrocarbon exploration (in France) and geothermal energy (Canton Geneva). The location of these seismic profiles can be seen as grey lines in figure 1. Information on the subsurface has been complemented by the drilling of petroleum wells and one geothermal well in Canton Geneva (well Thônex-1, Figure 105 and Figure 106). Part of this information has been published (e.g., Gorin et al., 1993; Jenny et al., 1995; Paolacci, 2012; Signer & Gorin, 1995). The exploration program of SIG and state of Geneva, Geothermie 2020 started in 2014, is providing news datas and interpretation through new seismic profiles acquisition and wells.

The Greater Geneva Basin is located between the folded Jura and the Alpine front marked by the Subalpine Massifs and the Prealps (Figure 105). It corresponds to the Molasse foreland basin. Seismic data provide a good representation of the sedimentary sequence and are calibrated by petroleum boreholes. Surface geology and seismic data have permitted the mapping of the fault pattern at Mesozoic level (Figure 105). The Greater Geneva Basin is crossed by a series of major NW-SE trending senestral strike-slip faults. All of them were active during the Alpine compression and seismic activity is continuing at present-day along the Vuache Fault (Baize et al., 2011; Sambeth and Pavoni, 1988). Part of these faults are deep-seated and reach the basement, and some of them

are probably older lineaments reactivated during the Alpine orogeny (Gorin et al., 1993, Signer and Gorin, 1995).
Whereas outcrops in the Salève and Jura Mountains exhibit mainly part of the Middle/Upper Jurassic and Lower Cretaceous competent rocks and those in Canton Geneva only small parts of the Lower Freshwater Molasse, a full stratigraphic section can be derived from deep oil wells in the area (Figure 106). For more details on the local stratigraphy, one can refer to Meyer (2000).
Above the *crystalline basement* (never reached by the drill but outcropping in the nearby Mont-Blanc Massif, a thick *Permo-Carboniferous* sequence can be locally present in half-graben basins such as those developed below the thrusted Salève range or below the frontal Alpine thrust. In the Greater Geneva area, Carboniferous sediments have never been reached by the drill, but Carboniferous coal strata may provide typical high-amplitude reflectors that permit the approximate mapping of the top basement (Gorin et al., 1993). Only the overlying Permian sandstones have been reached by wells such as Humilly-2 or Faucigny-1.
The *Triassic* is generally characterized by evaporites associated with the development of an epicontinental shallow water sea controlled by variable connection conditions with the Tethys. The Triassic sedimentary sequence, if not affected by halokinesis, reaches a thickness of some 500 m underneath the Molasse foreland basin. It is usually divided into three intervals according to the German classification: the *Buntsandstein* mainly composed of continental sandstones; the *Muschelkalk* recording the first marine transgression showing marly limestones, evaporites and dolomites; the *Keuper* comprising a lower thin interval called Lettenkohle made of lignite and dolomite, and a thick upper interval of evaporites (gypsum and halite). This interval acted as a decollement horizon for the Jura Mountains and Mount Salève (Figure 106). Finally, the Triassic terminates with *Rhetian* shales.

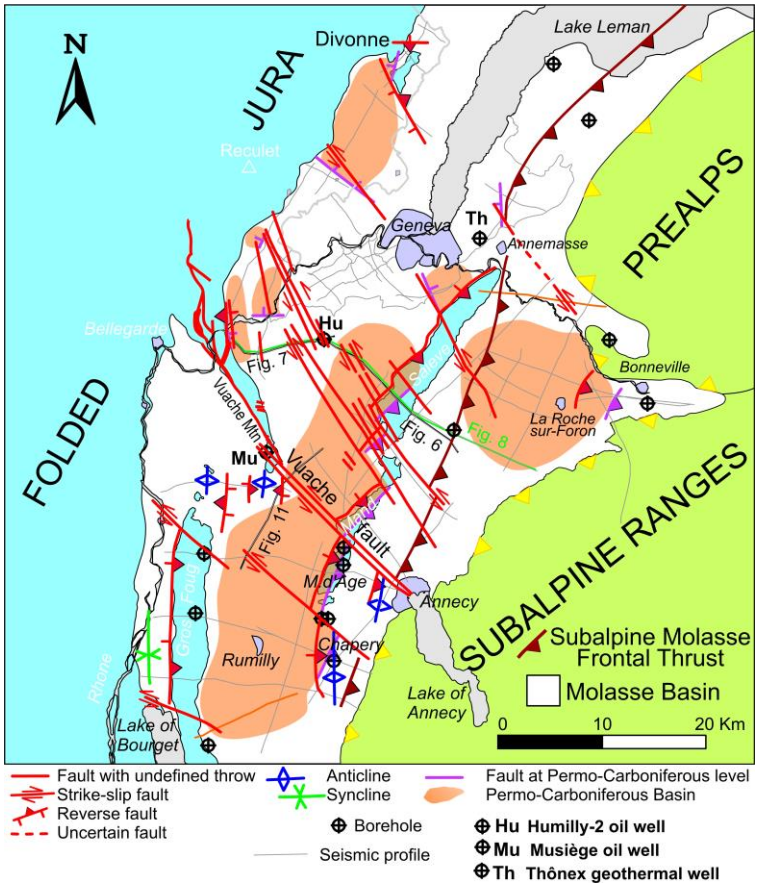

Figure 105 - Tectonic framework of the Greater Geneva area at Mesozoic level (after Paolacci 2012). Note: the fine grey lines correspond to the seismic grid (before start of the program Geothermie 2020).

A rapid marine transgression occurred in the *Liassic*. The predominant depositional facies is characterized by bioclastic muddy limestones in the lower part and a shaly upper part containing the organic-rich Posidonia shales. The overlying *Dogger* also developed in a relatively deep water environment and the Aalenian is sometimes difficult to distinguish from the underlying Liassic. It shows intercalated marls and crinoidal limestone with quartz-detritic input in the upper part. Seismic interpretation and the correlation between the wells Humilly-2 and Faucigny-1 show that the Liassic and Dogger show a significant thinning and finer-grained lithology towards the southeast. This is interpreting as corresponding to the transition from platform facies towards slope facies on the northern side of the Tethys Ocean (Gorin et al., 2003; Signer and Gorin, 1995). This zone of transition follows a general SW-NE trend and can be traced further to the northeast in cantons Vaud and Fribourd (Paolacci, 2012). Apart from a lower (essentially Oxfordian) more marly part, the *Malm* is characterized by competent, often massive, shallow platform carbonate deposits. Biohermal reefs facies are developed mainly during the Kimmeridgian-Thitonian interval, such as oolithic limestones, peri-reefal and reefal limestones, bioturbated and dolomitized lagoonal limestone and calcarenites.

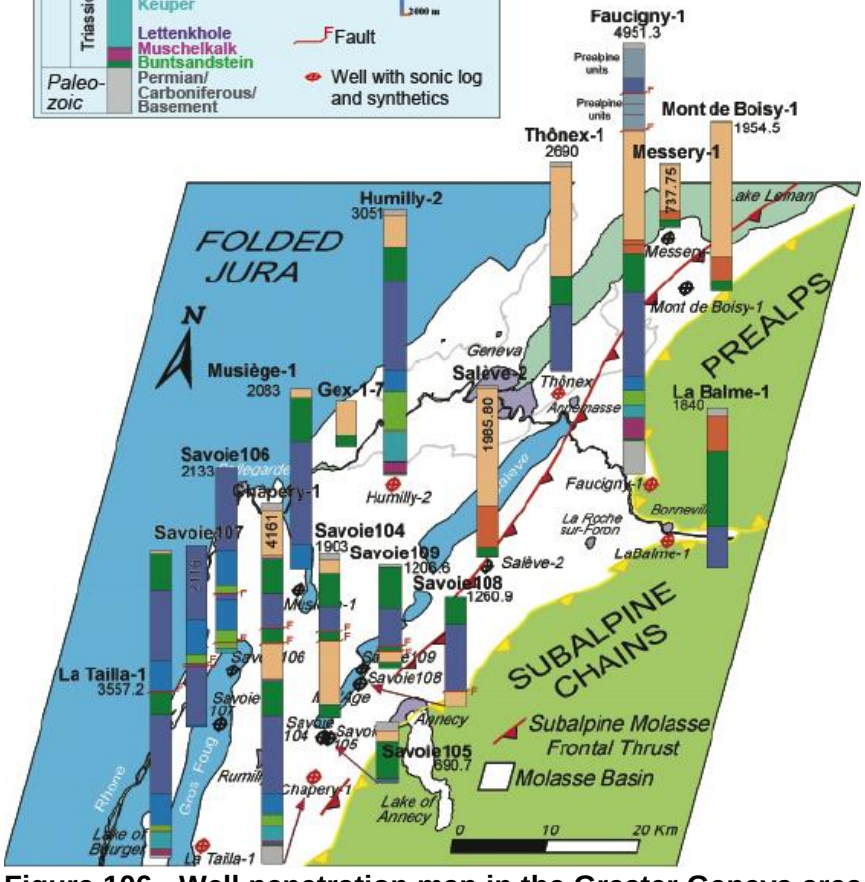

Figure 106 - Well penetration map in the Greater Geneva area (after Paolacci 2012). Note: all wells have been drilled for hydrocarbon exploration, except Thônex-1 for geothermal investigations

The last Jurassic stage is the “Purbeckian” which is more argillaceous than the underlying Malm deposits and is characterized by a widespread regression marked by emersive facies with dinosaur tracks.

In the *Early Cretaceous*, a shallow and warm water environment prevailed. Berriasian deposits are mainly fine grained/bioclastic and fine quartz-rich bioturbated limestones alternating with organic-rich marls. After a short emersion, a deepening upward trend is marked by a marly formation in the Hauterivian. A thick interval of bioclastic limestone developed in the Barremian (“Urgonian limestones”). *Upper Cretaceous* sediments were probably deposited, but because the Greater Geneva area became emerged at the end of the Cretaceous, Upper Cretaceous sediments (if deposited) were totally eroded. This is supported by the local occurrence of cherts in the karstified Lower Cretaceous surface.

In the *Early Tertiary*, a warm and subequatorial climate accelerated the karstification of Cretaceous carbonates. Red, locally iron-rich deposits called “Sidérolithique”, tentatively dated from the Eocene often fill the “Urgonian” karst fractures and sinkholes. The Alpine foreland basin was subsequently infilled by Molasse deposits (mainly sandstones and marls) with an alternation of shallow marine and continental episodes. Finally, the top of the Molasse sequence has been eroded by the Quaternary glaciations, which deposited locally thick glacial and fluvio-glacial sequences (essentially from the last Würmian glaciation).

4.3 The Thonex geothermal well

The Thônex geothermal well was drilled in 1993 following a large 2D reflexion seismic campaign carried out in 1987 around the Geneva area and a subsequent high-resolution seismic survey carried out in 1992 targeting more specifically the selected drilling site. The well location was chosen for both technical, operational and economic reasons: 1) a potential fractured zone was identified from seismic investigation here, 2) the depth of the two presumed aquifers formations were considered appropriate for geothermal exploitation, 3) the land owner of the field where the well location was identifies was (and still is) the State of Geneva State and 4) the successful discovery of a geothermal reservoir could have been easily turned in to a economically interesting development project especially because the proximity of a residential area and agricultural farming activities.
The borehole was drilled vertical until 630m depth from where is deviated of 25°. It was drilled in two sections with a 24’’1/2 and then 8 ‘’1/2 diameter hole. It was completed with and has a steel casing down to 1790 m.

The total measured depth of the borehole is 2790 m equivalent to a vertical depth of 2530 m. The two main reservoir targets were the Cretaceous carbonates at 1700m and the Upper Jurassic (i.e. the Kimmeridgien carbonates in the Malm time period) at 2700m (Figure 107).

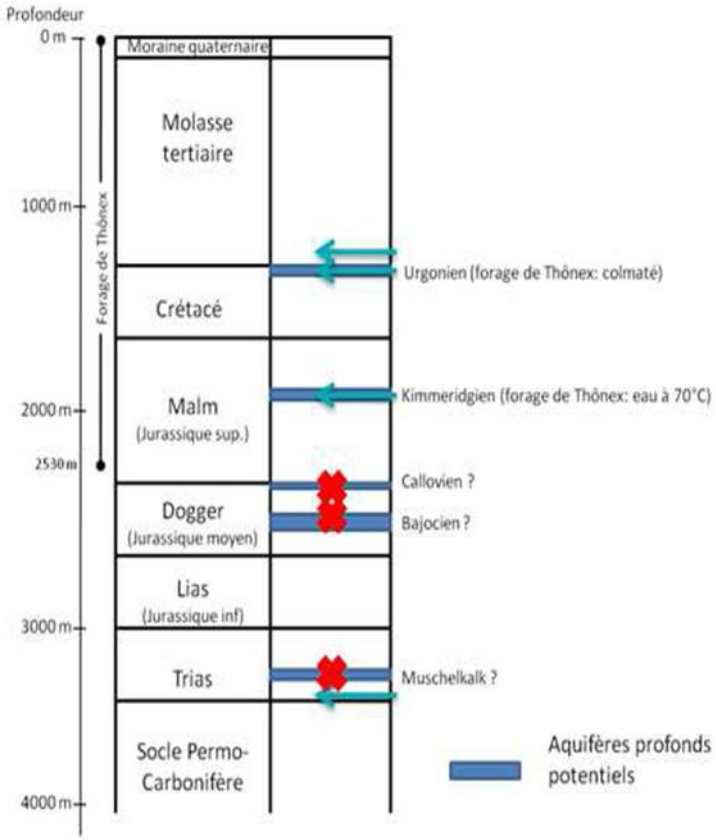

Figure 107 - Possible deep geothermal reservoirs in in the Swiss Plateau. The blue arrows indicate those likely present in the Thonex well location while the red cross the ones which do not seems to be developed in the same area.

Warm water flux was measured at the well head at a temperature of 70°C with a flow rate of 3 l/s . Because of the disappointing flow rate results, which were much lower than expected (20 l/s) the well was declared a failure and the overall geothermal project abandoned. The wellhead was thus closed leaving the possibility for future utilisation.
In 1997, SFOE decided to study the possibility to place a deep geothermal probe as it was successfully done with at Weggis in Switzerland. However the results of this study were not convincing. In fact the owner of the residential buildings potentially supporting this new utilisation of the well intended to use it for heat, which was required higher temperature then those found in the Thônex well for making it economical.
Then years later, in 2007, the SIG, the State of Geneva and SFOE decided to study the opportunity of re-use the borehole for exploration and exploitation purposes because the project of geothermal development for serving thousands of people was approved by the Canton.
This new study focused on the following activities:
1) Evaluate the status of the borehole (i.e. hole and collapse and obstructions, tubing integrity, corrosions, scaling etc.) using wire line logging tools such as sonic, caliper and a downhole video. The latter was specifically targeted to assess the extension of incrustations found at 1120 m depth.
2) Borehole cleaning. This was performed by Coiled Services, a contracting company which used coiled tubing with high pressure hose pipes to remove ferromagnesian organic incrustations along the tubing. Because of the high water pressure the cleaning job was not extended to the open hole section to avoid risk of damaging the hole.
3) Assessment of borehole quality after the cleaning job with a caliper tool resulting to the observation that the hole collapsed at 1850 m depth along hole and and was obstructed with limestone blocs.
Following this results, the study carried on to examine every possibility to re-use this borehole: 1) re-drill, 2) make a new hole and use this for injection, 3) place a deep geothermal probe, 4) equip the well with down hole seismographs for monitoring natural seismicity.

Following this study a new high-resolution seismic acquisition campaign to develop a geothermal doublet project was carried out.
After few months from the end of this study, the overall geothermal project in Thônex project was finally stopped and put on hold by SIG and the State of Geneva. At that time in fact several concerns amongst politicians, energy industry and the public were raised following the repeated failures of deep geothermal projects in Switzerland (Basel and Zurich).
In 2014, a rejuvenated interest around geothermal energy was demonstrated both at Cantonal and Federal level. In the Canton of Geneva, the State in partnership with SIG launched the "Geothermie2020" program which in its initial phase consists of a large study campaign of the Greater Geneva Basin subsurface. This includes analyses of existing data from old hydrocarbon boreholes drilled around Geneva, reprocessing of old 2D seismic lines, acquisition of new seismic lines other geophysical data such CSEM, gravimetry and natural seismicity records, in order to fill the knowledge gaps concerning the subsurface. This program also includes a larger set of aspects ranging from the economic, managerial, societal, environmental and legal aspects of geothermal energy in the Canton of Geneva (i.e. public acceptance, seismic monitoring and impact, data collection and management, legal framework for energy exploitation, economics of projects, etc.).

4.4 Vertical Seimic Profils in Thonex well

Vertical seismic profiling (VSP) is a field measurement procedure in which the seismic source is activated at a fix surface position and the seismic signal is recorded by sensors located in a well at successive depth levels. VSP provides a direct correlation between subsurface stratigraphy and seismic reflection measured in the surface. VSP resolution is higher than surface seismic because the received wave-field is direct arrival from the surface. In a surface seismic acquisition the higher frequency signal is attenuated by the two way travel time. This allows VSP survey to image structures too that could not be defined by surface seismic techniques.
Several configurations can be used for the acquisition of VSP data depending on the position of the source relative to the well. If the source is located near the well, the survey is called a Zero Offset VSP; if the source is far from the well, it is called an Offset VSP and if the sources are located above (for a deviated well) it is called walk above VSP. Data acquisition remain the same
During the acquisition one zero offset, 4 offsets and 5 walk above VSP were recorded in Thonex well near Geneva in Switzerland, from October 6th to 19th 2016 (Figure 108).

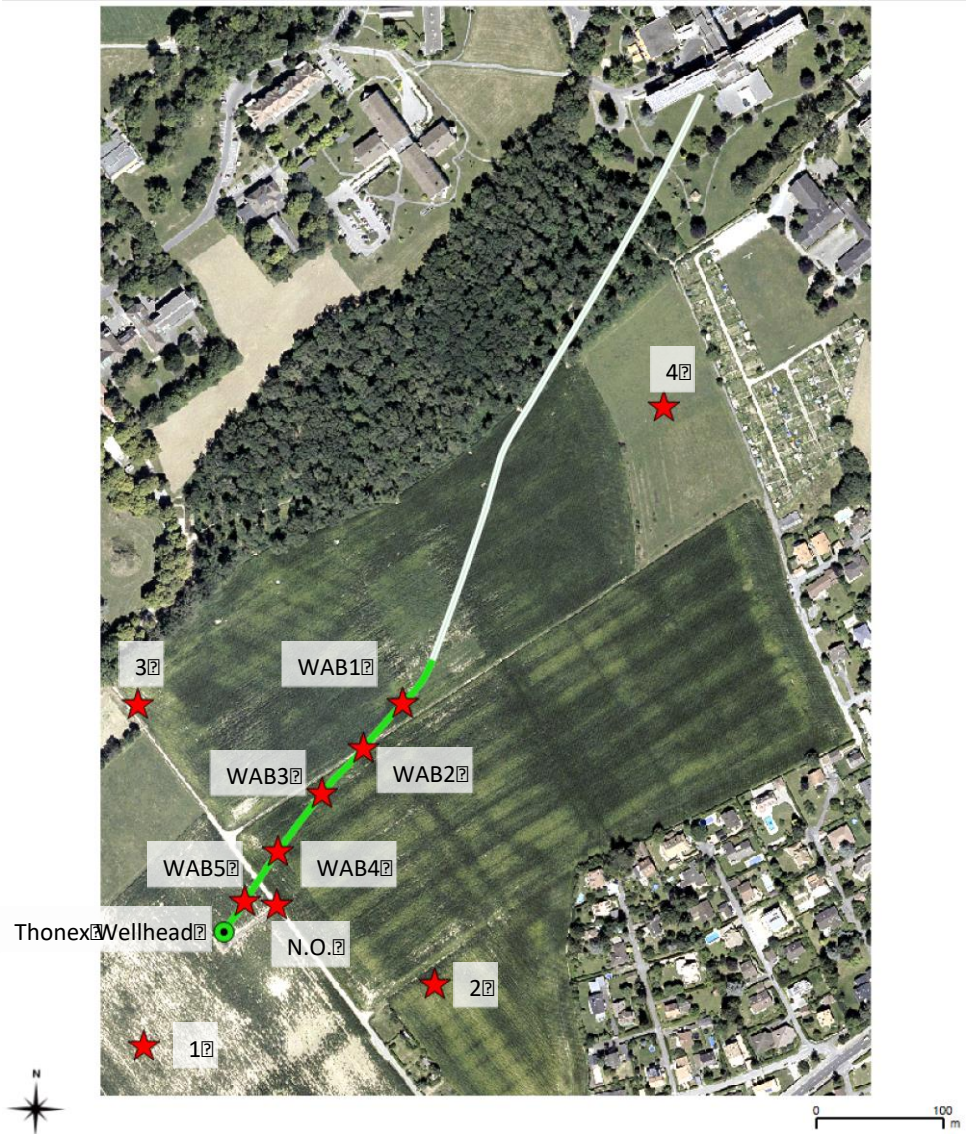

Figure 108 : Thonex well and vibration points map

The Thonex well was drilled in 1994 with aim of exploring the geothermal potential of the area. The final depth was over 2600 m depth, and the well was cased until 1800 m. In 2007 an inspection found an obstruction at about 1100 m, which was reopened by means of coil-tubing technique. Unfortunatly, cleaning hole process by coiled-tubing method allowed to give access only to the first 1500 m. The well was drilled with a deviation of 20° - 26° (Figure 109)

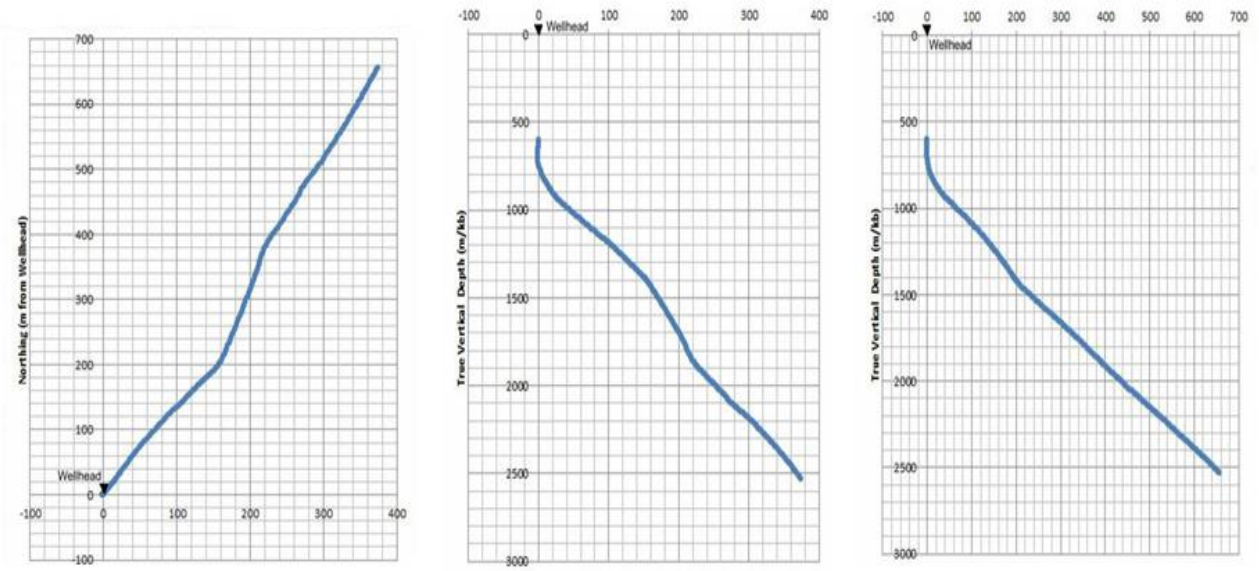

Figure 109 : Thonex well projection on the surface and deviation diagrams

4.4.1 Data acquisition

The acquisition campaign was carried out by OGS using two levels /three components (3C) VSP tool string from Avalone sciences Ltd (Figure 110). The borehole tool string is driven by a winch with 2000 m armored cable, supplied by a Honda voltage generator, with the assistance of a load indicator and the pulley providing the measure of the depth. The controls for all these equipment are installed in the control cabin, and recorded during the survey.
The record length was 20 sec with 1 ms sampling rate.
The energy source for this survey was a Prakla vibroseis (Figure 111), driven by a Seismic Source Force II control system which includes an encoder and a decoder units, respectively installed on the Vibroseis and in the control cabin, where the time break signal for the sweep start is delivered, and the reference signals, the pilots, are fed into the acquisition system.
The sweep duration was 14 sec. from 8 to 120Hz with 3 sweeps for vibration point. Sweeps were acquired at each tool depth before the tool was unlocked and move to the next level. The spacing between each tool in the array was 10 meters.
A walk above (WAB) survey is typically performed on a deviated well, in which the seismic source moves on the surface following the well deviation. Every source point covers a predefined interval of well length, paying attention to have double fold acquisition so that in every interval at least 2 shots for each position are recorded first and last interval excluded (Figure 112)
Acquisition desing was difined by ray tracing knowing the trajectory of the well assuming a stratified medium. In our experimantation 5 walk above VSP were recorded with 26 tool positions inside the well.

Figure 110 : Two levels tool strings used to acquire the survey

Figure 111 : Prakla vibroseis used as energy source for the VSP survey

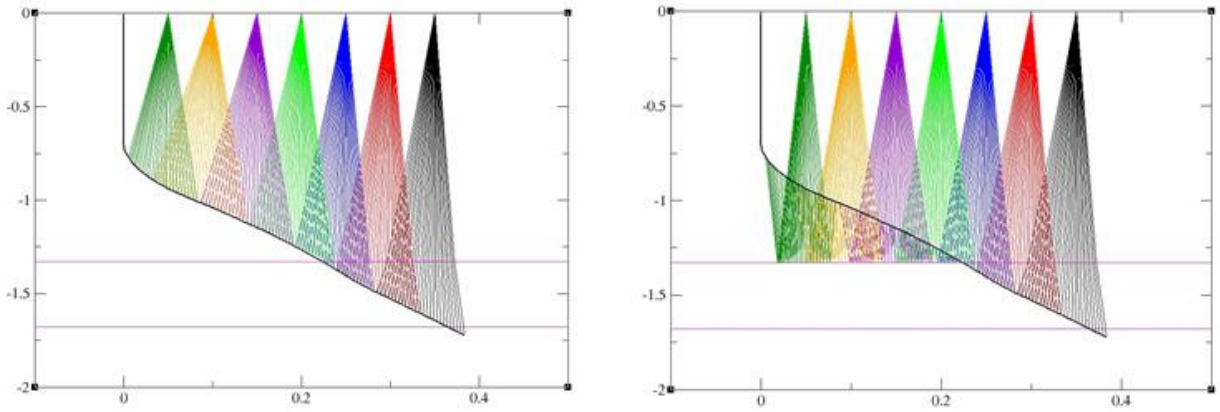

Figure 112 : Walk above layout design

4.4.2 Processing

Overall quality of data is good, with evidence of good direct arrivals and reflections (Figure 113). This is only true in the section of the well below 700-800 m depth from ground level. Above this depth, along the vertical section of the borehole, we observe effects probably due to the condition of the casing or to problems in the cement bonding. The presence of a strong high velocity resonant system makes it impossible to pick reliable first breaks on the vertical

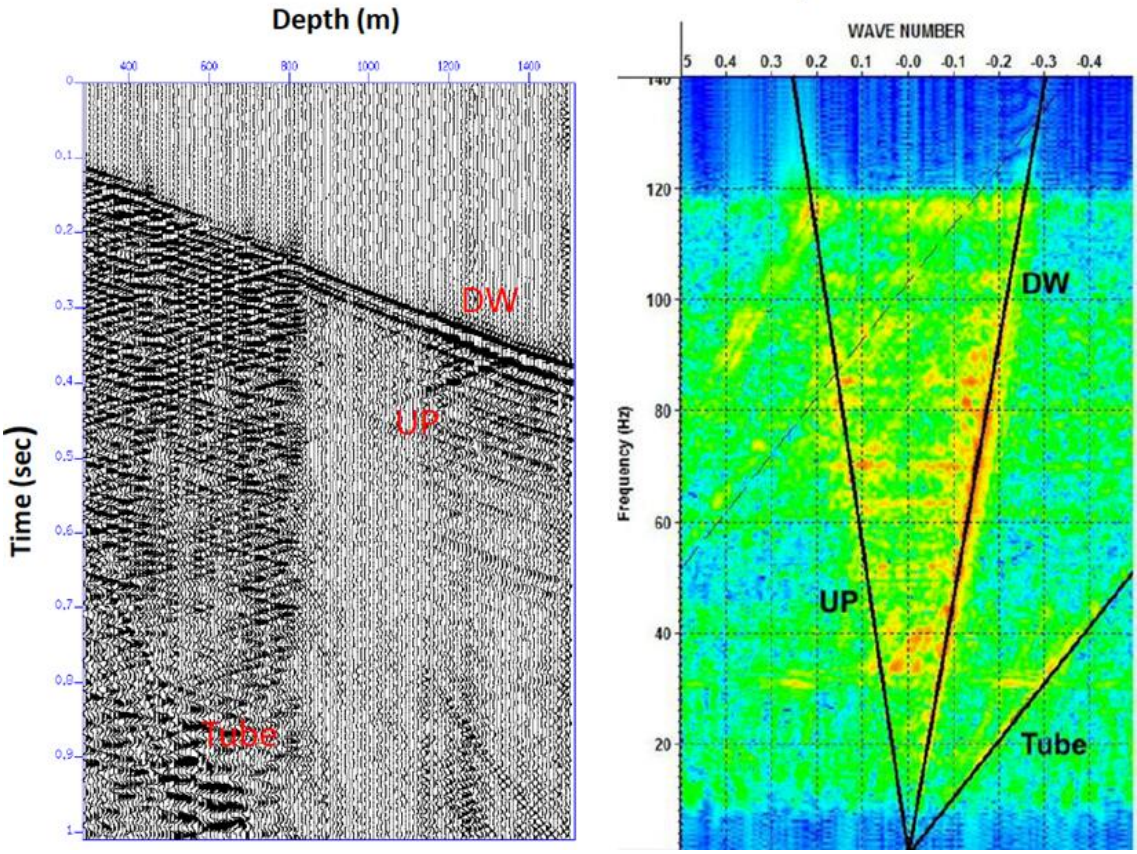

Figure 113 : Example showing data quality of the vertical component: DW-down going wave, UP- up-coming wave and tube wave. Poor quality data above 800m is probably due to casing condition.or ciment bond.

The data were processed by OGS using Vista Schlumberger software. Only the vertical component is considered. The main processing steps are:

- Header adjustment-
- Source receiver offset calculation
- Band pass filtering
- First break (FB) picking
- Velocity analysis
- Wave field separation
- Two way travel time (TWT) with and with pout NMO verticalisation
- Deconvolution
- Corridor mute and corridor stack
- Migration

After some trace editing and filtering VSP processing start with the first break picking. This allows us to determine interval velocities to geologic marker horizons (Figure 114).

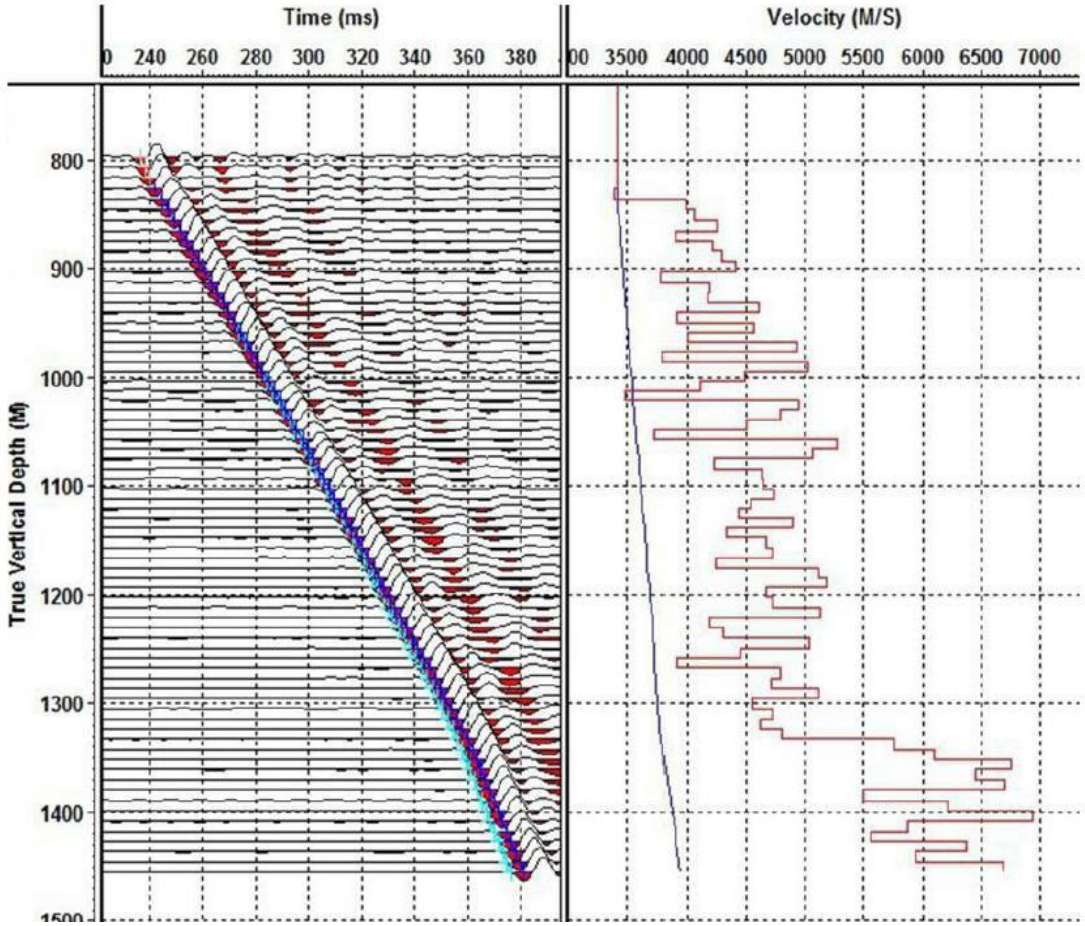

Figure 114 : First break picking on the near offset VSP and P wave interval velocity function

The first break picking was applied to all VSP and to all walk above data. Figure 115 shows the comparison between the interval velocity functions after smoothing with a three traces moving window. We observe a good fit between the different datasets that seems to display a common trend throughout the investigated area.

The next VSP processing step involves the separation of the down going waves from up-coming (reflections) waves. An approach to extracting upcoming wave is to use median filtering. We begin by applying first arrival time shifts to traces in VSP data set to flatten the downgoing waves. Then, apply the median filter to the VSP data with flattened downgoing to yield the downgoing waves. This result can be subtracted from the input data set to obtain the upcoming (reflections) waves. Another processing step for zero offset VSP data is the datuming of all receivers to the well head. This is

done by correcting each trace by an amount that is equal to one-way travel time down to the corresponding receiver location. The static corrections are then followed by deconvolution and filtering. Figure 116 shows the principal processing steps of zero offset VSP data set.

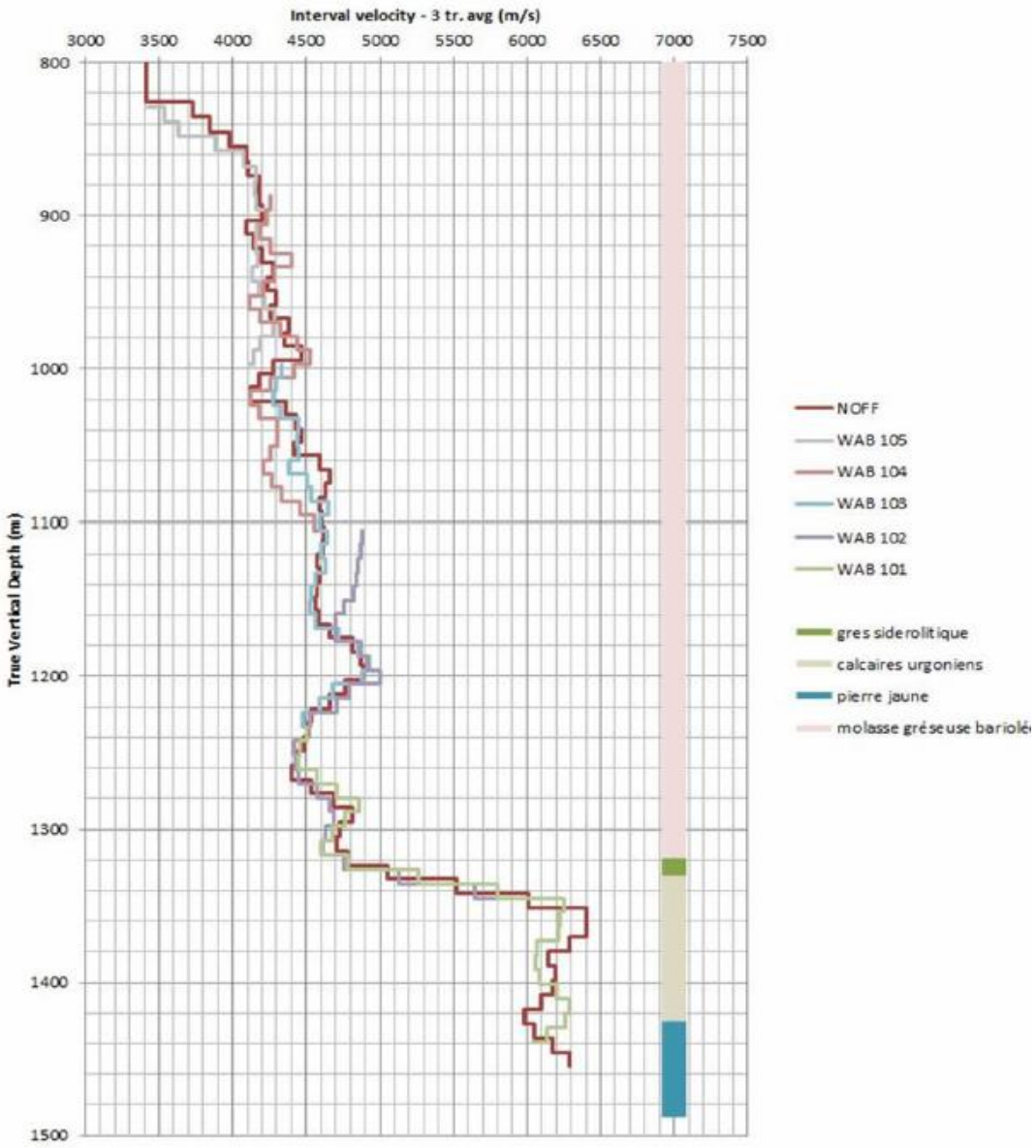

Figure 115 : Comparison between averaged interval velocities for zero offset VSP and walks above VSP

The offset VSP data are corrected for move out resulting from the distance separation between the receiver and the vibration point (Figure 116).
As for surface seismic, the final stage of data processing is migration process. The VSP migration is similar to the common shot gather migration of the seismic reflection except the shot axis is perpendicular to the receiver axis. A Kirchhoff 3d migration algorithm was applied to all VSP data to obtain a depth migrated seismic section along the well path. The velocity model used for migration was obtained from the near offset VSP after 3 traces averaging. Figure 117 shows the migration of walk above data. Before migration, the dataset is muted to remove any residual tube wave. Also the input VSP's are obtained without the F-K filter on the upcoming wavefield. The green dots represent the sensor position in the well under the different sources.

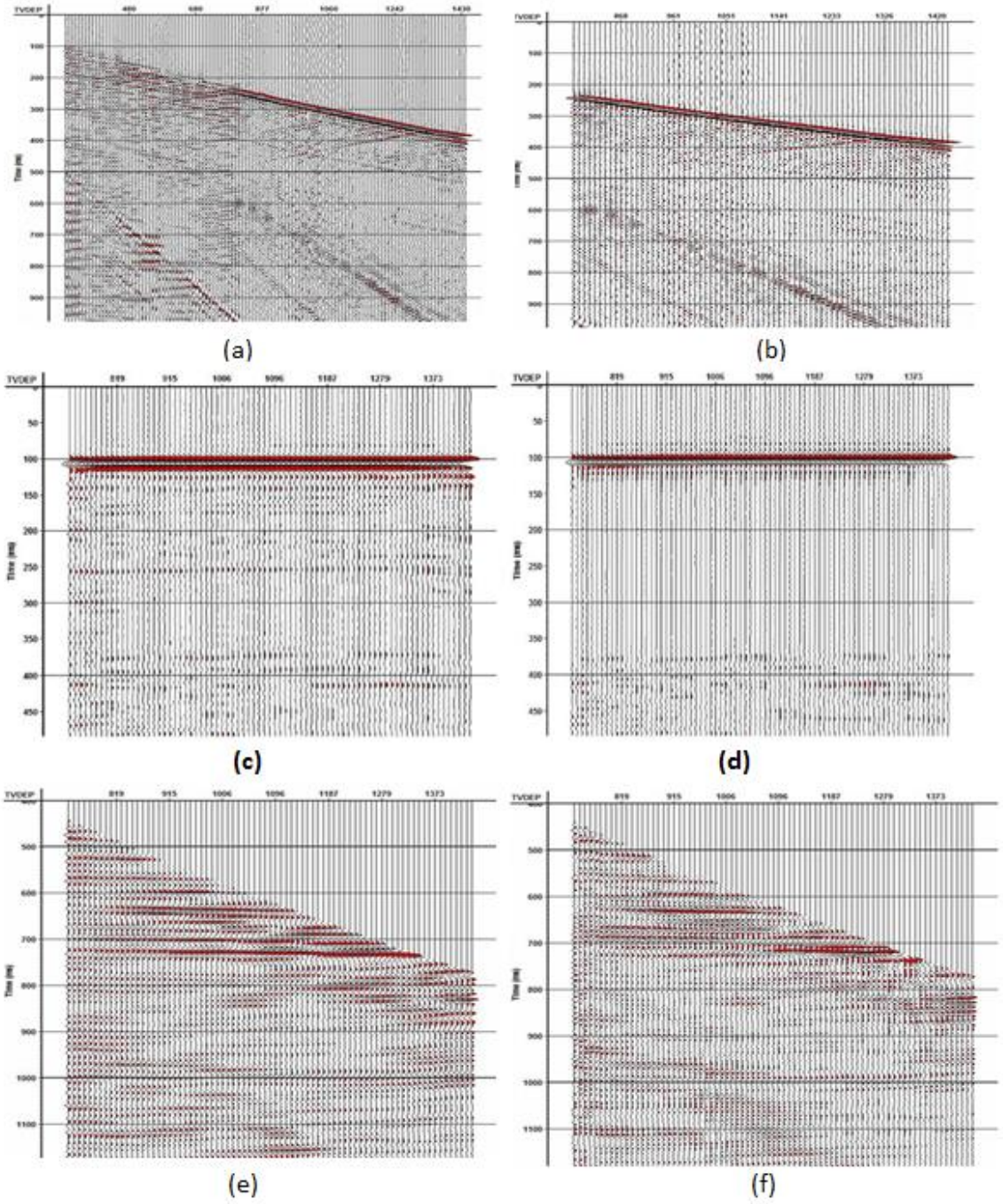

Figure 116 : Zero offset VSP data at various stage of processing sequence (a) total wavefield (all depths) and b- total wavefield (processed depth) (c) flatenned downgoing wavefield (d) deconvolved dowgoing wavefield (e) upcoming wavefield and (f) deconvolved upcoming wavefield

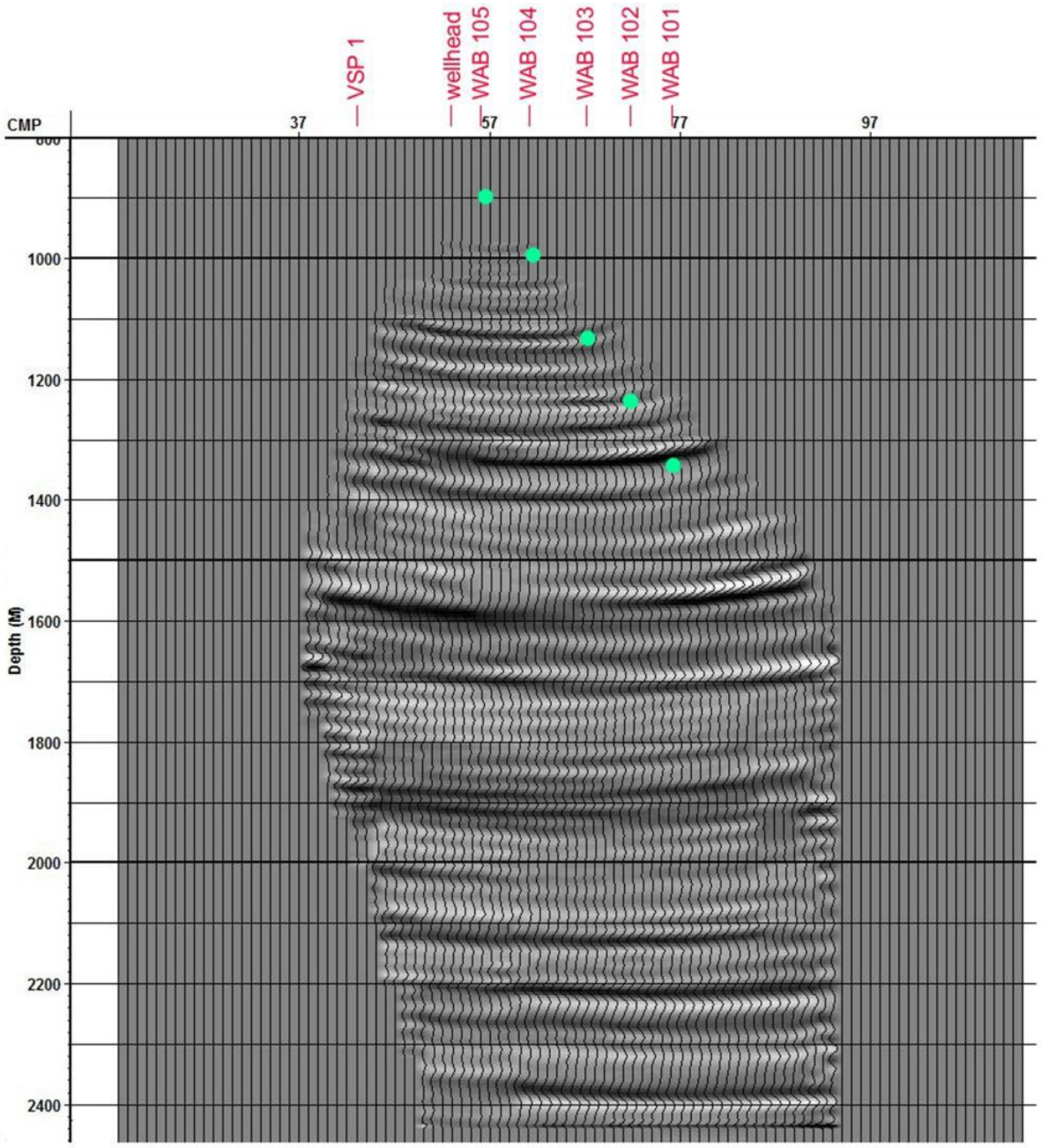

Figure 117 : Kirchhoff migration of walk above dataset. The green dots represent the sensor position in the well under the different sources

4.4.3 Results

The aim of the offsets VSP-2 and VSP-3 was to detect possible faults on both side of the well. These VSP's are symmetrical with respect to drilling trajectory and the travel time must be the same for each depth level Figure 118 shows the VSP-2 and VSP-3 first break picking and their average velocities functions. The very small difference in average velocities between VSP's eliminates any possible fault around the borehole.

Figure 119 shows the Kirchhoff migration of all VSP's data inserted to the Thonex-2 surface seismic section after depth conversion using zero offset VSP velocity function. As shown in Figure 119, VSP migration has a higher resolution than surface's seismic because one recorded direct wave-fields arrivals from the surface. In the surface seismic survey, high frequency signal is attenuated by the

two way travel paths. In spite of the very high resolution of VSP image, no prominent scattered evens from fault zone are observed.

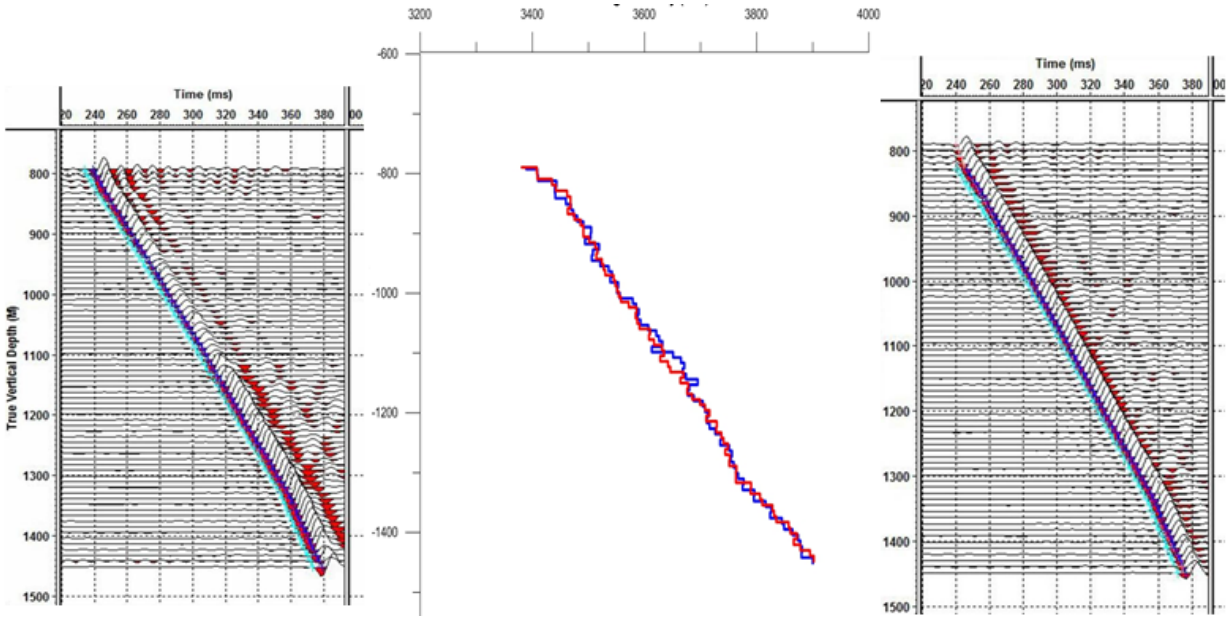

Figure 118 : VSP-2 (left) and VSP-3 (right) firs break picking and their average velocities (middle)

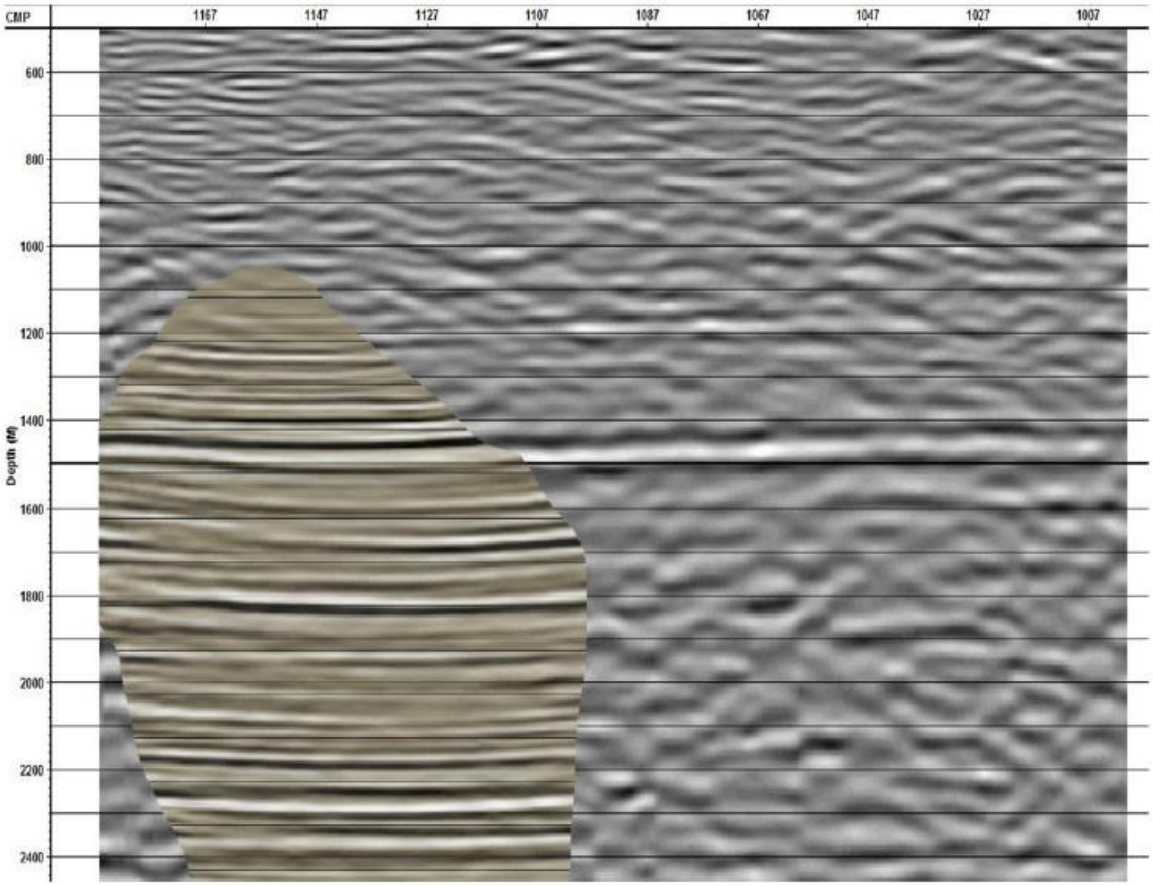

Figure 119 : . Kirchhoff migration of VSP's data inserted in Thonex-2 surface seismic section after depth conversion using zero offset VSP velocity function

4.4.4 Interpretation

4.4.4.1 Background

The well Thônex-1, drilled in 1996 as a geothermal well, intended to target deep permeable Mesozoic carbonate intervals presumably affected by open fracture associated with faults. The results were disappointing because the low flow rate attained (see above) and the well abandoned but left open in view of future opportunities developments and/or study.
The well Thônex-1 represents however the only deep well located on the Swiss territory in the Geneva Canton and intercepts both Base Cenozoic (BCen) and Top Upper Malm (TUMa) horizons. The well is deviated up to ca. 30° from vertical toward the NNE (Figure 120).

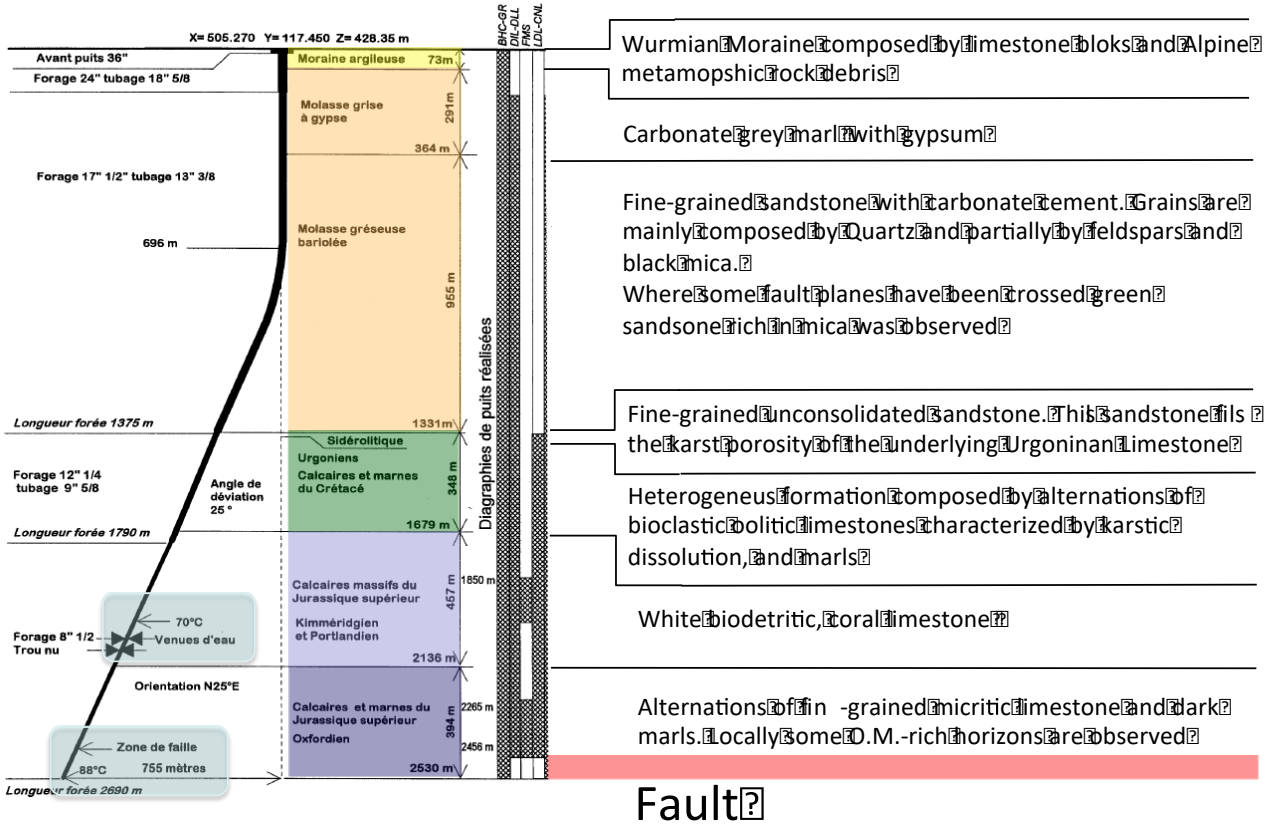

Figure 120 - Stratigraphic setting of the Thonex well

For this reason the Thônex-1 has a key importance to enable the calibration of the geological model and seismic time/depth conversion. In particular the Thônex-1 and the Humilly-2 wells are the only two wells in the region to penetrate the deeper TUMa (top Upper Malm) horizon which is an important stratigraphic marker regionally allowing the calibration of the velocity model of the SW sector of the Swiss Plateau (GEOMOL velocity model; Figure 121).

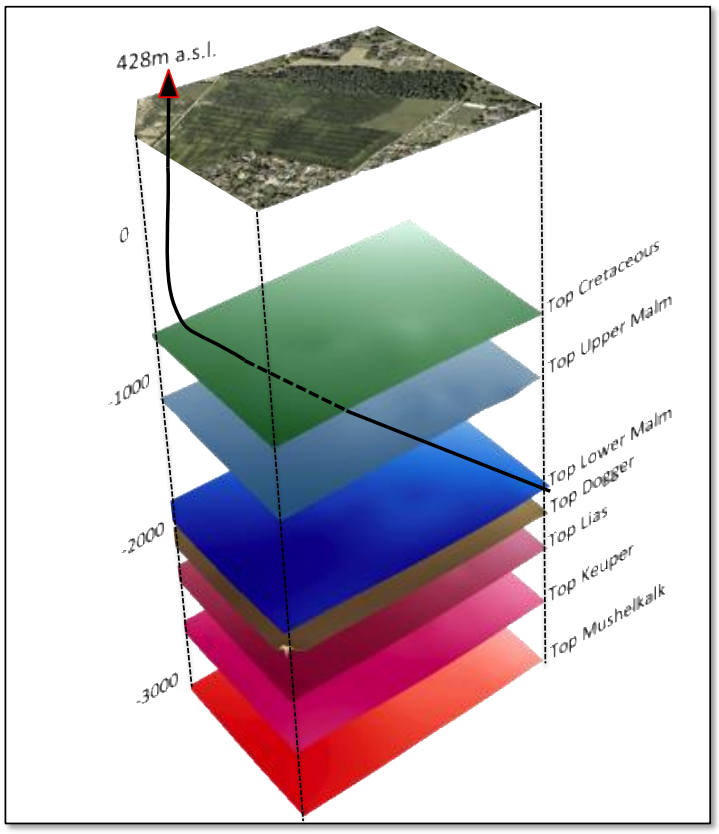

Figure 121 - 3D Geological horizons from GeoMol Model

Yet, the projection of the lower key stratigraphic marker TLMa (Top Lower Malm) inferred using the velocity model proposed for the Swiss plateau region resulted in a suspicious large discrepancy in sedimentary thickness between the Thônex-1 and Humilly-2 wells (located at approximately 14 km of distance) of the interval TUMa-TLMa. The lack of check shot data from the Thônex-1 and the possibility to re-enter the well made the acquisition of dedicated VSP an important opportunity to develop within the IMAGE research program. This activity had therefore these two main objectives:

(1) check the seismic TWT of specific deep stratigraphic interval
(2) better constrain the velocity model in this area of the basin.

Moreover, the acquisition of multiple VSP transect and walk above, was also used 3) to establish a better understanding of the presumed fault system which was originally inferred by the interpretation of two orthogonal 2D seismic lines acquired located nearby the Thônex-1 well.
Original SGY data from the Thônex 2010 campaign (Figure 122 and Figure 123) were available, allowing access to complete file header information with a seismic reference datum (SRD) at 500m asl.

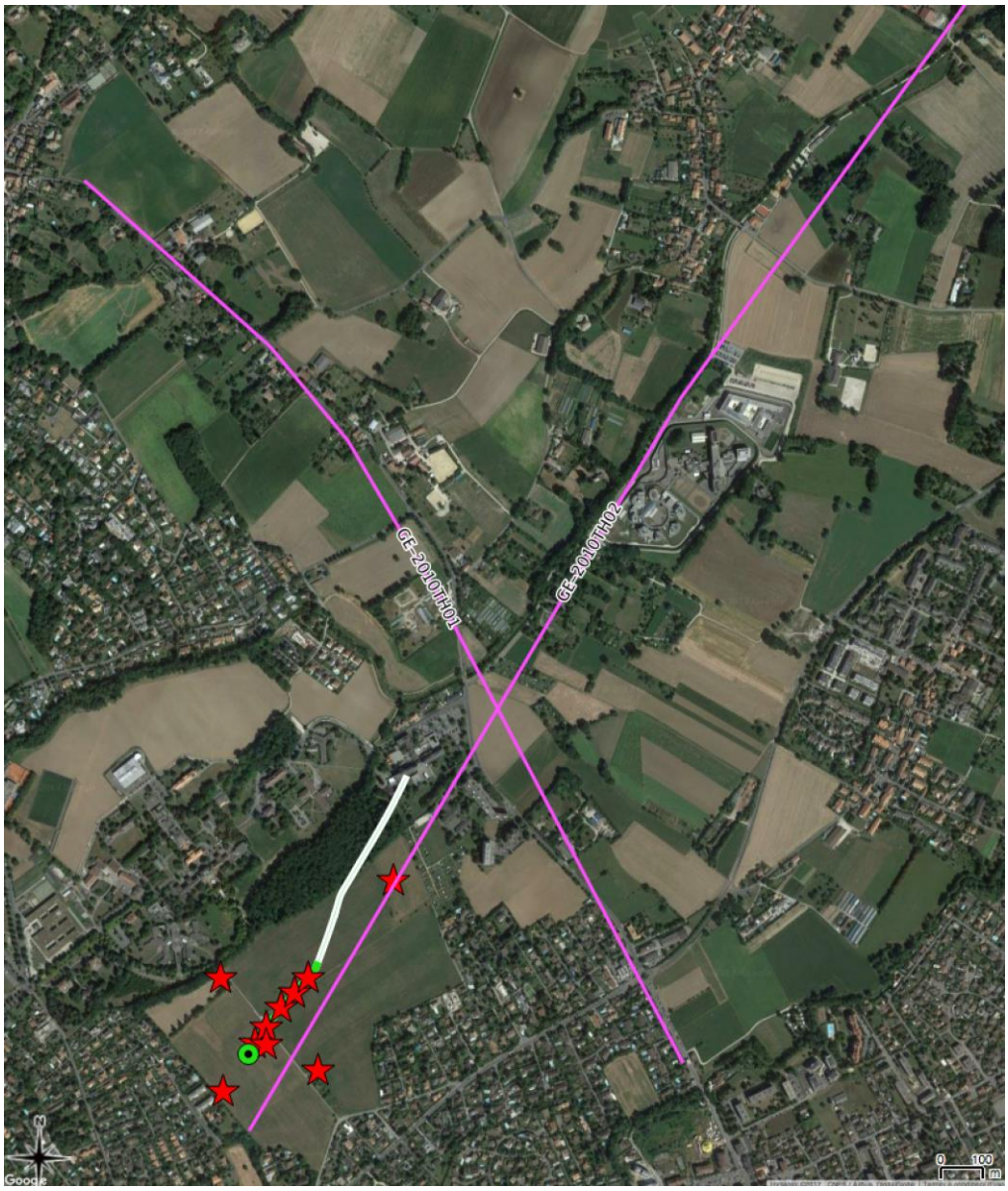

Figure 122 - Location of the 2D seismic lines acquired in 2010

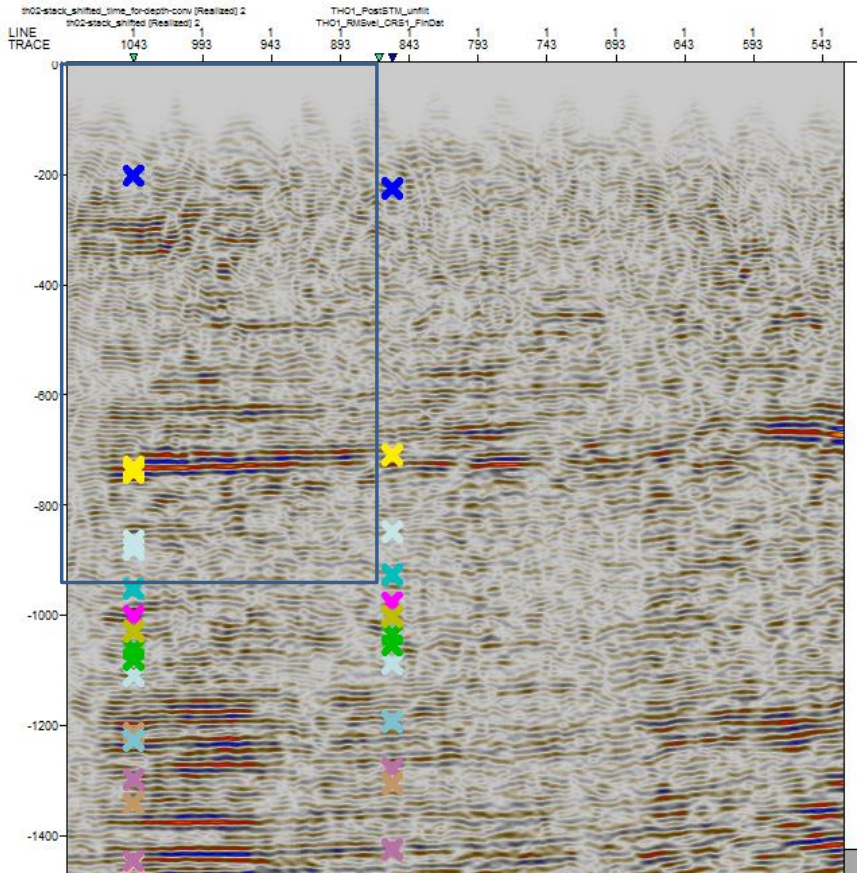

Figure 123 - Location of the VSP study area overthe Thonex2 seismic line

4.4.4.2 Results

The Molasse strata appear well visible on the VSP profile, as well as the top of the Mesozoic because of its high contrast of acoustic impedance (Figure 124). On the other hand, the Cretaceous and Upper Malm limestones are very transparent on the VSP. This could be explained by the fact that the acoustic impedance contrasts within these limestone units are much lower than those generated by the sandstone alternations of the Molasse or that generated by the Molasse-limestone contact.
In detail, several observations can be made on the VSP results:

1) The Molasse appears to be characterized by a series of intervals dominated by continuous and discontinuous reflector. The latter can be interpreted as lenticular bodies well represented by reflector terminations such as onlap and truncations suggesting the occurrence of channalised features. The continuous reflectors are interpreted as being laterally continuous, shale rich flood plain deposits.
2) The Cretaceous shows a variety of acoustic impedance, which can be interpreted as response to the well-known variability in lithology (i.e. limestone and marls alternations) and facies within this interval. In particular the high acoustic impedance at 1450 m has been calibrated with logs and core indicating that the strong seismic response is caused by the occurrence of a complex open and closed fracture system subsequently affected by infill (sedimentary dykes?) and dissolution (karst?) processes (Vallorbe Formation within the Urgonian Limestones,Figure 125).

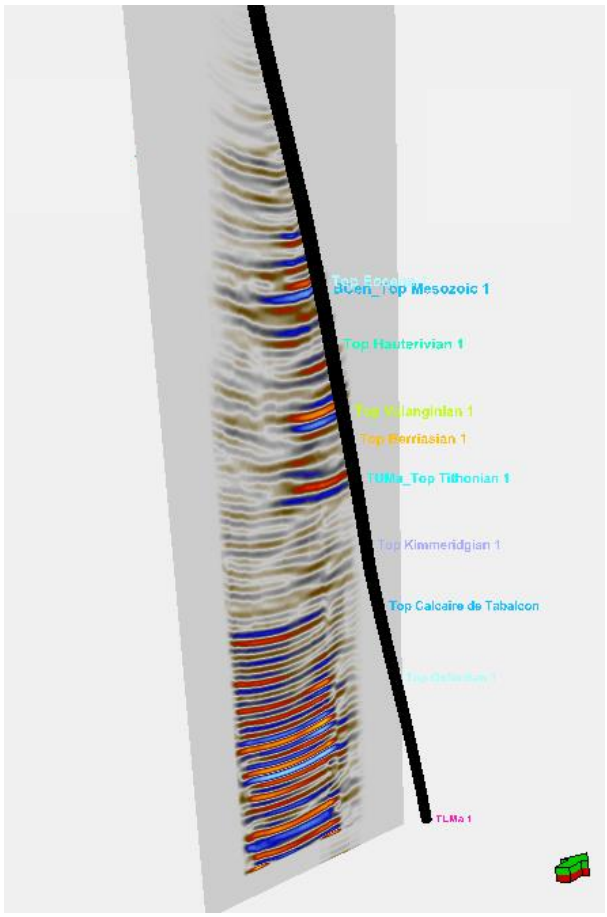

Figure 124 - Superposition of the well trace over the WAB VSP

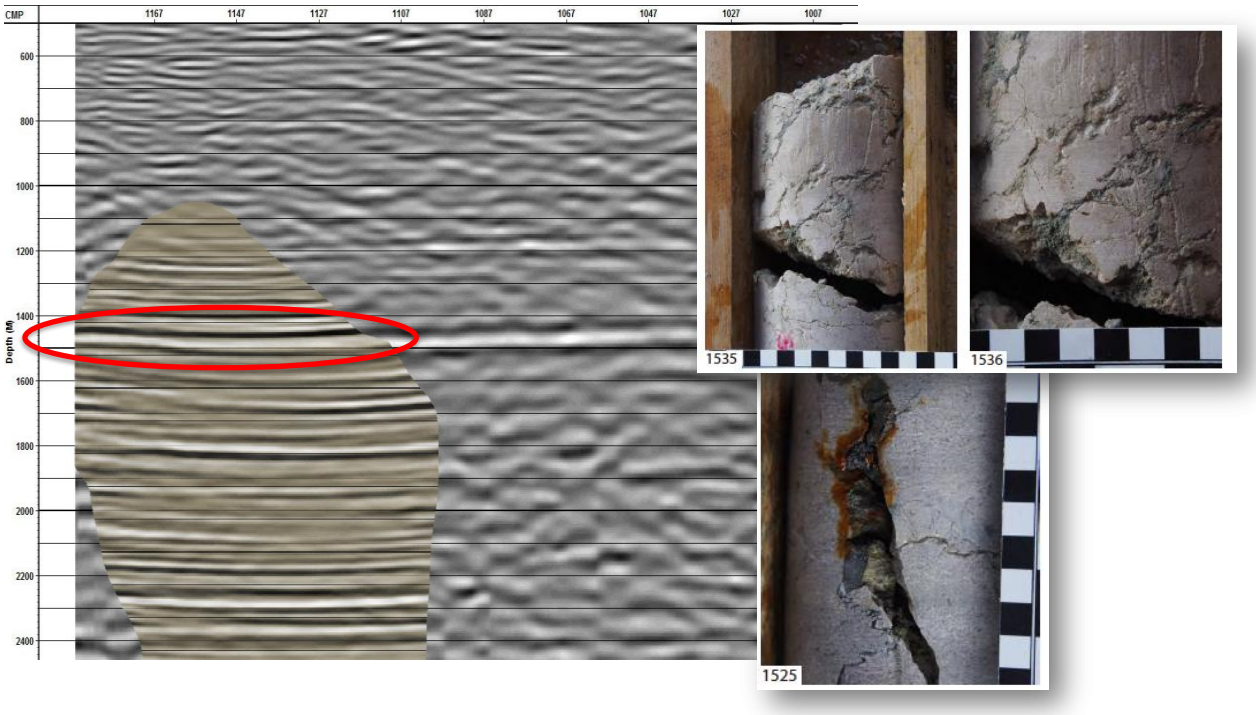

Figure 125 - Superposition of the WAB over the Thonex1 sesicmi line and correspoding fractured and karstified cores

4.4.5 Full waveform inversion

Full waveform inversion (FWI) is a powerful method to image the subsurface at sub-wavelength resolution. Compared to conventional seismic methods, FWI utilizes the full wavefield of the seismic record and, hence, the most complete representation of the subsurface is expected. The goal is to find a subsurface model that explains the measured waveform data as accurately as possible. In the elastic case, these models include for P-wave, S-wave velocity and density.

To date, FWI has not been applied in the geothermal context (Schmelzbach et al., 2016). Hence, it is important to test the potential of imaging geothermal reservoirs with FWI. Successful FWI studies have been reported for hydrocarbon exploration (e.g. Plessix and Perkins, 2010). The depth range of geothermal targets is similar to hydrocarbon reservoirs and, hence, the FWI-application for geothermal exploration can benefit from studies carried out in the oil and gas industry. In this section, the first results of FWI applied to the VSP data from Thonex are discussed.

Due to the non-linearity of the FWI problem, it is essential to start the inversion with an initial model that is close to the true model to avoid getting trapped in a local minimum. To establish the initial model, interval velocities were calculated based on the picked arrival times of the direct P-wave for the walk-above survey and VSP4. The initial model was created by combining and smoothing the different layer-based interval velocity model. The layer-based interval velocity model and the smoothed velocity model that are used as a 1D initial model for the FWI are shown in Figure 126. The initial S-wave velocity model was created from the P-wave model assuming a constant vp/vs ratio of $\sqrt{3}$ and the initial density model by applying Gardner's relation.

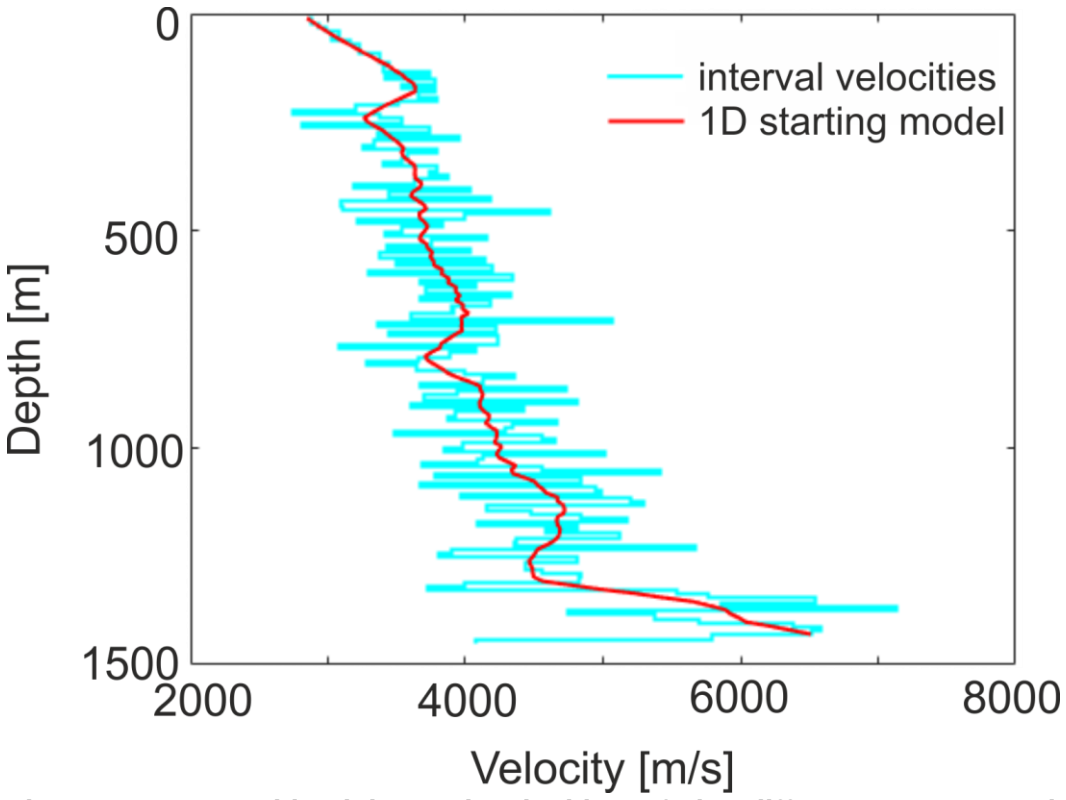

Figure 126 - Combined interval velocities of the different source positions (blue) and smoothed velocities (red) that were used as a 1D starting model for the FWI.

The first break times were re-picked since the algorithm requires the picks to be at the onset. The data before the first breaks were muted and a time-dependent amplitude damping starting at the first break times was applied to have a continuous decrease of the influence of later arrivals on the FWI results. Additionally, an exponential damping was applied after 0.6s to mute the later arriving high amplitudes and focus on the first part of the wavelet. A bandpass filter with corner frequencies of 8 and 50 Hz was applied to the dataset. The high-filter ramp was chosen such that still significant 60 Hz energy of is contained in the data. But, further testing of the appropriate frequency filter values needs to be done.

The inversion was performed in the frequency domain using single-frequency inversions with 40, 50 and 60 Hz. Considering only a few distinct frequencies rather than fitting every time sample of a seismogram during the inversion proved to be sufficient to obtain reasonable inversion results (Sirgue and Pratt, 2004).

Because source and receiver coupling may vary and if not taken into account may degrade FWI results, commonly individual source wavelets and receiver coupling functions are estimated (Maurer et al., 2012). Due to the sparse acquisition geometry of the Thonex VSP, it was not possible to invert for the receiver coupling. Only two source positions were recorded by one receiver position. More data would be required to include the receiver coupling in the inversion. Source wavelet estimation was carried out to find one single source wavelet for the entire data set, but also inversions with five different source wavelets were tested but turned out to be less stable.

During the inversion, P-wave, S-wave velocity and density were linked by using a cross-gradient coupling term to stabilize the inversion (Manukyan et al., 2016). The initial model and the inversion results for P-wave, S-wave and density after 20 iterations are show in Figure 127a-c and d-f, respectively. The RMS of the difference between the observed and modelled waveform data continuously decreased whereas the velocity model evolved with increasing iteration number. The final model resembles the initial model in terms of large-scale structures, but additional small scale structures can be observed in the final models.

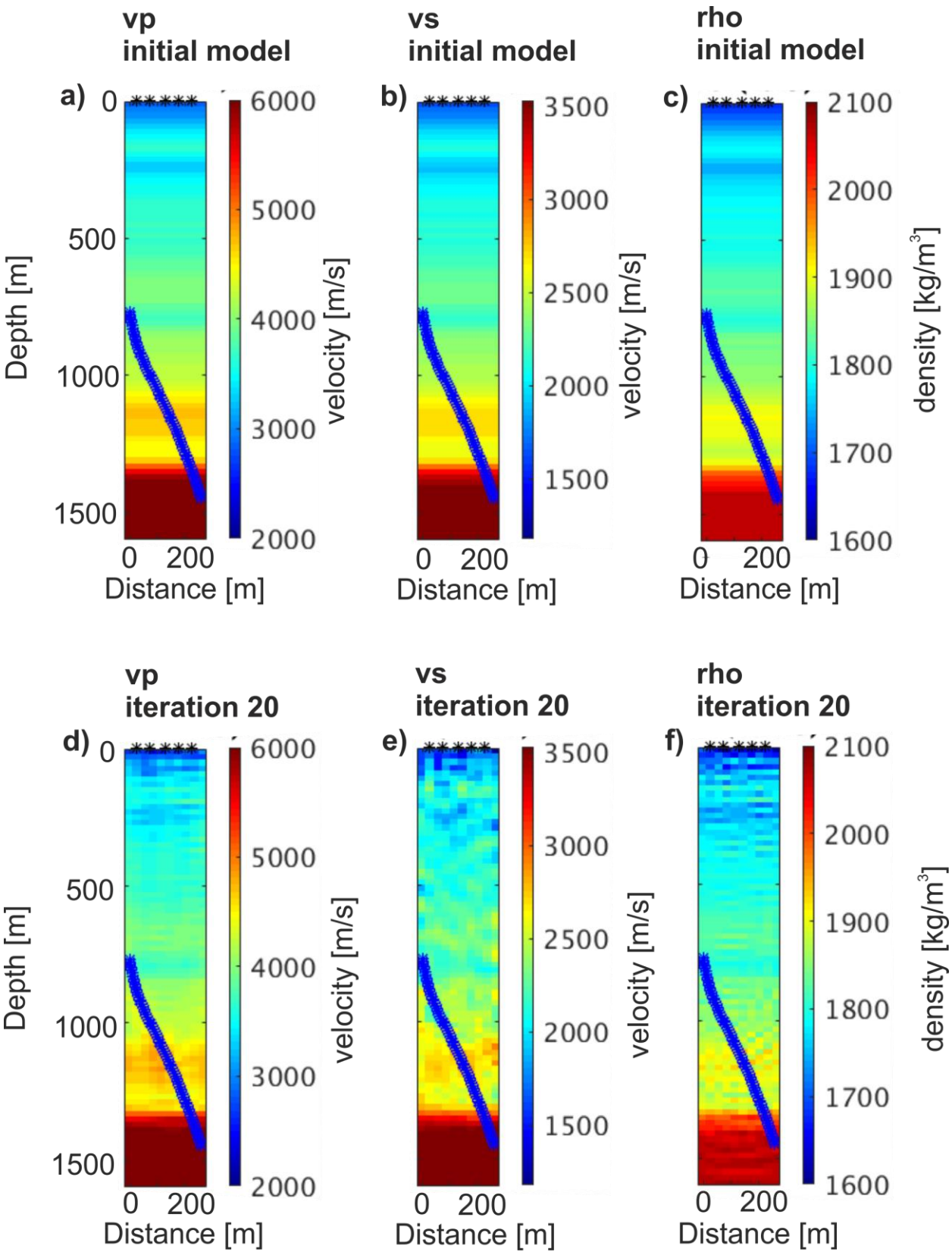

Figure 127 - (a-c) Initial models and (d-f) inversion results for P-wave, S-wave and density after 20 iterations, respectively. The velocity model evolves with the inversion and small scale structures can be observed in the final models.

To evaluate the data fit, an example of a seismogram comparison is shown in Figure 128. The seismogram of the field data (blue) is very similar to the seismogram resulting from the final inversion result (green). Also, the initial model already allows to model waveforms that are very close to the observed data, indicating that the initial model is already very accurate. Through the course of the inversion, the data fit further improves.

Additional parameter testing should be carried out to further improve the inversion results. For example, different starting models resulting from traveltime tomography of the picked first-arrival times could be tested, as well as more or different inversion frequencies or different weightings of the various cross gradient terms.

To conclude, the first FWI results of the VSP data at Thonex borehole look promising. A detailed starting model based on the interval velocities was beneficial for the successful application of FWI. Final elastic-parameter models were obtained that resolve small-scale velocity structures and result in seismograms that very closely match the actual field data.

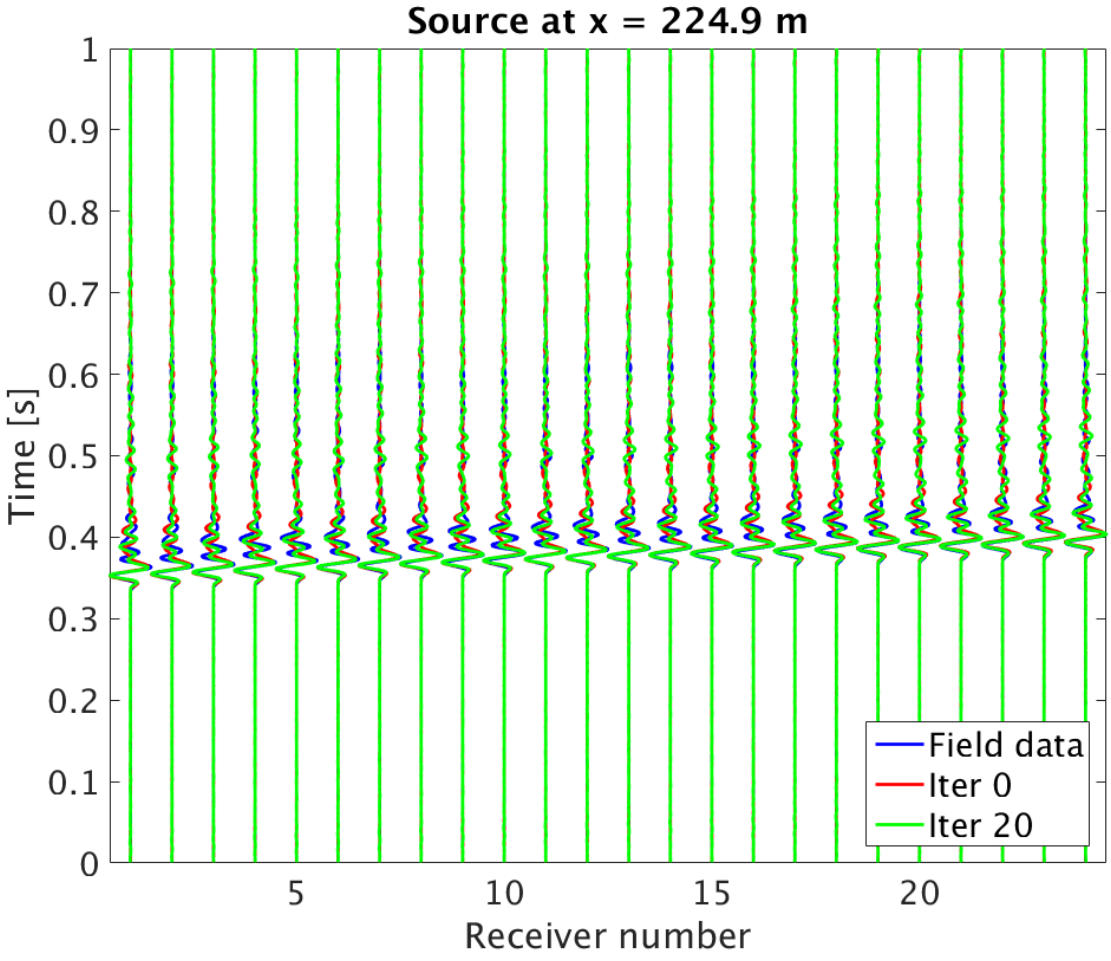

Figure 128 - Seismogram comparison of source gather WAB 101 (blue) after application of exponential damping, initial model (red) and final inversion result (green). Note that the seismogram resulting from the inversion result is very similar to the field data.

4.5 Thônex fluid geochemistry and geothermometric applications

4.5.1 Introduction

One of the main objectives of the task 7.3 of this project was to develop and validate chemical auxiliary geothermometers such as Na-Li, Mg-Li, Na-Rb, Na-Cs, K-Sr, K-F, K-Mn, K-Fe, K-W, etc., using the chemical compositions of fluids discharged from deep crystalline and sedimentary reservoirs, in order to better estimate their deep temperatures.

From the literature review carried out during this study, the Na-Li auxiliary thermometric relationships (Fouillac and Michard, 1981; Kharaka *et al.*, 1982; Kharaka and Mariner, 1989; Sanjuan *et al.*, 2014), less accurate than the classical geothermometers (Na-K, Na-K-Ca, silica, K-Mg, etc.), but often more reliable (low Li reactivity), are well known and can be very useful for geothermal exploration. For saline waters discharged from oil and geothermal sedimentary basins, only the Na-Li and Mg-Li auxiliary geothermometers were found in the literature (Kharaka *et al.*, 1982; Kharaka and Mariner, 1989). In addition to these thermometric relationships, other auxiliary geothermometers such as Na-Rb, Na-Cs, K-Sr, K-F, K-Mn, K-Fe and K-W were proposed by Michard (1990) for deep dilute thermal waters discharged from granitic reservoirs between 25 and 150°C in more than 60 European areas. In this project, three new auxiliary thermometric relationships (Na-Rb, Na-Cs and K-Sr) for brines in crystalline basement reservoirs (50-320°C) were developed using literature data, referring to 20 hot natural brines from granite and sedimentary reservoirs, mainly located in the Rhine Graben, France and Germany (70-230°C; Sanjuan *et al.*, 2016c), apart two which are at Salton Sea, USA (300-320°C; Werner, 1970; Williams and McKibben, 1989). All these results are detailed in the 7.08 and 7.03 technical reports (Sanjuan *et al.*, 2015; 2016a) and have been presented in the 2016 Goldschmidt Conference (Sanjuan *et al.*, 2016b).

It was also decided to test and validate the auxiliary thermometric relationships developed by Michard (1990) on the freshwaters discharged from the Litomerice geothermal borehole (PVGT-LT1) and the Teplice thermal spring (Pravridlo), in the Czech Republic, as well as on the freshwaters discharged from the Thônex (THX-1) and Lavey-les-Bains geothermal boreholes, in Switzerland. All these boreholes are quickly described in the 7.08 and 7.03 technical reports (Sanjuan *et al.*, 2015; 2016a). Most of the results acquired during this project, from the Litomerice area, in the Czech Republic, and the literature data from the THX-1 (Vuataz and Giroud, 2010) and Lavey-les-Bains (Sonney *et al.*, 2007) geothermal boreholes have been used for geothermometric development. The main results were presented in the 7.03 technical report (Sanjuan *et al.*, 2016a).

For the Lavey-les-Bains borehole, we selected the chemical composition estimated to be representative of the deep fluid at 105°C (Na-Cl-SO4 type; ≈ 1.9 g/l), from numerous analyses carried out between 1973 and 2007 (Sonney *et al.*, 2007). For the Thônex borehole, as we didn't know if the previously analysed fluid samples were fully representative of the bottom-hole conditions, due to the low flow-rate value measured in this borehole, and that we wanted to do additional analyses relative to the previous ones, two campaigns of fluid sampling were organized in July and October 2016 for geochemical analyses of the fluid discharged from the THX-1 borehole. The results obtained during and after these campaigns could not be integrated and exploited in the 7.03 technical report. It is mainly these results which will be exploited and used for geothermometric applications in this report.

4.5.2 Previous results obtained for the fluid discharged from THX-1

As exposed in deliverable D7.03 (Sanjuan *et al.*, 2016a), the THX-1 geothermal borehole extends down to 2 530 m vertical depth and is located in the Geneva basin. The borehole crosscuts Tertiary molasse, Cretaceous and Upper Jurassic sedimentary formations (Vuataz and Giroud, 2010). The Thônex-1 borehole was expected to be used as a geothermal borehole but its productivity remained far too low even after trials by acidification were attempted to enhance its production. The artesian flow-rate is lower than 1 m^3/h. Production tests were only carried out short time after the borehole

has been completed leading to a cumulative discharge of 1 135 m^3 in 5 days in 1993. Afterwards, tests were only performed thanks to the artesian flow-rate in 1993-1994 (discharge of less than 500 m^3) and in 1996-1997 (discharge of 2 160 m^3). New investigations have been done in 2009 showing clogging at 1840 m depth (open hole from 1970 m downwards); temperature was about 67°C, at that depth.
Several fluid samples have been collected from the THX-1 borehole between 1993 and 1997 (Vuataz and Giroud, 2010). During this period, the chemical analyses of these fluids indicated a marked influence of the injected fluids during the drilling and acidification operations (Tabl. 1). Since no representative samples were recovered from the borehole since its completion in the 90's, as relicts of drilling fluids and above all acidification fluids changed the chemical composition of the water, new borehole opening has been done in 2010. At this date, the CREGE geothermal laboratory carried out a study to better define the characteristics of the deep fluid (NaCl type; ≈ 1.3 g/l). About 780 m^3 of water were discharged in 6 months thanks to artesian flow. Chlorine content and fluid conductivity were indeed measured at the lowest values ever reached, respectively 431 mg/l and 1 954 µS/cm (Table 4).

Production test	Duration	Volume of discharged fluid (m^3)	Measurement date	Fluid conductivity (µS/cm)	Cl (mg/l)
18/09/93 - 19/09/93	2 days	340	-		
29/09/93 - 01/10/93	3 days	795	01/10/93	6260	3300
26/11/93 - 29/03/94	4 months	300 to 500	29/03/94	5670	2500
20/05/96 - 11/08/97	14 months	2158	05/11/97	2500	667
Jan. to June 2010	6 months	about 780	14/06/2010	1954	431

Table 4 : Fluid conductivity and Cl values measured during the different production tests carried out between 1993 and 2010.

The geochemical data of most of the analyses done between 1993 and 2010 (Vuataz and Giroud, 2010) are reported in Appendix 1. The interpretation of these data was also carried out by Vuataz and Giroud (2010).
This sampling phase of Thônex-1 borehole allowed Vuataz and Giroud (2010) to establish that the TDS value of the fluid is close to 1 466 mg/l with pH of 7.92. Water is likely to be infiltrated between 800 and 1 200 m in the Jura Mountains under colder climatic conditions (*c.a.* 10 000 years BP). The $\delta^{13}C$ isotope ratio shows a signature lower than that of the Upper Jurassic limestones and could be the result of CO_2 degassing and corresponding carbonate precipitation during the migration of the fluid in the borehole. The $\delta^{34}S$ of dissolved sulphates and sulphides indicate have atypical values for thermal waters. These values are attributed to the oxidation of rock sulphides at depth.

In their study, interesting information about chemical and isotopic geothermometry was also found.
A simulation of the THX-1 fluid heating from 16 to 90°C was carried out using the PHREEQC geochemical code in order to calculate the evolution of the Saturation Indices (SI) of this fluid with respect to some main minerals as a function of temperature. The fluid production areas recognized by well logging indicated a temperature value close to 70°C, but if the fluid comes from a deeper area, its temperature could be probably higher. Moreover, during its low ascent (low flow-rate measurements), the fluid temperature progressively decreases down to the underground temperature, at the surface.
The Figure 129 and Figure 130, made by Vuataz and Giroud (2010), allow illustrating the evolution of the SI values as a function of the temperature, and suggest that the temperature range, in which the maximum number of mineral phases are close to the chemical equilibrium (SI = 0) with the water, is between 60 and 80°C. Given the sampling conditions (very low fluid ascent), it was not possible to obtain a better estimation of the geochemical equilibrium conditions in the geothermal reservoir.

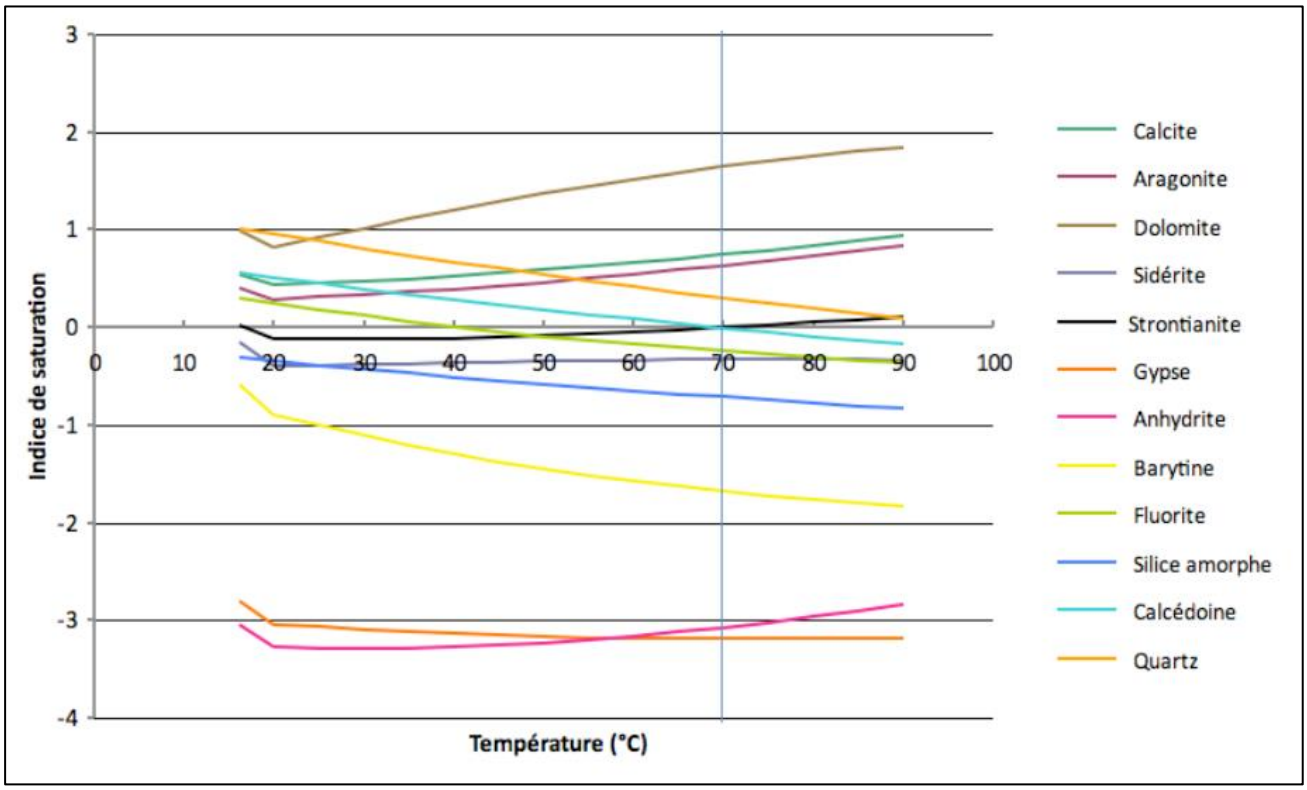

Figure 129 : Simulation of the Saturation Indices (SI) of the main minerals, except for the alumino-silicate minerals, during a progressive heating from 16 to 90°C (from Vuataz and Giroud, 2010).

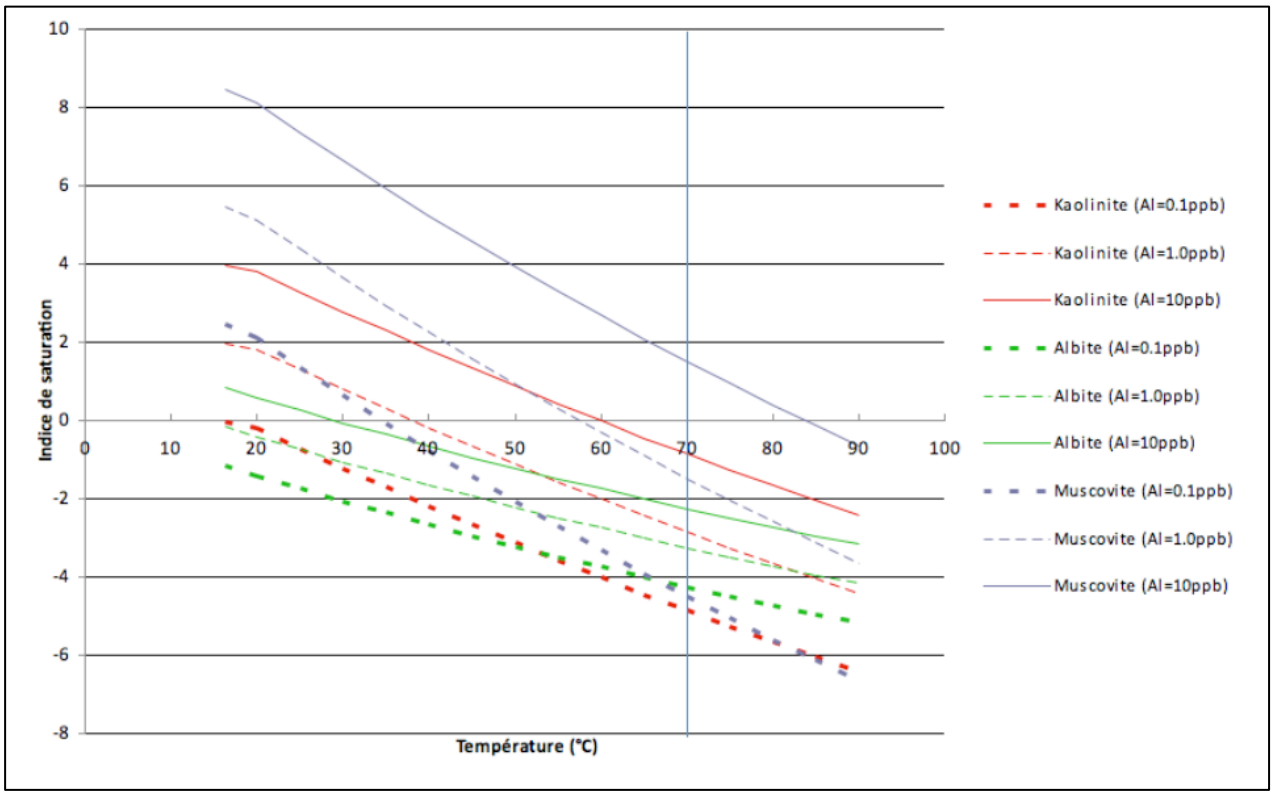

Figure 130 : Simulation of the Saturation Indices (SI) of the main alumino-silicate minerals, during a progressive heating from 16 to 90°C. In the absence of relevant data relative to the aluminium concentration, three values were considered (from Vuataz and Giroud, 2010).

Vuataz and Giroud (2010) also used classical chemical and isotopic geothermometers, such as Na-K, Na-K-Ca, K-Mg, silica (chalcedony and quartz) and $\delta^{18}O_{H2O-SO4,}$ in order to estimate the deep temperature of the THX-1 fluid. They also applied the Na-Li auxiliary geothermometer. Most of the results gave estimations of temperature ranging from 70 to 85°C, which is relatively accurate for a low-temperature geothermal system.
These results confirmed this fluid comes from a fractured system located between 2 000 and 2 500 m. No indication associated with the temperature calculations allowed envisaging a fluid ascent from a formation deeper than those crossed by the THX-1 borehole.
The Figure 130 indicates the THX-1 water is under-saturated with respect to albite and allows explaining the temperature value over-estimated (128-148°C; Vuataz and Giroud, 2010), using the Na-K geothermometer (Fournier, 1979; Giggenbach *et al.*, 1988), which is based on the chemical equilibrium between albite and K-feldspar. The $\delta^{18}O_{H2O-SO4}$ geothermometer (Lloyd, 1968; Mizutani and Rafter, 1968) gives under-estimated temperature values (37 and 26°C, respectively). In contrast, the Na/Li geothermometer gives over-estimated temperature values (129°C).

4.5.3 Fluid sampling campaigns (July and October 2016)

As exposed in the D7.03 technical report (Sanjuan et al., 2016a), in order to confirm and to be sure that the chemical and isotope composition determined in 2010 for the THX-1 geothermal water was representative of the deep reservoir (Vuataz and Giroud, 2010), it was proposed to carry out a new complete collection of samples for chemical and isotope analyses, from the THX-1 well-head, after a significant volume of discharged fluid, using the natural artesian flow-rate. This new complete collection of fluid samples (water and associated gases) was carried out by BRGM in collaboration with SIG and UNIGE on July 27, 2016, just after the borehole opening, and on October 25, 2016, after a significant discharged fluid volume. The non-condensable gases associated with the geothermal water were collected and analysed for the first time.
The THX-1 borehole has been opened on July 25, 2016. Electrical conductivity was similar to that measured in 2010 (1 974 $\mu S.cm^{-1}$ at 25°C), pH value was lower (7.27) and dissolved oxygen showed slight atmospheric contamination (3.1% sat.) that may vanish once water will naturally flow. Temperature of water at surface was 21.3°C.
The sampling itself was carried out on October 25, 2016. The borehole did not remained open during this time period of 3-months due to regulatory constraints. Water was flowing from July 25 to August 19, and between October 7 and 15. Sampling was then performed after 10 days of closure. The artesian flow-rate has not been continuously monitored but it has been regularly checked. These checks showed a rather rapid decrease of the flow-rate from 0.3 l/s at opening down to 0.12 l/s after one week of production. Volumes of discharged water are then estimated to fall in the range of 342 m^3 to 855 m^3 (Table 5); a rough estimate using a mean value of 0.2 l/s leads to a volume of about 570 m^3 (Table 5). Considering the borehole volume (≈ 147 m^3), this suggests that a minimum of two-three borehole volumes have been discharged at surface, before fluid sampling.

Dates	**25/07 -> 19/08/2016**	**19/08 -> 07/10/2016**	**07/10 -> 15/10/2016**
Number of days	25	49	8
Volume (m^3) of discharged water with a max. observed flow-rate: 0.3 l/s	648	closed well	207
Volume (m^3) of discharged water with a mean observed flow-rate: 0.2 l/s?	432	closed well	138
Volume (m^3) of discharged water with a min. observed flow-rate: 0.12 l/s	259	closed well	83

Table 5 : Estimations of fluid volume discharged from the THX-1 borehole between July 25 and October 15, during production tests (data given by SIG).

Characterisations of both the gas and liquid phases have been done and are reported in the following sections. Relative to the existing data, new isotopes (δ^7Li, δ^{11}B) were analysed. For some elements such as Cs, Rb, Ge, W, etc., few analyses were available.
Chemical major species and isotope δ^{13}C values for CO_2 and alkanes were analysed for the non-condensable gases associated with the discharged water, in the BRGM laboratories, using classical methods (Sanjuan *et al.*, 2016c).

For the water sample, the following analyses were performed:
- major species such as Na, K, Ca, Mg, Cl, SO_4, HCO_3, DOC, NO_3, SiO_2;
- trace species such as F, B, I, Br, PO_4, NH_4, Ba, Sr, Li, Cs, Rb, Ge, Fe, Mn, As, Al, W, Ni, Co, Cr, Cu, Pb and Zn;
- stable isotopes of the water (δD and δ^{18}O values);
- δ^{18}O and δ^{34}S values of the dissolved sulphates;
- δ^7Li and δ^{11}B values;
- ^{87}Sr/^{86}Sr isotope ratios.

As for the gas analyses, classical analytical methods of water geochemistry were used by the BRGM laboratories (Sanjuan *et al.*, 2016a, c). The corresponding analytical uncertainties are also given by these authors.

4.5.3.1 a) Gas sampling

Sampling was first done for collecting gas phase from the borehole. A first set of samples was collected in evacuated glass bulbs for further characterization of the dissolved gases that may be present. The glass bulb was simply connected to a flexible pipe which is evacuated to prevent from air contamination (Figure 131). The lower stopcock is then opened and the bulb partly filled with water. In case there is also a free gas phase then the sample is a mix of both phases and the phase(s) that is (are) oversaturated can be highlighted when dissolved gas concentrations are computed referring to Henry's law.

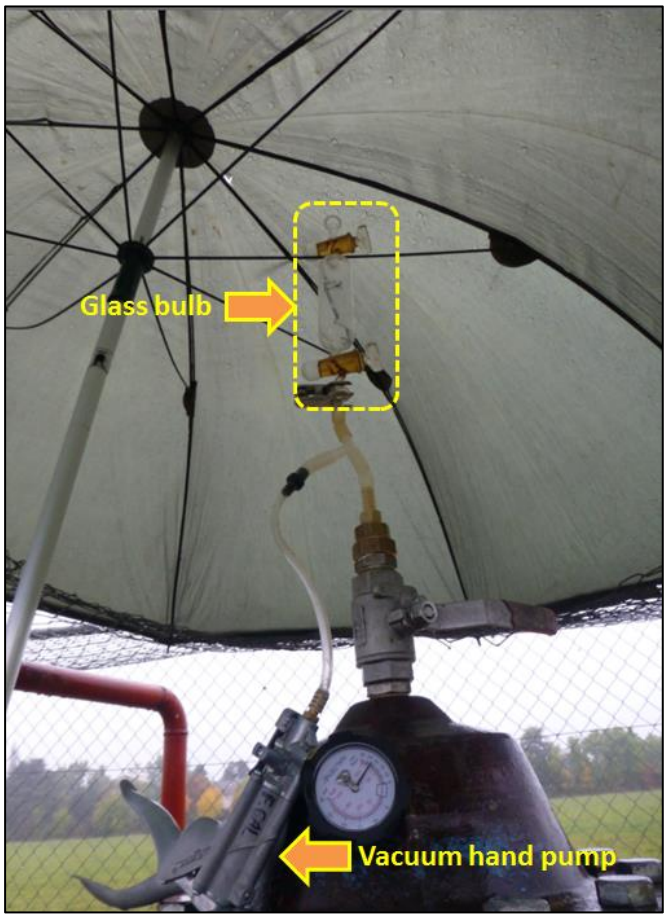

Figure 131 : View of the procedure used for sampling dissolved gases.

Once the dissolved gas phase has been sampled, a gas separator is used and plugged on the wellhead (Figure 132). Water is circulated at low flow-rate (see below) for allowing a headspace to be created at the top of the gas separator. Gas accumulates in this headspace and can be drawn to the sampling glass bulbs after a certain period of time. As the degassing of the water at surface is not occurring at high rate, sampling has been done along two procedures detailed in Figure 132. The first procedure requires the use of an infrared gas analyser (IRGA) which is plugged at the top of the gas separator. It allows a regular purge of the headspace volume to progressively withdrawn atmospheric air prior to get a sample that is more representative of the gas escaping from the water. Adjustment of the water flow-rate inside the gas separator also permits to regulate rises and falls of the water level and gives complementary control onto the degassing process and the headspace generation. The IRGA also gives relative estimates of the gas phase content during the purge of the headspace - the term “estimate” is preferred as changes in pressure as the headspace volume decreases as a result of pumping may also have impact onto the measurements. The first pumping thus indicates a gas phase rich in CH_4 (16.2% vol.) with near atmospheric CO_2 concentration and contamination by atmospheric O_2 (17% vol.). Further pumping lead to a maximum CH_4 concentration of 50% vol. with strong O_2 depletion (11% vol.).
The degassing occurred at low rate so that first sample of free gas was obtained at 9:50, a second at 10:40 and the last at 11:50. The third sample has been collected under more conventional scheme by simply connecting the glass bulb at the top of the gas separator (Figure 132). To avoid having too much air contamination, the glass bulb has been opened to allow pumping under vacuum several times prior to sampling.

Samples 1 and 3 have been managed by UNIGE, sample 2 by BRGM.

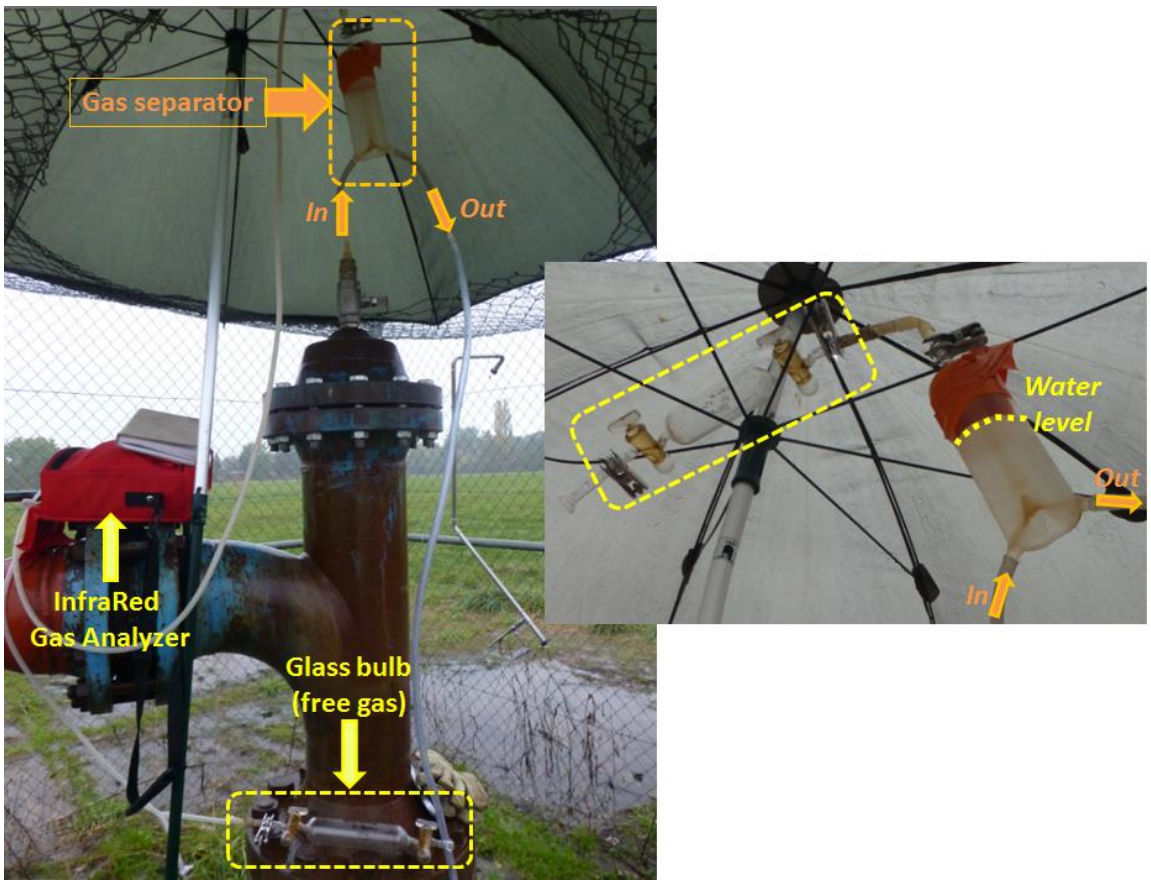

Figure 132 : View of the procedure used for sampling free gas phase. Left: with the use of an infrared gas analyser; right: classical procedure.

4.5.3.2 b) Water sampling

The sampling of the water phase has been done in between the different steps of the gas phase sampling as the contents in dissolved ions are not supposed to suffer from degassing - and for some of the samples, preservation through addition of acid induces water degassing if it has to occur.
The physico-chemical parameters are reported in Table 6. The electrical conductivity is strictly identical to that measured in June 2010 and shows only little variation to that measured in July 2016. As a consequence the fluids extracted during these surveys certainly have a common origin and comparison between them makes sense.
The fluid temperature is clearly dependent from the external temperature and the influence it has onto the temperature of the casing. The reduced flow-rate when artesian flow occurs does not allow compensating for this thermal disturbance.
A slightly more pronounced presence of dissolved oxygen is noted. It may be linked to a slight artificial oxygenation of the water due to the low flow-rate and the fact that the water flows in a pipe and then into a bucket in which the measurements are made. Nonetheless the water is in no way in contact with air during its flow to the bucket. The ORP is slightly higher than in 2010, which can be interpreted as the higher content in dissolved oxygen. In July 2016 the ORP was much lower despite dissolved oxygen concentration was intermediate between the October 2016 and the June 2010 concentrations so that the real influence of dissolved oxygen onto ORP may not be the main reason. Interaction of water in the casing may have an influence.

The pH value measured in October 2016 is slightly higher than the 2010 value. Part of the deviation (about 0.06 units) can be explained by the difference in water temperature between the two measurements. The residual deviation (0.05 unit) is similar (or even lesser) to the uncertainty on this type of measurement. Data from July 2016 is much lower but this pH value may be non-representative as a result of water evolution inside the tubing. Last, the alkalinity (expressed in HCO_3) is very similar over 6 years.

Date	Water Temperature (°C)	Electrical Conductivity ($\mu S.cm^{-1}$@25°C)	Dissolved oxygen (% sat. /ppm)	pH	ORP (redox potential; mV SHE)	Flow-rate ($L.min^{-1}$)	Alkalinity (as HCO_3; $mg.L^{-1}$)
25 October 2016 (10:30)	12.7	1929	7.3 / 0.78	8.03	+25	0.91	420
27 July 2016	21.3	1974	3.1 / -	7.27	-76	-	-
17 June 2010	16.2	1931	- / 0.12	7.92	-5.4	3.47	411

Table 6 : Physico-chemical parameters measured on site; ORP is expressed by reference to Standard Hydrogen Electrode (SHE). Alkalinity is expressed as the content in bicarbonate ion.

4.5.4 Laboratory analytical results

4.5.4.1 a) Gas analyses

4.5.4.1.1 Concentration in free gas phase

Two quantifications were done on the gas phase. The first is for the free gas phase resulting from induced degassing at surface and the second is for the gas phase that has been exsolved during fluid collection inside the evacuated glass bulb. Analyses are reported in Table 7 and in Figure 133. As may be postulated from the settings during the sampling and the limited degassing process, the "free gas" sample is contaminated by atmospheric air. The N_2/O_2 ratio of the atmosphere is 3.7, the ratio of the "free gas" sample is 4.3 whereas the ratio is 15.3 for the "dissolved gas" sample. Moreover, C4 and C5 alkanes are not monitored in the "free gas" samples and the CH_4 concentration is much higher in the "dissolved gas" sample. Therefore the sample that is more representative of gas content is the "dissolved gas" sample.

Concentration (% vol.)	Free gas phase	Gas phase of dissolved gas	Detection limit (% vol.)
CO_2	0.12	0.59	0.001
Ar	0.84	0.72	0.001
O_2	14.9	3.00	0.001
N_2	64.6	45.4	0.001
He	0.029	0.10	0.005
H_2	<0.005	<0.005	0.005
H_2S	0.018	0.055	0.005
CH_4	19.4	47.7	0.0002
C_2H_6	0.33	0.80	0.0002
C_3H_8	0.079	0.23	0.0002
Iso-C_4H_{10}	0.0086	0.046	0.0002
n-C_4H_{10}	0.010	0.054	0.0002
$\sum C_4H_{10}$	0.019	0.10	0.0004

$\sum C_5H_{12}$	<0.0002	0.012	0.0002
$\sum C_6H_{14}$	<0.0002	0.0038	0.0002
Pressure inside bulb (mbar)	1173	632	

Table 7 : Gas chromatography analyses - concentrations in free gas phase and in the gas phase created when transferring water under vacuum.

Figure 134 clearly shows that the “free gas” sample is very contaminated by atmospheric air and consequently, it is less representative than the “dissolved gas” sample. Whatever the sample, there is a residual presence of oxygen that is surprising considering the transit time at depth (more than 10 000 years; Vuataz and Giroud, 2010).

At depth, several processes may lead to O_2 consumption such as sulfur oxidation (pyrite, galena) or CH_4 oxidation but these processes also produce CO_2 through carbonates dissolution and H_2SO_4 production along the reaction pathway. The CO_2/O_2 ratio of the gas phase from Thônex-1 borehole (5:1) strongly differs from ratios of such reaction pathways (15:8, 2:1 and 2:1 respectively). Together with low CO_2 amounts, such O_2 consumption processes at depth cannot be highlighted. Referring to sulfur isotope ratios, Vuataz and Giroud (2010) however mention that sulfur oxidation may be active somewhere along the flow path. They also mention a possible decrease of CO_2 concentrations as a result of CO_2 degassing and subsequent carbonate precipitation occurring inside the borehole, especially when the fluid cools during its rise to the surface.

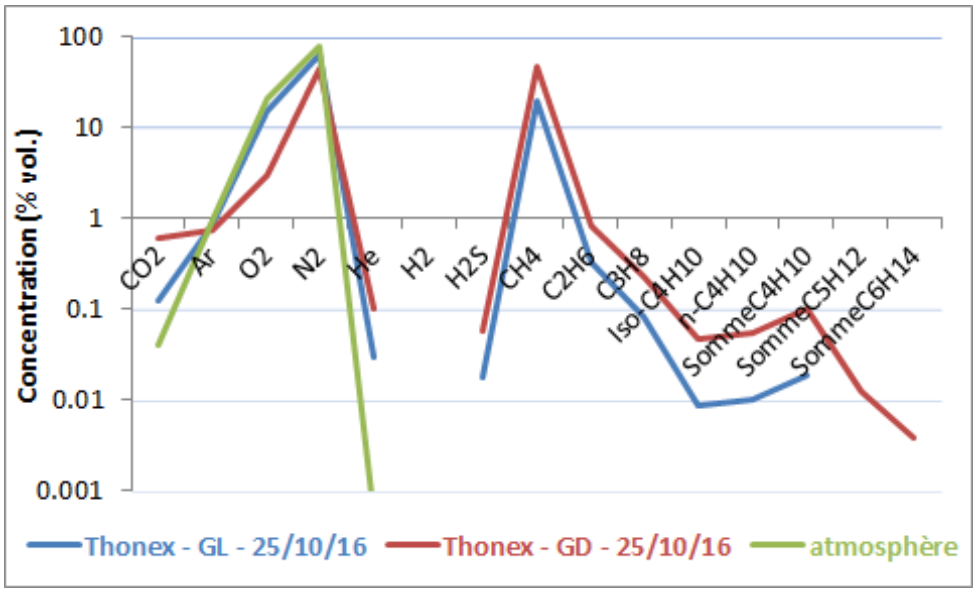

Figure 133 : Distribution of gas phases; data for the air reference are taken from http://encyclopedia.airliquide.com.

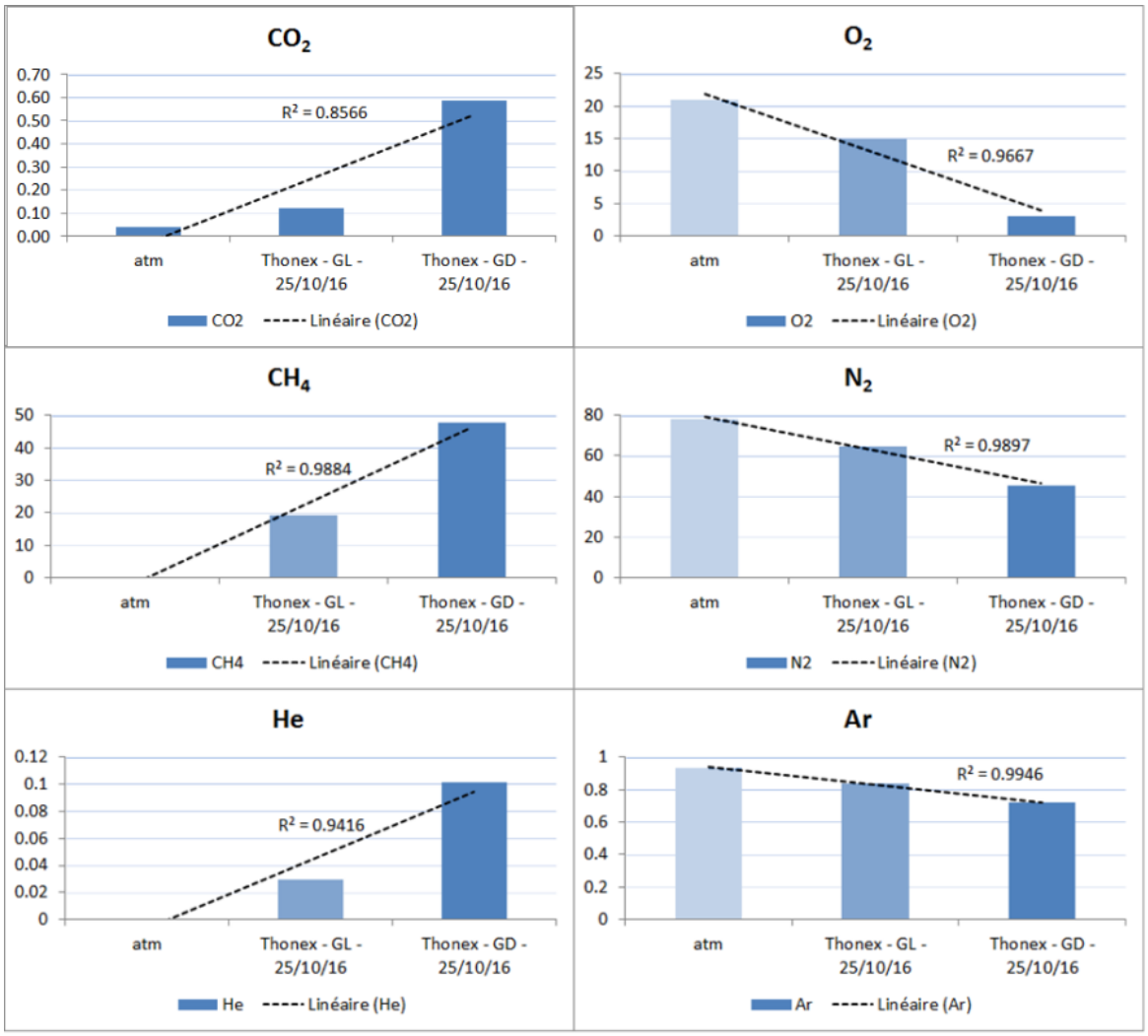

Figure 134 : Gas concentrations as a function of the sampling procedure.

Multiple reactions may then have occurred during water flow at depth or during water circulation inside the borehole and may alter the abundance ratios of one gas phase to the other. Deciphering in between the mechanisms that have led to the presence of traces of O_2 and low CO_2 amounts in the gas phase seems not to be easy.

If this residual presence of O_2 is considered to be the result of a sampling bias or of secondary processes inside the borehole, then this contamination has to be corrected to better evaluate the nature of the gas phase at depth. This is done in Table 8 by estimating that the “free gas” sample would be contaminated by 71.1% of atmospheric air (= 14.9% O_2 / 20.95% O_2) and that the “dissolved gas” sample would be only contaminated by 14.3% (3.0/20.95), using the O_2 contents (we assume that the O_2 content in the non-condensable gases associated with the deep geothermal water is close to zero).

Concentration (% vol.)	Free gas phase (corrected)	Gas phase of dissolved gas (corrected)	Atmospheric air
CO_2	0.32	0.68	0.039
Ar	0.62	0.68	0.934
O_2	0	0	20.95

N_2	31.4	39.9	78.08
He	0.10	0.12	0.000524
H_2	-	-	0.00005
H_2S	0.062	0.064	
CH_4	67.1	55.7	0.00017
C_2H_6	1.14	0.93	
C_3H_8	0.27	0.27	
$\sum C_4H_{10}$	0.07	0.12	
$\sum C_5H_{12}$	-	0.014	
$\sum C_6H_{14}$	-	0.0044	

Table 8 : Gas concentrations corrected from air contamination

We can note that the chemical composition of both samples indicates similar trend, after air contamination correction. However, if the presence of N_2 remains still significant, the N_2 content is higher for the "dissolved gas" sample (≈ 40% against ≈ 31% for the "free gas" sample) whereas the CH_4 content is higher for the "free gas sample" (≈ 67% against ≈ 56% for the "dissolved gas" sample). In both cases, methane (56-67%) and then nitrogen (31-40%) are the predominant gases. The CO_2 content varies from 0.32 ("free gas" sample) to 0.68% ("dissolved gas" sample). In contrast, the contents of the other gases are very close.

Relative proportion of alkanes expressed as the $\frac{C_1}{(c_2+c_3)}$ ratio shows a good homogeneity between the "free gas" sample and the "dissolved gas" sample. That points out a similar origin of the gas phase despite the contamination during the sampling of the "free gas" phase.

The gas phase from Thônex-1 borehole can be classified as a wet gas (or condensate) following petroleum charts ($\frac{C_1}{(c_2+c_3)} < 50$). Such gas phases are generally stemming from maturation in petroleum reservoirs (e.g. Wilen well; Etiope *et al.*, 2010). Similar gas phases are also found in the French Alps close to the Chartreuse Massif near Grenoble (Fontaine ardente de Rochasson; Figure 135) - dryer gas emissions (Fontaine ardente du Gua) are also reported on this figure.

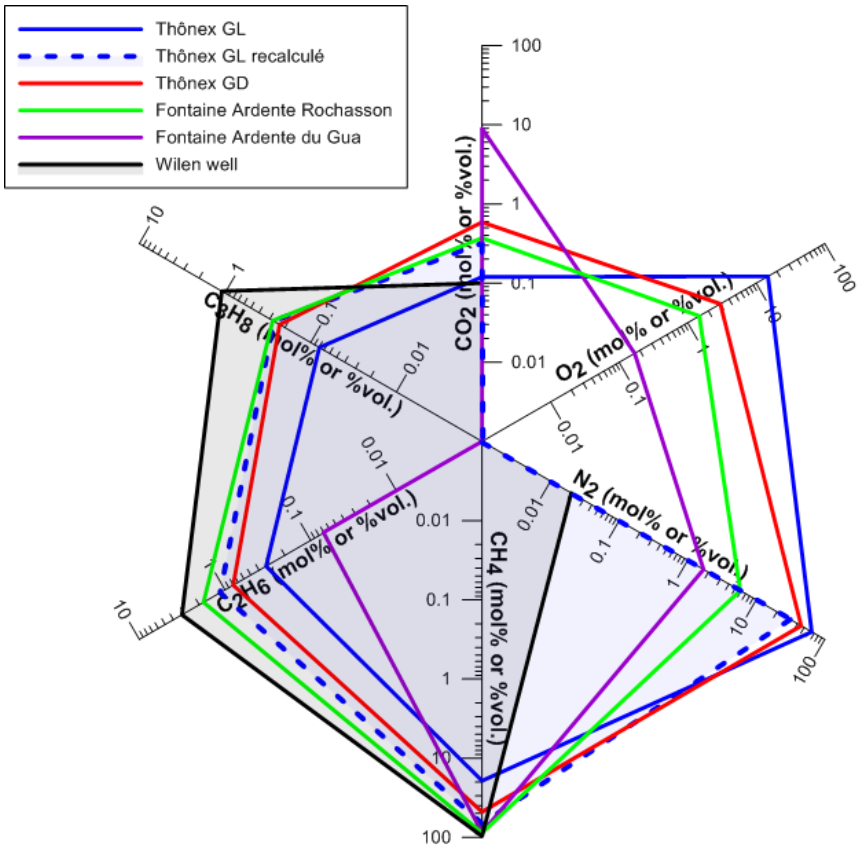

Figure 135 : Gas from THX-1 borehole (raw data and data corrected from O2 contribution). Data from the French Alps (Fontaine ardente de Rochasson - Chartreuse Massif; Fontaine ardente du Gua - Vercors Massif) are from Kloppmann et al. (2016); data from Wilen well are from Etiope et al. (2010).

4.5.4.1.2 Dissolved gas concentrations

The concentrations in dissolved gases are expressed in mol/l by reference to Henry's law (Table 9). There is no correction applied for water salinity (THX-1 borehole has low salinity) and the values are calculated at room temperature, at surface temperature and at expected temperature at depth. This last calculation has to be considered with caution as the effect of pressure is not taken into account. The presence of N_2 and CH_4 in the gas phase is well illustrated; these two species are the only ones that are present at concentrations higher than the maximum solubility of gas in water. The other gas species remain at low concentration levels but these levels are higher than the concentrations the water may have at equilibrium with the atmospheric air component. That suggests that the presence of residual O_2 is likely to be a consequence of sampling bias: there is no sufficient time for the water to interact with the atmosphere and re-equilibrate under atmospheric gas concentrations (and therefore loss gas).

The total dissolved alkane content was estimated at 236 mg/l, using the chemical composition given at 12.7°C in Table 9, with a CH_4 predominance (224 mg/l, or 95% of its contribution).

	mol.L^{-1} @24°C	mol.L^{-1} @12.7°C	mol.L^{-1} @70°C	Max. solubility	mol.L^{-1} at air saturation	mol.L^{-1} at

				@25°C	@12.7°C	air saturation @24°C
CO_2	$2.9x10^{-4}$	$3.5x10^{-4}$	$1.9x10^{-4}$	$3.41x10^{-2}$	$1.88x10^{-5}$	$1.32x10^{-5}$
Ar	$2.1x10^{-4}$	$2.2x10^{-4}$	$1.7x10^{-4}$	$1.38x10^{-3}$	$1.62x10^{-5}$	$1.29x10^{-5}$
O_2	$8.4x10^{-4}$	$8.8x10^{-4}$	$7.2x10^{-4}$	$1.25x10^{-3}$	$3.32x10^{-4}$	$2.64x10^{-4}$
N_2	$1.3x10^{-2}$	$1.3x10^{-2}$	$1.1x10^{-2}$	$6.07x10^{-4}$	$6.17x10^{-4}$	$5.02x10^{-4}$
He	$2.7x10^{-5}$	$2.8x10^{-5}$	$2.4x10^{-5}$	$3.75x10^{-4}$	$2.04x10^{-9}$	$1.97x10^{-9}$
H_2S	$5.5x10^{-5}$	$7.0x10^{-5}$	$3.0x10^{-5}$			
CH_4	$1.3x10^{-2}$	$1.4x10^{-2}$	$1.1x10^{-2}$	$1.25x10^{-3}$	$3.18x10^{-9}$	$2.50x10^{-9}$
C_2H_6	$2.3x10^{-4}$	$2.4x10^{-4}$	$1.9x10^{-4}$			
C_3H_8	$6.2x10^{-5}$	$6.5x10^{-5}$	$5.4x10^{-5}$			
$\sum C_4H_{10}$	$2.7x10^{-5}$	$2.8x10^{-5}$	$2.3x10^{-5}$			
$\sum C_5H_{12}$	$3.3x10^{-6}$	$3.4x10^{-6}$	$2.8x10^{-6}$			
$\sum C_6H_{14}$	$1.0x10^{-6}$	$1.1x10^{-6}$	$8.9x10^{-7}$			

Table 9 : Concentrations in dissolved elements (mol/l) calculated for different temperatures.

4.5.4.1.3 Isotopes

The origin of the gas phase has been searched for using stable isotopes of the carbon and of the hydrogen in CO_2 and in alkanes phases (Table 10[1]).

Isotope ratio	Free gas phase	Gas phase of dissolved gas	Uncertainty
$\delta^{13}C_{CO2}$ (‰ VPDB)	-13.0	-14.6	±0.1
$\delta^{13}C_{CH4}$ (‰ VPDB)	-44.8	-50.9	±0.5
δD_{CH4} (‰ VSMOW)	-157	-155	±5
$\delta^{13}C_{C2H6}$ (‰ VPDB)	-28.9	-31.3	±0.5
$\delta^{13}C_{C3H8}$ (‰ VPDB)	-27.0	-29.0	±0.5
$\delta^{13}C_{C4H10}$ (‰ VPDB)	-24.7	-27.0	±1

Table 10 : Stable isotope ratios of CO2 and alkanes.

If we take into account the atmospheric air contamination for the “free gas” and “dissolved gas” samples, and a $\delta^{13}C_{CO2}$ value ≈ -7.5‰ for atmospheric air (Pedroni *et al.*, 1999), we can recalculate the two $\delta^{13}C_{CO2}$ values reported in Table 10. A concordant $\delta^{13}C_{CO2}$ value of -14.7 ± 0.3‰ was found for both samples. This concordance is in very good agreement with an atmospheric air contamination of both samples (71.1% and 14.3% for the “free gas” and the “dissolved gas” samples, respectively). The $\frac{C_1}{(c_2+c_3)}$ vs $\delta^{13}C_{CH4}$ diagram (Figure 136) and the $\delta^{13}C_{CH4}$ vs. δD_{CH4} diagram (Figure 137) both suggest a thermogenic origin for the gas phase. The $\delta^{13}C_{CH4}$ vs. $\delta^{13}C_{C2H6}$ diagram (Figure 138) suggests that additional processes may affect the isotopic equilibrium - molecular fractionation may occur during gas transport. Differences in the solubility properties and adsorption properties may also play a role (Etiope *et al.*, 2009). As CO_2 may have been affected by secondary processes inside the borehole, its origin remains not well defined (Figure 139), but is probably a mixed origin, with a marked organic CO_2 end-member (decarbonatisation reactions, organic sediments with $\delta^{13}C_{CO2}$ values ≤ -20‰; Pedroni *et al.*, 1999).

[1] For the alkanes, deviations between the carbon isotope ratios measured on “free gas” and “dissolved gas” samples may be partly linked to the time limit (9 weeks) between the analysis and the sampling (interaction of water + gas mixture for the “dissolved gas” samples – no interaction for the other sample). The hydrogen ratios, measured 2 weeks after sample collection, are indeed not affected by this bias and point out to an identical ratio. Carbon isotope ratios measured on the “free gas” sample are then preferably used.

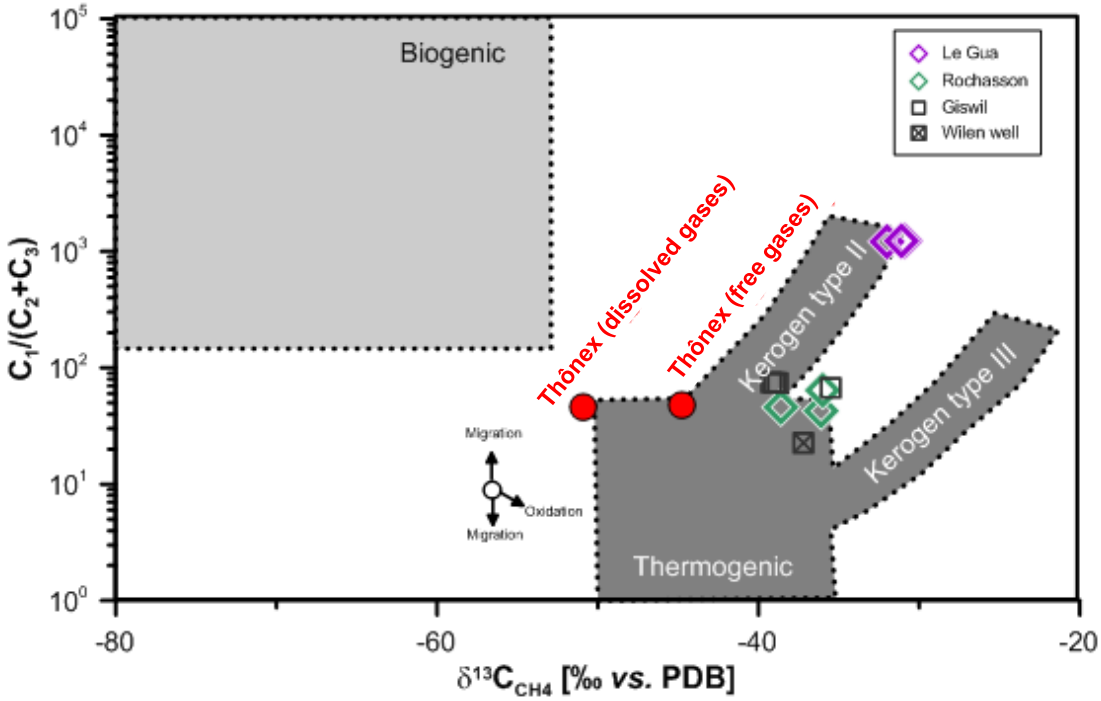

Figure 136 : Bernard diagram; data from Etiope et al. (2010) and Kloppmann et al. (2016) are reported.

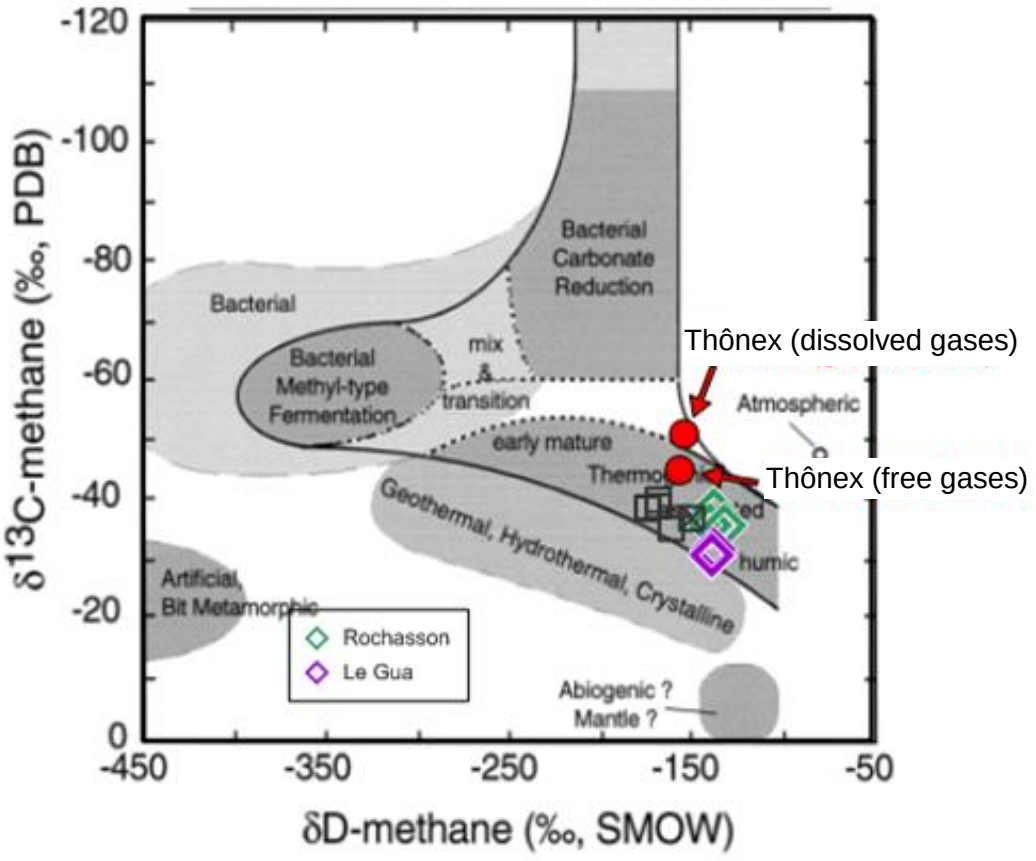

Figure 137 : δ13CCH4 vs. δDCH4 plot.

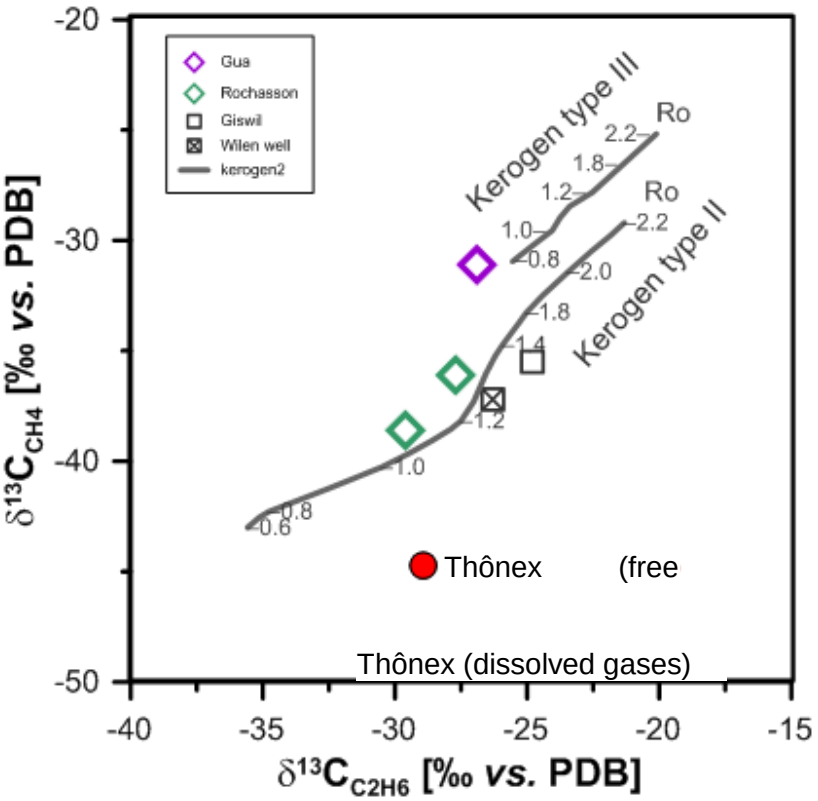

Figure 138 : δ13CCH4 vs. δ13CC2H6 plot.

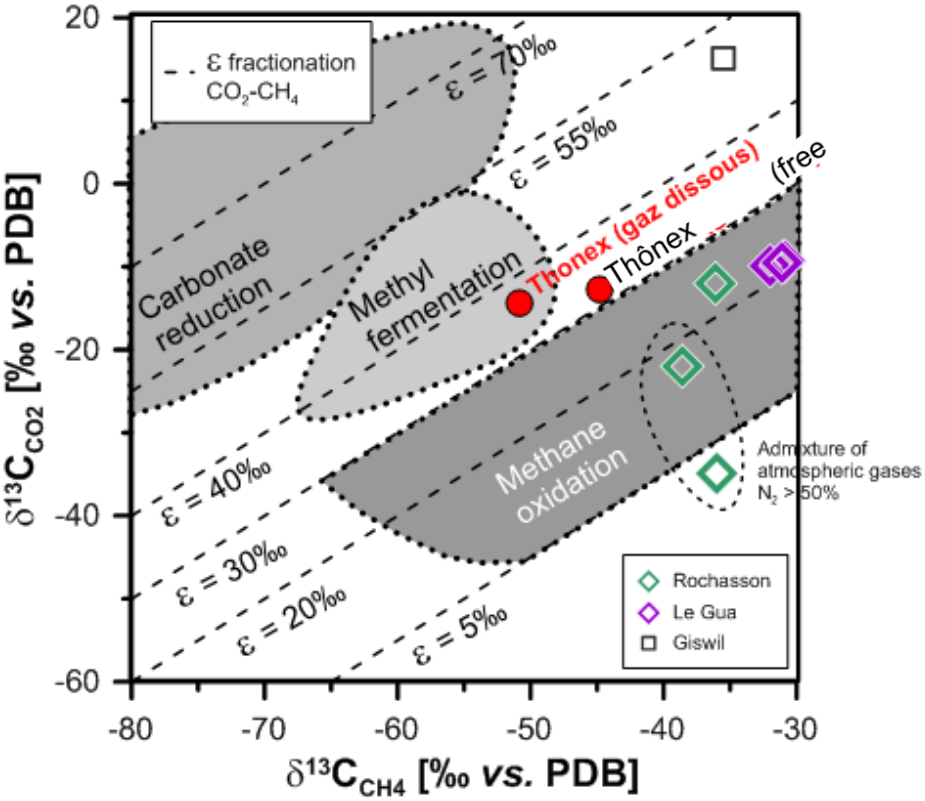

Figure 139 : δ13CCO2 vs. δ13CCH4 diagram.

4.5.4.2 b) Water analyses

4.5.4.2.1 Dissolved elements

The chemical analyses performed on the water are reported in Table 11 for the major species and in Table 12 for the trace species.

Date	pH	Na	K	Ca	Mg	Cl	HCO_3	SO_4	NO_3	SiO_2	TDS
25/07/2016	7.27	250	9.5	89.9	27.7	388	425	34.0	< LQ	69.4	1306
25/10/2016	8.03	277	8.6	58.1	24.2	390	420	22.7	< LQ	46.3	1263
17/06/2010	7.92	304	8.6	52.1	24.1	440	411	11.2	0	47.5	1356
Limit of Quantification		0.5	0.5	0.5	0.5	0.5	10	0.5	0.5	0.5	

Table 11 : Concentrations of dissolved major species (mg/l) . Ionic mass balance values are -2%, -3% and -4%, respectively (2010 data from Vuataz and Giroud, 2010).

Date	F	Br	B	I	PO_4	NH_4	Sr	Ba	Mn	Li	Rb	Cs
25/07/2016	6200	1659	1195	656	< LQ	1470	5892	144	262	667	16.5	0.64
25/10/2016	6200	1861	1312	365	< LQ	1730	5357	128	85.5	702	19.1	0.89
17/06/2010	5320	2260		44200	-	4260	4940	83	110	716	18.0	1.5
Limit of Quantification	100	1	0.5	1	50	50	0.1	0.05	0.1	0.1	0.1	0.5

Date	Fe	Al	As	Ge	Zn	Cu	Ni	Co	Cr	Pb	W
25/07/2016	0.143	0.52	0.05	9.16	< LQ	< LQ	0.12	< LQ	0.19	< LQ	4.29
25/10/2016	2.814	2.03	0.09	0.57	1.15	< LQ	< LQ	< LQ	< LQ	< LQ	3.09
17/06/2010	0.0887	< 1	0.33	-	< 1	-	-	-	-	< 0.02	1.2
Limit of Quantification	20	0.5	0.05	0.5	0.5	0.1	0.1	0.05	0.1	0.05	0.05

Table 12 : Concentrations of dissolved trace species (µg/l).

The water sampled at borehole opening (25 July 2016) has a chemical composition in major elements slightly different from that which has been determined when the borehole was left in natural flow for several weeks (sample from 25 October 2016).
On opening, the pH water (7.27) is higher than in June 2010 and in October 2016 (similar pH values close to 8.0). The water is enriched in Ca-Mg and SO_4, and the enrichment decreases when the water column is renewed (Figure 140). The large difference in Ca and SO_4 concentrations between the two 2016 samples raises questions about the origin of this mineralization, the Ca-SO_4 phases being still at under-saturated state (Table 13) and far from the equilibrium line (Figure 141). The presence of Ca and SO_4 at the beginning of purge could indicate either an evolution of the fluid in the borehole when the borehole is not flowing (?) or the presence of secondary supply (?). In any case, it seems that the fluid sampled at the opening has undergone a different evolution (partial CO_2 pressure ten times higher than for the samples obtained after water production from borehole).

The water sampled in October after artesian flow is enriched in Na, when compared with the fluid collected at borehole opening, which is at Na-Cl stoichiometric equilibrium, but the Cl concentration remains nearly constant (Figure 141). Since a part of Cl was attributed to residues of HCl which was massively injected during the production tests (Vuataz and Giroud, 2010), its parasitic effect on the water chemistry seems to be more and more reduced, if we consider the Cl concentration of the fluid sample collected in June 2010 (Figure 140 and Figure 141).

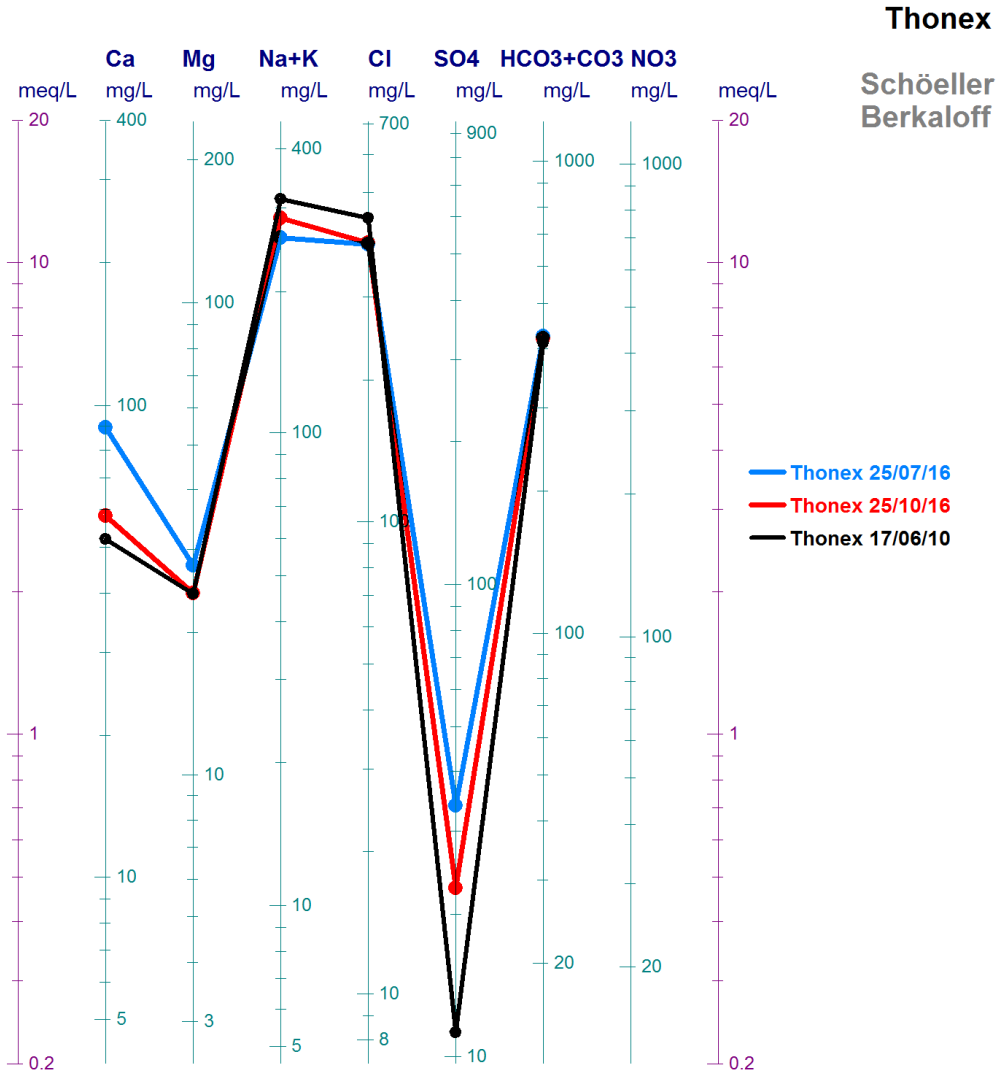

Figure 140 : Schöeller diagram

Date	calcite	aragonite	dolomite	gypsum	anhydrite	P_{CO2} (atm) eq.
25/07/2016	0.05	-0.09	-0.05	-1.92	-2.14	0.04022
25/10/2016	0.69	0.54	1.18	-2.29	-2.54	0.00312
17/06/2010	0.55	0.40	1.00	-2.80	-3.05	0.00412

Table 13 : Saturation Index (SI) calculated at surface temperature and pressure.

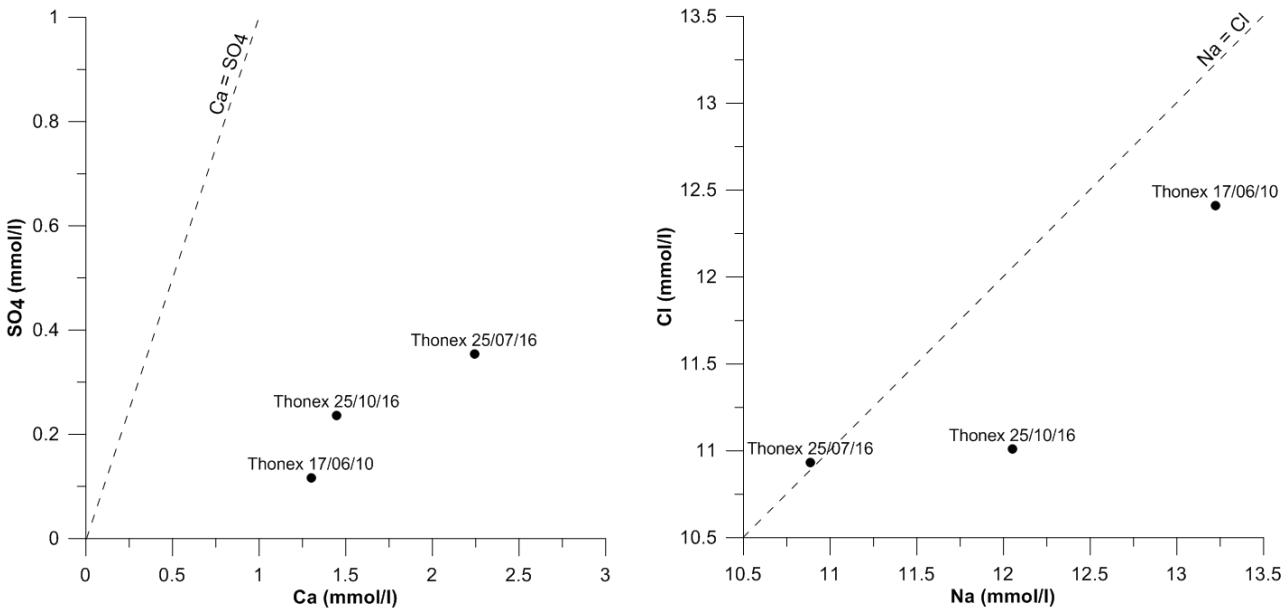

Figure 141 : Ca-SO4 and Na-Cl binary plots.

If we consider the previous analyses done on the THX-1 fluid (see Appendix 1; Vuataz and Giroud, 2010), we can observe that the chemical composition of this fluid relative to the major species (Figure 142) and most of the trace elements (Figure 143) tends to be relatively stable, since 2010. Strong discrepancies exist still for Mn, Fe (Figure 143), and some trace metals.

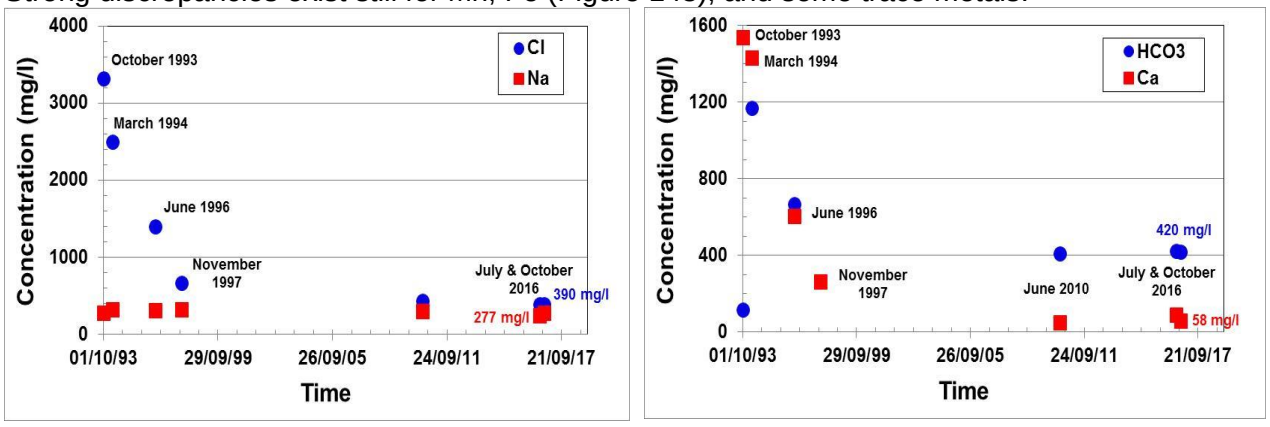

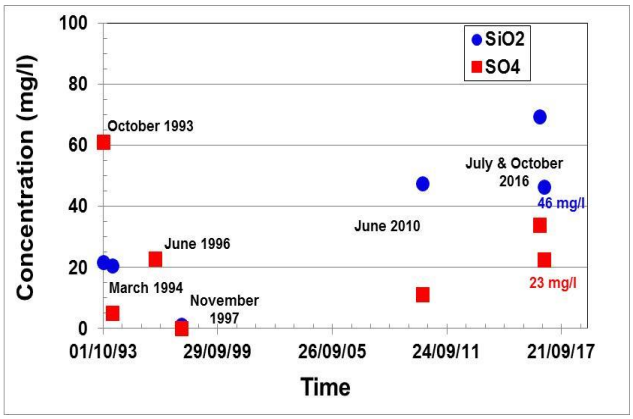

Figure 142 : Concentrations of major species (Na, Cl, Ca, HCO3, SO4, and SiO2) analysed in the THX-1 fluid as a function of time.

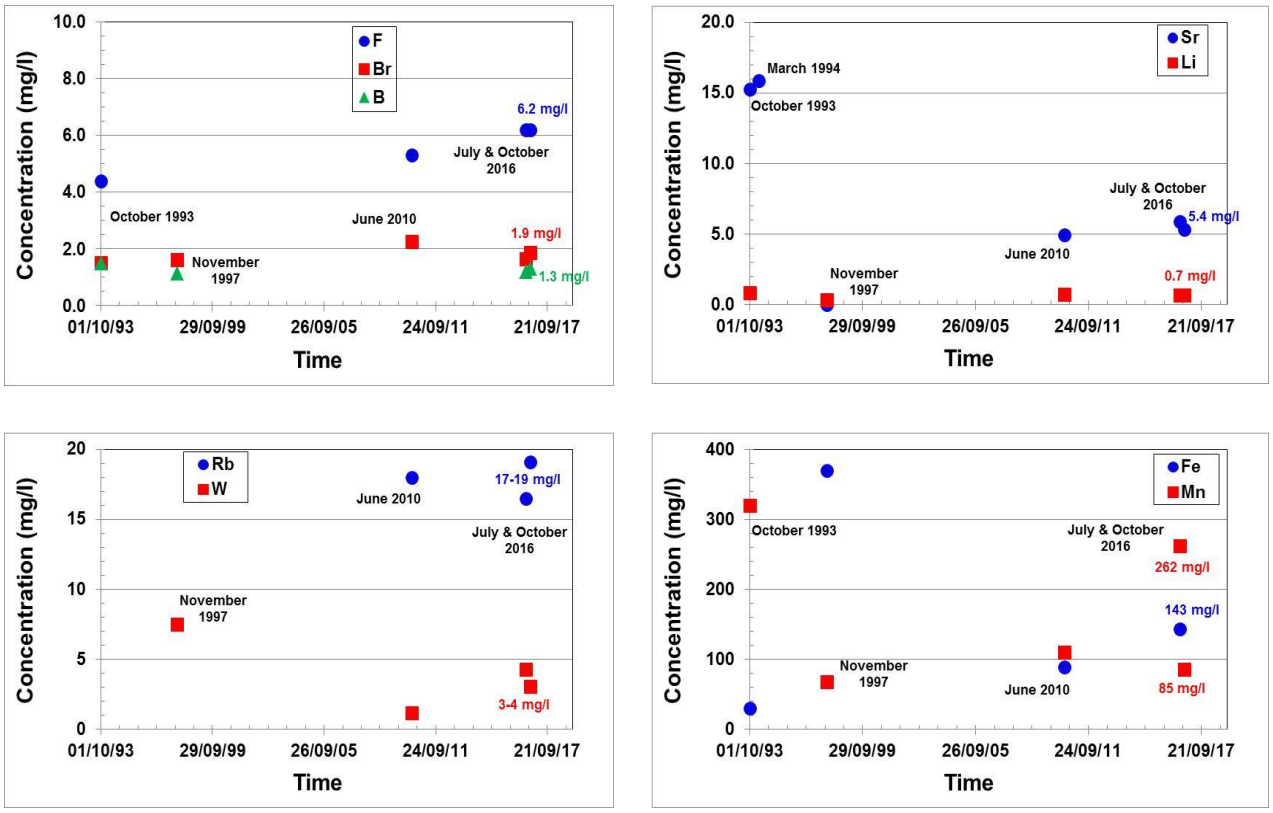

Figure 143 : Concentrations of major species (Na, Cl, Ca, HCO3, SO4, and SiO2) analysed in the THX-1 fluid as a function of time.

In the Cl-SO_4-HCO_3 triangular diagram (Figure 144), proposed by Giggenbach (1988), we can see that Cl and HCO_3 are the predominant anions in the last fluid samples collected in 2010 and 2016. As Na is the predominant cation, we can consider that the Na-Cl-HCO_3 fluid analyzed in October 2016, with a TDS value of about 1.3 g/l, is the most representative of the deep geothermal water discharged from the THX-1 borehole. The Na-Cl-HCO_3 facies of this water is the same one than that of the fluid discharged from the Litomerice PVGT-LT1 (Figure 144; Appendix 1).

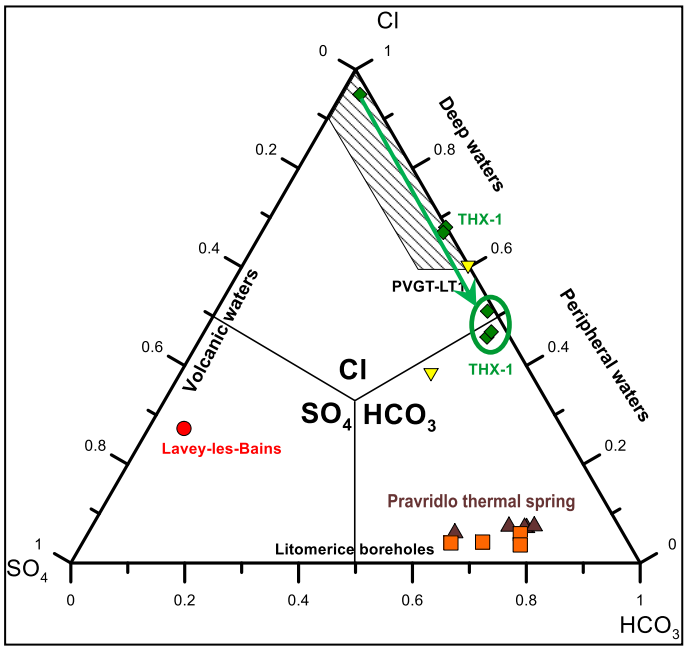

Figure 144 : Triangular diagram proposed by Giggenbach (1988) for the thermal waters from Czech Republic and Switzerland studied during this project, especially for the fluids discharged from the PVGT-LT1 and THX-1 boreholes, analysed in this study.

4.5.4.2.2 Isotopes

The different isotope values measured on water samples are reported in Table 14.

Date	δD (‰ SMOW)	$\delta^{18}O$ (‰ SMOW)	$\delta^{13}C_{TDIC}$ (‰ PDB)	$\delta^{34}S_{SO4}$ (‰ CDT)	$\delta^{18}O_{SO4}$ (‰ SMOW)	$\delta^{11}B$ (‰)	$\delta^{7}Li$ (‰)	$^{87}Sr/^{86}Sr$
25/07/2016	-82.2	-11.0	-	-	-	-	9.6	0.707639
25/10/2016	-81.7	-10.9	1.1	46.2	12.1	13.72	9.3	0.707646
17/06/2010	-81.0	-10.6	-2.3	87.5	17.6	-	-	0.707675

Table 14 : Isotope values measured on water samples.

The values measured on the water isotopes O and H (Table 14) are almost identical between the beginning and the end of the purge cycle and are very close to the values measured in 2010 and in 1993 (see Appendix 1; Vuataz and Giroud, 2010). It therefore appears that the waters sampled at surface have δD and $\delta^{18}O$ values close to those of the reservoir at 2 500 m depth.

These values don't fit the Global Meteoric Water Line (Figure 145), but seems to be in good agreement with a Local Meteoric Water Line, which could be similar as that proposed by Longinelli *et al.* (2008) for northern Italy rain waters, and integrated by Giustini *et al.* (2016), in their study relative to the mapping of oxygen stable isotopes of precipitation in Italy. We can also note that other precipitation waters from local or regional IAEA stations, located in France (Thonon-les-Bains) and in Germany (Regensburg, Stuttgart, Trier), have mean values of δD and $\delta^{18}O$ which fit this LMWL (IAEA, 1992). The Litomerice PVGT-LT1 water (Appendix 1) is also close to this LMWL (Figure 145).

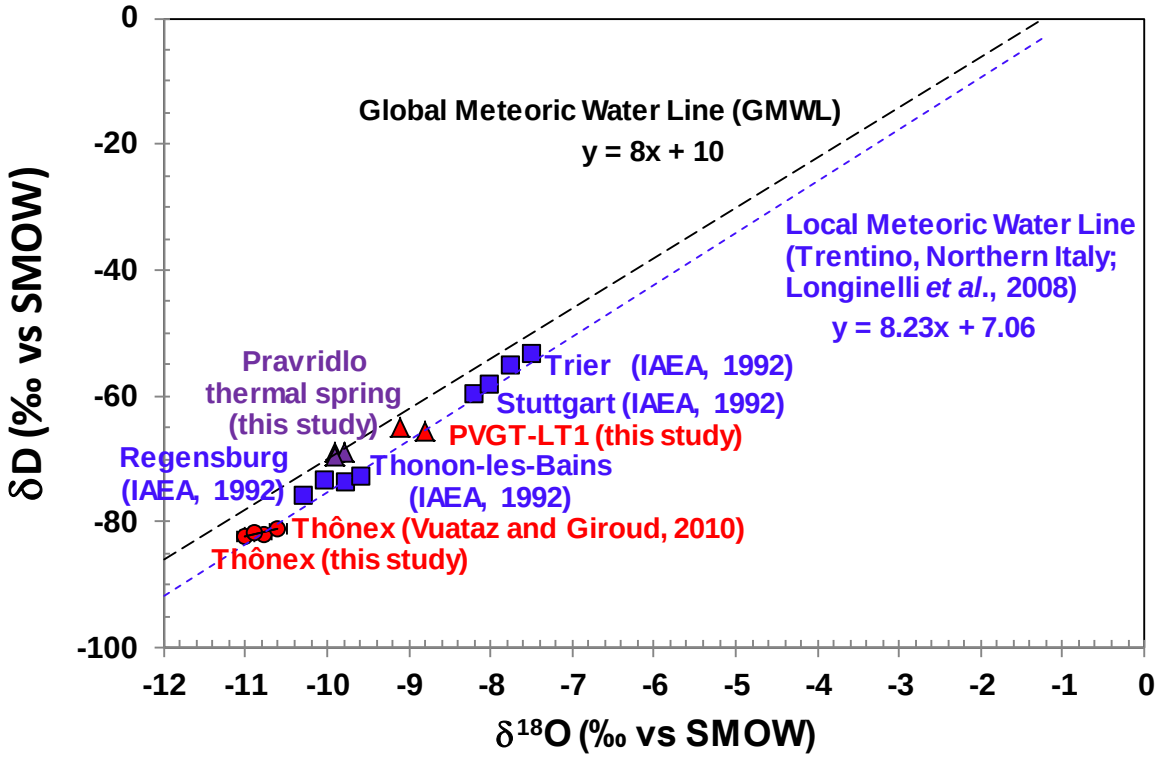

Figure 145 : δ18O-δD binary plot for the geothermal waters discharged from the THX-1 borehole and for local or regional rain waters. World Meteoric Water Line is indicated for reference (Craig, 1961).

The $\delta^{13}C$ value of the Total Dissolved Inorganic Carbon differs between 2010 and 2016 (Table 14). In 2016, this value is slightly positive (+1.1‰) whereas it was negative in 2010 (-2.3‰). Vuataz and Giroud (2010) report a value at -0.2‰ on a rock sample taken at a depth of more than 2 000 m and a value at +0.43‰ on the fluid in 1993 (see Appendix 1). It is possible that the variability of the carbon isotope ratio of the CITD is also related to isotopic exchange with the carbon of CH_4 in addition to the calcite precipitation mechanisms as evoked by Vuataz and Giroud (2010).

The $\delta^{34}S$ value of dissolved sulphate measured in 2016 (+46‰) also differs from the 2010 data (+87‰; Table 14) and is intermediate between this 2010 measure and the measure reported in 1993 (+22‰; see Appendix 1). As reported by Vuataz and Giroud (2010), an origin of sulphates linked to evaporite dissolution is difficult to conceive as confirmed by recent studies in eastern Switzerland (Strauss *et al.*, 2016) and on evaporites (Mazurek *et al.*, 2012). However, high values are reported by Fouillac *et al.* (1990) in the Dogger of the Paris basin (+48‰), these high values being measured in waters having high sulphide contents and being interpreted as the result of a Rayleigh distillation process. The waters of Thônex are not yet known for their richness in sulphides (Vuataz and Giroud, 2010).

The $\delta^{18}O$ value of dissolved sulphate measured in 2016 (+12.1‰) is also different from that determined in 2010 (+17.1‰; Table 14), but is close to the measurement made in 1993 (+11.5 ‰; see Appendix 1).

The isotopic ratio $^{87}Sr/^{86}Sr$ is very close to that determined in 2010 (Table 14), strongly suggesting equilibrium within sedimentary reservoir. Strontium ratios from limestone, clay limestone and marl-limestone formations from the molasse basin located north of Bern are indeed between 0.706923

and 0.708103 (de Haller *et al.*, 2011). $^{87}Sr/^{86}Sr$ is also congruent with that of Jurassic and Cretaceous sedimentary units from the Paris Basin (Millot *et al.*, 2011).

The $\delta^{11}B$ value was apparently not determined in previous investigations. The measured $\delta^{11}B$ value (+13.72 ‰; Table 14), as well as the concentration of dissolved B (1 312 µg/l; Table 14), are in agreement with the data collected on mineral and thermal waters by Barth (2000) in southern Germany and northern Switzerland (concentrations between 475 and 3 379 µg/l, and $\delta^{11}B$ values between -2.91 and +16.8 ‰). Such $\delta^{11}B$ isotope value is typically in the range of carbonate boron isotope (*e.g.* Millot *et al.*, 2011).

Data for $\delta^{7}Li$ values are also not available for Thônex-1 borehole. Determinations on the two 2016 samples give a range of 9.3 to 9.6‰ (Table 14) that is once again typical of sedimentary rocks of carbonate type (*e.g.* Millot *et al.*, 2011), and suggest relatively low temperature of the deep fluid (Sanjuan *et al.*, 2014).

4.5.5 Geothermometric applications

As previously mentioned in this report, the deep temperature estimated by Vuataz and Giroud (2010) applying classical geothermometers and geochemical modelling simulations on the THX-1 fluid analysed in 2010 (Table 11) indicates a range between 60 and 85°C, which is in accordance with the temperature measured (70°C), in the productive zones of this borehole.
Similar geothermometers were applied on the two fluid samples collected from the THX-1 borehole in 2016 (Table 11). The Na-K-Mg triangular diagram (Figure 146), proposed by Giggenbach (1988), indicates that these waters have a similar position as that analysed in 2010 (Table 11; Vuataz and Giroud, 2010). This position suggests all these waters are immature and have not reached a full equilibrium state at 70°C. They are only in equilibrium with some minerals such as chalcedony.
In this diagram (Figure 146), we can note that the thermal waters from the Litomerice and Teplice areas, in Czech Republic (Appendix 1), may also be classified as immature waters at low temperatures. Only the geothermal water from the Lavey-les-Bains borehole, in Switzerland, is positioned in the area of mature waters, but its deep temperature estimation (120-140°C) is a bit too high (rather 105°C).

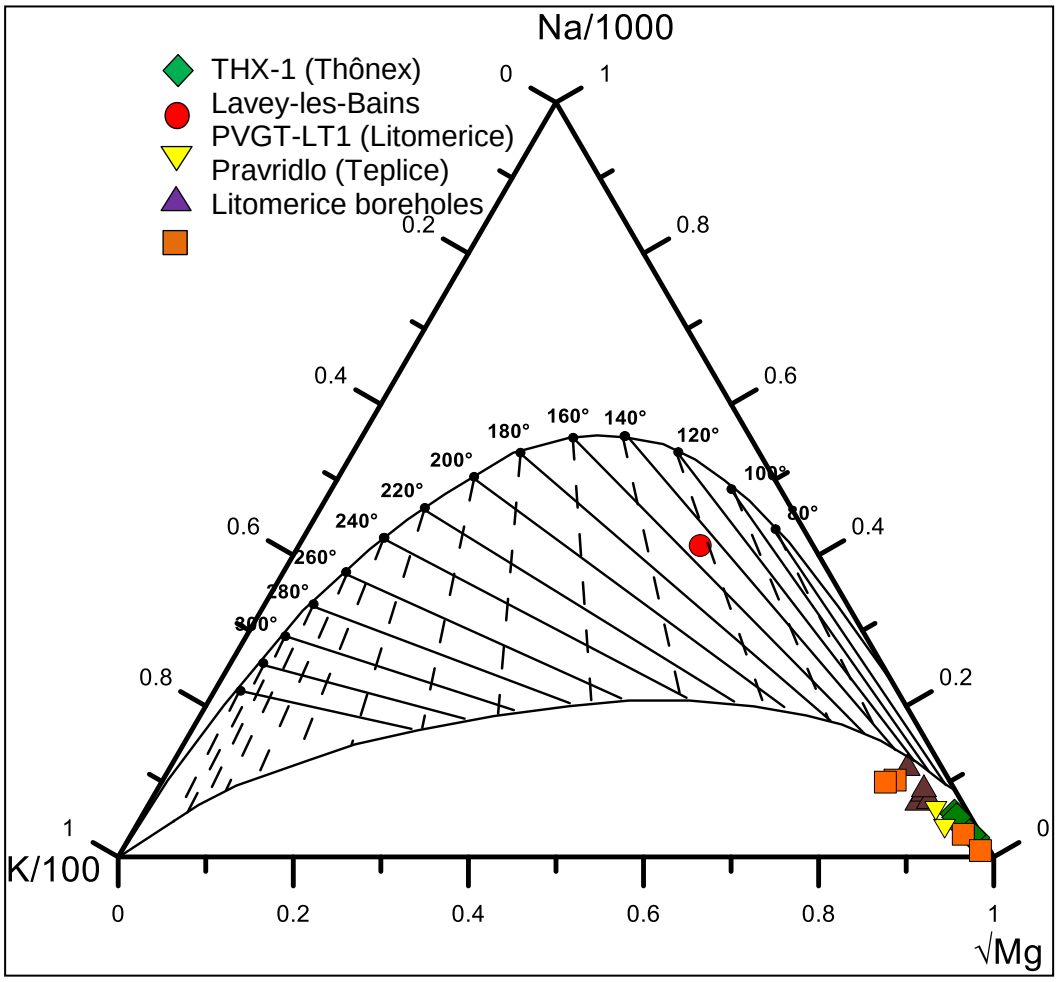

Figure 146 : Na-K-Mg triangular diagram proposed by Giggenbach (1988) for the thermal waters from Czech Republic and Switzerland studied during this project, especially for the fluids discharged from the PVGT-LT1 and THX-1 boreholes, analysed in this study.

The temperature values estimated using classical geothermometers on the two fluid samples collected from the THX-1 borehole in 2016 are reported in Table 15.

Well	Depth m	Geology	T °C	$T_{Chalc.}$ °C	T_{Na-K} °C	$T_{Na-K-Ca\ (1)}$ °C	$T_{Na-K-Ca\ (2)}$ °C	$T_{Na-K-Ca-Mg}$ °C	T_{K-Mg} °C	T_{Na-Li} °C	T_{Mg-Li} °C	T_{Na-Rb} °C	T_{Na-Cs} °C	T_{K-Sr} °C	T_{K-Fe} °C	T_{K-Mn} °C	T_{K-W} °C	T_{K-F} °C	$T_{18O(H2O-SO4)\ (1)}$ °C	$T_{18O(H2O-SO4)\ (2)}$ °C
TH-31, TH 31/62	159	Quartz	13,0	59	140	68		64	57	135	60				16	9				
TH-20	443	Gneiss	27,1	21	135	111		112	86						83			156		
TH-10, TH 10/61	500	Gneiss	31,0	28	148	123		111	92	139	93				33			160		
HV-3C	151	Phyllite	12,0	7	189	40	0	60	44	104	25				3	18		41		
PVGT-LT1 (May 2015)	2111	Gneiss	56,5	< 0	138	89	55	25	58	48	30			116	45	43		58		
PVGT-LT1 (November 2015)	2111	Gneiss	56,5	< 0	133	99	54	68	71	48	43	94	39	116	44	29	49	55		
Pravridlo (ancient spring)	54,3	Rhyolite	41,3	89	123	94		88	72	119	76	109	84	117	141	119		136	81	57
Pravridlo (November 24, 2015)	54,3	Rhyolite	35,9	97	110	92		94	72	106	76	107	84	111	129	50	96	137	148	116
Thonex-1 (01/10/1993) - Vuataz and Giroud (2010)	2530	Limestone	70,0	45	100	23			39	147	62	62		36	114	25	110	124	68	46
Thonex-1 (17/06/2010) - Vuataz and Giroud (2010)	2530	Limestone	70,0	71	92	85			53	129	76	58	32	53	84	38	75	127	37	18
Thonex-1 (25/07/2016) - This study	2530	Limestone	70,0	89	108	74			54	138	72	61	22	54	78	29	100	135		
Thonex-1 (25/10/2016) - This study	2530	Limestone	70,0	74	97	81			53	134	75	62	26	52	19	42	91	132	64	42
Lavey-les-Bains (Sonney *et al.*, 2007)	3000 ?	Gneiss	105,0	108	98	111		127	124	254	210	90	90	93	126	85	209	170	71	48

$T_{Chalc.}$, T_{Na-K}, T_{Na-Li}, T_{K-Sr}, T_{K-Fe}, T_{K-Mn}, T_{K-F}, T_{K-W}: Michard (1990).

$T_{Na-K-Ca\ (1)}$: Fournier and Truesdell (1973).

$T_{Na-K-Ca-Mg}$: Fournier and Potter (1979).

$T_{Na-K-Ca\ (2)}$: Paces (1975).

T_{Mg-Li}: Kharaka and Mariner (1989).

T_{K-Mg}: Giggenbach W.F. (1988).

$T_{18O(H2O-SO4)\ (1)}$: Lloyd (1968).

$T_{18O(H2O-SO4)\ (2)}$: Kusakabe and Robinson (1977).

Table 15 : Deep temperature values estimated using classical and auxiliary geothermometers on the thermal waters from Czech Republic and Switzerland studied during this project

In this table, we can note that the deep temperature values estimated using classical chemical geothermometers are similar not only for the two waters collected in 2016, but also for that collected in 2010 (Vuataz and Giroud, 2010). Besides, the estimated temperature values for the fluids collected in June 2010 and in October 2016 are the closest ones. These values vary from 53°C (K-

Mg) to 108°C (Na-K). Concordant values between 53 and 89°C (70°C ± 20°C) are given using the Chalcedony, Na-K-Ca and K-Mg geothermometers. For the fluid collected in October 1993 from this borehole, the estimations of deep temperature are relatively different (Table 15), but this fluid was very few representative of the deep geothermal water.

Among the different $\delta^{18}O_{H2O-SO4}$ thermometric relationships available in the literature (Boschetti, 2013), that proposed by Lloyd (1968) gives estimates of deep temperature of 67-68°C (Table 15) for the waters collected in October 1993 and 2016, very close to the temperature measured at depth. For the water collected in June 2010, this value is surprisingly under-estimated (37°C).

As for the non-condensable gases associated with the thermal water discharged from the Litomerice PVGT-LT1 borehole, in Czech Republic, CH_4 (≥ 55%) and N_2 (≥ 30%) are the predominant species in the non-condensable gases associated with the THX-1 water, with minor amounts of CO_2 (0.3-0.7%). No compatible deep temperature value could be estimated using gas geothermometers (D'Amore and Panichi, 1980; Giggenbach and Goguel, 1989; Giggenbach, 1991) applied to the chemical composition of these gases.

Relative to the auxiliary chemical geothermometers, preliminary investigations had been carried out on the fluid sample collected from the THX-1 borehole in June 2010 (Vuataz and Giroud, 2010) and were reported in the D7.03 technical report (Sanjuan *et al.*, 2016a). The use of Mg-Li, Na-Rb, K-Sr, K-Fe and K-W geothermometers gave temperature values varying from 53 to 84°C (Table 15), a temperature range around a value of 70 ± 20°C, whereas the Na-Li and K-F geothermometers gave over-estimated temperature values (≈ 130°C; Table 15). On the opposite side, the Na-Cs and K-Mn geothermometers gave under-estimated values (less than 40°C; Table 15). For the reconstructed chemical composition of the Lavey-les-Bains geothermal water (Sonney *et al.*, 2007), similar results were obtained using most of the geothermometers, which indicated a deep temperature close to 105 ± 20°C (Table 15). Only the Na-Li, Mg-Li, K-F and K-W indicated over-estimated temperature values (Sanjuan *et al.*, 2016a).

The application of the auxiliary geothermometers determined by Michard (1990) on the chemical composition of the two water samples collected from the THX-1 borehole in 2016 indicates similar results as those previously obtained using the 2010 analytical data (Table 15), which confirms these results. A part of these geothermometers (Na-Rb, K-Sr and K-W), as well as Mg-Li defined by Kharaka and Mariner (1989), give concordant temperature values around 70 ± 20°C, in agreement with the measured temperature and those estimated using classical chemical and isotope geothermometers (Table 15). The K-Fe geothermometer also gives concordant values, except for the fluid sample collected in October 2016. The Na-Li and K-F geothermometers yield over-estimated temperature values (127-138°C) whereas the Na-Cs and K-Mn geothermometers give under-estimations (≤ 42°C).

In the previous D7.03 technical report (Sanjuan *et al.*, 2016a), geothermometric investigations about the thermal waters discharged from the Litomerice-Teplice area, in Czech Republic, were presented. At temperatures > 50°C, the auxiliary chemical geothermometers such as Na-Li, Mg-Li, Na-Cs, K-Mn and K-W gave concordant temperature values for the Litomerice PVGT-LT1 water (55 ± 20°C) and for the Pravridlo thermal water, at Teplice (100 ± 25°C). However, some auxiliary geothermometers such as Na-Rb and K-Sr gave discordant temperature values for the Litomerice PVGT-LT1 water and concordant values for the Pravridlo thermal water (Table 15). Similarly, other auxiliary geothermometers such as K-Fe and K-F gave concordant temperature values for the Litomerice PVGT-LT1 water and discordant values for the Pravridlo thermal water (Table 15; Sanjuan *et al.*, 2016a). Note that the chemical composition of the PVGT-LT1 fluid is not probably fully representative of that of the fluid present at the bottom-hole because of the very low fluid flow-rate measured in the borehole, which does not allow discharging large volumes of fluid. In contrast to this water, overall chemical equilibrium between the Pravridlo thermal water and reservoir minerals seems to be reached at a temperature close to 100 ± 25°C.Figure 147 and Figure 147 illustrate the application of the auxiliary geothermometers defined by Michard (1990) on the thermal waters from Czech Republic and Switzerland studied during this project, especially on the fluids discharged from the PVGT-LT1 and THX-1 boreholes, analysed in this study.

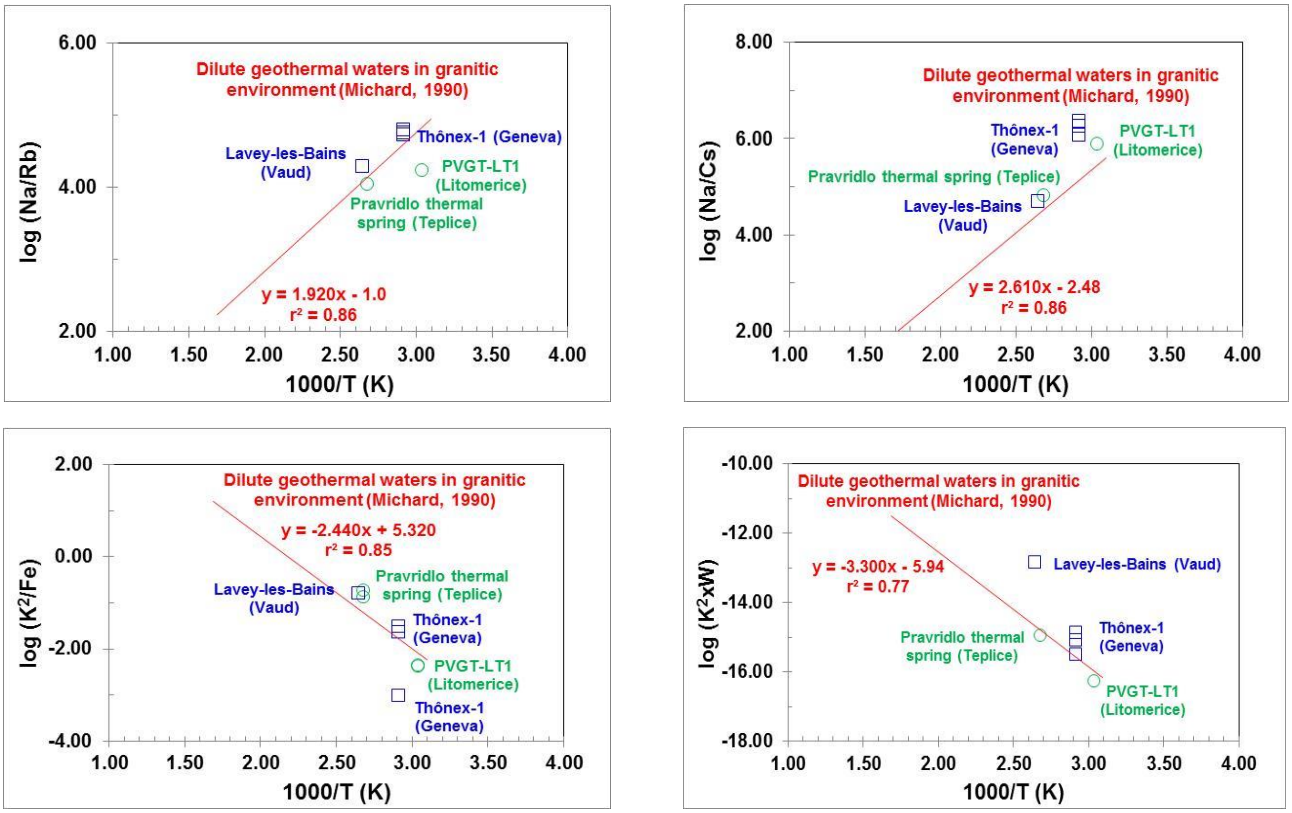

Figure 147 : Applications of the auxiliary chemical geothermometers defined by Michard (1990) on the thermal waters from Czech Republic and Switzerland studied during this project (molar element ratios).

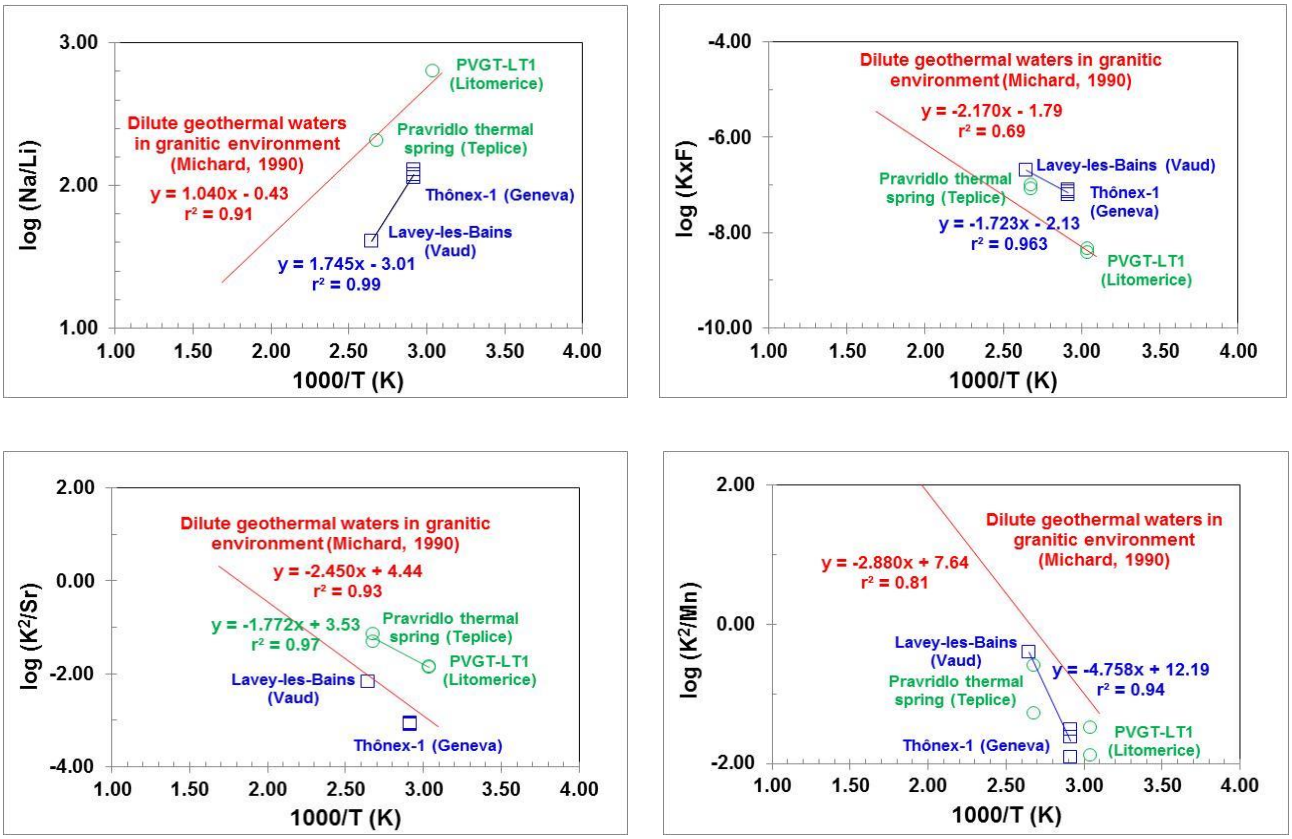

Figure 148 : Applications of the auxiliary chemical geothermometers defined by Michard (1990) on the thermal waters from Czech Republic and Switzerland studied during this project (molar element ratios).

In Figure 148, it clearly appears that the THX-1 and Lavey-les Bains waters don't fit the Na-Li, K-F and K-Mn thermometric relationships defined by Michard (1990). However, sub-parallel thermometric relationships could be defined for these waters. These thermometric relationships are respectively (with molar element ratios):

$$t\,(°C) = 1745 / [\log (Na/Li) + 3.01] - 273.15 \qquad r^2 = 0.99 \qquad (1)$$

$$t\,(°C) = -1723 / [\log (K \times F) + 2.13] - 273.15 \qquad r^2 = 0.96 \qquad (2)$$

$$t\,(°C) = 4758 / [12.19 - \log (K^2/Mn)] - 273.15 \qquad r^2 = 0.99 \qquad (3)$$

In a same way, the PVGT-LT1 and Pravridlo waters don't fit the K-Sr thermometric relationship defined by Michard (1990) in the Figure 148. A sub-parallel thermometric relationship could be defined for these waters, as follows (with molar element ratios):

$$t\,(°C) = 1772 / [3.53 - \log (K^2/Sr)] - 273.15 \qquad r^2 = 0.97 \qquad (4)$$

Once again, the existence of different thermometric relationships for a same couple of elements (Na-Li, K-F, K-Mn, K-Sr…) suggest these geothermometers not only depend on temperature, but also on other parameters such as the nature of the reservoir rock, its degree of alteration, the water-rock ratio, the fluid chemistry and salinity, etc.

All these results show that, even if some estimations of deep temperature can be erroneous, the auxiliary chemical geothermometers, which associate a major element with a trace element, may be very useful tools when a significant part of them gives concordant temperature, especially at low temperatures, where the chemical equilibrium conditions of the water-rock interactions are not always reached. These auxiliary geothermometers must be always used together and must be complementary tools of the classical geothermometers and of the integrated multicomponent solute geothermometry approach (Spycher *et al.*, 2014; Peiffer *et al.*, 2014), based on numerical calculations of equilibration temperature of the geothermal water concerning its saturation with respect to a suite of reservoir minerals. It is also necessary to combine these tools with a global geochemical data interpretation because if it is not the case, they may induce important errors in the estimations of the reservoir temperatures in geothermal exploration.

4.5.6 Conclusions

One of the main objectives of this last study about the development of auxiliary chemical geothermometers applied to environments of crystalline basement and sedimentary basin, within the framework of the FP7-IMAGE project, was to be sure that the fluid discharged from the THX-1 borehole was sufficiently representative of the deep geothermal reservoir to test, develop and validate these auxiliary geothermometers in order to better estimate the reservoir temperature.
After operations using massive HCl acid, carried out just after the drilling of this borehole in 1993, the THX-1 water was contaminated by residual HCl and its aggressive effects on the surrounding rocks for a long time because of the low productivity of this borehole. However, after some fluid production tests, chemical and isotopes analyses were conducted by Vuataz and Giroud (2010). They indicated that pH values had increased from 6.22 to 7.92 and Cl concentrations had drastically decreased from 3 325 to 440 mg/l.
The chemical analyses carried out on this fluid during our study, after some periods of fluid production, showed that final pH was close to 8.03 and Cl concentrations were about 390 mg/l. The chemical and isotopic compositions of the waters collected in June 2010 and in October 2016 were relatively similar (Na-Cl-HCO_3 type, with a TDS value close to 1.3 g/l), suggesting the last fluid sample had to be very close to the water of the geothermal reservoir, and could be considered as the most representative of this water.

Two gas samples associated with this thermal water were collected and analysed for the first time. They were mainly constituted of CH_4 (higher than 55%) and N_2 (higher than 30%), with minor amounts of CO_2 (0.3-0.7%), as the gases associated with the thermal water from the Litomerice PVGT-LT1 borehole (Sanjuan *et al.*, 2016a). No compatible deep temperature value could be estimated using gas geothermometers applied to the chemical composition of these gases.
As for the fluid analysed in 2010, the Chalcedony, Na-K-Ca, and K-Mg classical geothermometers applied on the waters collected in 2016 gave concordant temperatures ranging from 53 to 89°C, which allowed selecting an estimation of deep temperature of 70 ± 20°C, close to the measured value in the deep permeable areas. The isotopic $\delta^{18}O_{H2O-SO4}$ geothermometer (Lloyd, 1969) also yielded concordant temperature estimation (64°C). The Na/K geothermometer gave over-estimated temperature values (108 and 97°C).
Relative to the auxiliary chemical geothermometers, the Mg-Li relationship defined by Kharaka and Mariner (1989) and the Na-Rb, K-Sr and K-W proposed by Michard (1990) gave good estimations of deep temperature around 70 ± 20°C for the three THX-1 waters collected in 2010 and 2016. Among the other thermometric relationships defined by Michard (1990), the K-Fe relationship also yielded compatible temperatures, except for the water collected in October 2016.

The Na-Cs and K-Mn thermometric relationships gave concordant but under-estimated values. In the opposite side, the Na-Li and K-F relationships yielded over-estimated values.
For the Lavey-les-Bains water, the Na-Rb, Na-Cs, K-Sr, K-Fe and K-Mn auxiliary thermometric relationships gave good estimations of deep temperature around 105 ± 20°C, in agreement with the temperatures estimated using classical geothermometers such as Chalcedony, Na-K, Na-K-Ca and K-Mg. As for the previous waters, the Na-Li and K-F relationships yielded overestimated temperatures. It was also the case for the Mg-Li and K-W relationships.
From the chemical compositions of the THX-1 and Lavey-les-Bains waters, three new thermometric relationships were proposed as follows (with molar element ratios):

$t\ (°C) = 1745 / [\log (Na/Li) + 3.01] - 273.15$ $\quad r^2 = 0.99$
$t\ (°C) = -1723 / [\log (K \times F) + 2.13] - 273.15$ $\quad r^2 = 0.96$
$t\ (°C) = 4758 / [12.19 - \log (K^2/Mn)] - 273.15$ $\quad r^2 = 0.99$

Within the framework of this project, relative good results are obtained with the use of auxiliary chemical geothermometers if we consider that most of them have also given good estimations of temperature for the dilute waters discharged from the Litomerice PVGT-LT1 geothermal borehole (55 ± 20°C, except for the Na-Rb and K-Sr relationships) and the Pravridlo-Teplice thermal spring (100 ± 20°C, except for the K-Fe, K-Sr and K-Mn relationships), in Czech Republic. These results are detailed in the D7.3 and D7.8 technical reports (Sanjuan *et al.*, 2015, Sanjuan *et al.*, 2016a). For these waters, the following thermometric relationship is proposed (with molar element ratios):

$t\ (°C) = 1772 / [3.53 - \log (K^2/Sr)] - 273.15$ $\quad r^2 = 0.97$

We also remember that three new Na-Rb, Na-Cs and K-Sr auxiliary geothermometers (Sanjuan *et al.*, 2016a, c) have been statistically developed in this project, using literature data referring to 20 hot natural brines (70-320°C) mainly discharged from wells drilled in the sedimentary formations or the granite basement of the Rhine Graben (France and Germany), and at Salton Sea, in the Imperial valley (USA).
All these results show that, even if some estimations of deep temperature can be erroneous, the auxiliary chemical geothermometers, which associate a major element with a trace element, may be very useful tools when a significant part of them gives concordant temperature, especially at low temperatures, where the chemical equilibrium conditions of the water-rock interactions are not always reached. These auxiliary geothermometers must be always used together and must be complementary tools of the classical geothermometers and of the integrated multicomponent solute geothermometry approach, based on numerical calculations of equilibration temperature of the geothermal water concerning its saturation with respect to a suite of reservoir minerals. It is also necessary to combine these tools with a global geochemical data interpretation because if it is not the case, they may induce important errors in the estimations of the reservoir temperatures in geothermal exploration.

The existence of different thermometric relationships for a same couple of elements (Na-Li, K-F, K-Mn, K-Sr…) suggest these geothermometers not only depend on temperature, but also on other parameters such as the nature of the reservoir rock, its degree of alteration, the water-rock ratio, the fluid chemistry and salinity, etc. This allows concluding that it is essential to well define the environment in which these geothermometers will be applied before their use, and that additional investigations are absolutely necessary for each specific environment.

5 Molasse Basin (Germany) - Reprocessed seismic data for geothermy in Stadt Bad Waldsee

5.1 Introduction

Low cost exploration for geothermal energy is an important part of making geothermal business cases work. Currently, the budgets for geothermal projects are considerably lower than those of petroleum exploration and production (PE&P). This asks for cost-effective solutions that use seismic data to the fullest, thereby de-risking geothermal prospects as best as possible. Seismic reprocessing is one of the options for cost-effective (re-)use of seismic data, besides the smart acquisition of new data.

A fact is that seismic signals in the later parts of seismograms were not optimally processed for deeper, geothermal targets. These signals need to be enhanced to such an extent that geothermal reservoir structures emerge from the noisy seismic background. Application of reprocessing, attributes and revised interpretation on 2D and 3D vintage data must facilitate this. The reprocessed data will allow for superior interpretation and characterisation of the geothermal reservoir, fault zones and petrophysical properties. Further seismic attributes, AVO and inversion are then feasible on the reprocessed data. The newly gained insights lead to a revised reservoir model with reduced uncertainties, making a better business case for geothermal systems.

In many parts of the world, including Germany, raw field seismic records and log data are not abundant and not easily accessible. Getting hold of such data is also a costly affair, since they have to be purchased from the data owners. Then doing a pre-stack reprocessing on these data is another costly and time-consuming process which is sometimes necessary, but will lay a heavy claim on the geothermal project budget. If the seismic data are 3D, the necessary time and budget with respect to 2D data will increase even more. One of the goals of the IMAGE programme is to develop cost- and time-effective methods for seismic data reprocessing, in order to improve the business case of geothermal projects.

For the delineation of the geothermal reservoirs on existing surface seismic data, a new seismic processing technique has been developed at TNO in the context of the IMAGE programme. New generations of pre- and poststack noise-reduction and signal enhancement algorithms serve this purpose. Strong noise suppression together with edge preservation are necessary for revised reflection interpretation and fault delineation. Reprocessing will magnify the effect of subsequent attribute analysis and employing the combination of new data and attributes will enhance existing interpretations of the geothermal reservoirs and even allow new interpretations where previously there were none.

The Non Local Means (NLM) algorithm (Buades et al., 2005; Bonar and Sacchi, 2015) acts as a multi-dimensional adaptive filter on seismic data in the spatio-temporal domain. It averages a central seismic sample exclusively with weighted contributions of neighbouring samples having similar Gaussian neighbourhoods as the central sample under consideration. The algorithm scores as one of the best denoising techniques on synthetic seismic data because of its superior random and coherent noise suppression, reflection continuity enhancement albeit with edge and amplitude preservation. It is because of this edge preservation ability that we apply NLM in this study, where fault and fracture detection are of paramount importance.

In this study, a comparison is made between conventional, pre-stack seismic reprocessing and the newly developed reprocessing algorithm applied on post-stack data. The conventional pre-stack reprocessing is often the best possible result in terms of image quality (a ‘99% solution’) but at the

maximal costs in time and budget (at '100% costs'). The newly developed and implemented NLM algorithm works directly on post-stack data and improves the image quality to a level that is not much less than the pre-stack solution (an '80% quality solution') at only a fraction of the pre-stack costs (at '20% costs'). The comparison will demonstrate the benefit of using the NLM algorithm for seismic reprocessing in geothermal cases where the '80% quality at 20% costs' is sufficient.

5.2 Stadt Bad Waldsee

The municipality of Stadt Bad Waldsee (SBW) in southeast Germany (see fig. 1) is planning a geothermal system in the geological Muschelkalk formation, situated in the Molasse Basin, Germany. For background information on the project such as exact location, target formations, expected system performance, timeline of system construction and start of production we refer to the website of the municipality: Stadt Bad Waldsee, 2017. A regional geological model initially available to SBW was not sufficiently accurate as a basis for drilling to the Muschelkalk formation, the anticipated geothermal target. Therefore, SBW has chosen to acquire local vintage 2D seismic data and nearby well-logs from companies in the petroleum sector and have them pre-stack re-processed and re-interpreted for a new geological model. On basis of this new geological model, drilling locations and designs will be made to enable a further design of the system and a spud date in 2017-2018. SBW has decided to join the IMAGE programme and to do an in-kind contribution to IMAGE in the form of seismic data to apply our new NLM reprocessing on.

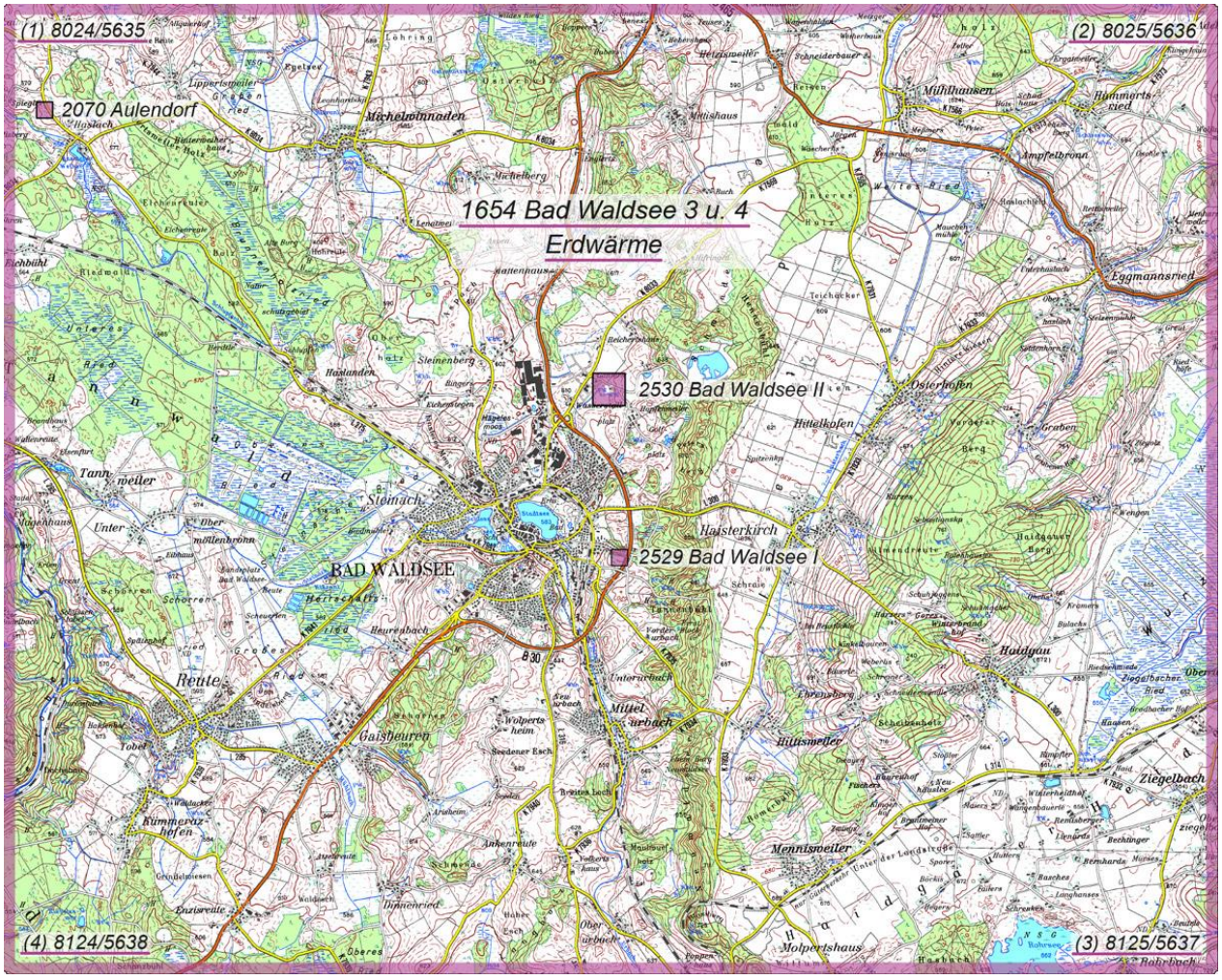

Figure 149 - Overview map of Stadt Bad Waldsee region and (prospect) geothermal sites

5.3 Pre-stack seismic reprocessing by DMT

The reprocessing was done by DMT, a German seismic acquisition, processing and interpretation firm with long track record in seismic surveying for geothermal projects. Due to confidentiality of the DMT seismic processing and interpretation report, details on the pre-stack seismic processing workflow cannot be disclosed. What can be said is that the workflow is considered an industry standard workflow with the latest technology and methods included. The vintage 2D seismic lines that were acquired from petroleum companies were supplied to TNO for benchmarking purposes and to be compared to the TNO implementation of the NLM algorithm. Figure 2 shows the location of the considered 2D seismic lines.

Figure 150 - Overview map of the 2D seismic lines covering the Stadt Bad Waldsee region, used in this study

5.4 The Non Local Means algorithm

The NLM algorithm takes advantage of the redundancy that can be found in most natural images. The redundancy is exploited through assuming that for every pixel in an image there are pixels that have a similar neighbourhood. Seismic images can be considered as prime examples of images with large redundancy. There are usually a lot of periodic structures and there is great similarity of the image structure in different neighbourhoods of the image. The NLM algorithm is based on a search for similar neighbourhoods for each pixel in an image. The pixels in a similar neighbourhood can then be used to predict a value for the pixel. It is non-local because not only the local neighbourhood around a pixel is used in the prediction, but the entire image contributes to the prediction. However, in a practical implementation the size of the search for similar neighbourhoods is restricted to a region around the pixel under consideration.

The NLM algorithm estimates the value of a denoised image *NL(v)* as an average of the values of all the pixels in the image *v* whose Gaussian neighbourhoods look like the neighbourhood of *(i,j)*:

$$NL(v)(i) = \sum_{j \in I} w(i,j)v(j)$$

$$w(i,j) = \frac{1}{Z(i)} e^{-\frac{\|v(\mathcal{N}_i) - v(\mathcal{N}_j)\|^2_{2,a}}{h^2}}$$

where the exponent of *e* is a kernel whose value is controlled by the difference magnitude || and *h* as filter parameters. Due to the kernel definition the weights *w(i, j)* depend on the similarity between the pixels *i* and *j* of *v*. The weights are computed from a similarity measurement of the neighbourhood of the pixels *i* and *j* of *v*. The similarity measurement is the Gaussian weighted Euclidean distance between the values of *v(i,j)* in the neighbourhood windows *Ni* and *Nj*. In this implementation we use square windows for the neighbourhoods *N*. The implementation also features a search window radius *S*, determining the search radius for neighbourhood windows around the pixel under consideration. All involved filter parameters are then: *N*, *S* and *h*. Figures 3a and 3b demonstrate this implementation in a 2D and 3D scheme respectively.

For further details and results of the NLM implementation by TNO, we refer to the IMAGE deliverable D7.01 of WP7.01 where the development, synthetic examples and application on a geothermal pilot case are described. The NLM code performs well on common workstations, taking in the order of minutes to run on 2D lines. Due to its sequential execution, it scales well in parallel computation and therefore it has been parallelised to run efficiently and scalable on the TNO High Performance Cluster. Processing large 3D seismic cubes currently takes several hours on the cluster, but this can be further reduced.

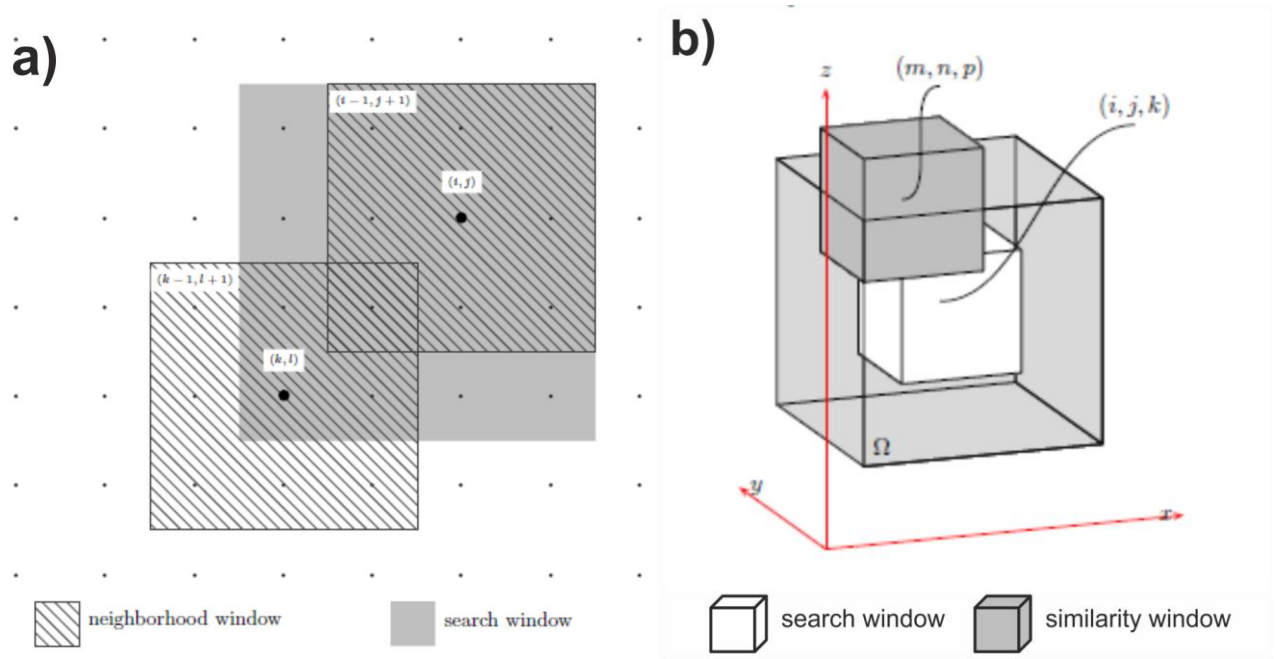

Figure 151 - . a)Schematic view of 2D NLM filter operator. b) Schematic view of 3D NLM filter operator

5.5 Comparison NLM post-stack reprocessing and pre-stack reprocessing

Figures 4-8 show the results of the TNO implemented NLM post-stack reprocessing and DMT pre-stack reprocessing compared to each other. In general, the two methods of reprocessing both show considerable improvement in the SBW 2D seismic data: Figure 4 demonstrates increased continuity along horizons and edge preservation at faults in 2D line 730023 resulting from NLM application. Absolute and relative amplitude information has been left mostly untouched in areas with high signal-to-noise ratio (S/N) and fault discontinuities are enhanced (yellow ellipses).

Resulting attributes on the seismic data, such as instantaneous phase (horizon emphasis for auto-tracking purposes) and coherence (discontinuity emphasis for fault tracking) profit substantially from the reprocessing. Figure 5 shows the improvement of NLM reprocessing on the instantaneous phase of the seismic line in Figure 4 (black ellipses). Figure 6 shows the improvement of NLM reprocessing (yellow ellipses) on the coherence of the seismic line in Figure 4.

When considering the DMT pre-stack reprocessing on 2D line 8604 (Figure 7c) as compared to the original data (Figure 7a), we observe that the improvement in terms of continuous reflectivity and signature of faults of pre-stack reprocessing is superior to that of NLM reprocessing (Figure 7b). This is due to the fact that the quality of the pre-stack data has been enhanced to such a degree, that the resulting stack constructively enhances S/N. Stacking power increases S/N most effectively of all processes. Taking into account that the effort to get the pre-stack data up to this quality was in the order of tens to hundreds of hours and that the NLM reprocessing took in the order of minutes to get to a slightly less result, the ‘80% quality at 20% costs’ rule applies here.

a)

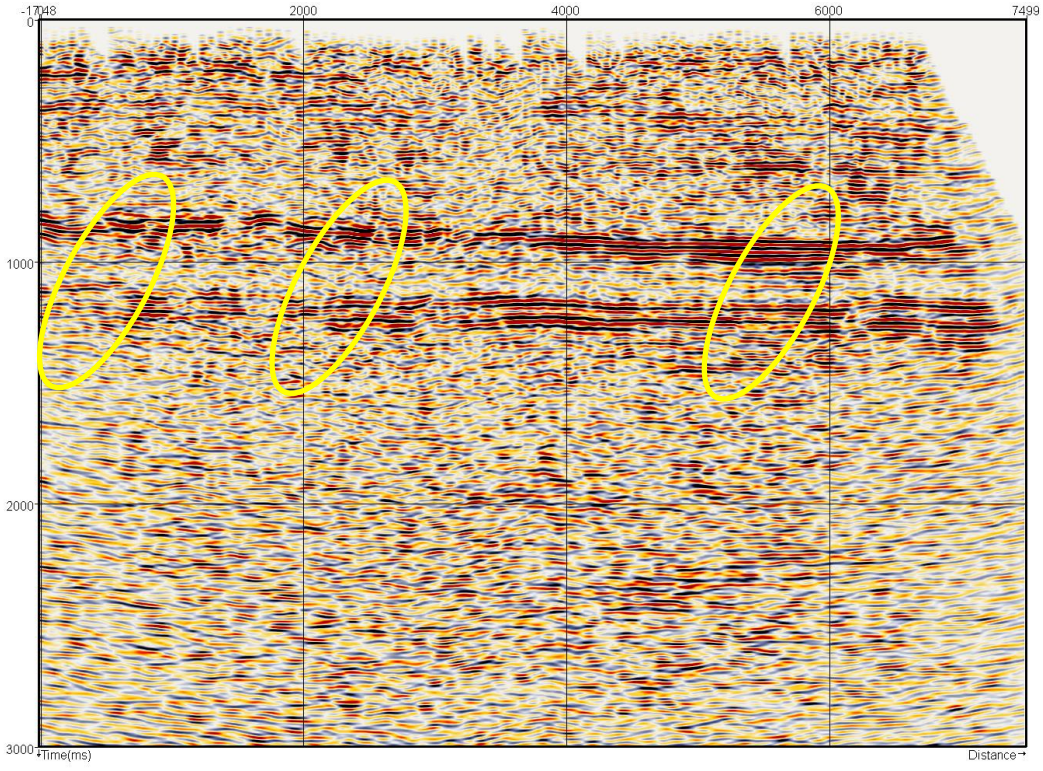

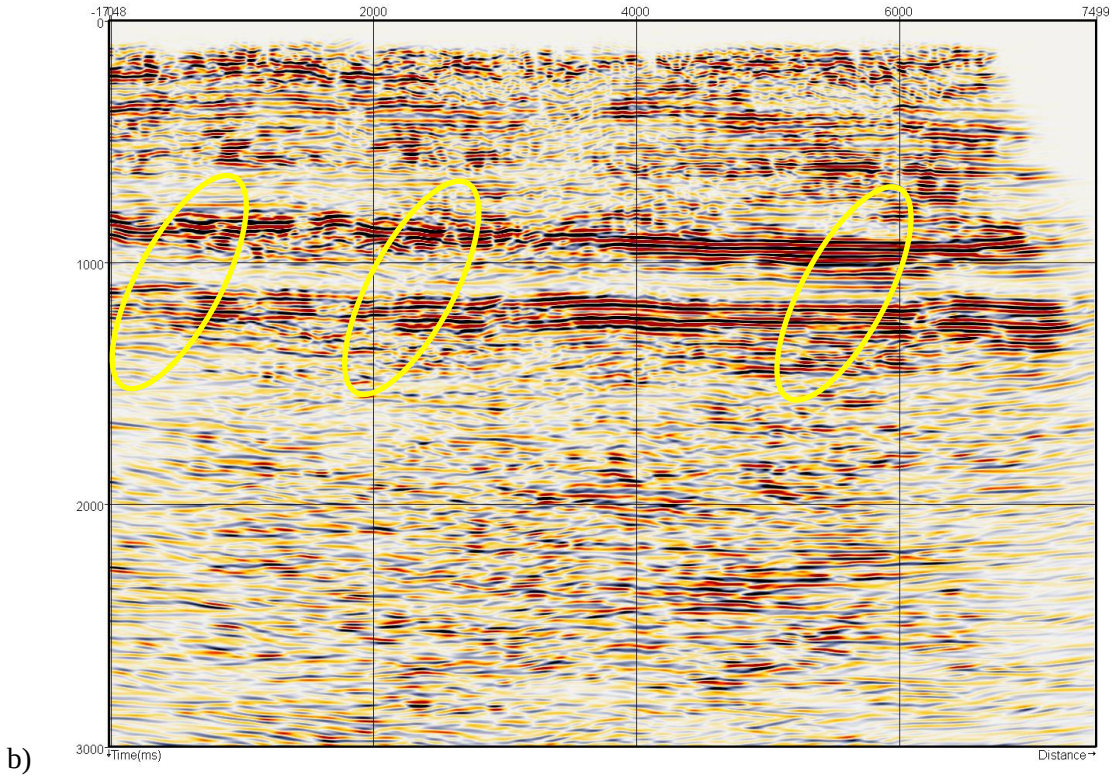

b)

Figure 152 – a) Amplitudes in original seismic line 730023. b) Amplitudes in NLM post-stack repro seismic line 730023

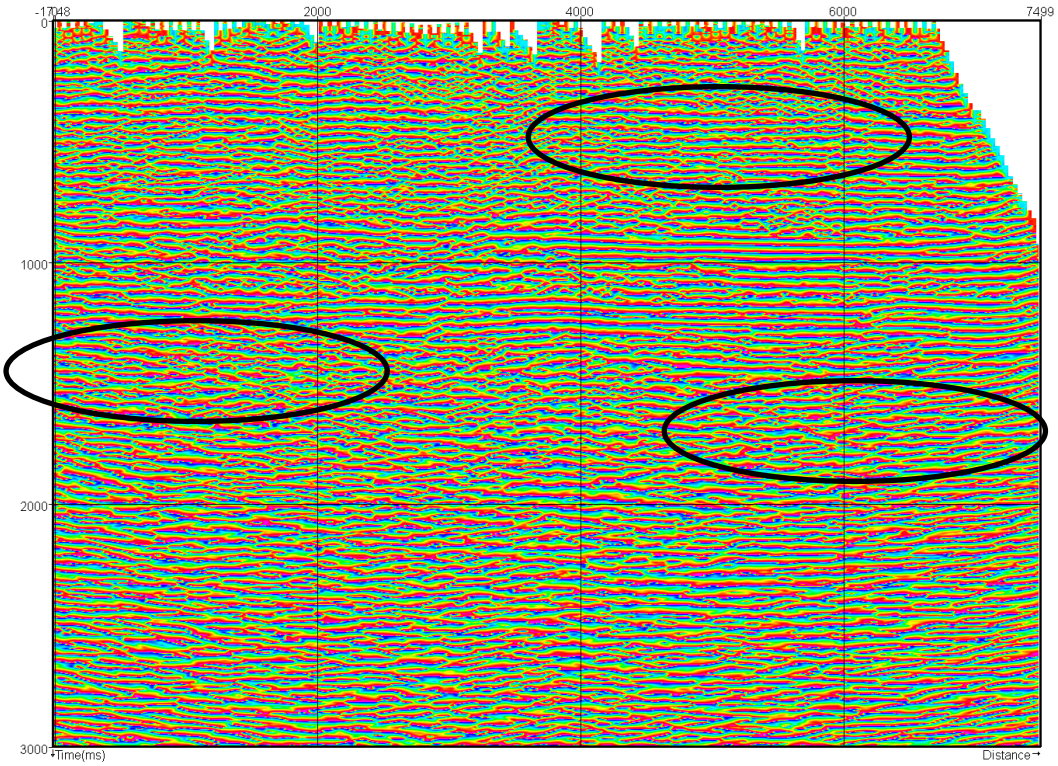

a)

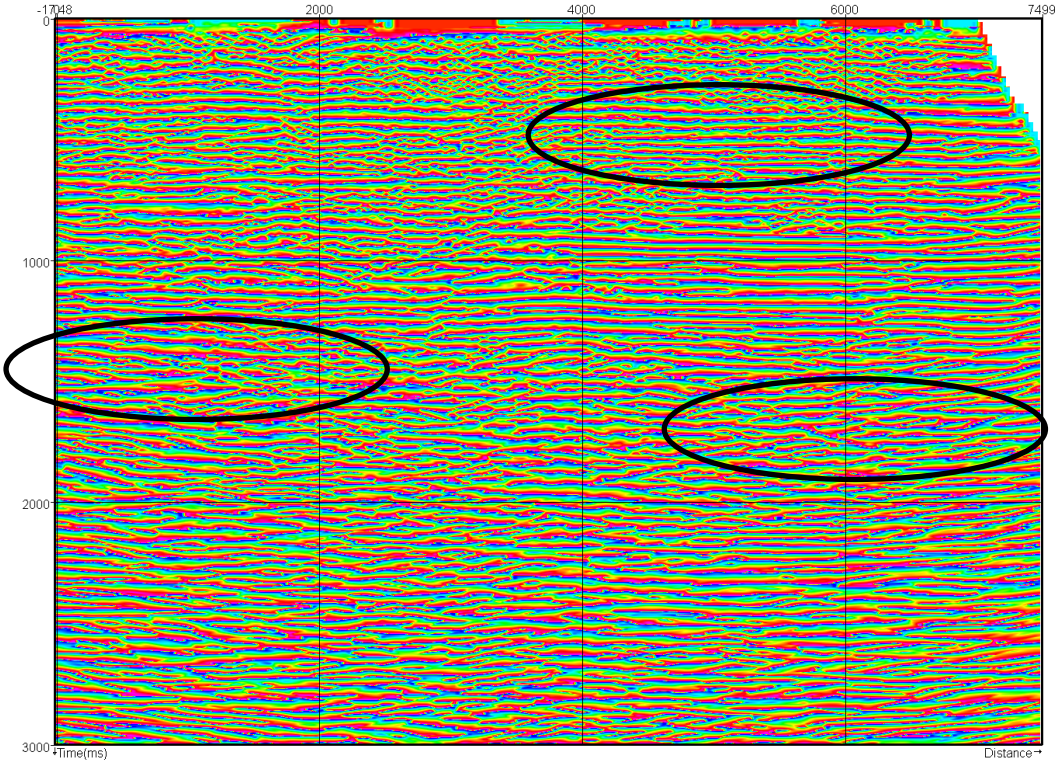

b)

Figure 153 – a) Instantaneous phase in original seismic line 730023. b) Instantaneous phase in NLM post-stack repro seismic line 730023

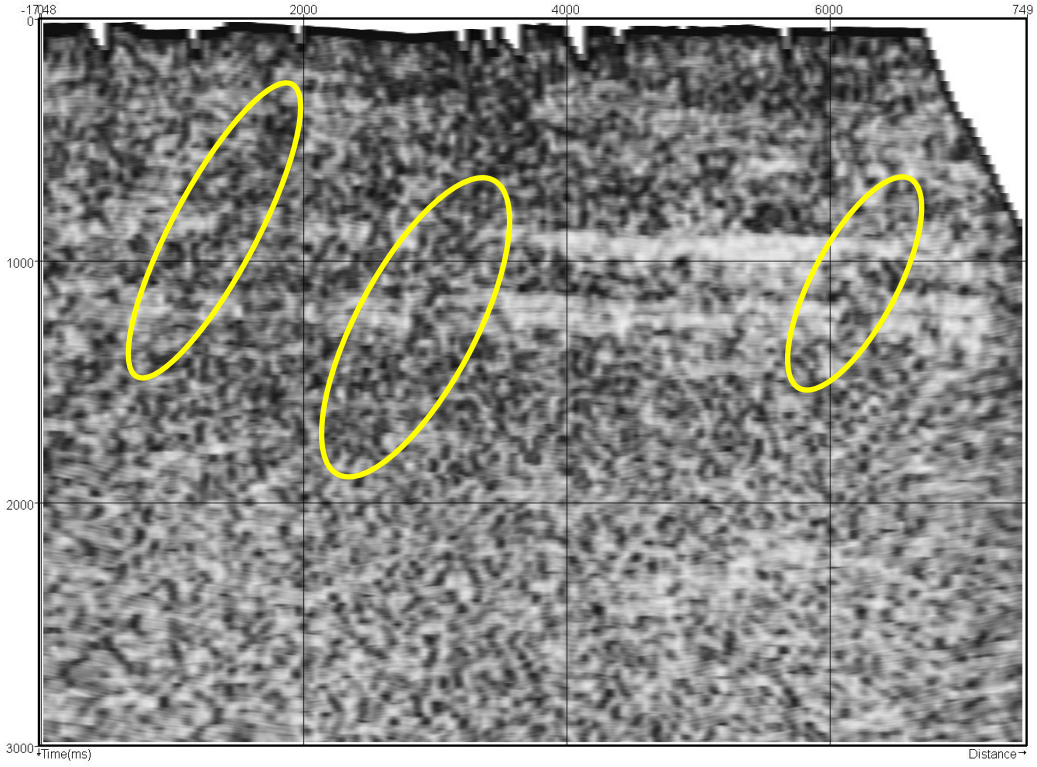

a)

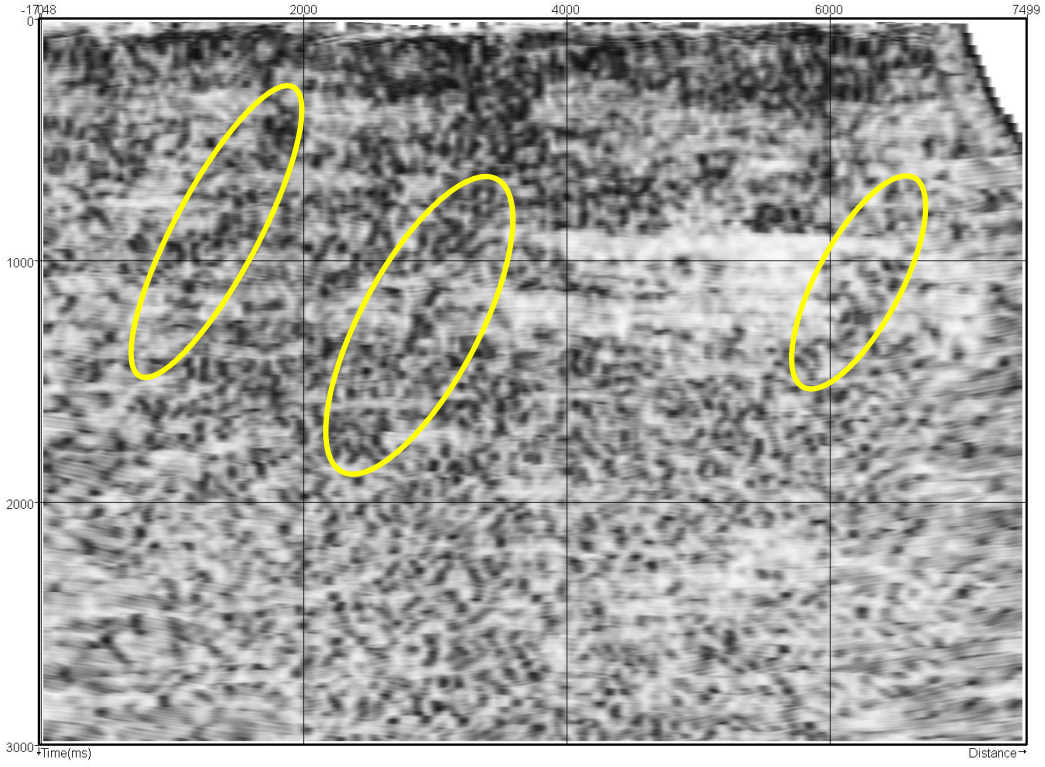

b)

Figure 154 – a) Coherence in original seismic line 730023. b) Coherence in NLM post-stack repro seismic line 730023

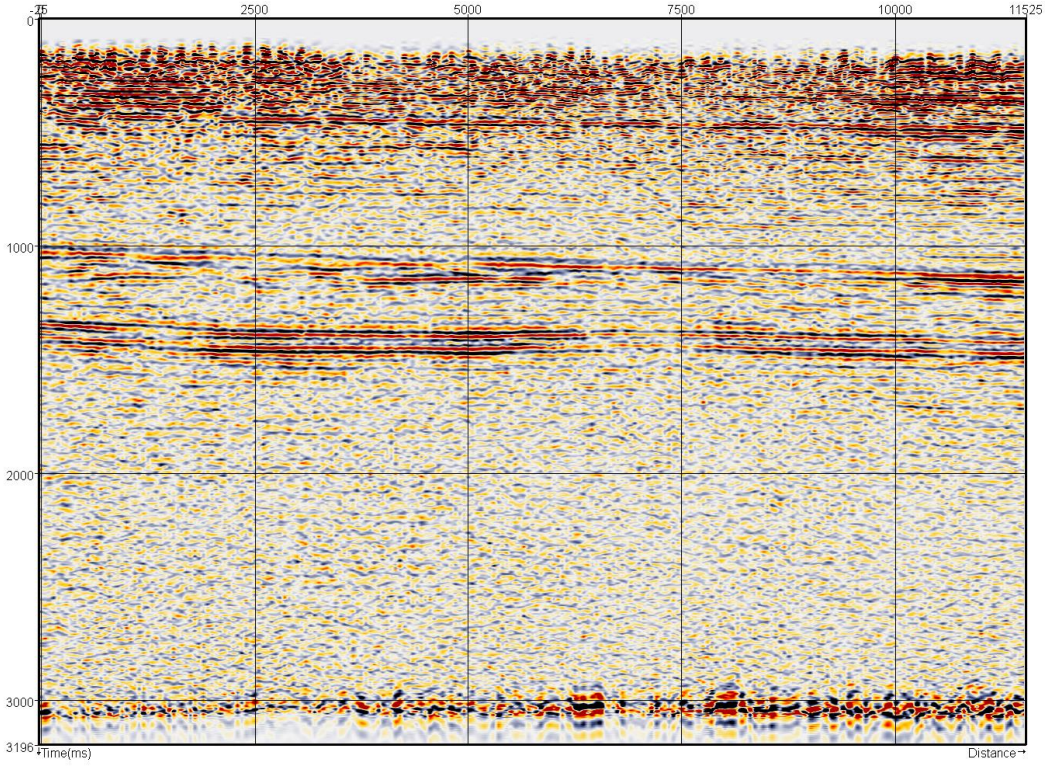

a)

b)

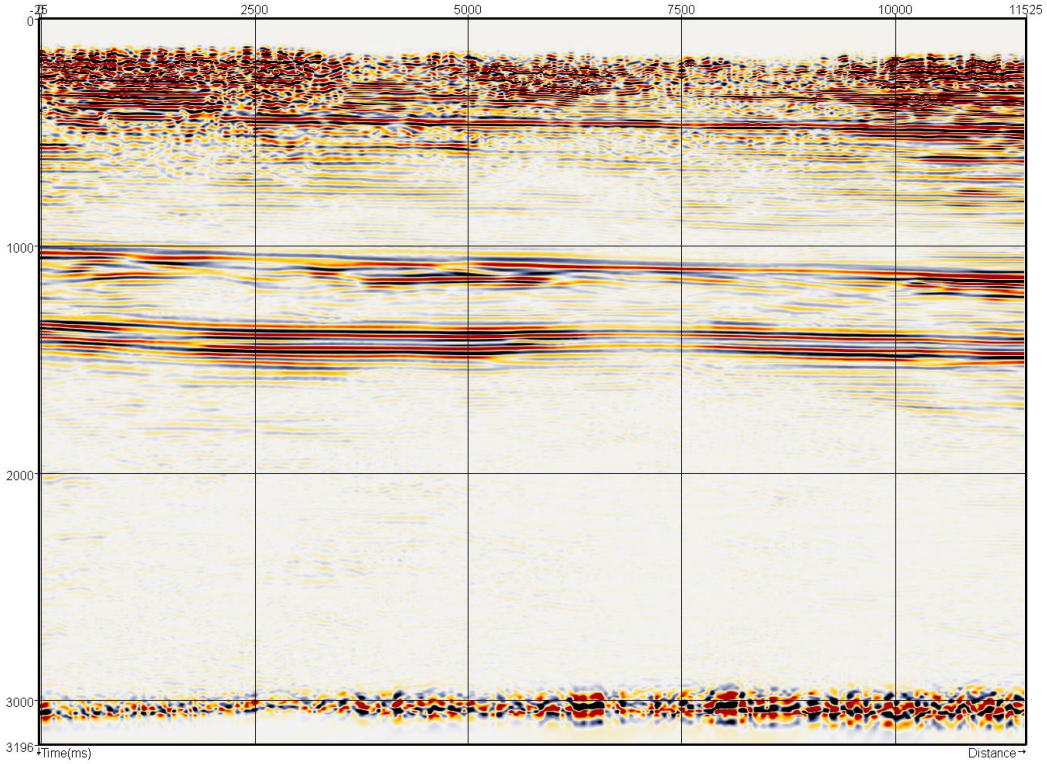

c)

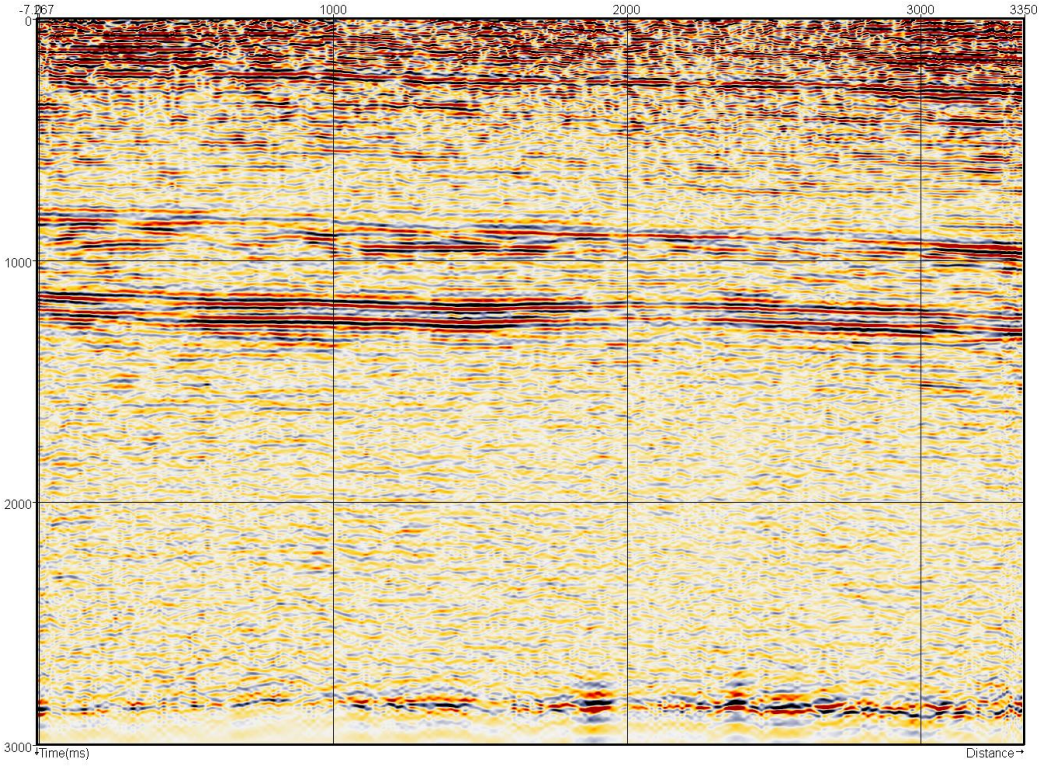

Figure 155 – a) Amplitudes in original seismic line 8604. b) Amplitudes in NLM post-stack repro seismic line 8604. c) Amplitudes in DMT pre-stack repro seismic line 8604

The same goes for the reprocessed 2D line 8802 in Figure 8. There, the most important features of the data, being the diffractions from reef structures above the geothermal reservoir (Figure 8a), are sufficiently improved (Figure 8b) as compared to the superior pre-stack reprocessing (Figure 8c).

5.6 Conclusions

For low cost exploration of geothermal energy to be a success, innovations in seismic acquisition and seismic processing need to be accelerated. Adopting parallel developments in video & image processing industry is a way to bring cross-domain technology into the seismic realm. For the purpose of this IMAGE study, we did exactly that and implemented the Non Local Means (NLM) algorithm into a seismic reprocessing tool. This results in a cost-effective tool that reprocesses seismic data for geothermal targets towards sufficiently enhanced seismic reflection data. In case the result is insufficient for de-risking geothermal drilling, pre-stack reprocessing is necessary.

The municipality of Stadt Bad Waldsee (SBW) has engaged in the exploitation and construction of a geothermal system. SBW has decided to join the IMAGE programme and to do an in-kind contribution to IMAGE in the form of seismic data to apply our new NLM reprocessing on for de-risking purposes. In this study, a comparison is made between conventional, pre-stack seismic reprocessing and the newly developed reprocessing algorithm applied on post-stack data.

It was found that ‘80% quality at 20% costs’ was achieved with the NLM reprocessing. Both the TNO and DMT reprocessed data constrain the geologic model better and de-risk the subsequent drilling. SBW is now working with the best possible seismic datasets and thus the lowest possible risk for the development and operation of the geothermal system. In the end, SBW has decided to base the geological model on the pre-stack DMT reprocessed data as this data was available.

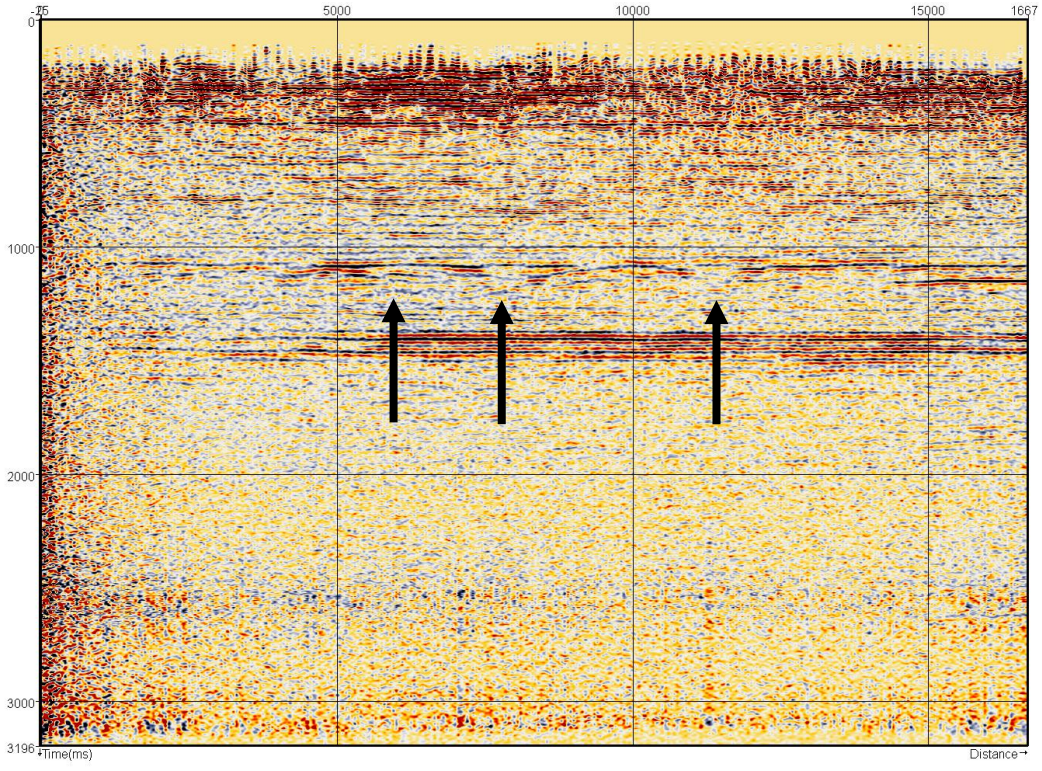

a)

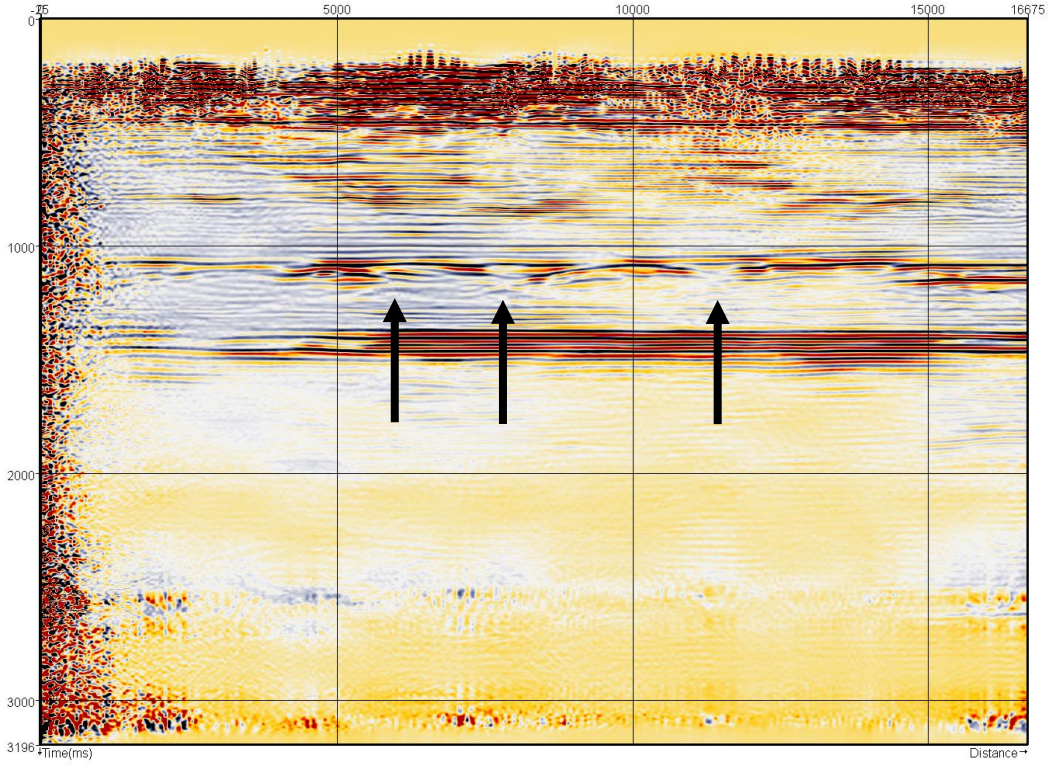

b)

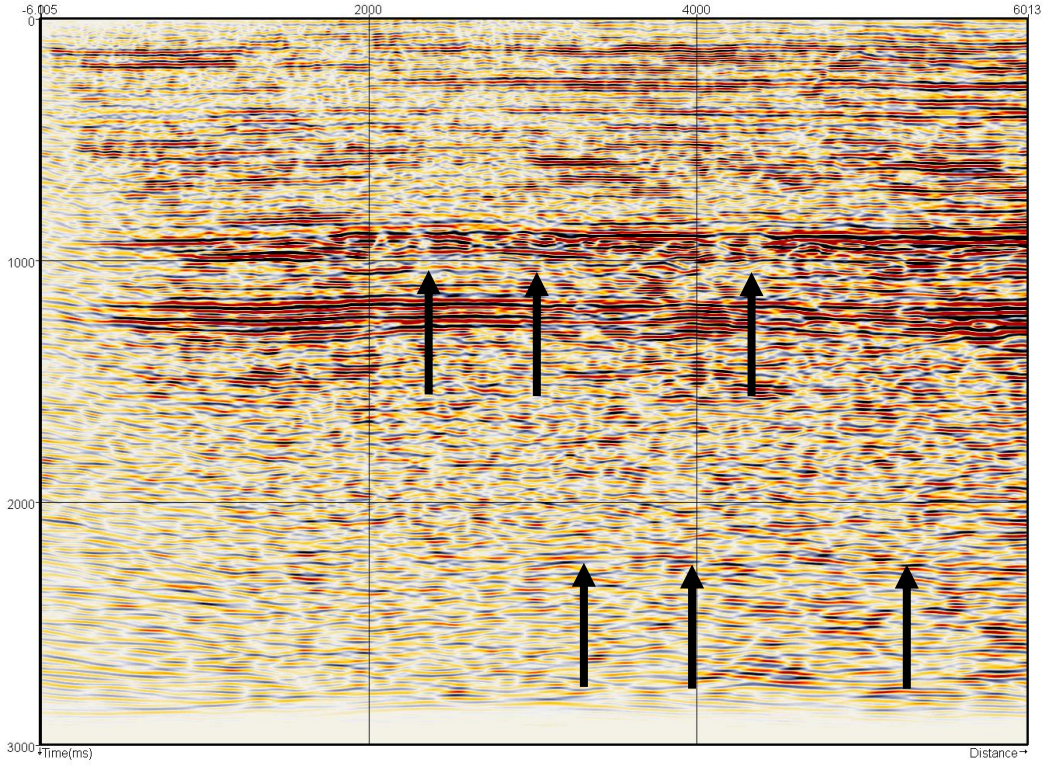

c)

Figure 156 – a) Amplitudes in original seismic line 8802. b) Amplitudes in NLM post-stack repro seismic line 8802. c) Amplitudes in DMT pre-stack repro seismic line 8802

6 Netherlands Basin - Grote Peel: Passive seismic acquisition for shear-wave velocity profiling of the shallow subsurface

6.1 Background

Geothermal exploration studies are aimed at finding possible reservoirs with enough enthalpy potential, and then map these as precisely as possible in order to help the drilling operations.

The seismic technique is known to be an effective tool for mapping deep (> 500 m) subsurface structures in a wide variety of geological settings. But the quality of such images could often be significantly improved if the overburden ('near-surface') overlying the target reservoir could be better defined. An important means to obtain more accurate near-surface information is provided by the dispersive nature of surface waves propagating in shallow layered structures.

Seismic exploration typically measures signals originating from a carefully constructed seismic source. If the same results can be accomplished without requiring a man-made source, but rather relying on randomly distributed ambient noise signals, significant cost reductions are possible.

The main goal of the research described in this section is to efficiently determine near-surface shear wave velocity profiles from surface waves retrieved from correlations of ambient seismic noise with a technique known as ANSI: ambient noise seismic interferometry.

These profiles, in turn, can serve to improve imaging of a deep reservoir. Shear wave velocities are generally used for computation of rock properties that act as key factors not only for deep reservoir imaging but also in building-construction as well as in mining and drilling.

We start with a description of the acquisition of passive seismic data along a single line in the Grote Peel area in The Netherlands with the purpose to retrieve surface waves from ambient noise. The term 'passive' refers to the fact that no man-made ('active') seismic sources are used in the survey and that the required surface wave information is retrieved solely from applying ANSI on continuous noise recordings. From the surface waves retrieved in this way, S-wave velocity-depth profiles of the shallow subsurface (for depths up to ~500 m) are subsequently determined using an inversion technique based on the exploitation of the dispersive properties of these waves.

It is shown that the ambient noise interferometry technique ANSI, combined with dispersion curve inversion, can be applied successfully for linking shear velocity versus depth profiles to formation transition depths obtained from borehole data.

Furthermore, when the dispersive passive surface waves are combined with surface waves obtained with active source data, the near-surface shear-wave velocity information can become more accurate: the combination of the relatively low-frequent passive data with the relatively high-frequent active data effectively extends the frequency bandwidth and thus the vertical resolution of the surface wave information and thereby the resolving potential of thin-layered sequences in the shallow subsurface.

6.2 Location details passive line and active vintage lines

A line of 33 seismic receivers was laid out near national park 'De Grote Peel' in the Netherlands. This linear geophone array recorded ambient seismic noise over a period of 35 days. A detailed description of equipment and operations can be found in IMAGE-D7.02, section 2.2.

More precisely, the studied area was chosen to be a 750 m line just west of the national park 'De Grote Peel' (Figure 157). The location satisfies a number of criteria, including the presence in the subsurface of a simple, approximately horizontally layered, geology and the absence of large regional faults in the close vicinity (such that the subsurface underneath the passive line can be assumed to be approximately 2D). Figure 158 shows a more detailed satellite image of the area, which may become subject to possible future geothermal exploration. Figure 159 shows the location and stacked sections (profiles) of two active vintage regional seismic 2D lines, almost perpendicular to each other, that were shot in the study area in the 1980s. The seismic lines in Figure 159b and c are each approximately 20 km long, and show 3.5 sec in two-way-time.

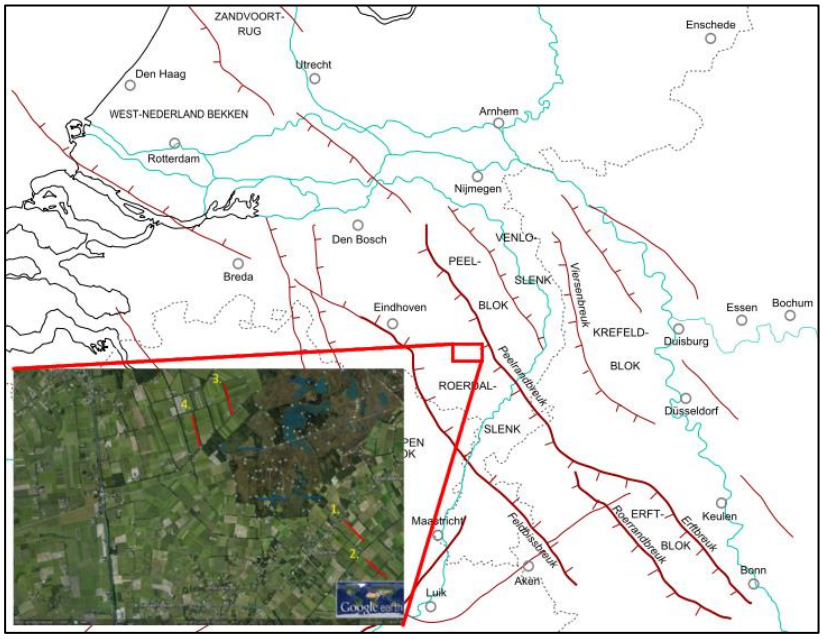

Figure 157 - Map view of main tectonic elements of the southern half of The Netherlands (ref Wikipedia) and a Google Earth image incl. part of the "National park the Grote Peel" and 4 possible locations for the seismic array marked in red. Line number 4 was selected.

We can see from a comparison of these stacked sections, that the NW-SE oriented line 8104N (Figure 159c) can be considered to approximate a "strike" line, showing mainly almost horizontal seismic reflectors such as the picked reflector indicated by the yellow line, and that the seismic line perpendicular to it (Figure 159b) indeed shows reflectors having somewhat larger dips in the line direction. In Figure 159b, also the interpreted locations of major faults are indicated (in red). The overall azimuthal direction of the major fault system is oriented NW-SE (see the brown lines in Figure 157).
A detail of the regional seismic 2D "strike" line 8104N is shown in Figure 160. TNO's passive seismic spread (red line segment) is located in the close vicinity of it and is oriented almost parallel to it. Figure 161 show a detail of the profile shown in Figure 159c, in which the double green arrow indicates the projected location interval of the passive spread.

Figure 158 - Satellite image of the survey area, with the 750 m receiver line coloured yellow. The equipment was controlled from the indicated farm slightly west of the line. Points A and B represent the locations of two borehole surveys. From Google Maps (2017).

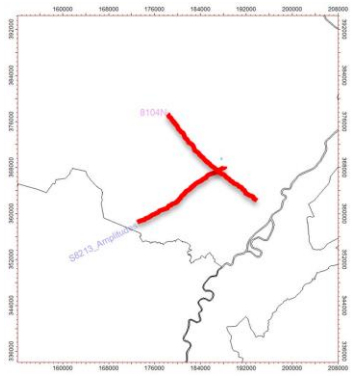

a)

SW NE

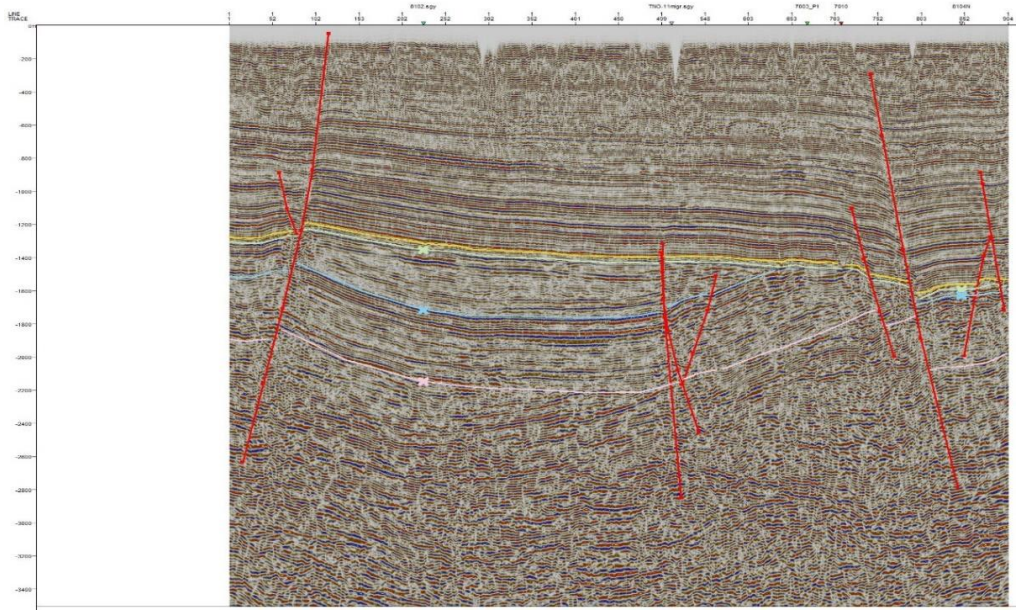

b)

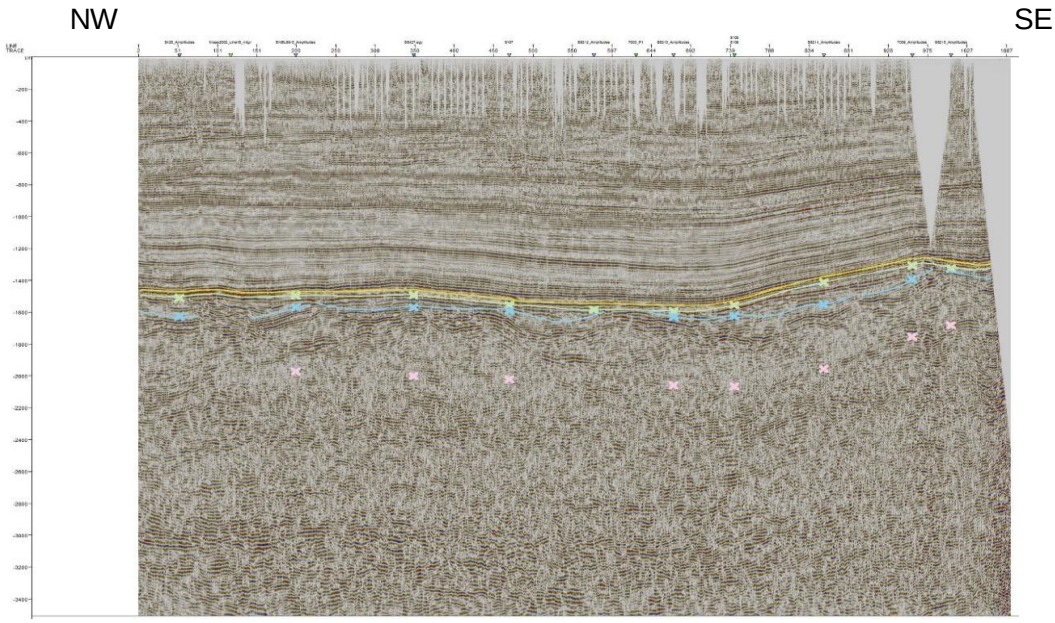

c)

Figure 159 - a) Overview map of two vintage regional seismic lines and corresponding 2D sections crossing near the actual location of TNO's passive seismic array. The main faults in the area follow a NW-SE trend (compare with Figure 157), b) SW-NE ''dip'' line, c) NW-SE ''strike'' line.

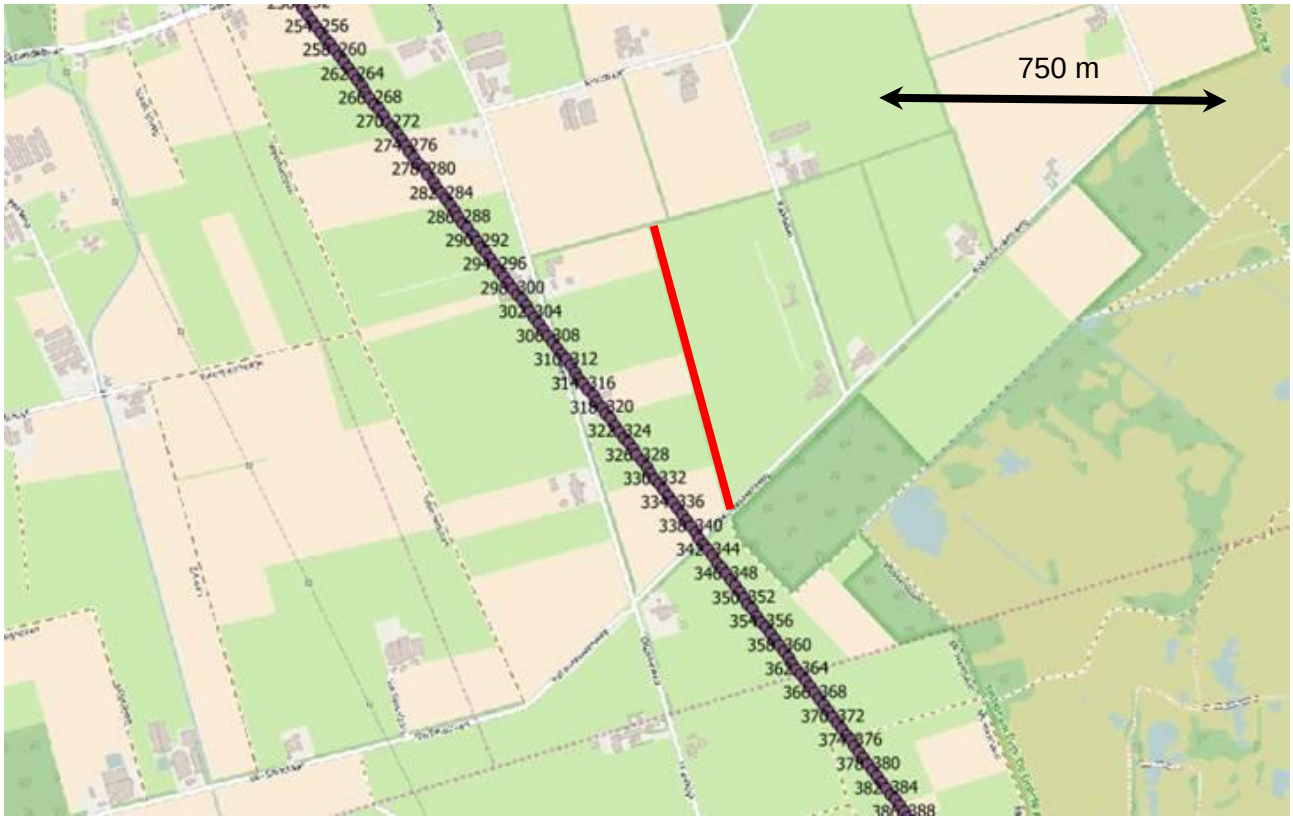

Figure 160 - Location map of regional seismic 2D "strike" line 8104N. TNO's passive seismic spread (red line segment) is oriented almost parallel to this line in the close vicinity (maximum distance ~ 300 meters, compare with Figure 158).

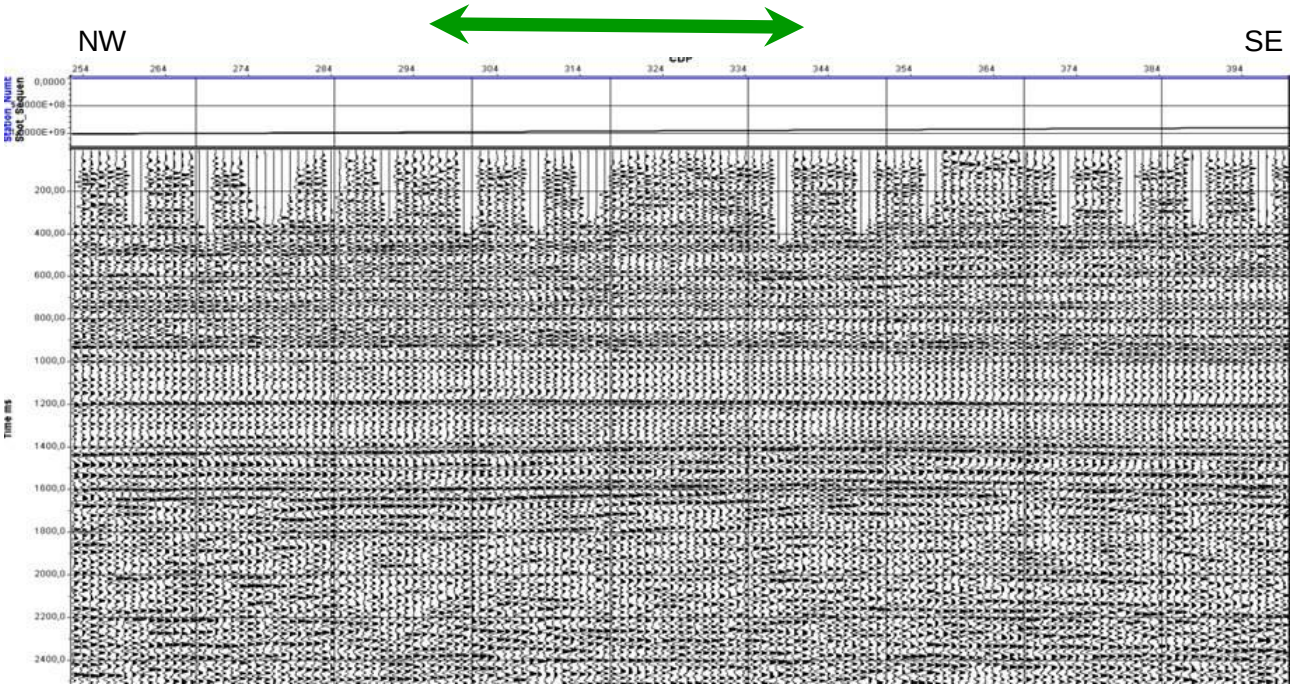

Figure 161 - Detail of vintage active NW-SE seismic profile for regional seismic 2D strike line 8104N, shot roughly parallel to the passive survey at a distance of several tens to several hundreds of metres (see Figure 160). The TNO passive seismic spread maps on the central part of this profile between CDP 297 and CDP 340, indicated by the green double arrow. From BP Nederland BV (1982).

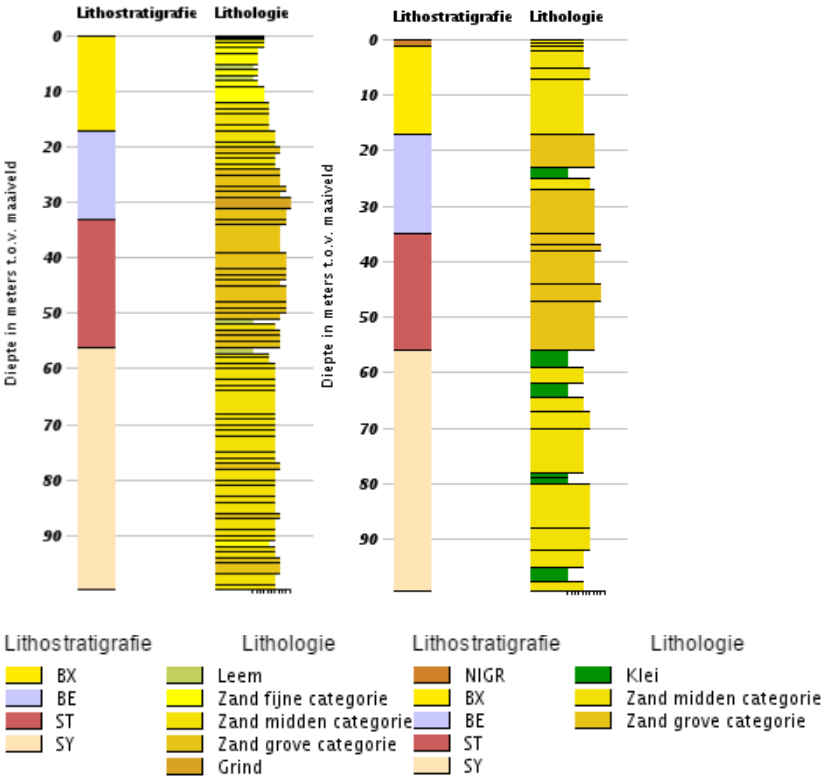

Figure 162 - Borehole survey results for the locations A (left) and B (right) in Figure 158. There is a distinct transition of the formation of Sterksel (ST; coarse river sands) into the formation of Stramproy (SY; fine sands and clays) at a depth of around 55m. From www.dinoloket.nl/ondergrondgegevens

A small number of geological borehole surveys were performed in the vicinity of the line. Their locations relative to the studied line are shown in Figure 157, with their results shown in Figure 162.

6.3 Passive data processing: ambient noise seismic interferometry (ANSI) by cross-correlation

6.3.1 Noise-based surface wave processing for shear-wave velocity profiling

Surface wave signals are extracted from passive seismic data through the process of 'ambient noise seismic interferometry' (ANSI). This involves cross-correlating the ambient noise that is continuously recorded along a line or by a 2D grid of receivers in order to create virtual source gathers.

Surface wave propagation speeds vary, and usually increase, with depth (Haskell, 1953). Surface waves components with a large wavelength will travel deeper in the subsurface than those with smaller wavelengths, therefore travelling faster. As a result, surface wave components originating at a point source will propagate at different speeds based on their wavelengths. This phenomenon is known as dispersion, and can be visualized by plotting a signal's phase velocity against frequency.

From the ANSI gathers that we produced (Figure 163) we indeed retrieved surface wave modes having different wavelengths, so these travel at different speeds and are thus dispersive. Dispersion curves can then be retrieved from these surface waves by transforming the gathers to the phase velocity versus frequency domain and picking the energy maxima in this domain (Figure 164). Next, using a neighborhood algorithm, the picked dispersion curves can be inverted to shear wave velocity versus depth profiles.

Shear-wave velocities are a key factor in calculating subsurface properties such as Poisson's ratio and rigidity. Furthermore, near-surface velocity information greatly improves imaging of the deep subsurface using (geothermal) exploration seismic surveys. The focus of our research concerned finding an efficient and effective method to ultimately extract near surface shear-wave velocity profiles from ambient seismic noise.

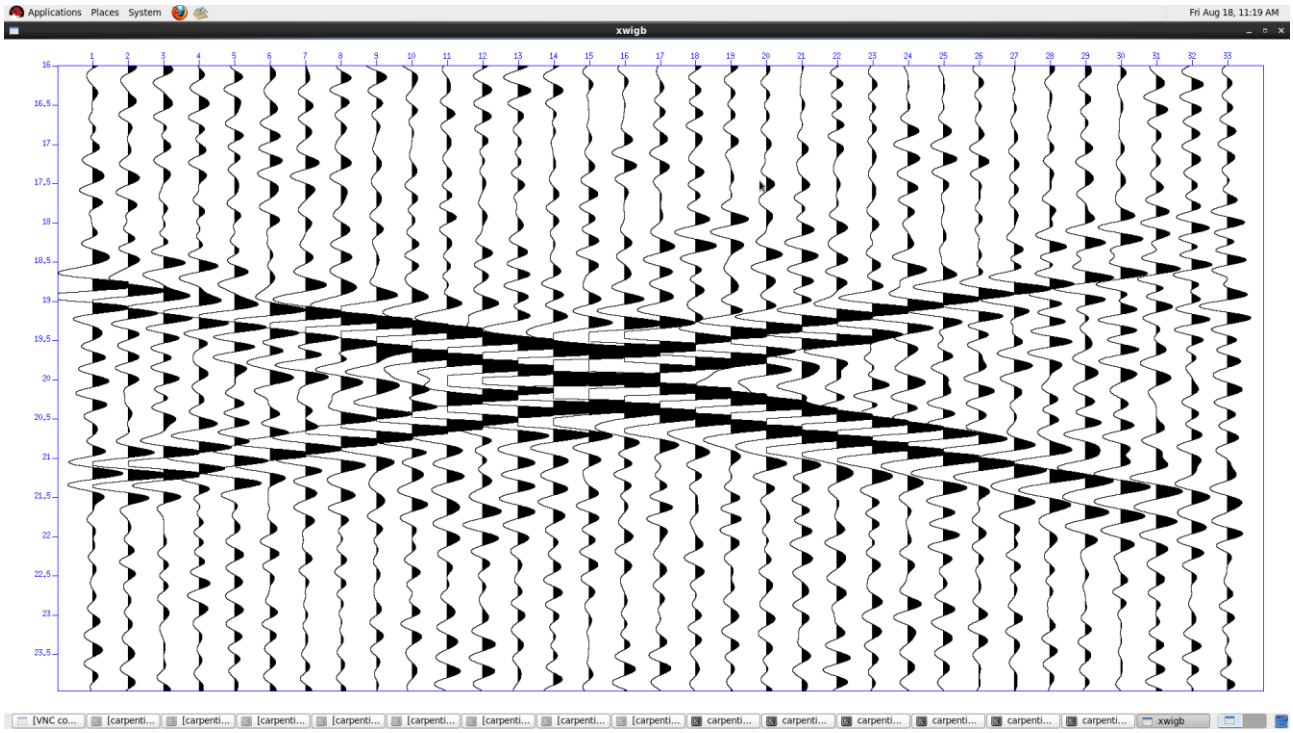
Applications Places System
Fri Aug 18, 11:19 AM
xwigb

a)

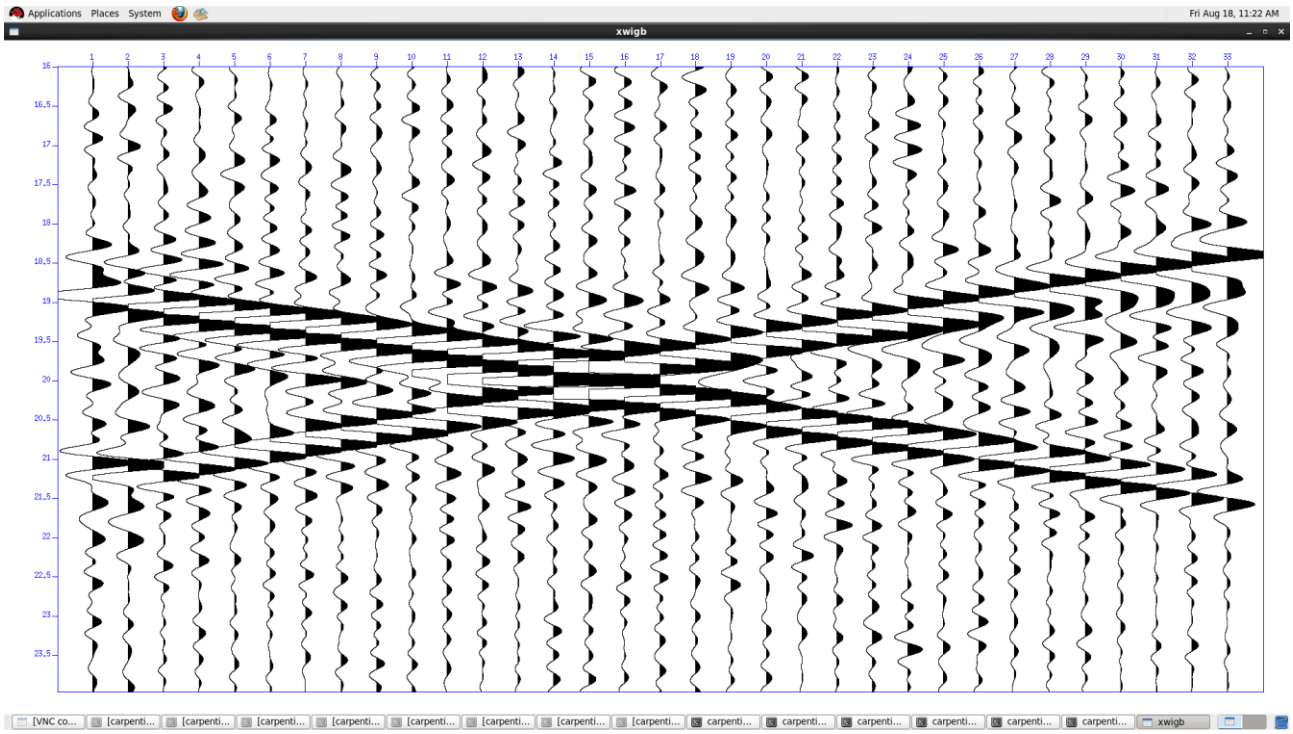
Applications Places System
Fri Aug 18, 11:22 AM
xwigb

b)

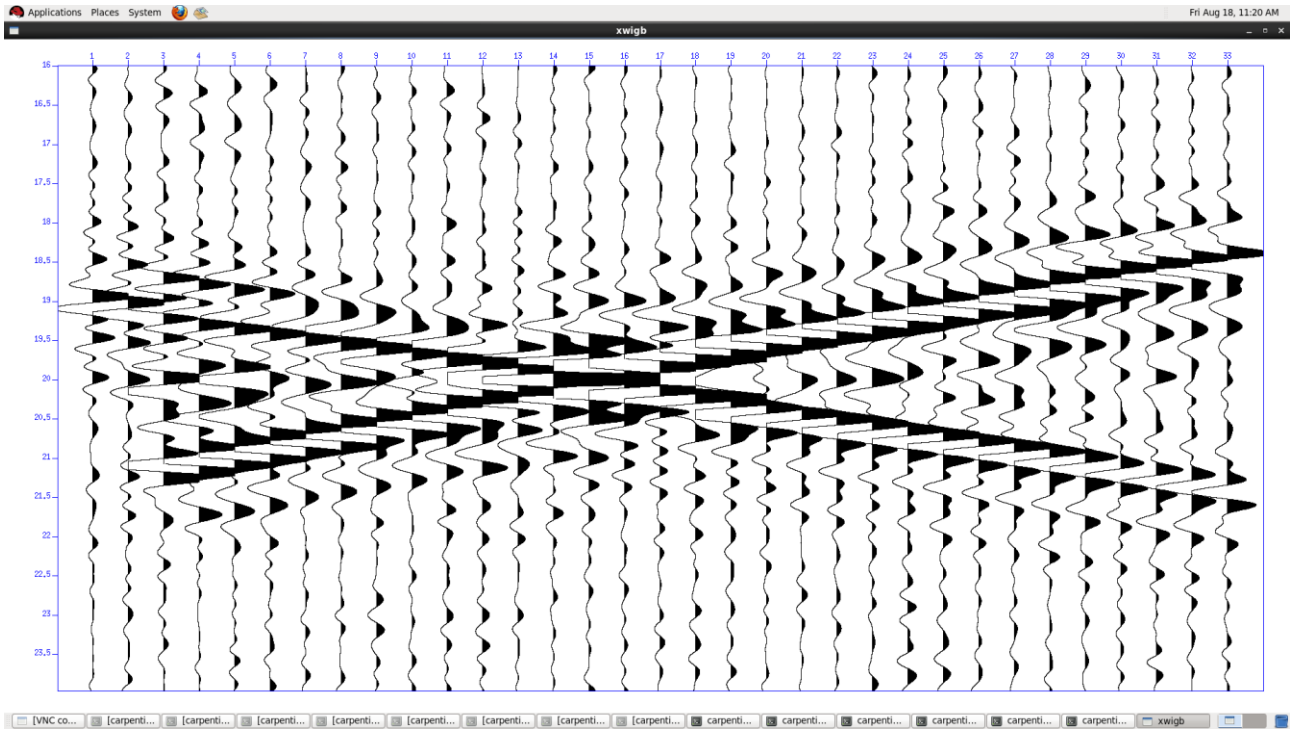

c)

Figure 163 - Virtual source panels for station number 15 obtained from cross-correlation and stacking of just one hour of raw data for day number 148.
a) vertical component b) in-line horizontal component c) cross-line horizontal component.

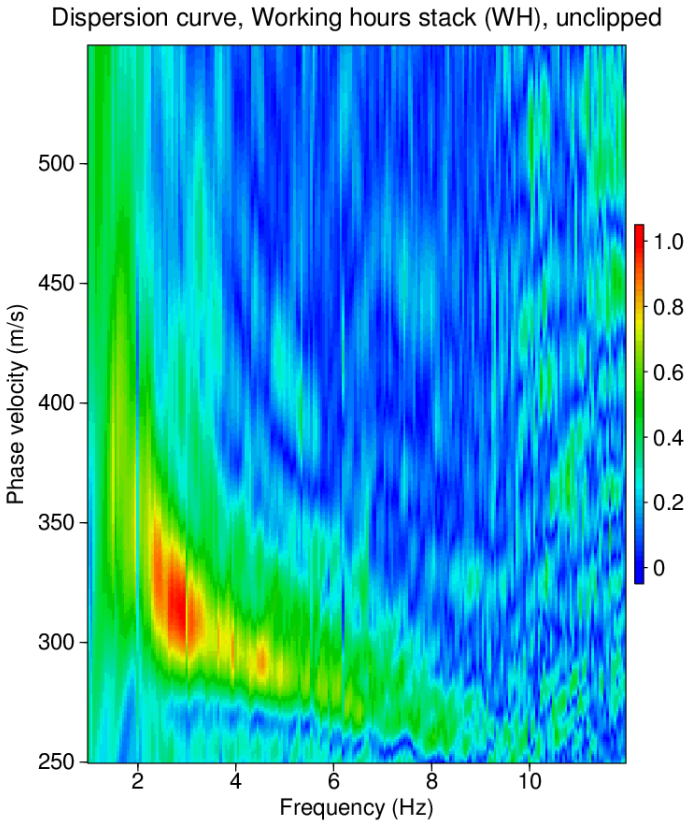

Figure 164 - Phase velocity against frequency plots. Picking the highest amplitudes in the area visible in the lower left corner provides the so-called 'dispersion curve' of the fundamental mode

6.3.2 Ambient noise seismic interferometry (ANSI) processing by cross-correlation

Along the passive line seismic background noise was measured over a total period of 40 days. The 33 stations were placed along a strip of farmland directly next to national park “De Grote Peel” with a spacing of 25m, totalling to a line with a length of 750m for stations 3-33 (stations 1 and 2 were placed slightly offline). Each station consisted of a DSU-3 three-component accelerometer that recorded with a sampling rate of 2 msec, over a bandwidth of 0 to 100 Hz. Each DSU-3 unit was attached to a battery powered RAU-D unit, with GPS and WIFI capabilities, that stored and transmitted the recorded data. The receiver stations are shown in Figure 165.

Figure 165 - Seismic stations in the workshop at TNO, Utrecht. The DSU-3 units are the smaller components with the metal point and orange top. The RAU-D units have a grey top with a small dome.

The final output of this setup was a dataset of around 55.000 ‘ambient noise panels’ of 33 traces wide and one minute long. An example of one of these panels is shown inFigure 166.

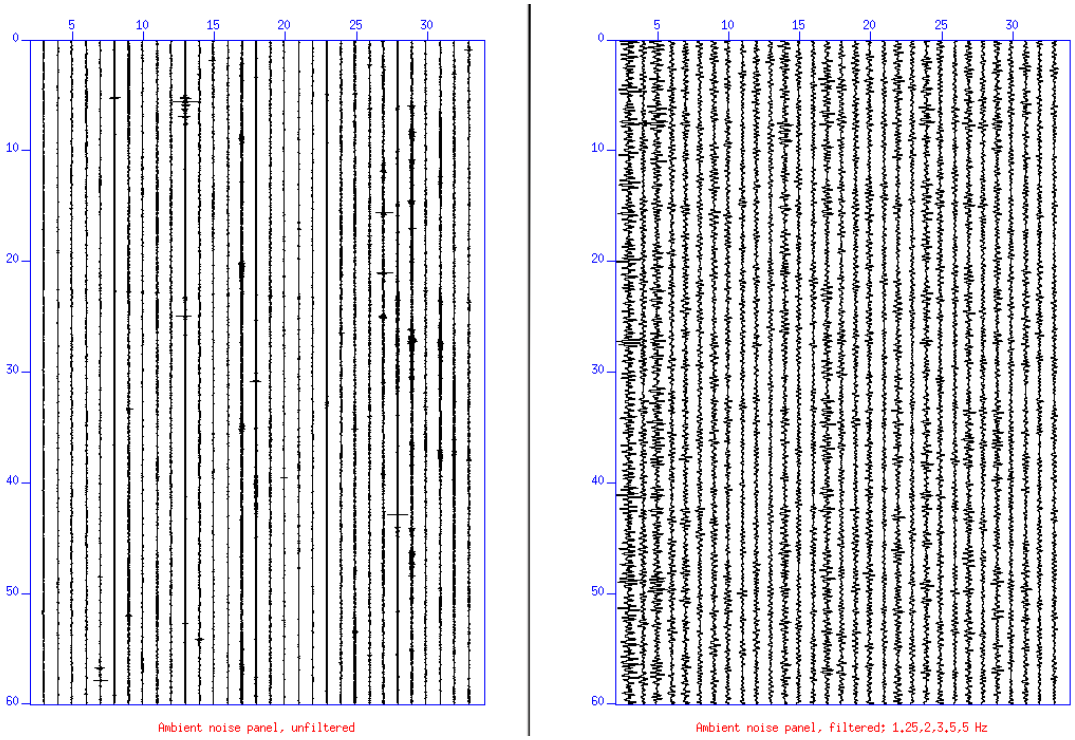

Figure 166 - Typical recorded raw ambient noise panel. It consists of 33 traces (spacing of 25 meters in the field), with 60 seconds of recorded noise. The panel on the right shows the same data, but has been bandpass filtered between 2 Hz and 3.5 Hz with filter slopes ending at 1.25 Hz and 5 Hz, respectively. This frequency band is chosen in order to best show surface waves.

Figure 163 shows an example of virtual source panels, produced by the cross-correlation and stacking of only a very limited amount of consecutive time segments of the continuous raw data from a fixed receiver station (here station number 15) with the same component recorded at all stations in the passive spread: This figure shows a result using *just one hour* of raw data. The causal and anti-causal parts (see Wapenaar et al, 2010) of the emerging surface waves are of high quality on all three components: the dispersive nature of the surface waves can clearly be observed on these panels. Therefore the exploitation of these surface waves for inversion to shear wave velocities was considered feasible.

Next, a lot of experimentation was done with the selection of time periods for cross-correlation and subsequent stacking. Theoretically, the S/N of the retrieved impulse response (ideal shot response) that is desired, grows with the square root of T, with T the total time interval in which correlation and stacking is applied.
But this relation is in practice often violated by the facts that the directional and spatial distribution of noise sources is not random and that the raw data quality Is otherwise affected by undesired sources of noise (presence of noise sources with small frequency-spectral peaks such as engines, pumps etc.).
For the very encouraging inversion result of Figure 167, all data recorded between 08:00-20:59 on weekdays (coloured curves) were selected.

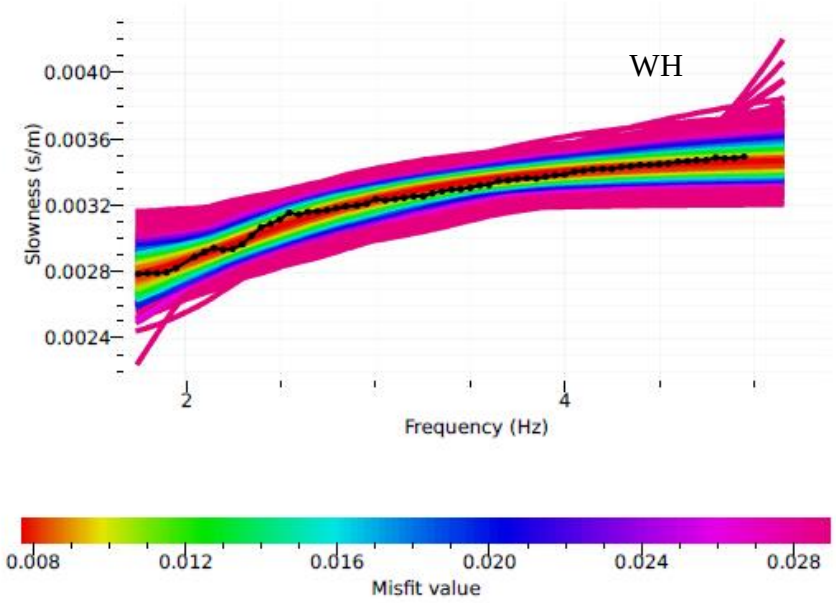

Input parameters for dispersion curve inversion (2-layered model)

Layer 1		
Compressional-wave velocity (Vp)	:	200 - 5000 m/s
Shear-wave velocity (Vs)	:	50 - 800 m/s
Density	:	1500 - 2500 kg/m3
Poisson's ratio	:	0.2 - 0.5
Layer 2 Transition depth	:	1 - 150m
Compressional-wave velocity (Vp)	:	200 - 5000 m/s
Shear-wave velocity (Vs)	:	50 - 800 m/s
Density	:	1500 - 2500 kg/m3
Poisson's ratio	:	0.2 - 0.5

Figure 167 - Dispersion curve fit for the 'Working Hours' data selection for station #28, i.e. all data recorded between 08:00-20:59 on weekdays (coloured curves) were selected. The dotted black line represents the picked dispersion curve that was used for inversion.

6.4 Parameter choices dispersion curve inversion

The inversion of dispersion curves can be finetuned through a number of subsurface input parameters. The parameters that are taken into account when performing a dispersion curve inversion are compression-wave velocity (Vp), shear-wave velocity (Vs), density and Poisson's ratio (the ratio of transverse strain to axial strain). Two parameter selections were made; one for a two-layered and one for a three-layered subsurface. In both cases Vs for each layer was chosen to lie between 50 and 800 m/s, and Vp was set to 200 to 5000 m/s for each layer. Poisson's ratio was constrained to a range of 0.2 to 0.5, and density to a range of 1500 to 2500 kg/m3. The two-layered model would have a layer-transition at a depth of 1 to 150 m. The three-layered model was set to have its first transition at a depth of 1 to 150 m, and its second transition at a depth of 1 to 200 m.

Realistic values for these parameters lie well within the chosen minima and maxima (Prasad et al., 2004). The table with input parameters for the two-layer inversion is provided in Figure 167.

The inversion itself is performed using Wathelet's modification (2008) of Sambridge's Neighborhood Algorithm (1999) considering 50 cells (nr) with 50 new random samples (ns) being generated and added with each iteration for a maximum of 50 iterations (itmax), until an acceptable solution is reached. This is done for all virtual source positions, for the stacked cross-correlations.

The optimal inversion results (with an ensemble of velocity-shear profiles as inversion solutions) are characterised by the smallest spreading of layer-velocities and layer transition depths. The two-layer model input provided results that are superior to the three-layer model input. Thereby the virtual surface wave data panels had been retrieved with a multi-day stack of a cross-correlation panels.

The transition found using the inversion with smallest misfit value at a depth of ±55m corresponds precisely with the transition of the Sterksel Formation to the Stramproy formation as found in nearby borehole survey data (Figure 168).

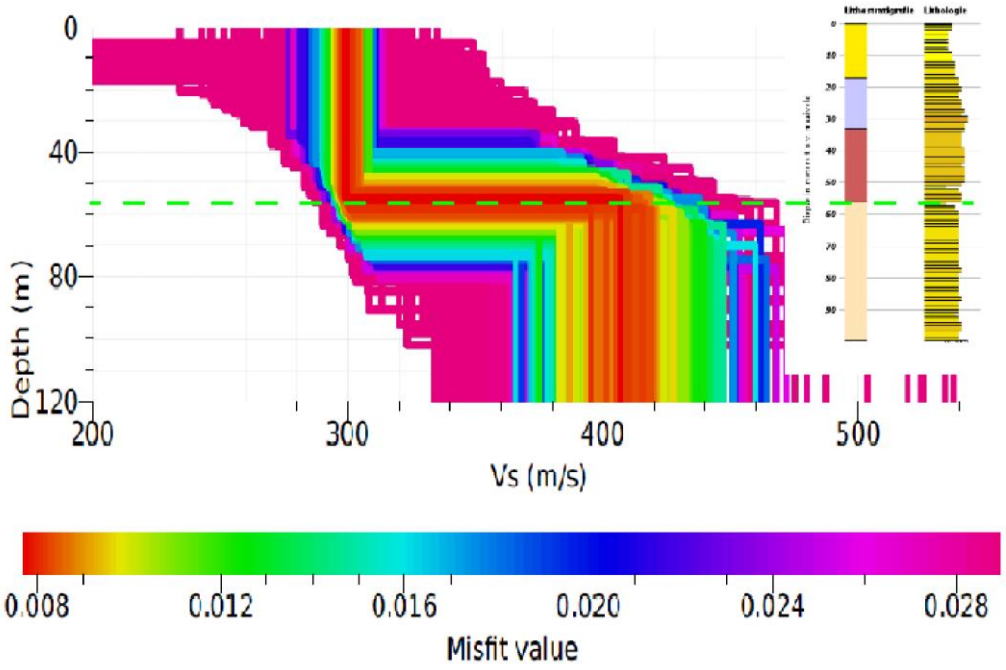

Figure 168 - Collection of shear wave velocity with depth profiles produced from inversion of the fitted curve in Figure 167, compared to borehole survey results (Figure 162). The transition found using inversion with smallest misfit value at a depth of ±55m corresponds precisely with the transition of the Sterksel Formation (dark brown) to the Stramproy formation (light brown). Adapted from B58A0122 (1985): www.dinoloket.nl/ondergrondgegevens.

That the dominant formation transition could be correctly located using ambient noise recordings, is a very satisfying result, but the question remained whether the depth resolution of such an inversion could possibly be improved by extending the bandwidth of the passive surface wave frequency spectrum on the high end by merging passive data with active data. This idea was tested using the active hammer-shot data described in the following.

6.5 Active survey results

For comparison with the passive data results, near the end of the acquisition period (July 2016) a relatively basic active survey was performed. Seismic events were created along the line of seismic stations by means of heavy hammer blows (Figure 169).

Figure 169 - Active seismic acquisition using a hammer and a metal plate.

The length of the active source line was approximately 800m, which equals the total length of the area accessible (Figure 158). The shot interval was half of the receiver spacing: 12.5 m. At each shot location at least 5 hammer blows were performed. During processing the individual hammer blows were stacked into one ‘shot’ for improvement of S/N ratio. Figure 170 shows a typical shot gather.

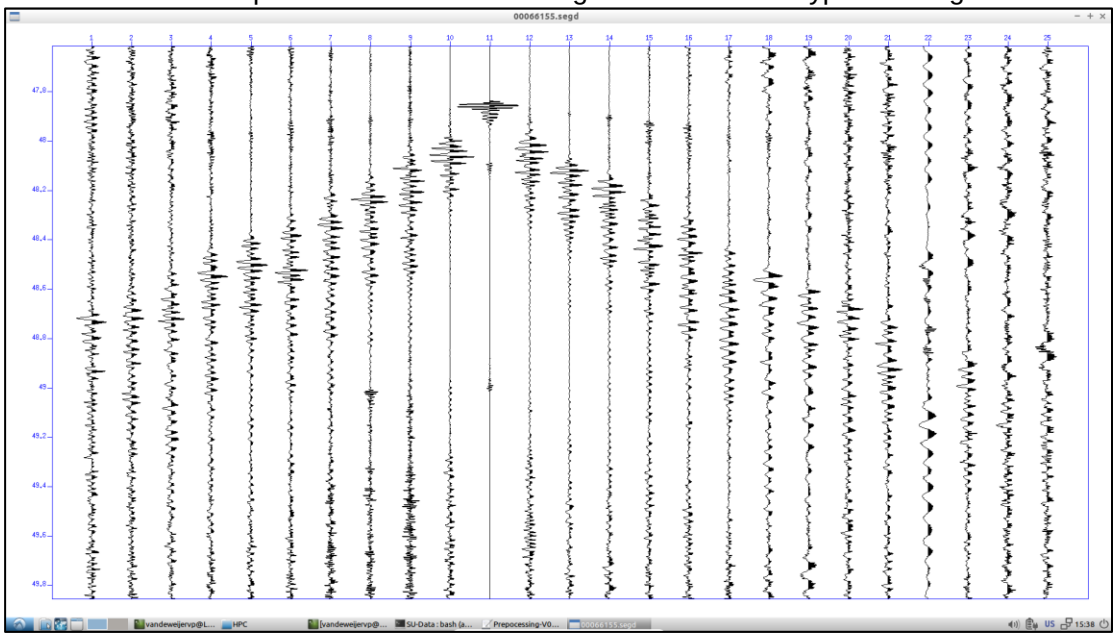

Figure 170 - Shot gather of a hammer blow at receiver location 11, displaying only data from the vertical component. Note that the total number of receivers (25) is slightly less than with the virtual source panels (33) of Figure 163.

Frequency analysis of the surface waves generated by this active source shows that they contain frequencies up to 60 Hz and that the dominant frequency lies around 30 Hz. Minimum frequency is about 15 – 20 Hz (no bandpass applied, only a dc-removal).
The fastest of these waves travel with a velocity of about 300 m/s. For the frequency band of interest, the corresponding minimum wavelength is about 5 m and the dominant wavelength 10 m, for lower velocities of about 180 m/s dominant wavelengths would be roughly 6 m. It is obvious that these actively generated surface waves are heavily aliased for a receiver distance of 25 m.
Therefore, we also looked at common receiver-gathers, because then the interval is 12.5 m, but, here also, the surface waves are still heavily aliased as can be seen in Figure 171.

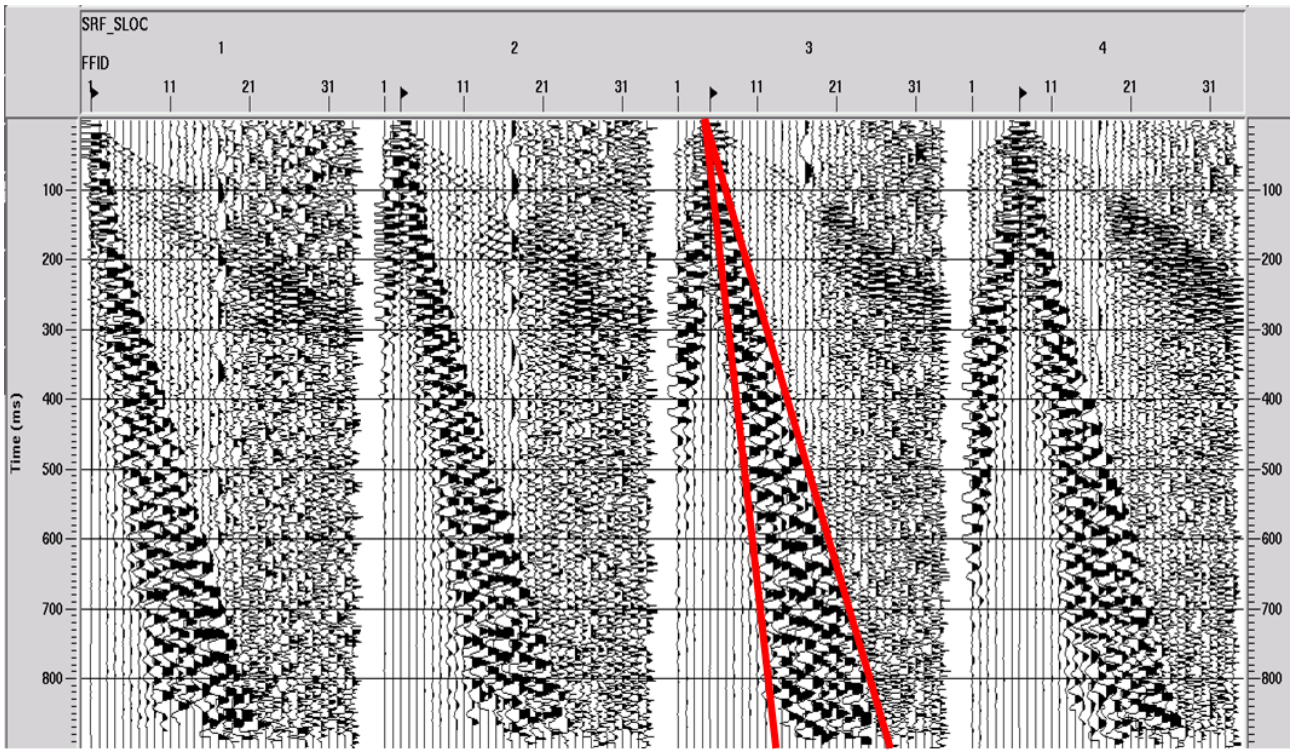

Figure 171 - A set of consecutive common receiver-gathers with receiver trace interval 12.5 m. Surface waves (present in cones as indicated by the red line segments) are still heavily aliased as can be seen in the figure.

Therefore, it was decided to apply linear moveout correction and sample-by-sample trace interpolation in the source-to-receiver offset domain. This approach can be justified by the fact that one can safely assume apparent velocity limits of the surface waves within cones as indicated by the red line segments on a receiver panel in Figure 171.

6.6 Extension of frequency-bandwidth and depth resolution of shear wave profiles by combining active and passive surface wave data

The result of testing the idea to extend the of frequency-bandwidth and depth resolution can be seen in Figure 172. The figure shows phase velocity versus frequency panels for ANSI-retrieved passive

surface waves (left panels in Figure 172a) and Figure 172b)), active hammer-shot-generated surface waves (centre panels in Figure 172a) and Figure 172b)), and merged active plus passive surface wave data results (panels on the right in Figure 172a) and Figure 172b)). The picked dispersion curves are indicated in red on the panels of Figure 172b).

We can observe that the dispersion curve picked on the merged data forms a smooth continuation to the high frequency side (up to ~30 Hz) of the dispersion curve picked on the passive data (up to ~10 Hz), thereby allowing shorter wavelengths to be used in the inversion with as result a shear-velocity versus depth profile with higher resolution (viz. thinner layers can be resolved).

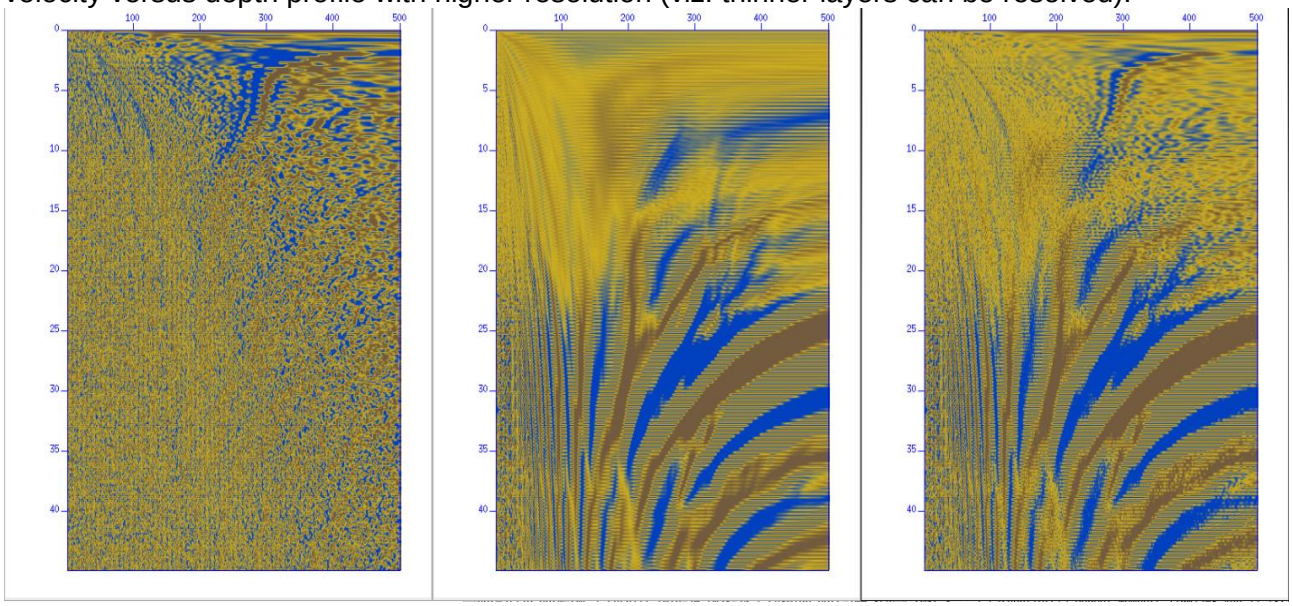

a)

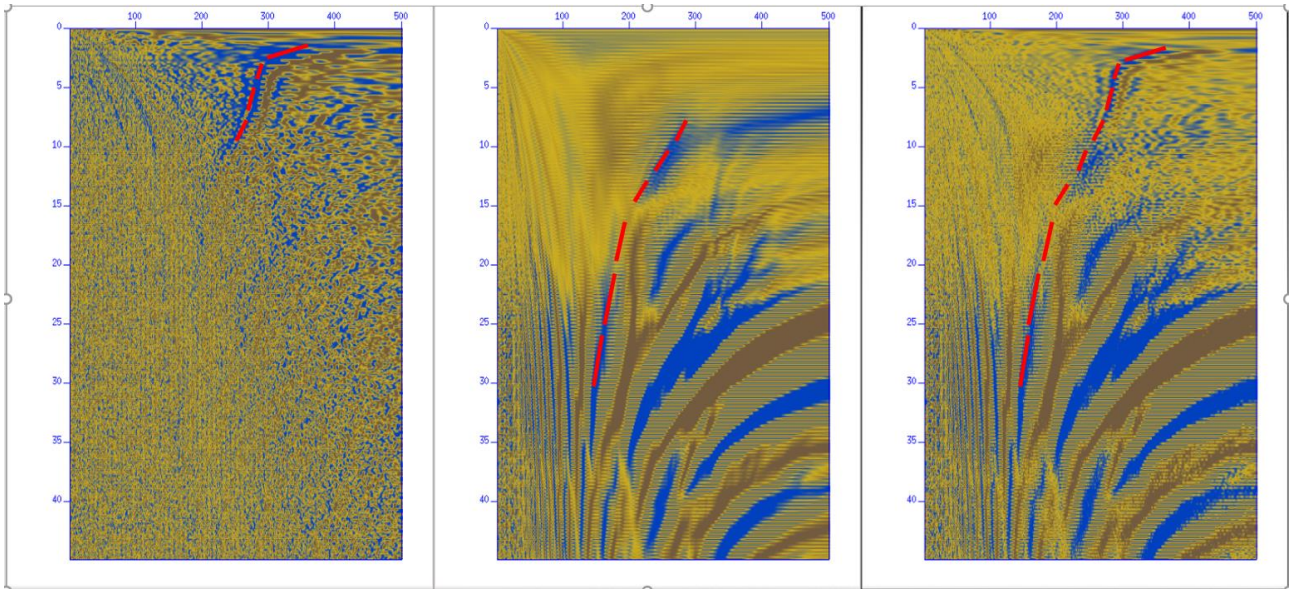

b)

Figure 172 - a) Phase-velocity (horizontal) versus frequency plots showing the dispersive character of measured (active) and retrieved (passive) surface waves. a) Left: passive data result; Centre: active data result; Right: merged active plus passive data result b) idem as a) but with a picked dispersion curve indicated in red on the panels. We can observe that the dispersion curve picked on the merged data forms a smooth continuation to the high

frequency side (up to approximately 30 Hz) of the dispersion curve picked on the passive data, thereby allowing shorter wavelengths to be used in the inversion with as result a shear-velocity versus depth profile with higher resolution (viz. thinner layers can be resolved).

6.7 Conclusions

Ambient noise seismic interferometry (ANSI) has proven to be an effective and efficient method for obtaining surface wave dispersion curves in the studied area. Inversion of these dispersion curves results in shear-wave velocity models, which can be used to give much needed insight into shallow subsurface properties.

As the ANSI method requires a relatively small fraction of the cost of an active seismic survey, it could be a valuable addition to future exploration. A combination of passive and active data allows for broadband subsurface analysis, thereby increasing the spatial resolution of the inversion, more specifically, increasing the resolution of shear velocity-versus-depth profiles/images in the subsurface.

Cross-correlation panels showed stronger surface wave signals during daytime hours for this passive survey. Several data selections have been made, the most efficient one including the data recorded between 08:00-20:59 on Mondays through Fridays. A manual data selection further improved the signal, but did not lead to a significant improvement in the final results. Therefore, the simple selection of daytime noise was preferred.

Inversion of the dispersion curves generated from cross-correlated ambient noise panels has resulted in shear-wave velocity profiles for the shallow subsurface (up to ±200m).

A dispersion curve picked on the merged active and passive data resulted in a smooth continuation to the high frequency side (up to ~30 Hz) of the dispersion curve picked on the passive data (up to ~10 Hz), thereby allowing shorter wavelengths to be used in the inversion with as result a shear-velocity versus depth profile/image with higher resolution (viz. thinner layers can be resolved). We consider this an important achievement.

A velocity transition was found at a depth of ± 55 m for the Working Hours (WH) data selection, which correlates very well with the transition of the Sterksel formation into the Stramproy formation as found in borehole studies. The shear-wave velocities found in this study can be used for improved structural imaging of geothermal reservoir potential, but also for computing rigidity and shear modulus of the subsurface which are vital properties for the construction industry.

All in all ANSI is an effective and low-cost acquisition and processing method for obtaining shallow shear-wave velocity profiles that can improve imaging of underlying reservoir structures. The TNO acquisition equipment proved to be very useful for testing this method.

References

Baize, S., Cushing, M., Lemeille, F., Gelis, C., Texier, D., Nicoud, G. and Schwenninger, J.L. (2011). Contribution to the seismic hazard assessment of a slow active fault, the Vuache fault in the southern Molasse basin (France). Bull. Soc. géol. France**,** 182/4, 347-365.

Abers GA, Hu X, Sykes LR (1995) Source scaling of earthquakes in the Shumagin region, Alaska: time-domain inversions of regional waveforms. Geophys J Int 123:41–58.

Agostinetti NP, Licciardi A (2015) SIM-CRUST Project - Seismic Imaging and Monitoring of the Upper Crust : Exploring the Potential Low-Enthalpy Geothermal Resources of Ireland. World Geotherm. Congr. 2015, Melbourne, Aust. 19-25 April

Allegre, C. J., Lemouel, J. L., Provost, A. (1982). Scaling Rules in Rock Fracture and Possible Implications for Earthquake Prediction. Nature 297, 47-49.

Ardhuin F., Stutzmann E., Schimmel M. and Mangeney A. (2011), Ocean wave sources of seismic noise, Journal of Geophysical Research, Vol. 116, C09004, doi:10.1029/2011JC006952

Bak, P., Tang, C., Wiesenfeld, K. (1988). Self-organized criticality. Phys Rev A Gen Phys 38, 364-374.

Barth S.R. (2000) - Utilization of boron as a critical parameter in water quality evaluation: implications for thermal and mineral water resources in SW Germany and N Switzerland. *Environmental Geology*, 40, 73-89.

Barton, C. A. & Zoback, M. D. (1992). Self-similar distribution and properties of macroscopic fractures at depth in crystalline rock in the Cajon Pass Scientific Drill Hole. Journal of Geophysical Research: Solid Earth (1978–2012) 97, 5181-5200.

Barton, C. C. (1995). Fractal analysis of scaling and spatial clustering of fractures. Fractals in the earth sciences: Springer, 141-178.

Bensen, G.D., Ritzwoller, M.H., Barmin, M.P., levshin, A.L., Lin, F., Moschetti, M.P., Shapiro, N.M., & Yang, Y., (2007). Processing seismic ambient noise data to obtain reliable broad-band surface wave dispersion measurements. *Geophys. J. Int.* (2007) 169, 1239-1260.

Boadu, F. & Long, L. (1994). The fractal character of fracture spacing and RQD. International journal of rock mechanics and mining sciences & geomechanics abstracts: Elsevier, 127-134.

Bonar,D. and Sacchi, M., Denoising seismic data using the nonlocal means algorithm. Geophysics 77 (1), 2012

Bonnet, E., Bour, O., Odling, N. E., Davy, P., Main, I., Cowie, P., Berkowitz, B. (2001). Scaling of fracture systems in geological media. Reviews of Geophysics 39, 347-383.

Boschetti T. (2013) - Oxygen isotope equilibrium in sulfate-water systems: A revision of geothermometric applications in low-enthalpy systems. *Journal of Geochemical Exploration*, 124, 92-100.

Bour, O. & Davy, P. (1999). Clustering and size distributions of fault patterns: theory and. Geophys Res Lett 26, 2001-2004.

Bour, O., Davy, P., Darcel, C., Odling, N. (2002). A statistical scaling model for fracture network geometry, with validation on a multiscale mapping of a joint network (Hornelen Basin, Norway). Journal of Geophysical Research: Solid Earth 107.

Buades, A., Coll, B., and Morel, J.M., A review of image denoising algorithms with a new one. Multiscale Modeling and Simulation, Vol. 4, No. 2, pp. 490–530, 2005

Carpentier, S., Steeghs, P., Final Report Work Package: New active seismic processing techniques developed. EU Project IMAGE, 7.1, 2016

Chave, A. D., & Jones, A. G. (Eds.). (2012). The magnetotelluric method: Theory and practice. Cambridge University Press.

Chave, A. D., & Thomson, D. J. (2004). Bounded influence magnetotelluric response function estimation. Geophysical Journal International, 157(3), 988-1006.

Clayton RW, Wiggins RA (1976) Source shape estimation and deconvolution of teleseismic body waves. Geophys J R Astron Soc 47:151–177.

Constable S., 2010, Ten years of marine CSEM for hydrocarbon exploration, Geophysics, Vol 75, No 5, P. 75A67–75A81, doi 10.1190/1.3483451

Constable, S. C., R. L. Parker, and C. G. Constable, (1987) – Occam's inversion – A practical algorithm for generating smooth models from electromagnetic sounding data. Geophysics, 52, 289–300.

Cowie, P., Knipe, R., Main, I. (1996). Special issue: Scaling laws for fault and fracture populations-Analyses and applications-Introduction. PERGAMON-ELSEVIER SCIENCE LTD THE BOULEVARD, LANGFORD LANE, KIDLINGTON, OXFORD, ENGLAND OX5 1GB.

Craig H. (1961) - Isotopic variations in meteoric waters. *Science,* 133, 1702-1703.

D'Amore F. and Panichi C. (1980) - Evaluation of deep temperatures of hydrothermal systems by a new gas-geothermometer. *Geochim. Cosmochim. Acta*, 44, 549-556.

Darcel, Bour, O., Davy, P. (2003). Stereological analysis of fractal fracture networks. Journal of Geophysical Research: Solid Earth 108, n/a-n/a.

Davy, Le Goc, R., Darcel, C., Bour, O., De Dreuzy, J.-R., Munier, R. (2010). A likely universal model of fracture scaling and its consequence for crustal hydromechanics. Journal of Geophysical Research: Solid Earth 115.

Davy, Sornette, A., Sornette, D. (1990). Some consequences of a proposed fractal nature of continental faulting. Nature 348, 56-58.

Day-Lewis, A. D. (2007). Characterization and modeling of in situ stress heterogeneity.

de Dreuzy, J. R., Davy, P., Bour, O. (2002). Hydraulic properties of two-dimensional random fracture networks following power law distributions of length and aperture. Water Resources Research 38.

de Dreuzy, J.-R., Davy, P., Bour, O. (2001). Hydraulic properties of two-dimensional random fracture networks following a power law length distribution 1. Effective connectivity. Water Resources Research 37, 2065-2078.

de Haller A., Tarantola A., Mazurek M., Spangenberg J. (2011) - Fluid flow through the sedimentary cover in northern Switzerland recorded by calcite–celestite veins (Oftringen borehole, Olten). *Swiss J Geoscience*, 104, 493-506.

Deere, D. & Deere, D. (1988). The rock quality designation (RQD) index in practice. Symposium on Rock Classification Systems for Engineering Purposes, 1987, Cincinnati, Ohio, USA.

Derode, A., E. Larose, M. Tanter, J. de Rosny, A. Tourin, M. Campillo, *and* M. Fink *(*2003*),* Recovering the Green's function from field-field correlations in an open scattering medium (L), J. Acoust. Soc. Am., 113, 2973–2976.

Dezayes C, And A, Valley B (2010) Structure of the low permeable naturally fractured geothermal reservoir at Soultz. C R Geosci 342:517–530.

DMT, report, Neubearbeitung 2D-seismischer Daten Bad Waldsee, 2016

Eagar KC (2011) FuncLab: MATLAB receiver function analysis toolbox, Version: 1.5.2 User Manual. 35.

Eagar KC, Fouch MJ (2012) FuncLab: A MATLAB Interactive Toolbox for Handling Receiver Function Datasets.

Eagar KC, Fouch MJ, James DE, Carlson RW (2011) Crustal structure beneath the High Lava Plains of eastern Oregon and surrounding regions from receiver function analysis. J Geophys Res 116:1–18. doi: 10.1029/2010JB007795

Eshelby, J. D. (1957). The determination of the elastic field of an ellipsoidal inclusion, and related problems. Proceedings of the Royal Society of London A: Mathematical, Physical and Engineering Sciences: The Royal Society, 376-396.

Etat de Géneve – Department des travaux publics et de l'energie (1994). Forage géothermique de Thônex – Rapport Final Volume 1

Etiope G., Feyzullayev A., Baciu C.L. (2009) - Terrestrial methane seeps and mud volcanoes: A global perspective of gas origin. *Marine and Petroleum Geology*, 26, 333-344.

Etiope G., Zwahlen C., Anselmetti F.S., Kipfer R., Schubert C.J. (2010) - Origin and flux of a gas seep in the Northern Alps (Giswil, Switzerland). *Geofluids*, 10, 476-485.

Evans, K. F. (2005). Permeability creation and damage due to massive fluid injections into granite at 3.5 km at Soultz: 2. Critical stress and fracture strength. Journal of Geophysical Research: Solid Earth 110.

Evans, K. F., Genter, A., Sausse, J. (2005). Permeability creation and damage due to massive fluid injections into granite at 3.5 km at Soultz: 1. Borehole observations. Journal of Geophysical Research: Solid Earth 110.

Fouillac C., Fouillac A. M., Criaud A. (1990) - Sulphur and oxygen isotopes of dissolved sulphur species in formation waters from the Dogger geothermal aquifer, Paris Basin, France. *Applied Geochemistry*, 5, 415-427.

Fournier R.O. (1979) - A revised equation for the Na/K geothermometer. *Geoth. Res. Council Trans*., 3, p. 221-224.

Fournier R.O. and Potter R.W. (1979) - Magnesium correction to the Na-K-Ca chemical geothermometer. *Geochim. Cosmochim. Acta*, 43, 1543-1550.

Fournier R.O. and Truesdell A.H. (1973) - An empirical Na-K-Ca geothermometer for natural waters. *Geochim. Cosmochim*. Acta, 37, p. 1255-1275.

Frassetto A (2013) Understanding the Earth by stacking receiver functions: The H-K method.

Gamble, T. D., Goubau, W. M., & Clarke, J. (1979). Magnetotellurics with a remote magnetic reference. Geophysics, 44(1), 53-68.

Genter, A., Evans, K., Cuenot, N., Fritsch, D., Sanjuan, B. (2010). Contribution of the exploration of deep crystalline fractured reservoir of Soultz to the knowledge of enhanced geothermal systems (EGS). Comptes Rendus Geoscience 342, 502-516.

Giggenbach W.F. (1988) - Geothermal solute equilibria. Derivation of Na-K-Mg-Ca geoindicators. *Geochim. Cosmochim*. Acta 52, p. 2749-2765.

Giggenbach W.F. and Goguel R.L. (1989) - Collection and analysis of geothermal and volcanic water and gas discharges. *Fourth Edition. Report CD2401, Chemistry Division, DSIR*, New Zealand.

Giggenbach, W.F. (1991) - Chemical techniques in geothermal exploration. *In: D'Amore, F., Applications of geochemistry in geothermal reservoir development*, 119-144.

Giustini F., Brilli M., Patera A. (2016) - Mapping oxygen stable isotopes of precipitation in Italy. *Journal of Hydrology: Regional studies*, 8, 162-181.

Gorin, G.E., Signer, C. and Amberger, G. (1993). Structural configuration of the western Swiss Molasse Basin as defined by reflection seismic data. -Eclogae geol. Helv., 86/1, 693-716.

Gurrola H, Baker GE, Minster JB (1995) Simultaneous time domain deconvolution with application to the computation of receiver functions. Geophys J Int 120:537–543.

Häring, M. O., Schanz, U., Ladner, F., Dyer, B. C. (2008). Characterisation of the Basel 1 enhanced geothermal system. Geothermics 37, 469-495.

Herrmann RB (2013) Computer programs in seismology: An evolving tool for instruction and research. Seism Res Lettr 1081–1088.

IAEA (1992) - Statistical treatment of data on environmental isotopes in precipitation. *International Atomic Energy Agency Technical report series* n° 331, 782 p.

International Discrete Fracture Network Engineering Conference DFNE 2014. Vancouver, BC, Canada.

Jenny, J., Burri, J. P., Muralt, R., Pugin, A., Schegg, R., Ungemach, P., Vuataz, F., and Wemli, R. (1995). Le forage géothermique de Thônex (Canton de Genève): Aspects stratigraphiques, tectoniques, diagénétiques, géophysiques et hydrogéologiques. Eclogae Geol. Helv., 88(2), 365-396.

Kennett BLN, Engdahl ER, Buland R (1995) Constraints on seismic velocities in the Earth from traveltimes. J Geoph Int 122:108–124.

Kerry K. (2009) – 1D inversion of multicomponent, multifrequency marine CSEM data: Methodology and synthetic studies for resolving thin resistive layers, Geophysics, 74 (2), F9–F20, doi: 10.1190/1.3058434.

Kharaka Y.K. and Mariner R.H. (1989) - Chemical geothermometers and their application to formation waters from sedimentary basins. In: Naeser, N.D. and McCulloch, T.H. (eds), Thermal history of sedimentary basins: methods and case histories. *Springer-Verlad*, New York, 99-117.

Kikuchi M, Kanamori H (1982) Inversion of complex body waves. Bull Seism Soc Am 72:491–506.

Kind R, Vinnik LP (1988) The upper mantle discontinuities underneath the GRF array from P-to-S converted phases. J Geophys 62:138–147.

Kloppmann W., Blessing M., Proust E., Gal F., Bentivegna G., Henry B., Defossez P., Catherine C., Humez P., Mayer B., Millot R., Gaucher E. (2016) - Natural gas seeps in the French Alps: Sources and pathways. *Geophysical Research Abstracts*, vol. 18, EGU2016-14484, EGU2016.

Konno K. and Ohmachi T. (1998) Ground-motion characteristics estimated from spectral ratio between horizontal and vertical components of microtremor, Bulletin of the Seismological Society of America, 88, p. 228-241.

Kraft, T. & Deichmann, N. (2014). High-precision relocation and focal mechanism of the injection-induced seismicity at the Basel EGS. Geothermics 52, 59-73.

Kusakabe M., Robinson B.W. (1977) - Oxygen and sulfur isotope equilibria in the system from 110 to 350°C and applications. *Geochimica et Cosmochimica Acta*, 41, 1033-1040.

Langston CA (1979) Structure under Mount Rainier, Washington, inferred from teleseismic body waves. J Geophys Res 84:4749–4762. doi: 10.1029/JB084iB09p04749

Leahy GM, Saltzer RL, Schmedes J (2012) Imaging the shallow crust with teleseismic receiver functions. Geophys J Int 191:627–636. doi: 10.1111/j.1365-246X.2012.05615.x

Lei, Q., Latham, J. P., Tsang, C. F., Xiang, J., Lang, P. (2015). A new approach to upscaling fracture network models while preserving geostatistical and geomechanical characteristics. Journal of Geophysical Research: Solid Earth 120, 4784-4807.

Levin V, Park J (1998) P-SH conversions in layered media with hexagonally symmetric anisotropy: a cookbook. Pure appl Geophys 151:669–697.

Licciardi A, Agostinetti NP (2014) High Frequency Receiver Functions in the Dublin Basin: Application to a Potential Geothermal Site. Energy Procedia 59:221–226.

Licciardi A, Agostinetti NP (2017) Sedimentary basin exploration with receiver functions: Seismic structure and anisotropy of the Dublin Basin (Ireland). Geophysics 82:KS41–KS55. doi: 10.1190/GEO2016-0471.1

Ligorria JP, Ammon CJ (1999) Iterative deconvolution and receiver-function estimation. Bull Seism Soc Am 89:1395–1400.

Lloyd, R.M. (1968) - Oxygen isotope behavior in the sulfate-water system. J. Geophys. Res.**, 73**, 6099-6110.

Longinelli A., Stenni B., Genoni L., Flora O., Defrancesco C., Pellegrini G. (2008) - A stable isotope study of the Garda Lake, Northern Italy: its hydrological balance. *Journal of Hydrology*, 360, 103-116.

Manukyan, E., Maurer, H., & Nuber, A. (2016). Improvements to elastic full waveform inversion using cross-gradient constraints. In SEG Technical Program Expanded Abstracts 2016 (pp. 1506-1510). Society of Exploration Geophysicists.

Maurer, H., Greenhalgh, S.A., Manukyan, E., Marelli, S., Green, A.G., 2012. Receiver-coupling effects in seismic waveform inversions. Geophysics 77, R57–R63.

Mazurek M., Waber H.N., Mäder U.K., Gimmi T., de Haller A., Koroleva M. (2012) - Geochemical synthesis for the Effingen member in boreholes at Oftringen, Gösgen and Küttigen. *NAGRA Technical Report 12-07*, 294 p.

McKibben M.A., Williams A.E., Elders W.A., Eldridge C.S. (1987) - Saline brines and metallogenesis in a modern sediment-filled rift: the Salton Sea geothermal system, California, USA. *Applied Geochemistry*, 2, 563-578.

Meyer, M., 2000. Le complexe récifal kimméridgien-tithonien du Jura méridional interne (France), évolution multifactorielle, stratigraphie et tectonique. Terre & Environnement (Université de Genève), 24, 179p.

Michard G. (1990) - Behaviour of major elements and some trace elements (Li, Rb, Cs, Sr, Fe, Mn, W, F) in deep hot waters from granitic areas. *Chem. Geol.*, 89, p. 117-134.

Millot R., Guerrot C., Innocent C., Négrel P., Sanjuan B. (2011) - Chemical, multi-isotopic (Li-B-Sr-U-H-O) and thermal characterization of Triassic formation waters from the Paris Basin. *Chemical Geology*, 283, 226-241.

Mizutani Y. and Rafter T.A. (1969) - Oxygen isotopic composition of sulphates, 3. Oxygen isotopic fractionation in the bisulphate ion-water system. *N. Zealand J. Sci.*, 12, p. 54-59.

Mohsen A (2004) A receiver function study of the crust and upper mantle across the Dead Sea Transform. Freien Universität Berlin

Newman, G. A., & Hohmann, G. W. (1988). Transient electromagnetic responses of high-contrast prisms in a layered earth. Geophysics, 53(5), 691-706.

Odling, Gillespie, P., Bourgine, B., Castaing, C., Chiles, J., Christensen, N., Fillion, E., Genter, A., Olsen, C., Thrane, L. (1999). Variations in fracture system geometry and their implications for fluid flow in fractured hydrocarbon reservoirs. Petroleum Geoscience 5, 373-384.

Paces T. (1975) - A systematic deviation from Na-K-Ca geothermometer below 75°C and above 10^{-4} atm pCO_2 - *Geochimica et Cosmochimica Acta*, 39, 541-544.

Paolacci, S., 2012. Seismic facies and structural configuration of the Western Alpine Basin and its substratum (France and Switzerland). Ph.D. thesis, University of Geneva, unpublished.

Park J, Levin V (2000) Receiver functions from multiple-taper spectral correlation estimates. Bull Seism Soc Am 90:1507–1520.

Pedersen, L. B. (1982). The magnetotelluric impedance tensor—Its random and bias errors. Geophysical Prospecting, 30(2), 188-210.

Pedroni A., Hammerschmidt K. and Friedrichsen H. (1999) - He, Ne, Ar, and isotope systematics of geothermal emanations in the lesser Antilles Islands Arc. *Geochim. Cosmochim*. Acta, Vol. 63, n° 3/4, p. 515-532.

Peiffer L., Wanner C., Spycher N., Sonnenthal E.L., Kennedy B.M., Iovenitti J. (2014) - Optimized multicomponent vs. classical geothermometry: Insights from modeling studies at the Dixie Valley geothermal area. *Geothermics*, 51, 154-169.

Plessix, R.-É., Perkins, C., 2010. Full waveform inversion of a deep water ocean bottom seismometer dataset. First Break 28, 71–78.

Pollard, D. & Segall, P. (1987). Theoretical displacements and stresses near fractures in rock: with applications to faults, joints, veins, dikes, and solution surfaces. Fracture mechanics of rock 277, 277-349.

Power, W. L. & Tullis, T. E. (1991). Euclidean and fractal models for the description of rock surface roughness. Journal of Geophysical Research: Solid Earth (1978–2012) 96, 415-424.

RESIF; (1995): RESIF-RLBP French Broad-band network, RESIF-RAP strong motion network and other seismic stations in metropolitan France; RESIF - Réseau Sismologique et géodésique Français. http://dx.doi.org/10.15778/RESIF.FR

Sambeth, U. and Pavoni, N. (1988). A seismotectonic investigation in the Geneva Basin, southern Jura Mountains. Eclogae geol. Helv., 81, 433-440

Sanjuan B., Gal F., Millot R., Dezayes Ch., Jirakova H., Frydrych V. (2015) - Chemical geothermometers and tracer tests. *FP7-IMAGE D7.08 technical report*, 39 p.

Sanjuan B., Gal F., Millot R., Dezayes Ch., Jirakova H., Frydrych V., Nawratil de Bono C., Martin F. (2016a) - Chemical geothermometers and tracer tests. *Final FP7-IMAGE D7.03 technical report*, 74 p.

Sanjuan B., Millot R., Asmundsson R., Brach M., Giroud N. (2014) - Use of two new Na/Li geothermometric relationships for geothermal fluids in volcanic environments. *Chemical Geology,* 389, 60-81.

Sanjuan B., Millot R., Dezayes Ch. (2016b) - Three new auxiliary chemical geothermometers for hot brines from geothermal reservoirs. *Goldschmidt 2016 Conference Abstract, June 26 - July 1*, *Yokohama, Japan,* 1 p.

Sanjuan B., Millot R., Innocent Ch., Dezayes Ch., Scheiber J., Brach M. (2016c) - Main geochemical characteristics of geothermal brines collected from the granite basement in the Upper Rhine Graben and constraints on their deep temperature and circulation. *Chemical Geology,* 428, 27-47.

Savage MK (1998) Lower crustal anisotropy or dipping boundaries? Effects on receiver functions and a case study in New Zealand. J Geophys Res 103:15069–15086.

Schmedes J, Saltzer RL, Roth JB, Leahy GM (2012) Imaging the shallow crust using teleseismic tomography. Bull Seism Soc Am 102:1276–1282. doi: 10.1785/0120110217

Schmelzbach, C., F. Reiser, S. A. Greenhalgh, J. F. Girard, F. Bretaudeau, L. Capar, and A. Bitri (2016), Advanced seismic processing/imaging techniques and their potential for geothermal exploration, Interpretation, 4(4), SR1–SR18, doi:10.1190/INT-2016-0017.1.

Shamir, G., Zoback, M. D., 1992. Stress orientation profile to 3.5 km depth near the san andreas fault at cajon pass, california. Journal of Geophysical Research 97 (B4), 5059-5080.

Sheehan AF, Abets GA, Leruer-Lam AL, Jones CH (1995) Crustal thickness variations across the Colorado Rocky Mountains from teleseismic receiver functions. J Geophys Res 100:20391–20404. doi: 10.1029/95JB01966

Signer, C. and Gorin, G.E. (1995). New geological observations between the Jura and the Alps in the Geneva area, as derived from reflection seismic data. Eclogae geol. Helv., 88/2, 235-265.

Sirgue, L., Pratt, R.G., 2004. Efficient waveform inversion and imaging: A strategy for selecting temporal frequencies. Geophysics 69, 231–248.

Sornette, D. (2006). Critical phenomena in natural sciences: chaos, fractals, selforganization and disorder: concepts and tools: Springer Science & Business Media.

Sornette, D., Davy, P., Sornette, A. (1990). Structuration of the lithosphere in plate tectonics as a self-organized critical phenomenon. Journal of Geophysical Research: Solid Earth 95, 17353-17361.

Spycher N., Peiffer L., Sonnenthal E.L., Saldi G., Reed M.H., Kennedy B.M. (2014) - Integrated multicomponent solute geothermometry. *Geothermics*, 51, 113-123. DOI: DOI:10.1016/ j.geothermics.2013.10.012.

Spyropoulos, C., Scholz, C. H., Shaw, B. E. (2002). Transition regimes for growing crack populations. Physical Review E 65, 056105.

Stadt Bad Waldsee, website, http://www.stadtwerke-bad-waldsee.de/geothermie.html, 2017

Strauss H., Chmiel H., Christ A., Fugmann A., Hanselmann K., Kappler A., Königer P., Lutter A., Siedenberg K., Teichert B.M.A. (2016) - Multiple sulphur and oxygen isotopes reveal microbial sulphur cycling in spring waters in the Lower Engadin, Switzerland. *Isotopes in Environmental and Health Studies*, vol. 52, n°1-2, 75-93.

Streich, R., Becken, M., & Ritter, O. (2013). Robust processing of noisy land-based controlled-source electromagnetic data. Geophysics, 78(5), E237-E247.

The 2014 ISRM European Rock Mechanics Symposium (EUROCK 2014). In: Alejano, L. R., Perucho, Á., Olalla, C., Jiménez, R. (eds.) Eurock 2014: Rock Engineering and Rock Mechanics: Structures in and on Rock Masses. Vigo, Spain: CRC Press, 463-468.

Valley, B. & Evans, K. (2014). Preliminary assessment of the scaling relationships of in-situ stress orientation variations indicated by wellbore failure data

Valley, B., Jalali, M. R., Ziegler, M., Evans, K. F. (2014). Constraining DFN characteristics for deep geothermal projects by considering the effects of fractures on stress variability

Varentsov, I. M. (2006). Arrays of simultaneous electromagnetic soundings: design, data processing and analysis. Methods in Geochemistry and Geophysics, 40, 259-273.

Vuataz F.-D. and Giroud N. (2010) - Caractéristiques géochimiques du fluide profond du forage géothermique Thônex-1, Genève. *Rapport du Laboratoire de géothermie - CREGE*, 29 p.

Wathelet, M. (2008). An improved neighborhood algorithm: parameter conditions and dynamic scaling. Geophysical Research Letters, 35, L09301, doi:10.1029/2008GL033256

Werner H.H. (1970) - Contribution to the mineral extraction from supersaturated geothermal brines, Salton Sea area, California. *U.N. Symposium on the Development and Utilization of Geothermal Resources, Pisa 1970,* vol. 2, Part 2, 1651-1655.

Zandt G, Ammon CJ (1995) Continental crust composition constrained by measurements of crustal Poisson's ratio. Nature 374:152–154. doi: 10.1038/374152a0

Zhu L, Kanamori H (2000) Moho depth variation in southern California from teleseismic receiver functions. J Geophys Res 105:2969–2980. doi: 10.1029/1999JB900322

Ziegler, M., Valley, B., Evans, K. F. (2015). Characterisation of natural fractures and fracture zones of the Basel EGS reservoir inferred from geophysical logging of the Basel-1 well. World Geothermal Congress Melbourne, Australia, 19-25.

Zonge, K.L. and Hughes, L.J., 1991, "Controlled source audio-frequency magnetotellurics", in Electromagnetic Methods in Applied Geophysics, ed. Nabighian, M.N., Vol. 2, Society of Exploration Geophysicists, pp. 713-809.

Aknowledgements

For their help in the framework of the geophysic surveys around Strasboug, authors want to thank:
- SDIS du Bas-Rhin;
- Communes Ittenheim, Lingolsheim, Mittelhausbergen, Dingsheim, Wiwersheim;
- L'entreprise LINGENHELD;
- Mme Mall.

And the Canton of Geneva for the Thonex VSP survey.

Appendix 1. Detailled VSP survey in the Thonex well.

In the framework of the H2020 Image Project, a partnership between the University of Geneve, Services Industriels and BRGM required OGS to perform a VSP survey in Switzerland, Geneva, in the geothermal well Thonex-1.

1- Survey Planning (Synthesis of INOGS official Acquisition Report - Report OGS 2017 / 7 GEO 4 GEOP)

1.1- Well description and 1st Planning

The well is located nearby Geneva, in Thonex, as reported in Table 16. The well was drilled with a deviation of 20° - 26°[2] (Fig. 1b, c)

Table 16 - Well data

Name	East (CH1903)	North (CH1903)	Water Level	Notes
Thonex-1	505214.807	117501.95	0	Deviated well, accessible down to 1800m MD

[2] Etat de Géneve – Department des travaux publics et de l'energie (1994). Forage géothermique de Thônex – Rapport Final Volume 1

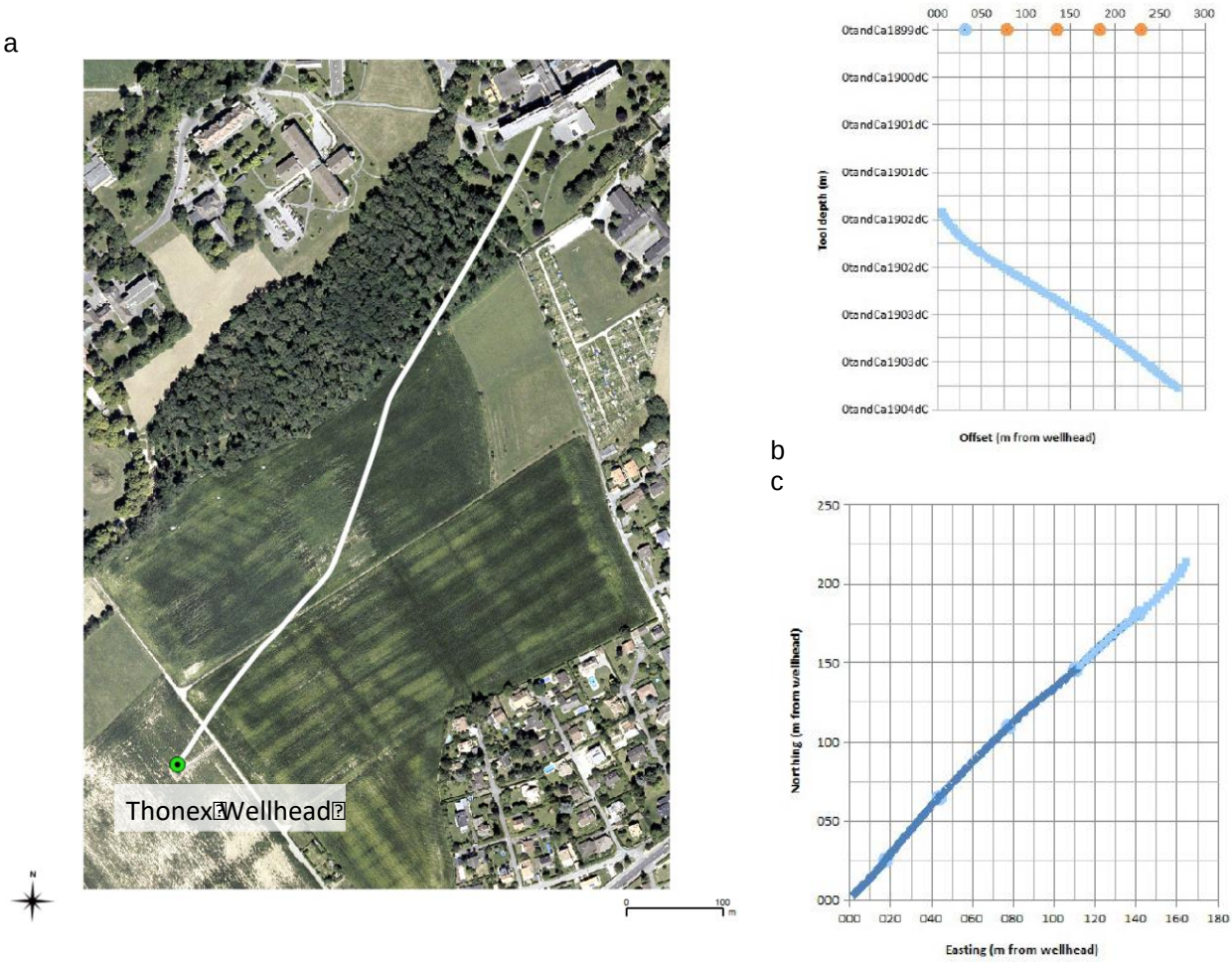

Fig. 1 – a. Well Map and well deviation line (b. deviation on vertical section and c. projection over horizontal section)

The well was drilled in 1994, with a casing design as diplayed in Fig. 2. The final depth was over 2600 m depth, and the well was cased until 1800 m. In 2007 an inspection found an obstruction at about 1100 m, which was reopened by means of coil-tubing technique. The open hole at this date was already obstructed.

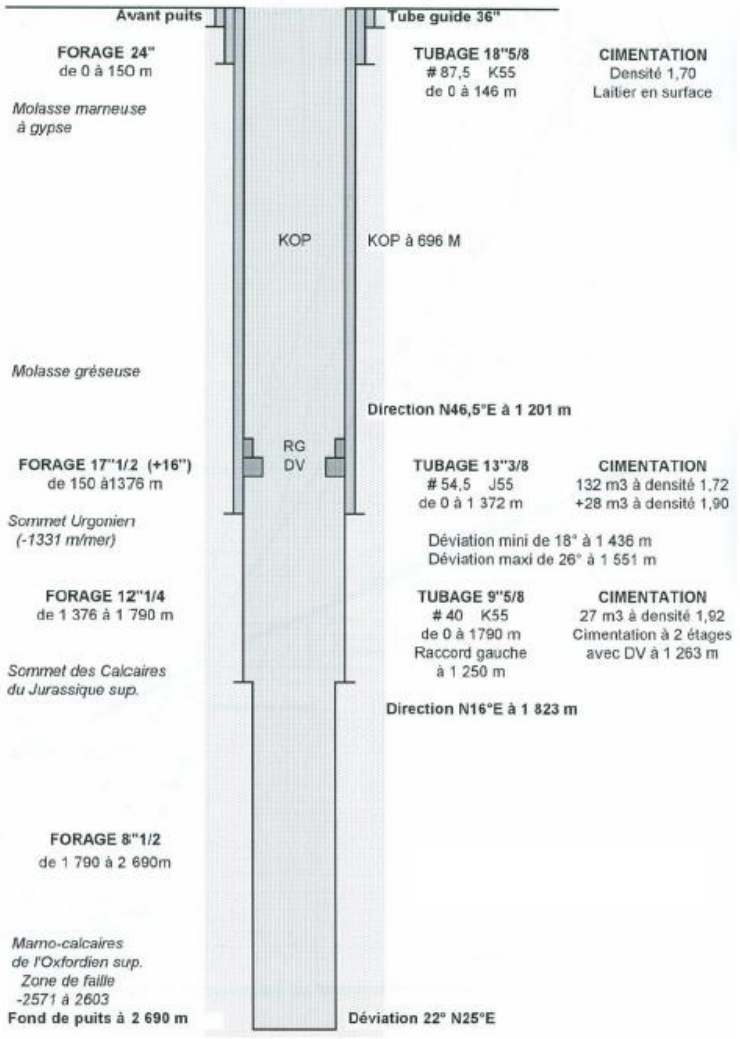

Fig. 2 – Well design

In the first survey design two offsets were planned: one near offset and another offset in the direction of the deviation. Moreover a walk above survey was proposed as optional. In the original project the energy source would have been provided by two Vibroseis controlled by a Sercel System, and the walk above was planned to cover a path relative to 1800 m depth with 7 vibration points, and double fold coverage for the whole deviation except the 12 downhole positions nearest to the well and the 12 farthest from the well.
After the installation the first descent in the well cannot proceed deeper than 1500 m depth. Moreover a problem occurred on the connector of the winch, and the repairing operations take two days.
At the operative meeting, the problem is discussed and it is agreed to suspend the operations, due to lack of remaining survey time. The survey is rescheduled to the next available time slot, when a suitable timing can be fixed, in order to complete all the planned operation.

1.2- Second Planning
The second planning has been more ambitious, and started by an operative meeting, where three offsets and a walk above were planned (Fig. 3).

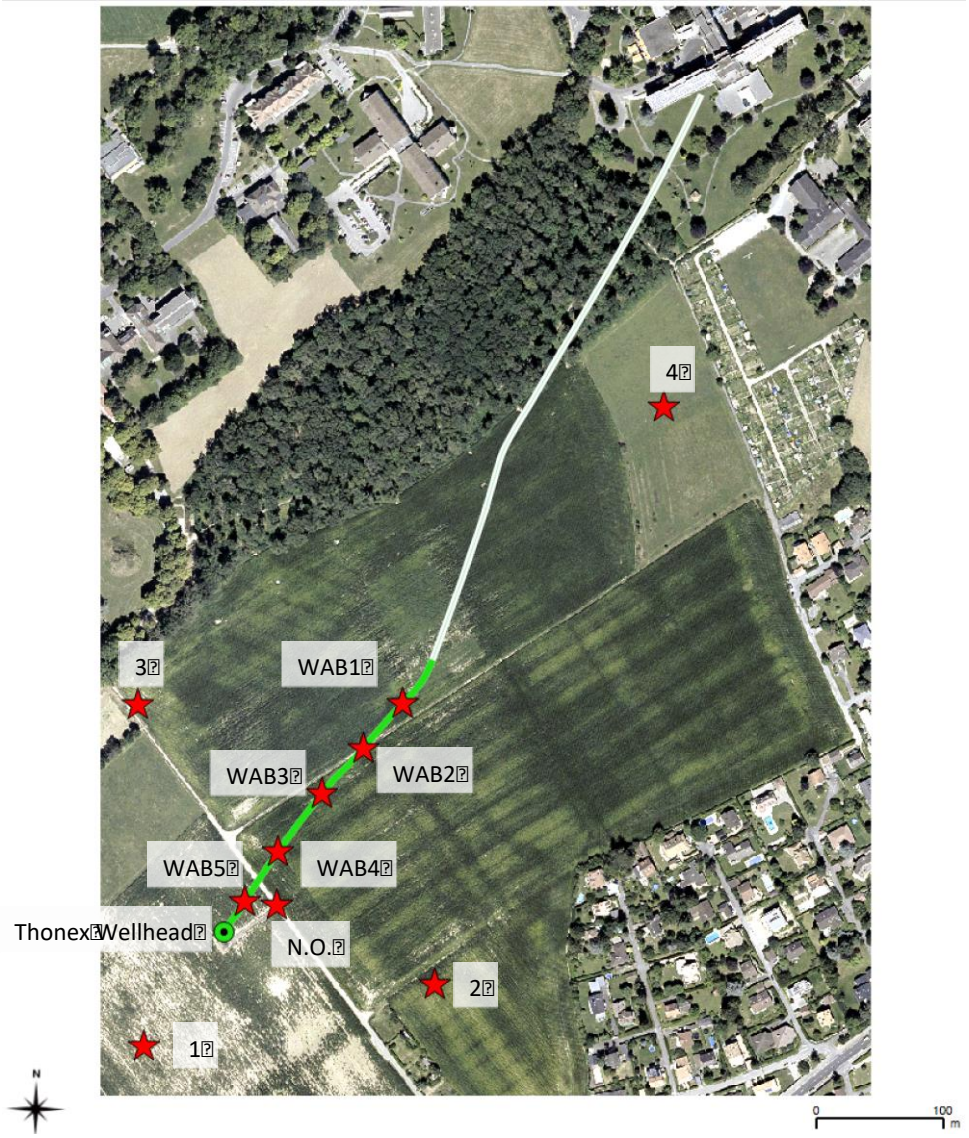

Fig. 3 – Second design showing the location of the Vibro-points

In this second survey the source is provided by OGS, a Prakla Vibroseis contolled by a Seismic Source Force II system.
Following the result of the first survey, a maximum depth of 1500 m is stated. This condition forces a walk above survey design modi_cation in 5 vibro points, to be completed alternatively in two different trips, as reported in depth and offset.

2. Survey Desing (Synthesis of INOGS official Acquisition Report - Report OGS 2017 / 7 GEO 4 GEOP)

In order to meet the planning speci_cations reported in the introduction, the following details have to be de_ned.
1. Instrumentation required
2. Acquisition parameters
3. Acquisition sensors and channels
4. Sources characteristics
5. Source positions
6. Walk above design

2.2. Intrumentation

The instrumentation required for the survey can be divided in _ve groups, as illustrated in **Error! Reference source not found.**Fig. 4.

1. borehole section
2. source and source controls
3. acquisition system
4. acquisition scheduling and controls
5. pre-processing and Quality Control System

All the instruments datasheets are reported in Appendix A.3 of the Acquisition report

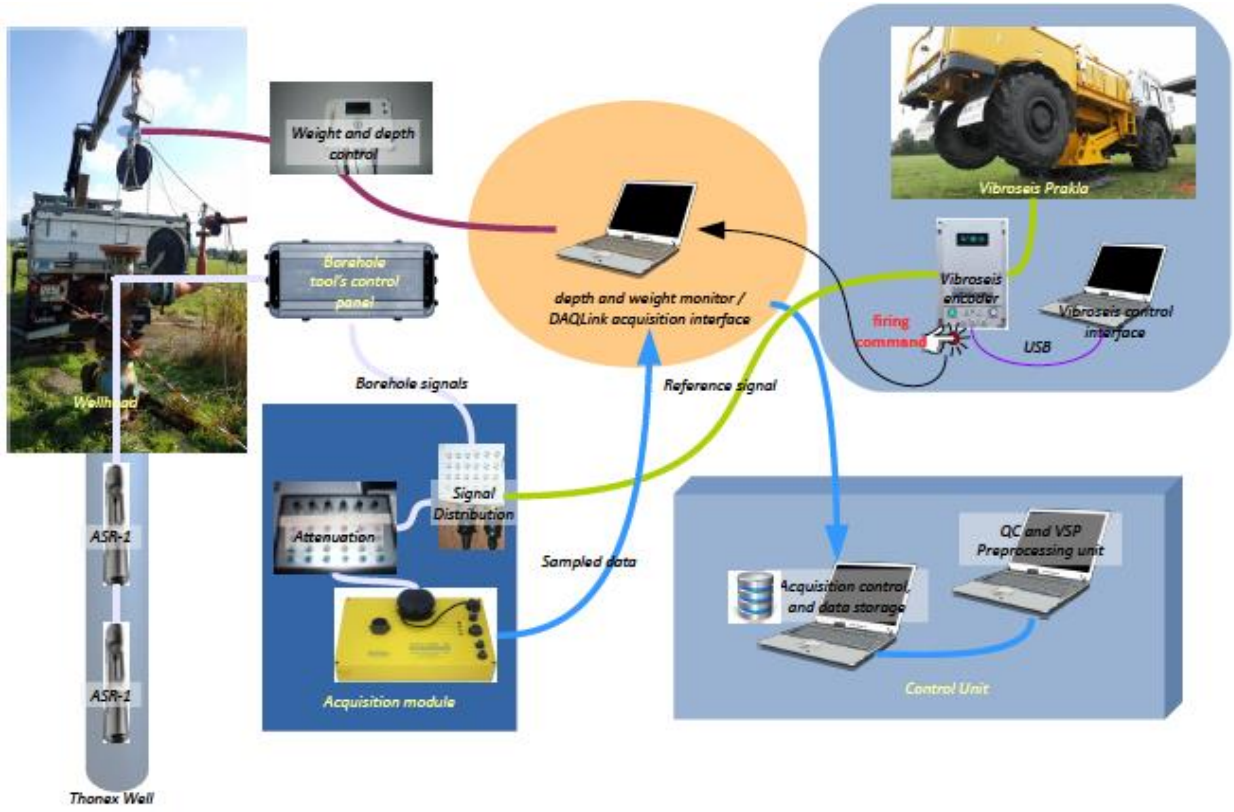

Fig. 4 - Instruments and Connection Schema

2.3. Borehole

The operations in well involve two borehole geophones from Avalon Sciences Ltd. as signal sensors receiver. The borehole geophones are driven by a winch with 2000 m armored cable, supplied by a Honda voltage generator, with the assistance of a load indicator and the pulley providing the measure of the depth. The controls for all these equipment are installed in the control cabin, and recorded during the survey.

2.4. Source and Source Controls

The energy source for this survey is a Prakla Vibroseis, driven by a Seismic Source Force II control system which includes an encoder and a decoder units, respectively installed on the Vibroseis and in the control cabin, where the time break signal for the sweep start is delivered, and the reference signals, the pilots, are fed into the acquisition system.

2.5. Acquisition System and QC

The acquisition system is a single Seismic Source DAQLink III station, as all the signals are gathered into the control cabin. The signals are collected by a Signal Distribution box, and then attenuated if necessary by an Attenuation box.
The acquisition system is managed by its proprietary software, which handles the acquisition and record the data on a dedicated PC, which also monitors and controls the depth and load weight.

2.6. Acquisition Scheduling and Control

All the survey operation and the management of the acquisition information relative to each record are controlled by the acquisition control and data storage unit, which collects the data from all the acquisition system (in this case the DAQLinkIII system only), and produces the files in the final format with all the needed in the header. Moreover the same system manages the data storage and backup. After the acquisition the data are available for pre-processing to another system, on which the operator elaborates QC information.

2.7. Acquisition Parameters

In order to maximize the information content of the data to match the investigation purposes, _rst the following survey parameters have to be tuned:

- record parameters
- acquisition channels
- vibration points
- source parameters

2.8. Record parameters

The record parameters are mainly the record length (or duration), sampling interval, and the recorded time interval before the trigger signal, or pretrigger, which is 0 in this case. As marked in red in the last line of Table 16, all these parameters remain constant during the whole survey.

Table 17 - Acquisition Parameters

Parameters			
Dual ASR-1 borehole geophone Field records range: 1-805 812-1248 1292-1298 1302-2038 Borehole Channels Attenuation lev.2: -6 dB Field records range: 1249-1266			
Borehole Channels Attenuation lev.3: -12 dB Field records range: 1267-1281 1299-1301			
Borehole Channels Attenuation lev.4: -18 dB Field records range: 1282-1284			
Borehole Channels Attenuation lev.5: -24 dB Field records range: 1285-1291			
Acq name	**Rec length**	**dtus**	**Pretrigger**
DAQLinkIII	20	1000	0

Another parameter related to the borehole channels only (i.e. the two triaxial geophones in the two borehole tools), is the attenuation level. In order to prevent the borehole signals from saturation, as the tool ascends and the distance between the receivers and the source decreases, the attenuation increases in a sequence of field records ranges, as reported in the Table 17.

2.9. Acquisition Channels

The acquisition channels are reported in Table 18. All channels have the same con_guration in the whole survey except for a small range of field records, when the connections with two channels coming from DAQ Link (channel 7 and 9) are inverted.

Table 18 - Acquisition channels

Channels and Sensors Table DAQ Link 1074				
tracf	Sensor Type	Ch Name	DAQ Ch	DAQ out
Dual ASR-1 borehole geophone Borehole Channels Attenuation lev.2: -6 dB Borehole Channels Attenuation lev.3: -12 dB Borehole Channels Attenuation lev.4: -18 dB Borehole Channels Attenuation lev.5: -24 dB				
7	GPS Pulse Per Second (PPS)	PPS	6	6
51	Geophone SM-4 HT 10Hz (ASR1 GIMBAL)	Tool 1 GEO Z	10	10
52	Geophone SM-4 HT 10Hz (ASR1 GIMBAL)	Tool 1 GEO HX	11	11
53	Geophone SM-4 HT 10Hz (ASR1 GIMBAL)	Tool 1 GEO HY	12	12
61	Geophone SM-4 HT 10Hz (ASR1 GIMBAL)	Tool 2 GEO Z	7	7
62	Geophone SM-4 HT 10Hz (ASR1 GIMBAL)	Tool 2 GEO HX	8	8
63	Geophone SM-4 HT 10Hz (ASR1 GIMBAL)	Tool 2 GEO HY	9	9
91	accelerometer	VIBRO RADIO SIM (GF)	3	3
92	accelerometer	VIBRO RADIO REF	4	4
93	accelerometer	VIBRO W.L. REF	5	5
96	accelerometer	VIBRO T-REF (SYNTH)	2	2
9000	no sensor	no data	1	1
Dual ASR-1 borehole geophone - records subset from 700 to 680 for Offset1				
51	Geophone SM-4 HT 10Hz (ASR1 GIMBAL)	Tool 1 GEO Z	10	10
52	Geophone SM-4 HT 10Hz (ASR1 GIMBAL)	Tool 1 GEO H1	11	11
53	Geophone SM-4 HT 10Hz (ASR1 GIMBAL)	Tool 1 GEO H2	12	12
61	Geophone SM-4 HT 10Hz (ASR1 GIMBAL)	Tool 2 GEO Z	7	9
62	Geophone SM-4 HT 10Hz (ASR1 GIMBAL)	Tool 2 GEO H1	8	8
63	Geophone SM-4 HT 10Hz (ASR1 GIMBAL)	Tool 2 GEO H2	9	7
91	accelerometer	Ground Force	3	3
92	accelerometer	Base Plate	4	4
93	accelerometer	Reaction Mass	5	5
96	accelerometer	Synthetic	2	2
9000	no sensor	no data	1	1

2.10. Vibration Points

The initial design of the second stage of the survey plans 3 offsets and a walk above in 5 vibration points. Initially the three offsets are: the Offset 0, the Near Offset, and 2 offsets laying on directions parallel to the the well deviation, on the two sides of the well. A further offset perpendicular to the deviation line is planned as additional, should that be possible. During the survey the project is slightly modified. The final survey design ha 4 offsets on 2 perpendicular lines: offset 1 and offset 4 along the deviation line and o_set 2 and o_set 3 perpendicular to the deviation line.
All the vibration points are reported in Table 19, including the walk above.

Table 19 - Acquisition channels

Vibration points				
Name	Stake	X	Y	Notes
Offset 0	0	505255.614	117525.729	Calibration Near Offset
Offset 1	1	505153.71	117414.23	Parallel to Deviation, same Direction
Offset 2	2	505381.34	117461.77	Perpendicular to Deviation, Right Side
Offset 3	3	505148.91	117681.59	Perpendicular to Deviation, Left Side
Offset 4	4	505560.64	117915.573	Parallel to Deviation, Opposite Direction
Walkabove VSP 1	101	505356.207	117682.84	
Walkabove VSP 2	102	505325.267	117647.770909	
Walkabove VSP 3	103	505292.669	117611.745	
Walkabove VSP 4	104	505258.359142	117566.657857	
Walkabove VSP 5	105	505232.3545	117527.4575	Both Near Offset and Walkabove point closest to the well

2.11. Walk Above

A walk above survey is tipically performed on a deviated well, in which the seismic source moves on the surface following the well deviation. Every source point covers a prede_ned interval of well length, paying attention to have double fold acquisition so that in every interval at least 2 shots for each position are recorded, _rst and last interval excluded. To address this goal on every borehole geophones position there must be record two vibration points. In order to minimize the tool's

movements inside the well, and prevent the Vibroseis from moving when the vibrations on a stake are non _nished yet, two di_erent strategies are designed:
• First survey, 7 vibration points, two Vibroseis. It is planned to energize using the two Vibroseis alternatively from near vibration points.
• Final survey, 5 vibration points, one Vibroseis. More than one roundtrip is necessary. It is planned to complete position 101, 103, 105 before, and then position 102 and 104. In this way the walk above can be completed in two roundtrips.
Table 20 - Walk Above Survey with two trips in well and 5 VP

Walk Above survey								
	source	offset	Measured Depth		n			distance
trip	stake	from well	first	last	of levels	Easting	Northing	on surface
Trip 1	WA1	229,6	1500	1270	25	141,4	180,89	82,78
Trip 2	WA2	182,93	1380	1140	25	110,46	145,82	91,88
Trip 1	WA3	134,6	1260	1020	25	77,86	109,8	100,71
Trip 2	WA4	78	1130	890	25	43,55	64,71	96,41
Trip 1	WA5	30,96	1010	770	25	17,55	25,51	78,00

A preliminary velocity model retrieved from literature and analysis of available vintage seismic lines, was provided by UniGe to INOGS in order to run some synthetic modelling to properly planify the whole survey (Fig. 5).

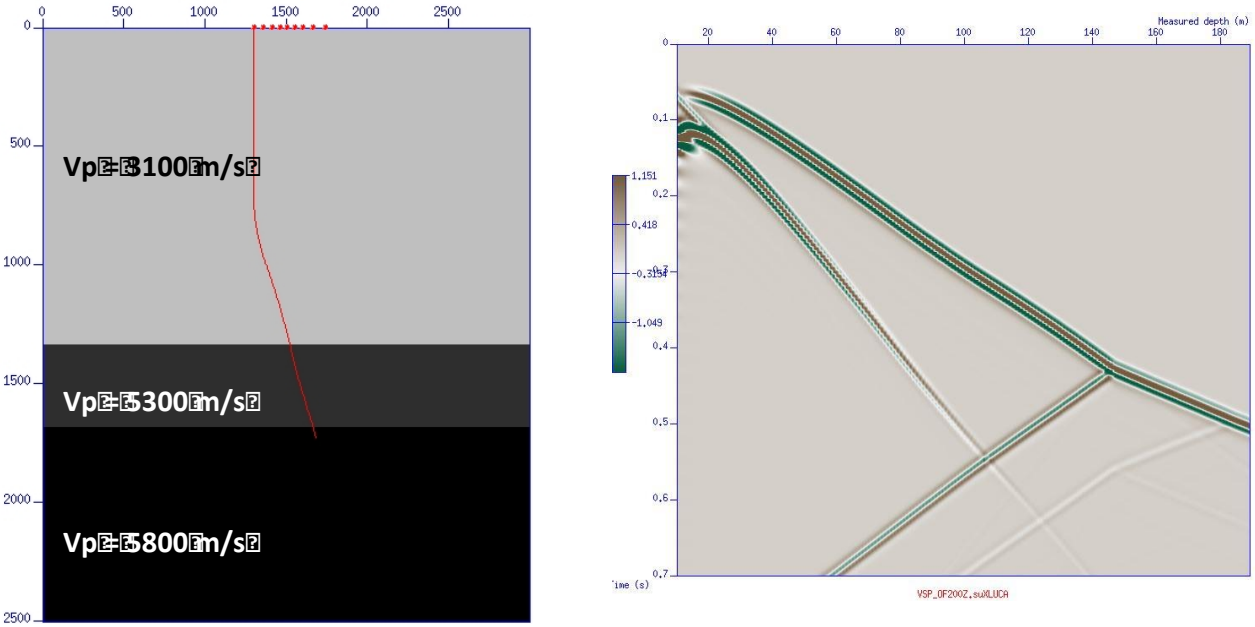

Fig. 5 - Well Provisional Velocity model and example of sysntethic signal

Walk-above design according to:

1. Ray tracing
2. Synthetic data processing

The final layout was composed by gathers of 24 traces and 5 source positions (Fig. 6).

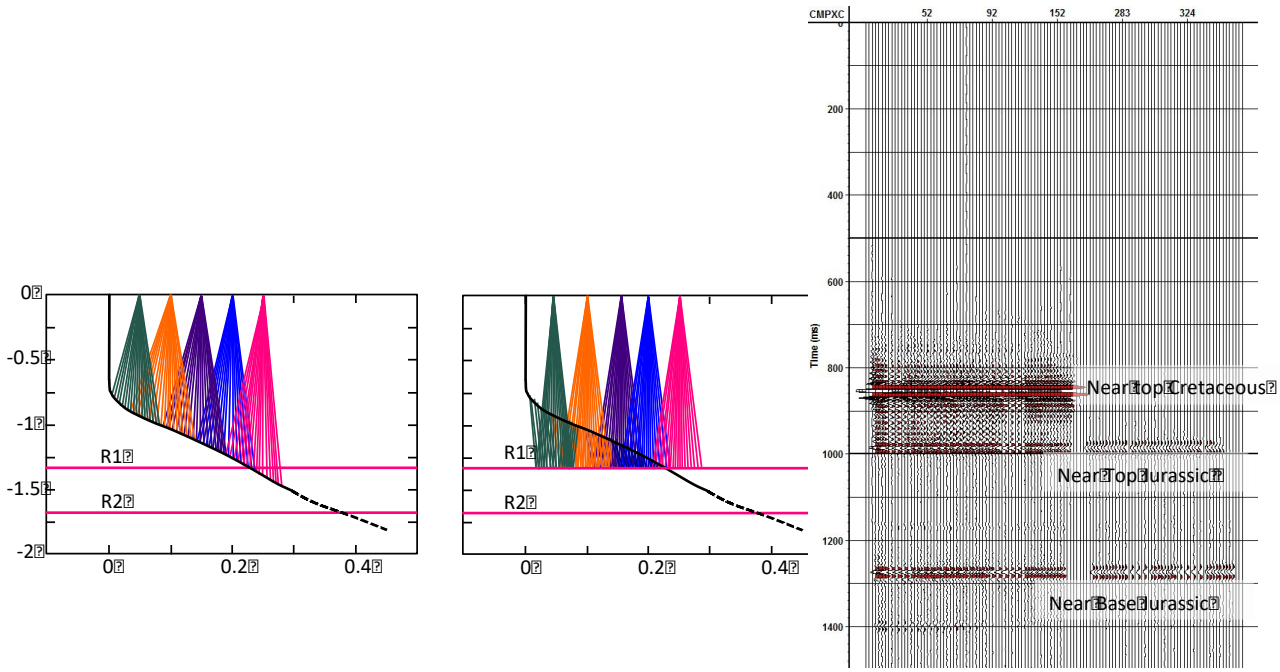

Fig. 6 - Example of WAB synthetic subset-data processing (separated reflections)

3. Data acquisition (Synthesis of INOGS official Acquisition Report - Report OGS 2017 / 7 GEO 4 GEOP)

3.1. First Survey

The first survey begins on 24th July. Operations are performed from 26th to 27th July.
The move in and installation phase is realized in the following steps:

1. Crane placement
2. Wellhead opening
3. positioning and connection of winch trailer and winch control tools
4. installation of the acquisition system
5. installation of recording and transmission circuitry on the Vibroseis
6. System configuration and testing
7. Well depth and wall test with suitable weight
8. Descent with ASR tool and Vibroseis parameters test at 100 m and 1500 m depth.

Points 1 and 2 are performed in the first morning in cooperation with SIG. In the point 5 in the first Survey, two acquisition modules are installed on the two Vibroseis, because in the acquisition design they should execute the vibrations alternatively in two different positions, and the control system is not able to switch the two systems fast enough. After the well check test (point 7) it becomes clear that there is an obstruction at 1500 m depth, and the survey has to be limited by this obstruction at this depth, instead at 1800 m. The walk above Survey is also restricted to 5 vibration points, the last two points being farther than the deepest reachable tool position.
Finally, after the last descent with the tool at 100 and 1500 m (point 8), the Vibroseis parameters are defined.
After the setting of the Source Parameters. a problem occurs on the winch cable and tool connector of the borehole system. In order to fix the problem a technician of the producer, Avalon Inc, comes from U.K.. Trip and repair cause a too long delay, considering the vibrators costs and availability to complete properly the Survey. It is decided to complete the Survey later, at the _rst suitable time window.

3.2. Second Survey

The last part of the survey begins at October 6th with move in operations (Fig. 7). The installation procedure were the same as the first survey, only the tests on depth are skipped. Moreover, to speed up the acquisition procedure and for backup purposes one more tool ASR is added to the survey tools. This time one Vibroseis only is present on _eld and the reference signals are provided by the encoder installed in the Control Unit.

(a) WellHead (b) Pulleys, Weight and depth Control (c) trailer positioned

(d) Cable and Pulley (e) Trailer, Winch, Tools

Fig. 7 – Move in and installation operation for the second phase

Activities description

The first period after installation, from October 9th to 11th , is dedicated to verify vibroseis parameters, reported in Table 21, to test the Dual Borehole Geophones configuration and to design a calibration procedure to increase the depth measure precision. Evaluating the first results, it is decided to modify the planning by adding 2 VP, Offset 3 and 4, and performing the offset 1, 2 and 3 from 1500 m to 300 m depth. The final data acquisition begins on October 12th and ends on 15th, calibration activities included.

Table 21 - Source Parameters

Sources						
Type	Description	Min Hz	Max Hz	Load Kg	Sweep s	Taper s
VIBRO1	Vibroseis Prakla OGS - Seismic Source Force III	8	120	467	14	0.3

The field QC highlighted that good quality data were observed below 800m depth (0.25ms), poor quality data above 800m most probably due to bad coupling between the well casing and the surrounding rock possibly due to dissolution of the cament bond (Fig. 8).

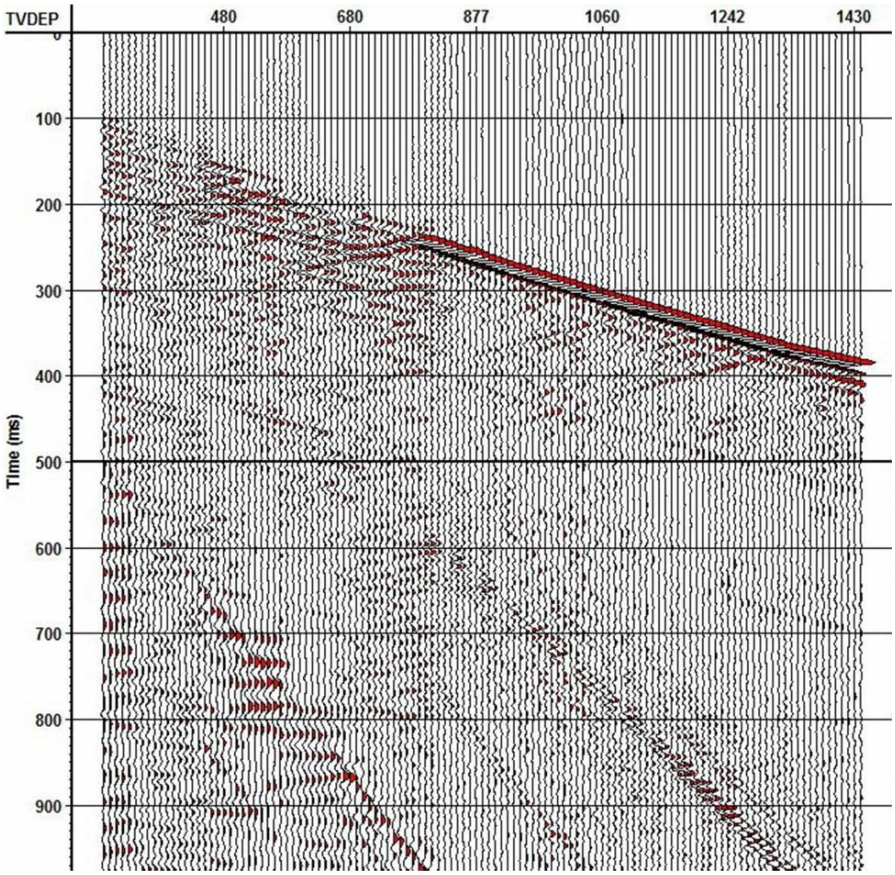

Fig. 8 – Example showing data quality

3.3. Processing (Synthesis of the INOGS official processing report OGS 2017 / 48 GEO 12 GEOP)
All the processing is done on the Z component and is referenced to Ground Level (428 m amsl).
The main processing steps are

- Header adjustment from Seismic Unix to Schlumberger Vista format
- Geometry check and source receiver offset calculation
- Bulk shift -5000 ms to correct from correlation times to seismic times
- Frequency analysis
- Band Pass 8- 12- 110-120 Hz (Ormsby filter)
- FB picking
- Velocity analysis
- Wavefield separation
    - Mean scaling of Direct Arrivals in a 20 ms window centered on the First Breaks

- Median filter (7 traces)
- Band Pass 8- 12- 110-120 Hz (Ormsby filter) to remove whiskers after median filtering
- FK filter design
- FK filter applied for upgoing wavefield enhancement
- Output to Two Way Time (TWT) with and without NMO verticalization
- Design of deconvolution operator from downgoing wavefield
  - Predictive decon
  - Operator length 250 ms
  - Prediction lag: 2nd zero crossing
  - Design window 400 ms
- Deconvolution using the designed operator
- Wave shaping deconvolution
- Spherical divergence recovering
- Corridor mute and corridor stack

- Kirchoff Migration (Note that when joint migrating the WAB datasets, a bulk static of 1.28 and 1.54 ms was added to WAB 101 and WAB 105 for proper alignement)
- Component rotation: a test of component rotation was performed on VSP 2

3.3.1. Data Quality

Overall quality of data is good, with evidence of good direct arrivals and reflections. This is only true in thesection of the well below 700-800 m depth from ground level as above this depth, along the vertical section of the borehole, we observe effects probably due to the condition of the casing or to problems in thecement bonding.

The presence of a strong high velocity resonant system makes it impossible to pick reliable first breaks on the vertical section of VSPs 1, 2 , 3 and on the Near offset VSP. On VSP 4, although the first breaks are of better quality, the upgoing wavefield is also contaminated by the said resonant system.

Synthetic wavefields have been computed for all the VSPs to investigate the problem. In Fig. 9 we show an example of comparison between real and synthetic data from the Near Offset VSP. We observe that below 700-800 m depth the agreement is good apart from a small bulk shift of few ms, while above, in the vertical section of the well the data don't fit.

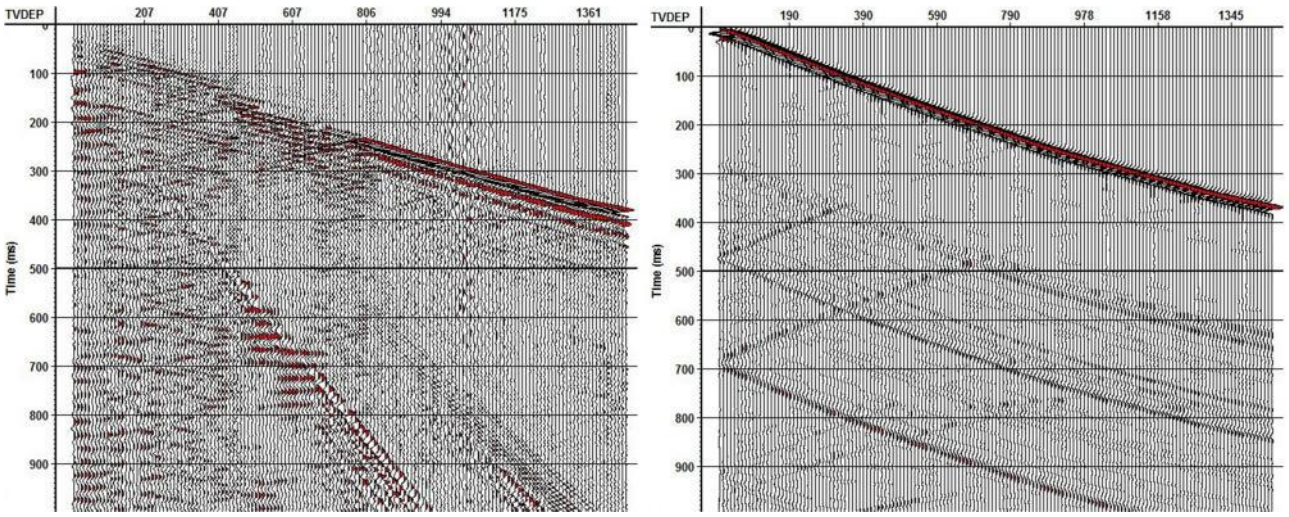

Fig. 9 – Comparison between real Near Offset VSP (left) and synthetic data (right). The section above
700-800 m depth is affected by the resonant system acting as a secondary source.

In Fig. 10 we also observe the presence of strong tube waves in the lower part of the record. This is valid for all the VSPs.

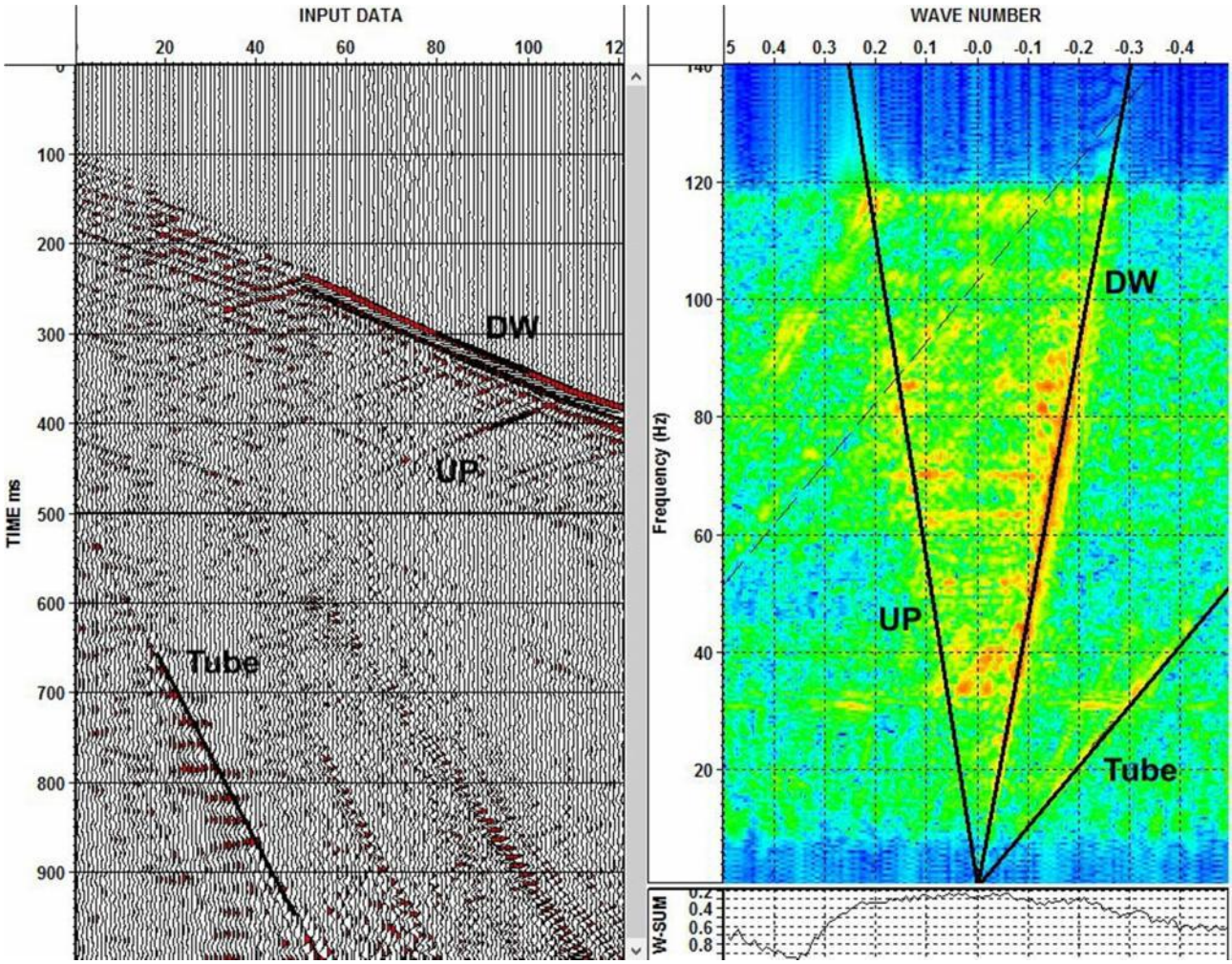

Fig. 10 - Example showing data quality

3.3.2. Velocity analysis results

We show here the results of the velocity analysis performed using the first breaks of each VSP. In Fig. 11 we show tha compairison between the P-wave interval velocities to show the good fitting between the different offsets.

In Fig. 12Fig. 11 we show a comparison between the interval velocity functions after smoothing with a three traces moving window. We observe a good fit between the different datasets that seems to display a common trend throughout the investigated area.

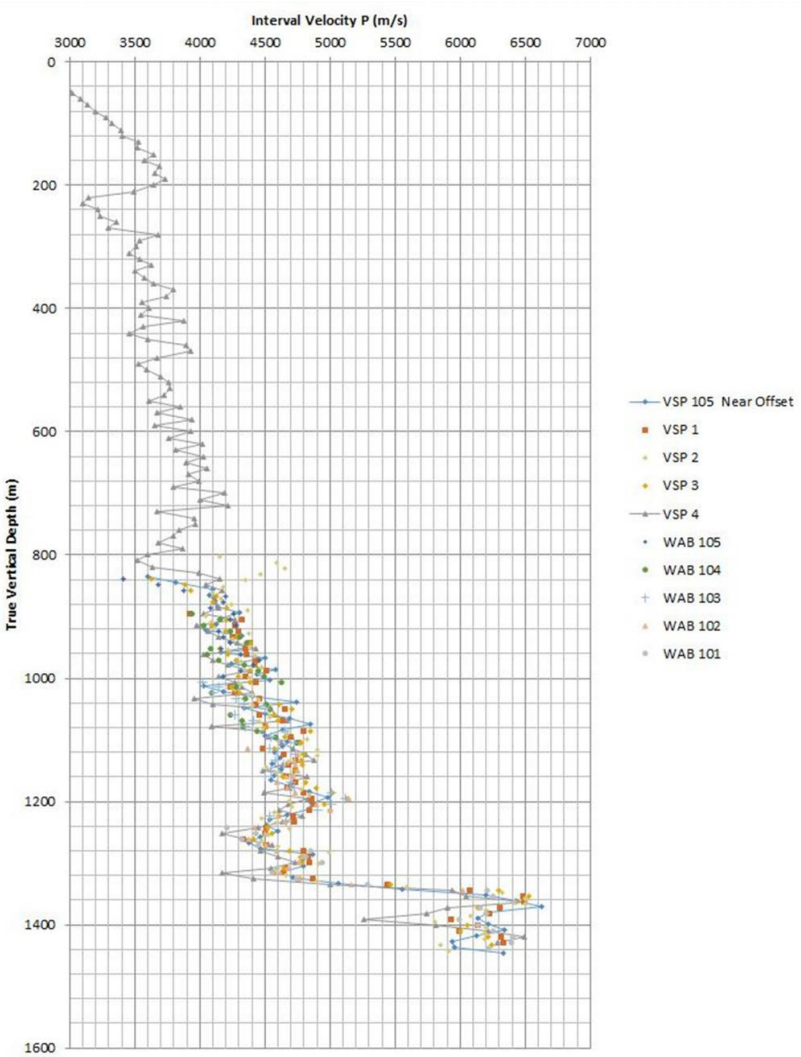

Fig. 11 - Interval velocity for P waves. 3 point moving average applied

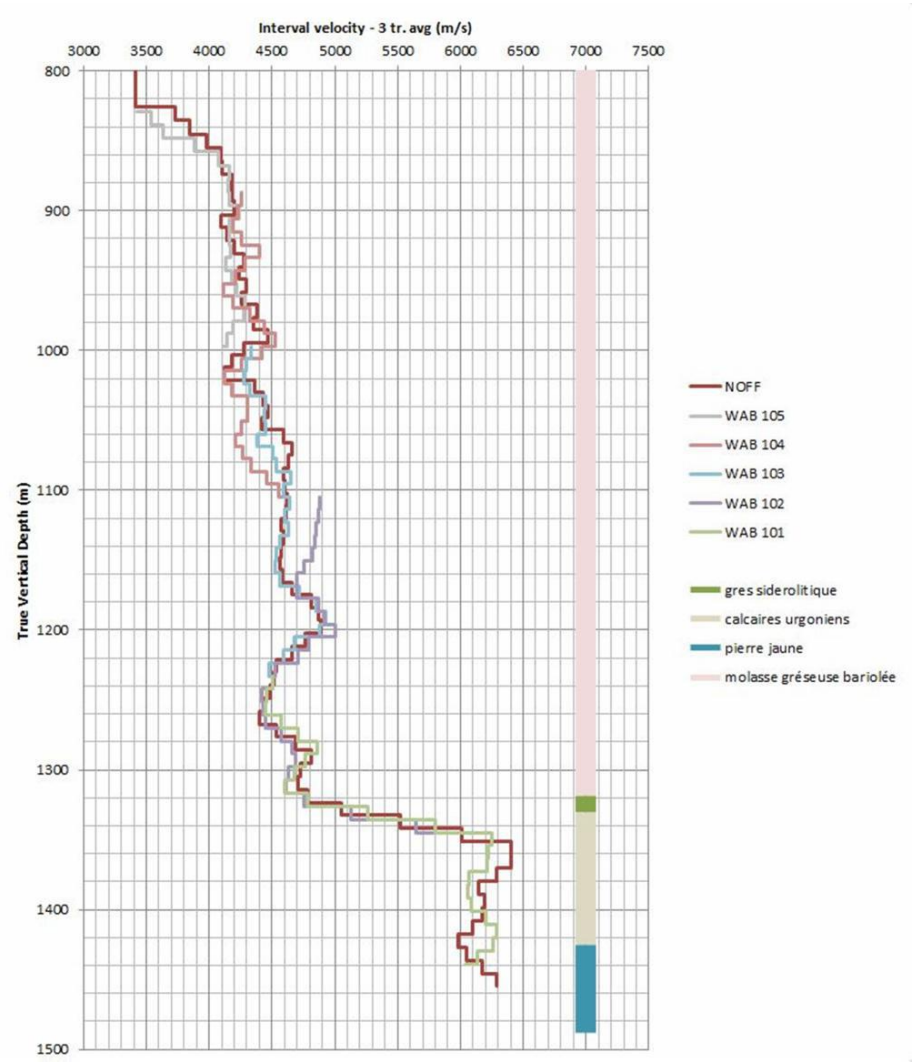

Fig. 12 - Comparison between averaged interval velocities for Near offset VSP and Walkabove VSP's

3.3.3. Wavefield separation

The following figures depict the main results for selected offsets from the wavefield separation processing

VSP1

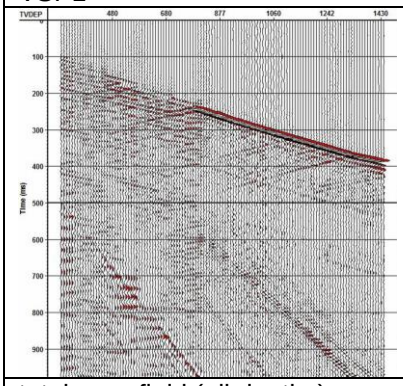

total wavefield (all depths)

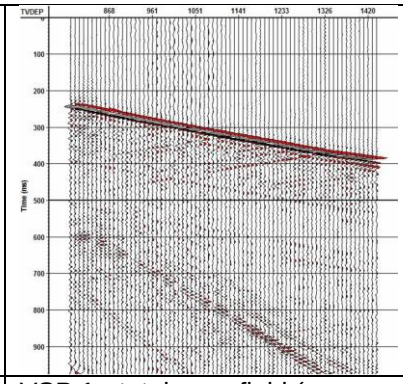

VSP 1 - total wavefield (processed depth)

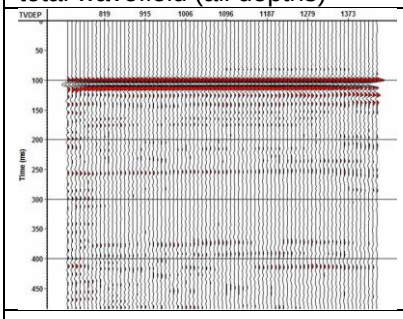

VSP 1 - Downgoing wavefield aligned at 100 ms

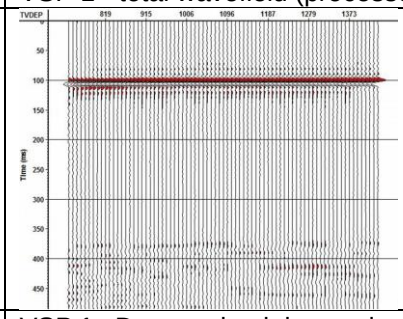

VSP 1 - Deconvolved downgoing wavefield aligned at 100 ms

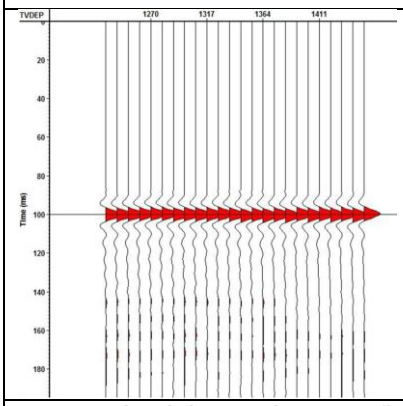

Deconvolved downgoing wavefield aligned at 100 ms after wave shaping

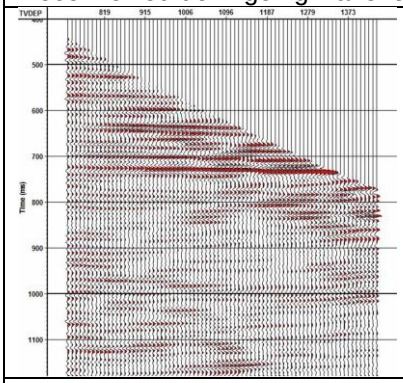

VSP 1 - Deconvolved upgoing wavefield TWT

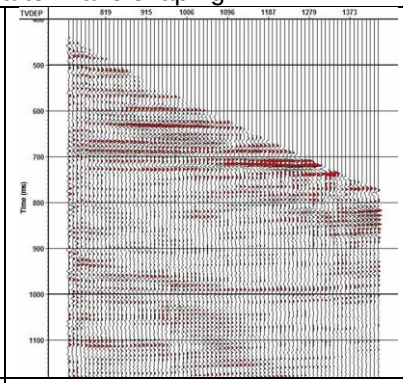

VSP 1 - Deconvolved upgoing wavefield TWT

VSP4

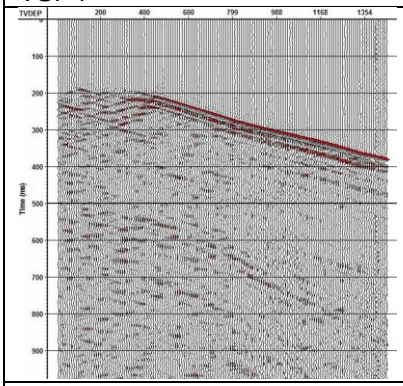

VSP1 - total wavefield (all depths)

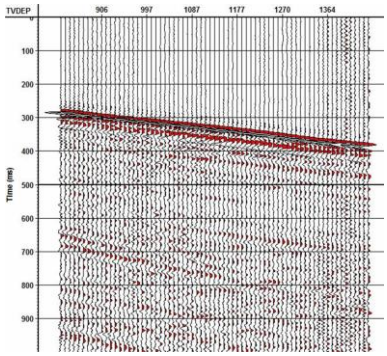

VSP 4 - total wavefield (processed depth)

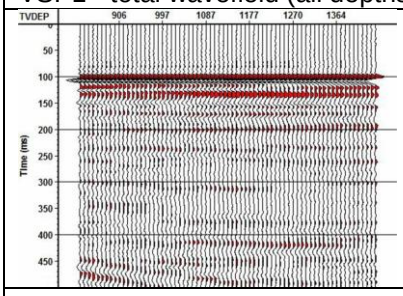

VSP 4 - Downgoing wavefield aligned at 100 ms

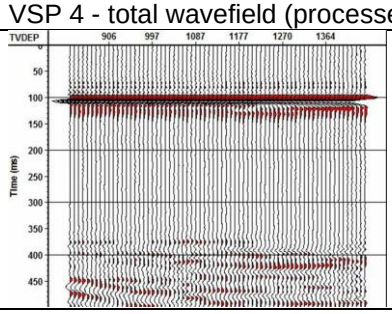

VSP 4 - Deconvolved downgoing wavefield aligned at 100 ms

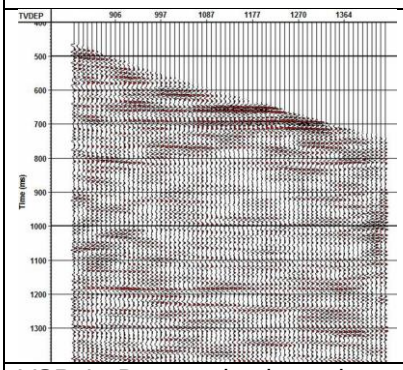

VSP 4 - Deconvolved upgoing wavefield TWT NMO

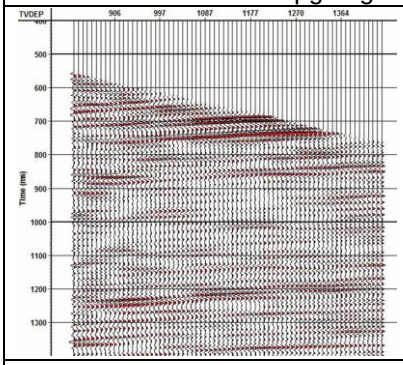

VSP 4 - Deconvolved upgoing wavefield TWT

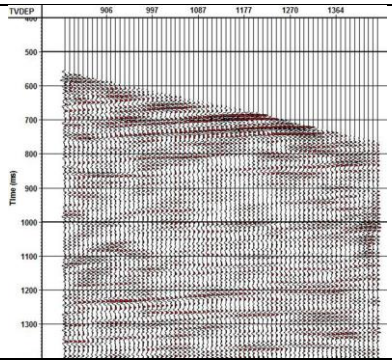

VSP 4 - Deconvolved upgoing wavefield TWT

3.3.4. Corridor stack

We show here the corridor stacks obtained by muting the TWT NMO corrected and deconvolved upgoing wavefield outside a 100 ms corridor and then stacking the traces. Interpretation of the corridor stacks should be made also taking into account the unmuted upgoing wavefields where contribution from residuals of wavefields different from the upgoing (tube waves) can be evaluated and rejected (Fig. 13).

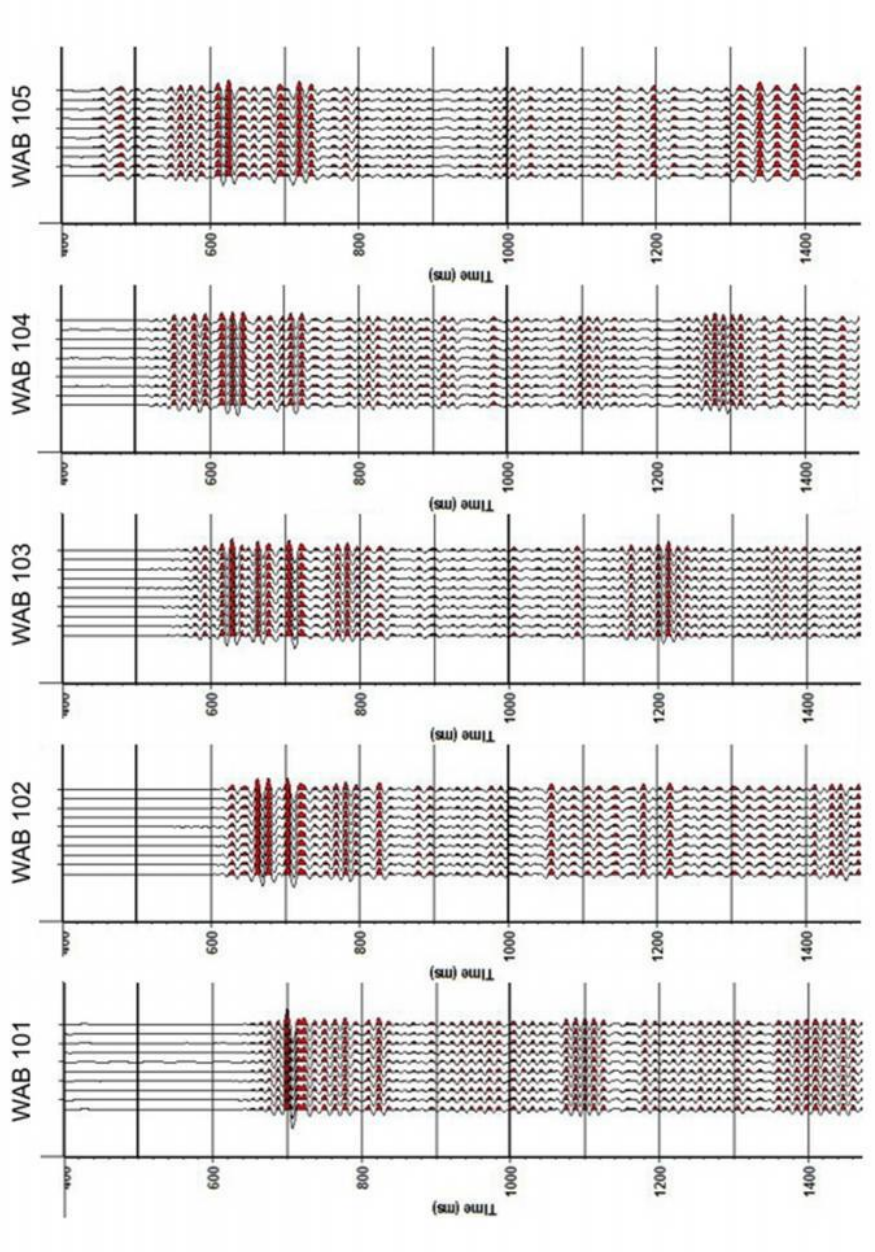

Fig. 13 - Comparison between corridor stacks

3.3.5. Migration

A Kirchoff 3d migration algorithm was applied to WAB data alone and to WAB, NOFF, VSP 1 and VSP 4 toobtain a depth migrated seismic section along the wellpath. The velocity model used for migration was obtained from the Near Offset VSP velocity function after 3 traces averaging

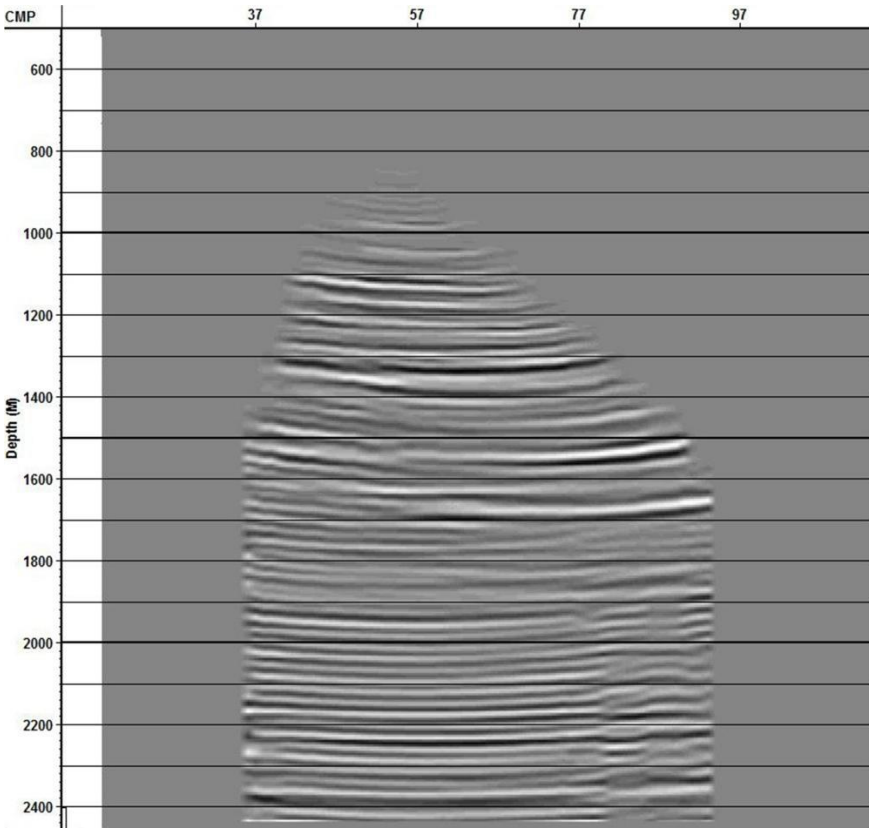

Fig. 14 - Migrated section (using only WAB). After 1800 m TVD we can observe what is probably noise from residual tube waves in the input data.

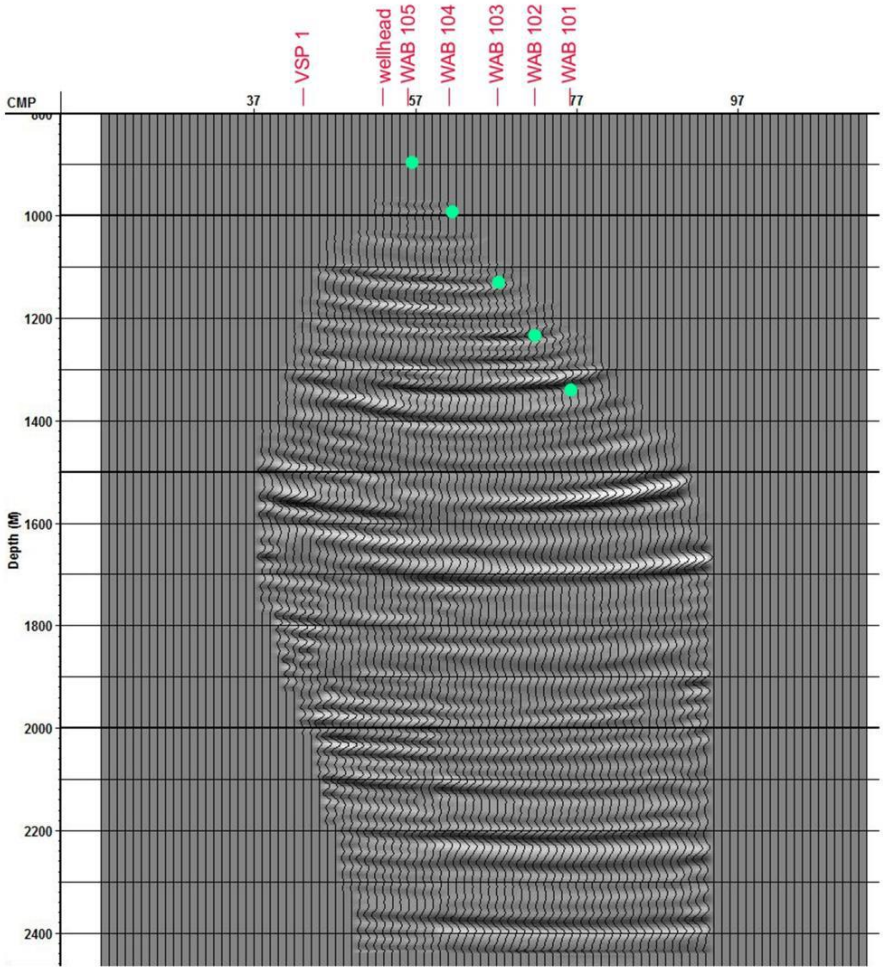

Fig. 15 - Migrated section (only WAB) using a smoothed model (3 traces average). The input dataset is muted to remove any residual tube waves. The green dots represent the sensor position in the well under the different sources.

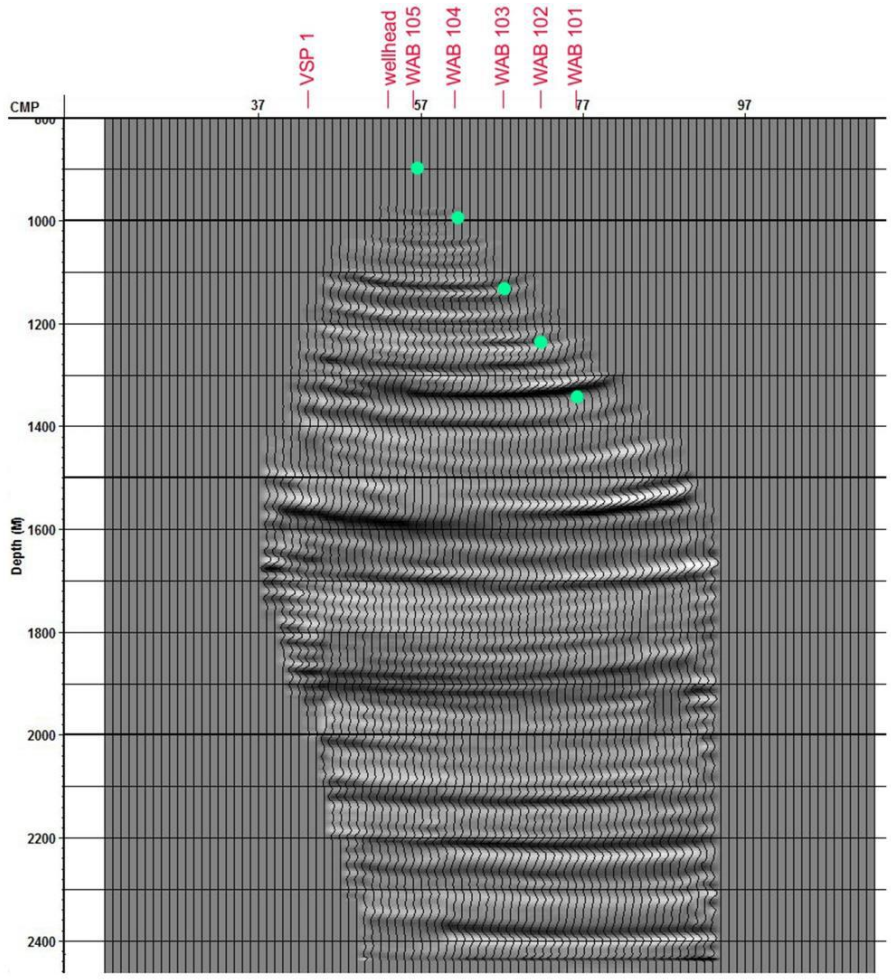

Fig. 16 - Migrated section (only WAB) using a smoothed model (3 traces average). The input dataset is muted to remove any residual tube waves. Here the input VSP's are obtained without applying the FK filter on the upgoing wavefield. The green dots represent the different sources

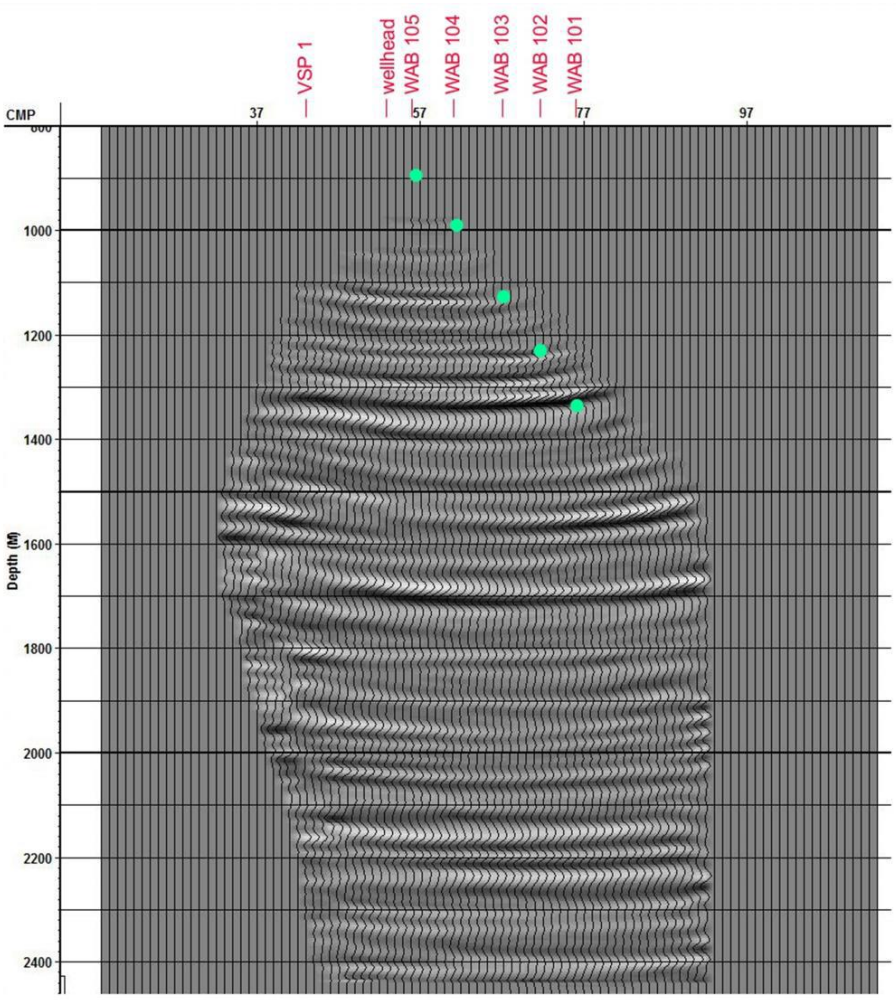

Fig. 17 - Migrated section (WAB, NOFF, VSP 1) using a smoothed model (3 traces average). The input dataset is muted to remove any residual tube waves. The green dots represent the sensor position in the well under the different sources.

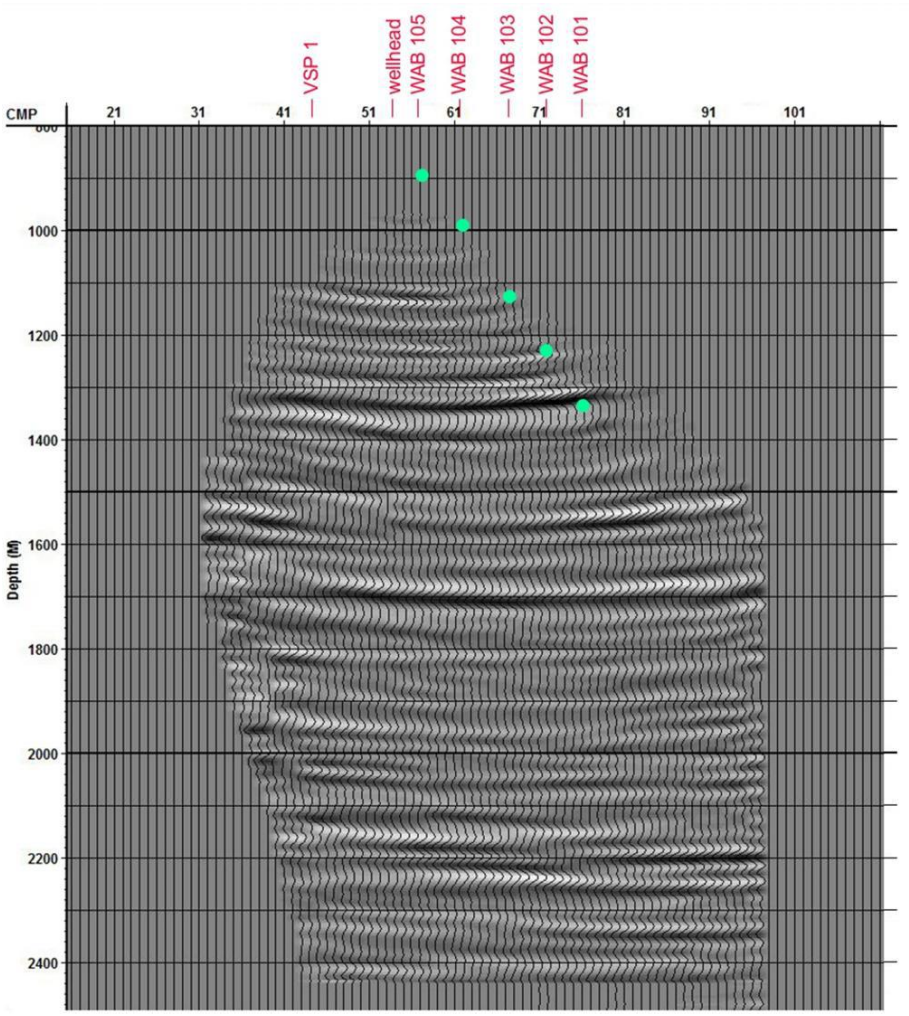

Fig. 18 - Migrated section (WAB, NOFF, VSP 1 and VSP4) using a smoothed model (3 traces average). The input dataset is muted to remove any residual tube waves. The green dots represent the sensor position in the well under the different sources.

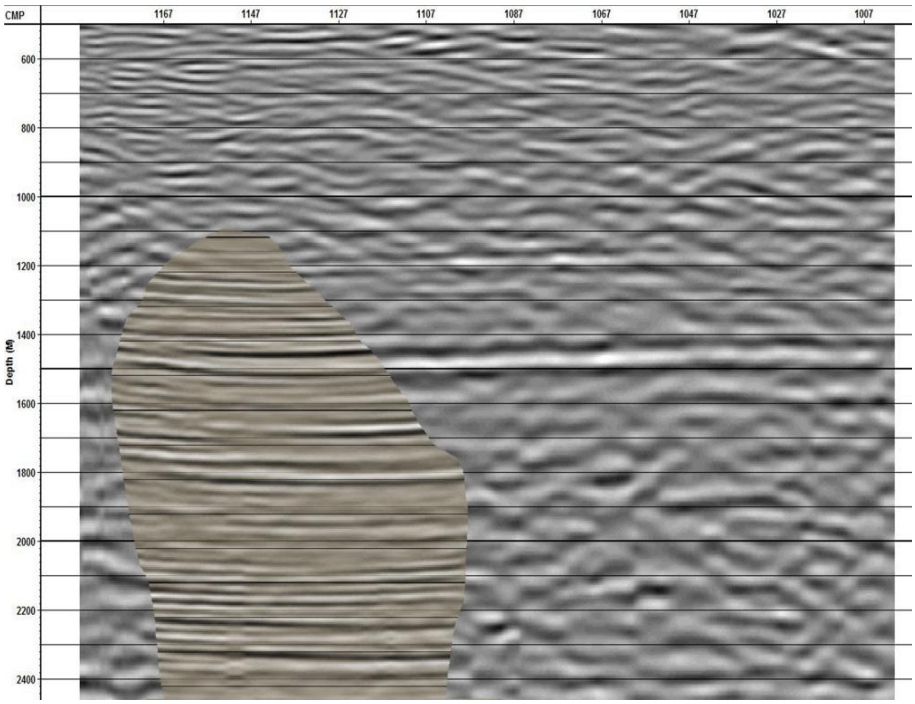

Fig. 19 - migrated section inserted in Thonex-2 seismic section after depth conversion (only WAB data).

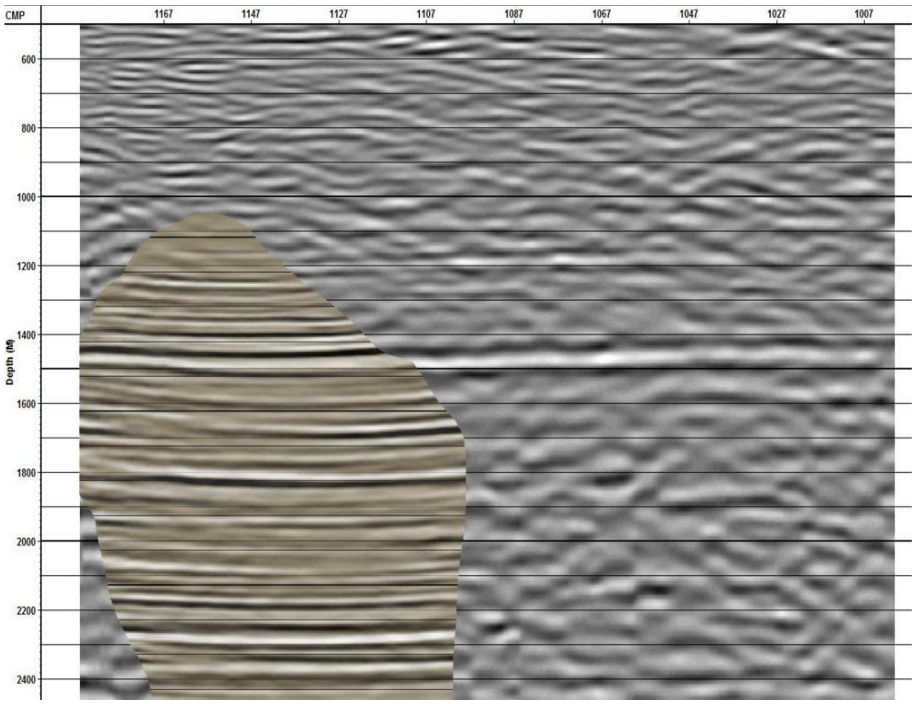

Fig. 20 - migrated section inserted in Thonex-2 seismic section after depth conversion (WAB, NOFF,VSP 1).

Appendix 2. Characteristics, and chemical and isotopic compositions of the waters discharged from the Litomerice boreholes and Teplice Pravridlo thermal springs, in Czech Republic, and from the Thônex-1 and Lavey-les-Bains geothermal boreholes, in Switzerland

Well	Location	Country	ID	X_MAP	Y_MAP	Latitude °	Longitude °	Z	Depth m	Stratigraphy	Geology	Water level m	T °C
TH-31, TH 31/62	Oldrichov	Czech Republic	278	-779836.60	-975339.20	50.6430430	13.7722250	246.83	159	Permian Spodni	Quartz	12.7 - 159.0	13.0
TP-41, TP 41/88	Teplice	Czech Republic	305	-774819.90	-976024.70	50.6434588	13.8438082	218.35	546	Carbon	Granite	494.1 - 542.0	44.2
TH-20	Modlany	Czech Republic	283	-771087.40	-975489.00	50.6530443	13.8949501	194.45	443	Proterozoic	Gneiss	342.8 - 368.6	27.1
TH-10, TH 10/61	Predlice	Czech Republic	326	-763721.70	-976443.80	50.6539889	13.9999707	143.72	500	Proterozoic	Gneiss	373.4 - 440.8	31.0
HV-3C	Jestrebi	Czech Republic	560	-723123.00	-987014.00	50.6102305	14.5889443	255.26	151	Proterozoic	Phyllite	133.8 - 145.9	12.0
SR-1	Stremy	Czech Republic	1028	-728547.20	-1010162.80	50.3974582	14.5569988	211.30	1241	Proterozoic	Phyllite		33.0
PVGT-LT1	Litomerice	Czech Republic				50.5329800	14.1534200		2111	Proterozoic	Gneiss	1600 - 1800	56.5
Pravridlo (ancient spring)	Lazne Teplice	Czech Republic		-776056.00	-976474.00			217.00	54.3	Palaeozoic	Rhyolite		49.0
TP-28	Lazne Teplice	Czech Republic		-776068.00	-976278.00			217.00	973	Palaeozoic	Rhyolite	883-942	45.7
Thônex-1	Geneva	Switzerland				46.1928370	6.2027670	428.35	2530	Upper Jurassic	Limestone	~ 2100	70.0
Lavey-les-Bains	Vaud	Switzerland				46.2213052	7.0121187	431.75	3000 ?	Hercynian	Gneiss		105.0

Well	Location	Depth	Stratigraphy	Geology	Water level	Flow-rate	$T_{measurements}$	Cond. 25°C	pH	Eh	O_2	Na	K	Ca	Mg	Cl	Alk.	DOC	SO_4	NO_3	SiO_2	TDS
		m			m	m^3/h	°C	µS/cm		mV	mg/l	mg/l	mg/l	mg/l	mg/l	mg/l	mg/l HCO_3	mg/l	mg/l	mg/l	mg/l	mg/l
TH-31, TH 31/62	Oldrichov	159	Permian Spodni	Quartz	12.7 - 159.0		13.0					91.0	6.0	35.7	8.3	21.6	276		65.8		23.3	531
TP-41, TP 41/88	Teplice	546	Carbon	Granite	494.1 - 542.0		44.2															
TH-20	Modlany	443	Proterozoic	Gneiss	342.8 - 368.6		27.1					231	14.0	31.7	3.6	28.7	475		173		10.7	975
TH-10, TH 10/61	Predlice	500	Proterozoic	Gneiss	373.4 - 440.8		31.0					234	17.5	28.9	3.8	28.0	445		215		12.6	997
HV-3C	Jestrebi	151	Proterozoic	Phyllite	133.8 - 145.9		12.0		7.30			28.2	3.7	44.1	10.7	9.6	202		50.4		7.5	358
SR-1	Stremy	1241	Proterozoic	Phyllite			33.0															
PVGT-LT1 (November 2007)	Litomerice	2111	Proterozoic	Gneiss	1600 - 1800	≤ 0.02	56.5	1170	8.30			140	14.0	93.0	12.0	190	220		88.0	< 2		761
PVGT-LT1 (May 2015)	Litomerice	2111	Proterozoic	Gneiss	1600 - 1800	≤ 0.02	53.8	575	8.91		0.21	140	8.9	31.0	17.0	180		17.3	14.0	< 1	< 2.5	399
PVGT-LT1 (November 26, 2015)	Litomerice	2111	Proterozoic	Gneiss	1600 - 1800	≤ 0.02		1040	8.35	80	0.55	164	9.6	24.5	5.9	227	151		1.0	< 0.5	1.3	594
Pravridlo (ancient spring) - Cadek *et al.* (1968)	Lazne Teplice	54.3	Palaeozoic	Rhyolite	?		41.3		6.90			224	16.0	23.0	7.5	51.4	551		118		34.5	1033
Pravridlo - Dupalova *et al.* (2012)	Lazne Teplice	54.3	Palaeozoic	Rhyolite	?		40.0		7.14			229	10.6	37.2	5.8	49.8	528		116	0.531	40.9	1025
TP-28 - Dupalova *et al.* (2012)	Lazne Teplice	973	Palaeozoic	Rhyolite	883-942		41.0		7.26			335	11.3	33.6	5.8	56.6	600		275	< 0.05	45.7	1371
Pravridlo (ancient spring, http://lazneteplice.cz)	Lazne Teplice	54.3	Palaeozoic	Rhyolite	?							212	10.6	40.7	6.5	50.8	502		133		38.6	1000
Pravridlo (ancient spring, November 24, 2015)	Lazne Teplice	54.3	Palaeozoic	Rhyolite	?	~ 0.03	35.9	1160	7.29	330	3.30	217	8.5	32.2	4.5	46.4	481		92	< 0.5	43.5	933
Thonex-1 (01/10/1993) - Vuataz and Giroud (2010)	Geneva	2530	Upper Jurassic	Limestone	~ 2100	~ 7-11	39.1	6933	7.27			283	9.3	1536	116	3325	115		61.0	1.1	21.7	5482
Thonex-1 (29/03/1994) - Vuataz and Giroud (2010)	Geneva	2530	Upper Jurassic	Limestone	~ 2100	~ 0.1-0.2	17.4	6280	6.22			323	12.1	1429	96.0	2500	1169		5.0		20.7	5555
Thonex-1 (14/06/1996) - Vuataz and Giroud (2010)	Geneva	2530	Upper Jurassic	Limestone	~ 2100	~ 0.21						311	11.3	606	102	1400	667		22.8			3120
Thonex-1 (05/11/1997) - Vuataz and Giroud (2010)	Geneva	2530	Upper Jurassic	Limestone	~ 2100	~ 0.21		2500	6.99			330	3.7	265	36.5	667			< 1	< 1	1.2	1308
Thonex-1 (17/06/2010) - Vuataz and Giroud (2010)	Geneva	2530	Upper Jurassic	Limestone	~ 2100	0.21	16.2	1931	7.92	-5.4	0.12	304	8.6	52.1	24.1	440	411		11.2	0	47.5	1356
Thonex-1 (25/07/2016) - This study	Geneva	2530	Upper Jurassic	Limestone	~ 2100	~ 0.7	12.7	1974	7.27	-76	0.33	250	9.5	89.9	27.7	388	425		34.0	< 0.5	69.4	1306
Thonex-1 (25/10/2016) - This study	Geneva	2530	Upper Jurassic	Limestone	~ 2100	0.055	21.3	1929	8.03	25	0.78	277	8.6	58.1	24.2	390	420		22.7	< 0.5	46.3	1263
Lavey-les-Bains (Sonney *et al.*, 2007)	Vaud	3000 ?	Hercynian	Gneiss			105	2503	7.20			525	16.4	61.0	0.34	315	72.0		768	< 0.1	96.0	1878

Well	Br	F	B	I	HPO_4	NH_4	Li	Ba	Sr	Mn	Fe	Ti	Rb	Cs	Ge	W	Al	As	Zn	Cu	Ni	Co	Cr	Pb	Ag	Sb	Sn	U	Th
	mg/l	mg/l	mg/l	mg/l	mg/l	mg/l	mg/l	mg/l	mg/l	mg/l	mg/l	µg/l	µg/l	µg/l	µg/l	µg/l	µg/l	µg/l	µg/l	µg/l	µg/l	µg/l	µg/l	µg/l	µg/l	µg/l	µg/l	µg/l	µg/l
TH-31, TH 31/62						0.3	0.21			0.47	1.7																		
TP-41, TP 41/88																													
TH-20		7.6									0.24																		
TH-10, TH 10/61		6.8			0.19	0.3	0.57				5.0																		
HV-3C		0.4			0.10		0.040			0.090	1.7																		
SR-1																													
PVGT-LT1 (November 2007)		< 0.5			< 0.04	3.1				0.13	0.55																	5.0	< 500
PVGT-LT1 (May 2015)	1.78	0.38	0.110		0.10	2.3	0.066	2.60	0.32	0.086	0.66						100		3200	< 5	25.0	23	< 0.11	< 0.5	< 5				
PVGT-LT1 (November 26, 2015)	2.09	0.30	0.060		< 0.05	3.8	0.078	2.18	0.39	0.25	0.81		35.5	1.2	< 0.5	0.16	1.42	0.45	6.83	< 0.1	35.6	0.60		< 0.05	< 0.01	0.34	< 0.05	0.27	< 0.1
Pravridlo (ancient spring) - Cadek *et al.* (1968)	0.147	7.8					0.29																						
Pravridlo (ancient spring) - Dupalova *et al.* (2012)		7.2				0.023	0.39	0.090	0.29	< 0,013	0.022							< 18			1.60								
TP-28 - Dupalova *et al.* (2012)		6.8				0.104	0.53	0.083	0.32	0.016	0.52							45			0.90								
Pravridlo (ancient spring, http://lazneteplice.cz)	0.157	5.7	0.066	0.008	0.024		0.38	0.010	0.44	0.002	0.015		75.0	18						0.59				< 0.5	0.43	< 0.8	0.8		
Pravridlo (ancient spring, November 24, 2015)	0.216	7.3	0.083		< 0.05	< 0.05	0.32	0.082	0.36	0.050	< 0.02		72.2	19	1.64	4.3	1.23	3.64	8.17	22.8	0.52	< 0.05		0.24	0.01	0.07	< 0.05	4.35	< 0.1
Thonex-1 (01/10/1993) - Vuataz and Giroud (2010)	1.50	4.4	1.5	2.4		1.6	0.85	< 10	0.85	0.32	0.030						38.0		< 100					< 50					
Thonex-1 (29/03/1994) - Vuataz and Giroud (2010)																													
Thonex-1 (14/06/1996) - Vuataz and Giroud (2010)																													
Thonex-1 (05/11/1997) - Vuataz and Giroud (2010)	1.61		1.2	0.60			0.36	0.20	0.36	0.068	0.37	7.1			5.6	7.5	11.2	1.8	1.4										
Thonex-1 (17/06/2010) - Vuataz and Giroud (2010)	2.26	5.3		44.2		4.3	0.72	0.083	0.72	0.11	0.089	< 0.1	18.0	1.5		1.2	< 1	0.33	< 1					< 0.02				0.04	
Thonex-1 (25/07/2016) - This study	1.66	6.2	1.2	0.66	< 0.1	1.5	0.67	0.144	0.67	0.26	0.14		16.5	0.64	9.2	4.3	0.52	0.05	< 0.5	< 0.1	0.12	< 0.05	0.19	< 0.05					
Thonex-1 (25/10/2016) - This study	1.86	6.2	1.3	0.37	< 0.1	1.7	0.70	0.128	0.70	0.086	2.8		19.1	0.89	0.57	3.1	2.0	0.09	1.2	< 0.1	< 0.1	< 0.05	< 0.1	< 0.05					
Lavey-les-Bains (Sonney *et al.*, 2007)	3.30	9.3	3.4	0.40	< 0.5	0.50	4.8	0.030	2.8	0.024	0.061		100	60	26	150	25.0	< 5	12	6	< 10	< 10	< 10	< 1				< 0.1	

Well	δD_{H2O} ‰	$\delta^{18}O_{H2O}$ ‰	^{3}H TU	$\delta^{13}C_{DIC}$ ‰	$\delta^{34}S_{SO4}$ ‰	$\delta^{34}S_{H2S}$ ‰	$\delta^{18}O_{SO4}$ ‰	$\delta^{11}B$ ‰	$\delta^{7}Li$ ‰	$^{87}Sr/^{86}Sr$
TH-31, TH 31/62										
TP-41, TP 41/88										
TH-20										
TH-10, TH 10/61										
HV-3C										
SR-1										
PVGT-LT1 (November 2007)										
PVGT-LT1 (May 2015)	-64.9	-9.1								
PVGT-LT1 (November 26, 2015)	-65.7	-8.8		-8.4	n.d.		n.d.	5.88	0.9	0.710048
Pravridlo (ancient spring) - Cadek *et al.* (1968)										
Pravridlo - Dupalova *et al.* (2012)	-69.0	-9.9		-5.4	1.78		10.4			0.718600
TP-28 - Dupalova *et al.* (2012)	-69.0	-9.8		-6.5	1.39		10.5			
Pravridlo (ancient spring, http://lazneteplice.cz)										
Pravridlo (ancient spring, November 24, 2015)	-69.5	-9.9		-4.5	3.40		2.8	9.30	1.2	0.720322
Thonex-1 (01/10/1993) - Vuataz and Giroud (2010)	-81.9	-10.8	3.5	0.43	22.2		11.5			
Thonex-1 (29/03/1994) - Vuataz and Giroud (2010)										
Thonex-1 (14/06/1996) - Vuataz and Giroud (2010)										
Thonex-1 (05/11/1997) - Vuataz and Giroud (2010)										
Thonex-1 (17/06/2010) - Vuataz and Giroud (2010)	-81.0	-10.6	< 0.4	-2.3	87.5	52.3	17.6			0.707675
Thonex-1 (25/07/2016) - This study	-82.2	-11.0							9.6	0.707639
Thonex-1 (25/10/2016) - This study	-81.7	-10.9		1.1	46.2		12.1	13.72	9.3	0.707646
Lavey-les-Bains (Sonney *et al.*, 2007)	-98.5	-13.4	< 0.5		21.9	-9.5	8.5			